UNIVERSITY OF CALIFORNIA SAN DIEGO

Inorganic Nanoparticles Increasing Stem Cell Contrast and Therapeutic Efficacy in Myocardial Infarction Treatment

A dissertation submitted in partial satisfaction of the requirements
for the degree Doctor of Philosophy

in

Materials Science & Engineering

by

Fang Chen

Committee in charge:

Professor Jesse V. Jokerst, Chair
Professor Shaochen Chen
Professor Yi Chen
Professor Michael J. Sailor
Professor Liangfang Zhang

2019

The Dissertation of Fang Chen is approved, and it is acceptable in quality and form for publication on microfilm and electronically:

_____

_____

_____

_____

_____

Chair

University of California San Diego

2019

DEDICATION

To Mr. Yuqi Chen and Ms. Xiaonian Cao,

for their endless love and support.

To the Great Almighty,

the author of knowledge and wisdom,

for His countless love.

EPIGRAPH

Guard your HEART above all else, for it is the source of life.

Proverb 4:23

TABLE OF CONTENTS

LIST OF FIGURES

LIST OF TABLES

ACKNOWLEDGEMENTS

First, I would like to thank my advisor, Professor Jesse Jokerst, for his devotion in the guidance to me and being a perfect modal as an enthusiastic scientist. My deepest gratitude is the trust from Prof. Jokerst and the confidence he helped me build up. With the four years training in his lab, I find my position and confidence in research.

All the members of the Jokerst's Bioimaging Lab have been supportive and helpful. Particularly, I would like to thank my coworkers, Eric, Ghanim, and Sean, for their engagement and effort in the designated projects without any complaints.

Thanks to the UCSD, for cultivating such an open atmosphere for collaborations. Thanks to all my collaborators, in particular, Dr. Ming Ma, Dr. Yusu Gu, Dr. Jingting Li, Prof. George Sen, and Prof. Gongyi Li, for their inspirations and all the discussions.

Many thanks to my committee members, Professor Liangfang Zhang, Professor Michael J. Sailor, Professor Shaochen Chen, and Professor Yi Chen, for their comments on my project and dissertation as well as their support and suggestions on my future career.

I want to express sincere gratitude to my family. Thanks to my husband for his accompany, support, and valued assistance. Thanks to my parents for their endless love and unconditional support. This dissertation is dedicated to them.

Foremost, I would like to thank Almighty for giving me the strength, knowledge, ability, and opportunity to undertake this research study. Thanks to all the people He used to help me.

The text of Chapter 1, in part, is a reprint of the material as it appears in "Multifunctional nanomedicine with silica: Role of silica in nanoparticles for theranostic, imaging, and drug monitoring" by Fang Chen, Ghanim Hableel, and Jesse V. Jokerst, Journal of colloid and interface science, 2018. The dissertation author was the primary researcher of this paper.

The text of Chapter 2, in part, is the reprint of the material as it appears in

"Exosome-Like Silica Nanoparticles: A Novel Ultrasound Contrast Agent for Stem Cell Imaging" by Fang Chen, Ming Ma, Junxin Wang, Fang Wang, Shixiong Chen, Eric R. Zhao, Anamik Jhunjhunwala, Sean Darmadi, Hangrong Chen, Jesse V. Jokerst, Nanoscale, 2017. The dissertation author was the primary researcher of this paper.

The text of Chapter 3, in part, is the reprint of the material as it appears in "Cellular toxicity of silicon carbide nanomaterials as a function of morphology" by Fang Chen, Gongyi Li, Eric R. Zhao, Jingting Li, Ghanim Hableel, Jeanne E. Lemaster, Yuting Bai, George L. Sen, Jesse V. Jokerst, Biomaterials, 2018, and "Silicon carbide nanoparticles as photoacoustic and photoluminescent dual-imaging contrast agent for long-term cell tracking" by Fang Chen, Eric R. Zhao, Tao Hu, Yuesong Shi, Donald J. Sirbuly, Jesse V. Jokerst, to be published, 2019. The dissertation author was the primary researcher of both papers.

The text of Chapter 4, in part, is the reprint of the material as it appears in "Organosilica Nanoparticles with an Intrinsic Secondary Amine: An Efficient and Reusable Adsorbent for Dyes" by Fang Chen, Eric R. Zhao, Taeho Kim, Junxin Wang, Ghanim Hableel, Philip J.T. Reardon, Soundaram J. Ananthakrishna, Tianyu Wang, Santiago Arconada-Alvarez, Jonathan C. Knowles, Jesse V. Jokerst, ACS Applied Materials & Interfaces, 2017. The dissertation author was the primary researcher of this paper.

The text of Chapter 5, in part, is the reprint of the material as it appears in "Increases Efficacy of Stem Cell Therapy via Triple-functional Inorganic Nanoparticles" by Fang Chen, Eric R. Zhao, Ghanim Hableel, Tao Hu, Taeho Kim, Jingting Li, Natalia I. Gonzalez-Pech, David J. Cheng, Jeanne E. Lemaster, Yijun Xie, Vicki H. Grassian, George L. Sen, Jesse V. Jokerst, to be published, 2019. The dissertation author was the primary researcher of this paper.

VITA

2008 Bachelor of Science, Southeast University (Nanjing, China)

2009 University of Science and Technology of China (Hefei, China)

2011 Master of Engineering, Shanghai Institute of Ceramics Chinese Academy of Sciences (Shanghai, China)

2019 Doctor of Philosophy, University of California San Diego (La Jolla, USA)

PUBLICATIONS

- **Chen F**, Zhao E, Hableel G, Hu T, Kim T, Li J, Gonzalez-Pech NI, Cheng DJ, Lemaster JE, Xie Y, Grassian V, Sen GL, Jokerst JV. Triple-functional nanomedicine increases stem cell therapy efficacy in ischemia reperfusion injury mice hearts. *ACS Nano*. Under revision.
- **Chen F**[#], Zhao E[#], Hu T, Shi Y, Sirbuly D, Jokerst JV. SiC nanoparticles working as photoacoustic and luminescent dual imaging contrast agents for stem cells tracking. *Nano Letters*. Submitted.
- Hariri A, **Chen F**, Moore C, Jokerst JV. Non-invasive Staging of Pressure Ulcers Using Photoacoustic Imaging. Under review.
- Wang J, Hsu S, Gonzalez-Pech NI, Jhunjhunwala A, Hariri A, **Chen F**, Grassian V, Tao A, Jokerst JV. Copper Sulfide Nanodisks and Nanoprisms for Photoacoustic Ovarian Tumor Imaging. Under review.
- Lemaster JE, Wang Z, Hariri A, **Chen F**, Hu Z, Huang Y, Barback C, Cochran R, Gianneschi N, Jokerst JV. Gadolinium doping enhances the photoacoustic signal of synthetic melanin nanoparticles: a dual modality contrast agent for stem cell imaging. *Chemistry of Materials*. **2018**, 31, 251-259.
- **Chen F**, Li G, Zhao E, Li J, Hableel G, Lemaster JE, Bai Y, Sen GL, Jokerst JV. Cellular toxicity of silicon carbide nanomaterials as a function of morphology. *Biomaterials.* **2018**, 179, 60-70.
- **Chen F**, Ghanim Hableel, Zhao E, Jokerst JV. Fantastic voyage with silica: application of hybrid silica nanoparticles in theranostic nanomedicine and multimodal imaging. *Journal of Colloid and Interface Science*. **2018**, 521, 261-279.
- Lemaster JE, **Chen F,** Kim T, Hariri A, Jokerst JV. Development of a trimodal contrast agent for acoustic and magnetic particle imaging of stem cells. *ACS Applied Nano Materials.* **2018**, 1, 1321-1331.

- Dhong C, Edmunds S, Ramirez J, Kayser L, **Chen F**, Jokerst JV, Lipomi D. Optics-free, non-contact measurements of fluids, bubbles and particles in microchannels using metallic nanoislands on graphene. *Nano Letters*. **2018**, 18(8), 5306-5311.
- Wang J, Humphries K, Jeevarathinam AS, Jhunjhunwala A, **Chen F**, Hariri A, Miller B, Jokerst JV. A mechanistic investigation of methylene blue and heparin interactions in phosphate buffered saline. *Bioconjugate Chemistry.* **2018**, 29, 3768-3775.
- **Chen F**, Zhao E, Kim T, Wang J, Hableel G, Reardon PJ, Ananthakrishnan SJ, Wang T, Arconada-Alvarez SJ, Knowles JC, Jokerst JV. Organosilica nanoparticles with an intrinsic secondary amine: an efficient and reusable adsorbent for dyes. *ACS Applied Materials & Interfaces*. **2017**, 9, 15566-15576.
- **Chen F**, Ma M, Wang J, Wang F, Chern S, Zhao E, Jhunjhunwala A, Darmadi S, Chen H, Jokerst JV. Exosome-like silica nanoparticles: a novel ultrasound contrast agent for stem cell imaging. *Nanoscale*. 2017, 9, 402-411.
- Lin CY, **Chen F**, Hariri A, Chen CJ, Wilder-Smith P, Takesh T, Jokerst JV. Photoacoustic imaging for noninvasive periodontal probing depth measurements. *Journal of Dental Research*. 2017, 97, 23-30.
- Kim T, Lemaster JE, **Chen F**, Li J, Jokerst JV. Photoacoustic imaging of human mesenchymal stem cells labeled with prussian blue-poly (l-lysine) nanocomplexes. *ACS nano*. **2017**, 11, 9022-9032.
- Wang J, **Chen F**, Arconada-Alvarez SJ, Hartanto J, Yap LP, Park R, Wang F, Vorobyova I, Dagliyan G, Conti PS, Jokerst JV. A nanoscale tool for photoacoustic-based measurements of clotting time and therapeutic drug monitoring of heparin. *Nano Letters*. **2016**, 16, 6265-6271.
- **Chen F**, Zhu Y. Chitosan enclosed mesoporous silica nanoparticles as drug nano-carriers: sensitive response to the narrow pH range. *Microporous and Mesoporous Materials*, **2012**, 150, 83-89.

FIELDS OF STUDY

Major Field: Engineering

Studies in Biomaterials, Nanotechnology, Bioimaging, and Bioengineering.

Professor Jesse V. Jokerst

ABSTRACT OF THE DISSERTATION

Inorganic Nanoparticles Increasing Stem Cell Contrast and Therapeutic Efficacy in Myocardial Infarction Treatment

by

Fang Chen

Doctor of Philosophy in Materials Science and Engineering

University of California San Diego, 2019

Professor Jesse V. Jokerst, Chair

Cardiovascular diseases are a leading cause of death. Although the existing therapies can lower early mortality rates and reduce the risk of further heart attacks, patients can suffer from existing damage for their rest of life due to the very limited regeneration capacity of heart. Therefore, many efforts have been made to regenerate and repair cardiac tissue via stem cells. However, stem cell therapy in cardiovascular diseases treatment is challenged by mis-injection, poor survival, and low retention of cells. Solutions to these challenges can be multimodal imaging contrast agents, sustained or controlled drug delivery, and magnetic manipulation of cells, all of which bring attention to nanotechnology. In this dissertation, I will demonstrate how nanotechnology can benefit stem cell therapy with inorganic silicon-based nanomaterials and mesenchymal stem cells. Mesenchymal stem cells (MSCs) are used in this dissertation because they are particularly promising due to their abundance, potent proliferation, and multi-lineage differentiation capacity.

First, the role of hybrid nanoparticles in multi-modal imaging and theranostic

nanomedicine and an introduction to medical imaging modalities and therapeutic methods are reviewed.

The second chapter describes a novel discoid silica nanoparticle, which offered the most enhanced ultrasound signal of MSCs compared to three other classical silica structures including Stober silica, mesoporous silica, and mesocellular foam silica.

The third chapter first introduce the biocompatibility of silicon carbide nanomaterials. Silicon carbide nanowires inhibited proliferation and differentiation of MSCs while silicon carbide nanoparticles showed no impact on the MSCs' viability and functions. In the second part, the potential of silicon carbide nanoparticles in stem cell long-term imaging/tracking via photoacoustic and photoluminescence imaging is shown.

The fourth chapter studies the drug adsorption behavior of organosilica nanoparticles with intrinsic amine groups.

Last, a biocompatible multi-functional silica-iron oxide nanoparticle is designed. This nanoparticle increases MRI and ultrasound contrast, cell viability, and retention of MSCs. *In vivo* studies show that labeling stem cells with this nanoparticle increase the stem cell therapy efficacy in murine animals injured by a ligation/reperfusion surgery.

Chapter 1.

Application of inorganic hybrid nanoparticles in multi-modal imaging and theranostic nanomedicine

1. Introduction

A microscopic system that can help doctors diagnose and treat diseases has fascinated the public and researchers since 1966. The emergence of nanotechnology in the 1980s pushed this dream closer to reality. Efforts towards building a multifunctional nanomedicine device include studies in multimodal imaging and theranostic nanomedicine[1, 2]. These tools can diagnose patients using a variety of imaging modalities and can deliver cargo for imaging and/or therapy.

1.1. Definition and categories of nanomaterials

Nanomaterials are materials that have unique properties as a function of their intrinsic features smaller than 1000 nm. These materials typically differ in physical properties from bulk materials[3]. Nanomaterials that are popular in biology and medicine can be either man-made or natural. Man-made nanomaterials include carbon nanotubes[4-7], graphene[8-11], liposomes[12-15], dendrimers[16-20], polymers[21-27], silicon[28] and silicas[29-35] and other sol-gels[36], quantum dots[37-40], up-conversion nanoparticles (UCNPs)[41-45], superparamagnetic iron oxide nanoparticles[46-50], other metal oxides nanoparticles[51-54], and noble metals[55-59]. Natural nanomaterials used in nanomedicine are mainly deoxyribonucleic acid (DNA)[60-63]. In nanomedicine, these nanomaterials are commonly synthesized in the form of nanoparticles which range in size between one and several hundred nanometers[4, 64].

1.2. Properties of nanomaterials

Regardless of the underlying material, nanoparticles have a large surface area and high surface-to-volume ratio. These particles are comparable to the size of DNA plasmids,

antibodies, enzymes, other biological macromolecules as well as cell products like exosomes[65]. This large surface area enables a high loading capacity of functional molecules such as therapeutics and imaging agents. Also, some nanoparticles have large porosity which is beneficial to high loading. Important factors that influence the nanoparticles' biodistribution include size, surface charge, dispersity, and hydrophobicity[66]. Generally, nanoparticles with a size smaller than 8 nm will be rapidly cleared by the kidneys. Larger nanoparticles between 30 to 200 nm can accumulate in tumors by the enhanced permeability and retention (EPR) effect[67]. The small size of nanoparticles also benefits cell endocytosis[68, 69]. The surface properties are also important for nanoparticles because altering the surface chemistry of a nanoparticle will change its hydrodynamic size and surface charge as well as its reactivity (e.g., binding affinity).

Nanoparticles with positive surface charge are often more toxic because of complications such as hemolysis and platelet aggregation. Positively charged nanoparticles can also have shorter circulation half-lives than negative and neutral counterparts[67]. Hydrophobic nanoparticles will be rapidly cleared by the reticuloendothelial system (RES)[66].

While nanoparticles share a small size and high surface area, they differ in terms of the endogenous properties that govern their biocompatibility. The advantages and disadvantages as well as applications of various nanoparticles are presented in **Table 1.1**. Carbon nanotubes are pseudo one-dimensional nanomaterials that can penetrate through different cellular barriers. The high specific surface area and void in the center of carbon nanotubes can be used for drug delivery[4-7]. Graphene is a two-dimensional (2D) sheet of sp^2-hybridized carbon atoms packed into a honeycomb lattice. The high surface area gives

graphene a high adsorption capacity for molecules[8-11].

Table 1.1. The primary advantages, disadvantages, and main biological applications of common nanoparticle types. (NP: nanoparticles; SPION: superparamagnetic iron oxide nanoparticles; CT: computerized tomography; MPI: magnetic particle imaging; MRI: magnetic resonance imaging; PAI: photoacoustic imaging[70]; PDT: photodynamic therapy; PTT: photothermal therapy; RES: reticuloendothelial system). Reprinted with permission from JCIS[2].

Nanomaterials	Advantages	Disadvantages	Applications
Carbon nanotubes[4-7]	Extravasation, small in one dimension	Toxic in certain formats, non-biodegradable	Raman, PAI, drug delivery
Graphene[8-11]	High thermal conductivity, Flexible, large surface area	Non-biodegradable, Poor dispersibility	Biosensors, PTT, drug delivery, optical image
Liposomes[12-15]	Biocompatible, load both hydrophobic and hydrophilic cargos, fuse with cells	Unstable storage, rapid leakage of hydrophilic drugs, low encapsulation	Ultrasound, lipofection, drug delivery
Dendrimers[16-20]	Controlled morphologies and degradation, high ligand density, homogeneity	Multistep synthesis, high cost	Drug delivery, gene delivery, blood substitution
Polymer NPs[21-26, 71]	Biocompatible, wide variety, high encapsulation	Unstable structure, drug leakage	Ultrasound, drug delivery
DNA[60-63]	Exquisite size control, functional designs	Unstable	Drug delivery
Silica NPs[29-35]	Tunable morphologies, easy surface modification, biocompatible, degradable	Poor biodistribution	Ultrasound, drug delivery, define sentinel lymph nodes
Quantum dots[37-40]	Tunable emission, single excitation, good biodistribution	Toxic components, non-biodegradable	Optical imaging, PTT
UCNPs[41-45]	Narrow emission spectra, long luminescence lifetime chemically stable	Low brightness, size, surface, laser power density dependent quantum yield	Optical imaging, PTT, photo-induced drug delivery, biosensors
SPION[46-50]	MRI T2-weighted contrast, stable, biodegradable	Weak signal, high dose, RES accumulation	MRI, MPI, hyperthermia, directing, separation
Other metal oxide NPs[51-53]	Tunable morphology, degradable	Poor biocompatibility	Antimicrobial agents, drug delivery
Noble metals NPs[55-59, 72]	Tunable, stable, inert, thermally conductive, plasmonic	Weak signal, low drug loading, poor biodistribution, non-biodegradable	CT, PAI, PDT, PTT

Liposomes are spheres composed of lipid bilayer similar to biological membranes. Liposomes have been used to load cargos such as therapeutic molecules, nucleic acids, and fluorocarbon gas to achieve drug delivery, lipofection, and ultrasound contrast agents.[12-15] Dendrimers are highly branched polymers that can form nanoparticles with voids to load drugs and genes. Dendrimers can also be used as a blood substutite[16-20]. DNA origami utilizes the nanoscale folding of DNA and has been applied to drug delivery[60-63]. Quantum dots are luminescent zero-dimensional particles, and their photoluminescence can be manipulated to specific wavelengths by controlling the particle diameter[73]. They are commonly used in fluorescence/luminescence imaging[37-40].

UCNPs are nanoparticles that absorb two or more incident photons of relatively low energy[74]. These are then converted into one emitted photon with higher energy. These nanoparticles usually contain transition metals and are used for bio-imaging[41-45]. Superparamagnetic iron oxide nanoparticles have also been widely used as MRI contrast agents and manipulators combined with magnetic fields[46-50]. Other commonly investigated metal oxides nanoparticles include titanium oxide, zinc oxide, and manganese oxide (MnO) nanoparticles[51-53]. Noble metal nanoparticles are usually nanoscale particles composed of gold and/or silver, and these have surface plasmon resonance (SPR) that can enhance the sensitivity of several spectroscopic measurements such as fluorescence, Raman scattering, and second harmonics[75, 76]. Other emerging nanomedicines include fullerenes[77], nanoclays[78], and micelles[79].

1.3. Potential and challenges of nanomaterials in medicine

Nanomedicine based on the above nanomaterials has been reported to improve the medical imaging and treatment of various diseases, such as cancers[80-83], degenerative

diseases[84, 85], heart disease[86, 87], diabetes[88, 89], and toxin detection[90]. Some nanomaterials are commercially available for their medical applications. For example, Abraxane, Doxil, and Megace ES are Food and Drug Administration (FDA)-approved nanotechnology-based drugs used to treat cancers[81]. Moreover, there are many nanomaterials that are currently in clinical trials. For instance, Cornell Dots (C-dots) are a nanoparticle-based diagnostic tool that is used for imaging tumors[91] and currently in clinical trials. However, these commercial nanosystems have only one function.

Indeed, diagnosis and therapy are currently two separate steps. Multiple nanosystems are needed if each nanosystem can only perform one of those functions, but can results in problems with interference and dosage. First, nanosystems may interfere with each other causing unexpected side effects or decreasing the diagnostic and/or treatment efficacy. Second, using a higher dosage of materials increases the risk of toxicity. Therefore, developing multifunctional systems has a critical role in improving human health.

Multifunctional diagnostic and therapeutic incorporate several nanomaterials into one host material. This material must be compatible with a wide variety of functional molecules and/or nanoparticles. Silica nanoparticles are an excellent example for a host material because they demonstrate multi-functionality, biocompatibility, stability, and biodegradability.

1.4. Advantages of silica nanoparticles

Silica nanoparticles have many advantages for medicine. First, the chemistry is easily tuned to create nanomaterials with defined sizes, shapes, and surface properties[92]. The easily modifiable chemistry in silica is essential for optimal biocompatibility and

biodistribution[29, 93]. Silica nanoparticles synthesis has a history spanning over 60 years. Monodispersed amorphous silica nanoparticles were first synthesized by Kolbe in 1956[94] and was then improved by Stöber and Fink in 1968[95]. Stöber's method tunes the size of silica nanoparticles from tens of nanometers to several micrometers in diameter by changing the ratio of catalyst and precursor. In the early 1990s, "Template"-guided synthesis methods for mesoporous silica nanoparticles were reported by scientists from Japan and the Mobil corporation[96-98]. Examples of tunable silica nanomaterials include solid spheres[94, 95], mesoporous particles[96-99], mesoporous hollow spheres[100, 101], rattle-typed spheres[102], foam-like nanoparticles[103], nanotubes[104], mesoporous red blood cell-shaped nanoparticles, *etc*. **Figure 1.2** show examples of silica nanoparticles with different morphologies[32]. In addition, the surface of silica nanoparticles can be easily modified with functional molecules[105] including spacers for colloidal stability[106], antibodies for active targeting[107], fluorophores for imaging[108], magnetic nanoparticles[109] for manipulation or MRI, gating molecules to stimulate drug release[110], functional groups to tune surface charge[33], and therapeutic agents[111] (**Figure 1.2I**).

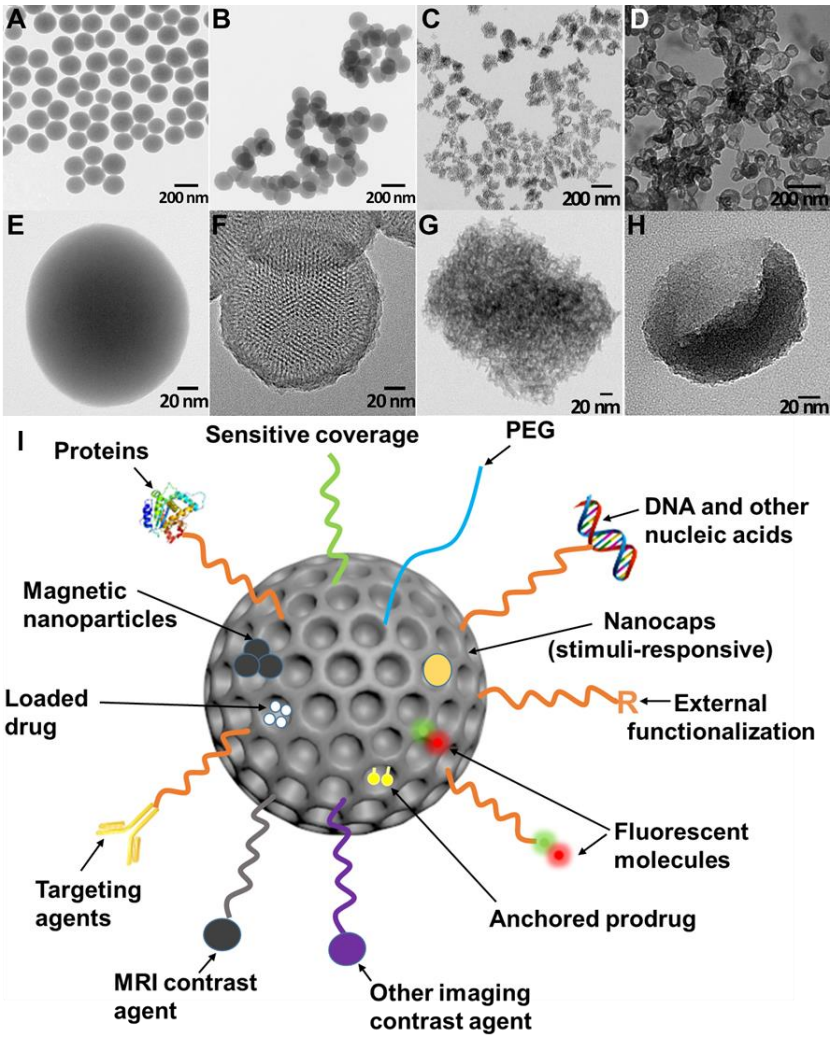

Figure 1.2. TEM images and modification scheme of silica nanoparticles. TEM images of solid Stöber silica nanoparticles (A, E), MCM-41 mesoporous silica nanoparticles (B, F), mesocellular foam silica nanoparticles (C, G), and exosome-like silica nanoparticles (D, H) (Adapted from reference[32]). (I) Multifunctionality of silica nanoparticles. PEG is polyethylene glycol. Reprinted with permission from JCIS[2].

Silica nanoparticles may have good biocompatibility because they degrade to nontoxic silicic acid *in vivo*[112-114], and silicic acid is naturally found in many tissues and can be excreted from the body through urine[113]. However, the toxicity depends on their dosage[115], crystallinity[35, 115, 116], particle size[92, 117, 118], surface properties[117, 119], and administration route[120, 121]. Higher dosage increases the risk for toxicity. Crystal silica nanoparticles are toxic and cause silicosis[116]. But amorphous silica has been used as a food

additive for decades because of its excellent biocompatibility[35, 115].Smaller particles have been reported to be less biocompatible than larger ones[92, 117, 118], possibly due to the increased specific surface area. However, this is still controversial[122]. Decreasing the surface hydroxyl groups increases the silica nanoparticles biocompatibility[119]. The size and surface properties of amorphous silica nanoparticles can easily be tuned to increase the biocompatibility. Nanoparticles administered orally have less immunotoxicity than intravenous, intraperitoneal, and subcutaneous route, but also lower bioavailability with less availability for the immune cells to interact with the nanoparticles[122].

Silica nanoparticles are intrinsically stable, and moreover their degradability and circulation time can be tuned[123-126]. Generally, silica nanoparticles carry drug in their mesopores and release the drug through diffusion. Therefore, stability is important to enable the silica nanoparticles to be retained in the body and release the drug. This stability also guarantees no drug leakage from capped porous silica nanoparticles that release drug as a function of external stimuli[125, 127]. Though silica nanoparticles are usually cleared by the human body within a short time, surface modifications such as PEGylation can prolong the circulation period of silica nanoparticles[128]. On the other hand, imaging contrast agents need to be quickly cleared to decrease background signal and prevent interference with future scans. In this case, increasing the pore size of silica nanoparticles and doping them with metal ions can accelerate their degradation to get a short circulation time[114, 126].

Finally, pure silica nanoparticles have intrinsic theranostic potentials stemming from high acoustic mismatch with most soft tissues. Also, silica nanoparticles can be customized to label cells and tissues and therefore increase their ultrasound contrast after transplantation[32, 69, 129, 130]. The therapeutic effects of silica nanoparticles result from their

large surface area and porous structures. The large surface area provides plenty of conjugation sites or physical binding sites for therapeutic molecules[131-133], and the pores in the silica nanoparticles can physically hold and protect cargo[134-136].

In summary, silica nanoparticles are ideal for nanomedicine and biomaterials research due to their various morphologies, facile chemical modification, tunable pore size and porosity, biocompatibility, tunable stability and biodegradability, and theranostic potential.

2. Synthesis, modification, and integration of silica nanoparticles

2.1. Synthesis of silica nanoparticles

Silica nanoparticles can be prepared via bottom-up or top-down methods. Bottom-up synthesis usually involves catalyzed hydrolysis and condensation of silica sources[95, 99]. The top-down synthesis of silica nanoparticles includes electrochemical etching of silicon wafer and pyrolysis of quartz sand[119, 137].

Bottom-up synthesis is very common in laboratory research because it is simple, safe, and can make various morphologies. Bottom-up synthesis typically uses an aqueous or ethanol-based solvent, and this method usually involves silica sources, catalysts, and templates. The most prevalent silica source is an alkoxide of silicon scuh as tetraethyl orthosilicate (TEOS). The alkoxide first hydrolyzes and produces silicate species and alcohol (Equation 1.1). The silicates then condense and form Si-O-Si linkages (Equation 1.2). In addition, organosilanes such as aminopropyl-trimethoxysilane and mercaptopropyl-methoxysilane are usually used as co-precursors, which can introduce functional groups to the silica nanoparticles surface[1].

$$Si(OR)_4 + H_2O \rightarrow (RO)_3Si(OH) + ROH \qquad \text{Equation 1.1}$$

$(RO)_3Si(OH) + (HO)Si(OR)_3 \rightarrow (RO)_3Si\text{-}O\text{-}Si(OR)_3 + H_2O$ Equation 1.2

R represents alkyl groups and is usually methyl or ethyl groups. The hydrolysis of silica sources can be catalyzed either by acids or bases. Under basic conditions, the polymerization and condensation of silicate species are reversible, which makes it easier to obtain homogenous silica products. On the contrary, highly acidic conditions lead to rapid hydrolysis and precipitation of silica particles. The production of silica nanoparticles can be accelerated by decreasing pH, but that often results in poly-disperse products[99]. Templates are used to generate porous structure in the silica nanoparticles. The most common templates are surfactants that form micelles in solvents and create mesopores that are smaller than 5 nm. This pore size is suitable for small molecule cargos. Larger pores are needed to load macromolecules and small nanoparticles such as quantum dots. To enlarge silica nanoparticles pores, polymers and pore expanding agents are normally used[138]. Interestingly, cells and organs can also be used as templates[139, 140].

Top-down methods are more hazardous to implement because they require highly corrosive hydrofluoric acid (electrochemical etching) or high temperatures (>1500 ℃, pyrolysis)[141]. Moreover, tuning silica nanoparticles morphology is difficult using top-down methods. For example, fumed silica nanoparticles prepared by pyrolysis are nonporous and range in size from 5 to 50 nm. These nanoparticles are commonly used as light abrasives in toothpaste or as anticaking agents and desiccants. On the contrary, the silica nanoparticles obtained by electrochemical etching have an irregular 2D porous structure. The direct products from electrochemical etching are porous silicon stand-free films. To create porous silica nanoparticles, the silicon films are broken down by sonication and then oxidized[137, 142].

2.2. Surface modification of silica nanoparticles

The surface of silica nanoparticles can be modified with polymer chains either chemically (by covalent bonding) or physically (by physisorption)[143]. Physical modification is usually reversible. It is not as common as chemical modification due to the instability of the non-covalent bond[144].

Subsequent chemical modification is enabled by the silanol and siloxane groups on the silica. The number and form of the silanol groups changes as a function of synthesis route[119]. Colloidal silica nanoparticles are almost completely hydroxylated, and all silanols have hydrogen bonds. Fumed silica nanoparticles have much lower silanol contents—only about half of the surface has silanols. Approximately 10% of the silanols on fumed silica nanoparticle surfaces are isolated. Heat treatment can decrease the silanol content on both types of silica nanoparticles.[119]

Silanol groups are the main reason underlying the facile modification of silica nanoparticles. These groups can react with abundant and commercially available silane reagents. Silanes then introduce other functional groups onto the surface of silica nanoparticles. The most frequently used silanes have amine or sulfur groups at the end of an alkylsilane along with various PEG-silanes. Amine or thiol-ended groups offer a facile linker chemistry with commonly used linking moieties such as N-hydroxysuccinide (NHS) functionalized molecules, isothiocyanates, maleimides, etc[107, 145]. Both of these functional groups can also be used to tune the surface charge of the silica nanoparticles[33, 146]. Alkylsilanes are used for hydrophobic surface treatment and to increase the echogenicity of silica nanoparticles[147]. PEG-silanes graft PEG onto silica nanoparticles, improve the particles stability in biological fluids, and prolong the *in vivo* circulation time[148, 149]. **Table**

1.3 presents the most frequently used silanes for nanoparticle surface modification and their functions.

Table 1.3. The most frequently used silanes used for surface modification on silica nanoparticles (NPs) and their functions. Reprinted with permission from JCIS[2].

Silanes	Function Group	Application
(3-aminopropyl)trimethoxy silane (APTMS) (3-aminopropyl)triethoxy silane (APTES)	-NH_2	Reduced aggregation[106], fluorescent labeling[145], surface charge modification[146], DNA binding and protection from enzymatic cleavage[150]
(3-mercaptopropyl)-trimethoxy silane (MPTMS)	-SH	Conjugate with maleimides[107], thiol/disulfide exchange reactions to attach oligonucleotides[151], surface charge modification[33, 152]
Polyethylene glycol-silane (PEG-silane)	-PEG	Increased circulation time[153], reduced aggregation and increase particle dispersity in aqueous solution[128]
Alkylsilane	Alkyl chain	Hydrophobic coating[154], Increase ultrasound contrast[155]
Carboxyethylsilanetriol	-COOH	Functionalize silica NPs and provide reactive sites for amine[156]
3-trihydroxysilylpropyl methylphosphonate	-PO_3^-	Functionalize silica NPs and provide reactive sites for amine[157]
(3-isocyanatopropyl)-triethoxy silane	-NCO	Functionalize silica NPs and provide reactive sites for amine[158]

2.3. Formulations/functions of silica in integrated nanoparticles

Silica mainly exists as a core, shell, or matrix for doping in integrated nanoparticles. **Table 1.4** summarizes the major functions of silica as a function of its formulation in the nanoparticles along with relevant literature sources. The synthesis of nanoparticles with a silica core involves the preparation of silica nanoparticles followed by a multi-step modification[107, 159, 160]. The synthesis of the silica core is similar to the preparation of silica nanoparticles—mainly polymerization and condensation of silica sources[99].

Table 1.4. Functions of silica in integrated nanoparticles. Reprinted with permission from JCIS[2].

Formulations	Function
Silica core	High dielectric constant enhances light absorption[161] Therapeutic reservoir for drug delivery[159, 162, 163] Increase ultrasound contrast[130]
Silica shell	Facilitates functionalization of NPs surface[161, 164] Amplifies photoacoustic signal[165] Therapeutic reservoir for drug delivery[166] Enhances colloidal and chemical stability of the core[167] Separates core from outside layer[168] Decreases cytotoxicity of core[169]
Silica matrix	Prevents photobleaching of fluorophores[145] Decreases cytotoxicity[114, 170, 171]

Similarly, the core/silica shell structures are made via a multistep procedure[169]. Generally, the silica shell is formed by growing a layer of silica on the surfaces of other nanomaterials such as gold nanoparticles, gold nanorods, quantum dots, and iron oxide nanoparticles. The surfaces should have a significant chemical or electrostatic affinity for silica[172], otherwise the surfaces need to be activated. For example, the surfaces of gold nanomaterials have a weak has and therefore stabilizers are typically used on the surface of gold to prevent coagulation. Therefore, the gold surface is usually treated with MPTMS before coating with silica[173].

Doping functional ions, functional groups, and/or molecules into the silica matrix is another method to create multi-functional nanoparticles[174, 175]. There are two methods to dope silica nanoparticles. The first method is a one-pot sol-gel synthesis that mixes silica sources with a wide variety of organic dye molecules, metal ion chelators, or even iron oxide or quantum dots[175]. The other method is reverse microemulsion, which is suitable for doping hydrophobic organic dyes into silica nanoparticles[176-178]. This method involves creating a homogeneous mixture of water, oil, and surfactant molecules; the dye molecules

often need to be modified to increase their affinity for silica[176].

One big challenge for the translation of hybrid silica nanoparticles is simplified synthetic steps that integrate both cargo and carrier. It is currently difficult to achieve one-pot synthesis whereby the cargo is loaded into the nanoparticles as they are being synthetized. This is due to the multiple components involved—especially when sensitive therapeutic/diagnostic molecules are added. Thus, post-synthetic loading remains common to retain the biological activity of the sensitive molecular cargo. However, this method is time-consuming and inefficient, which is difficult to be used industrially. Future research efforts should design creative ways to solve this problem.

3. Biomedical applications of integrated silica nanoparticles

3.1. Imaging modalities

Imaging reveals internal structures under the skin and bones. The right choice of imaging modality is critical to diagnose disease and assess the therapy efficacy. Conventional medical imaging includes nuclear imaging, magnetic resonance imaging, radiography, optical imaging, and US imaging[69].

3.1.1. Nuclear imaging

Nuclear imaging uses trace amounts of radionuclides labeled compounds to provide diagnostic information[179]. The radionuclides will be taken by the patients, decay, and then emit gamma rays or high-energy photons. The gamma rays or photons have significant energy and therefore can penetrate the body. Then, the gamma rays or photons are captured by an external, position-sensitive gamma-ray detector and form an image of the distribution of the radionuclides[179]. Therefore, unlike other imaging modalities, nuclear imaging offers not anatomical images but functional images.

There are two major nuclear imaging modalities: single photon emission computed tomography (SPECT) and positron emission tomography (PET). Both modalities can collect data from multiple angles and form tomographic images[179]. However, SPECT and PET form images with different signals. SPECT uses radionuclides emitting gamma rays, and directly produce images with the gamma rays[69]. While PET uses radionuclides that emit positrons. The emitted positrons then annihilated with an electron quickly and simultaneously produces two high-energy photons. These photons are detected by the PET camera and provide data for images[69, 180].

3.1.2. MRI

Medical MRI uses strong magnetic fields, radio waves, and field gradients to excite hydrogen atoms and detects the relaxation signal from nuclei of hydrogen atoms to generate anatomic images. There are two types of relaxation signal including longitudinal relaxation (T1) and transverse relaxation (T2). The longitudinal relaxation time is known as T1 or spin-lattice relaxation, and it depends on the strength of the external magnetic field as well as the internal motion of the molecules (i.e., the interactions with environment)[69]. The spinning hydrogen proton with an electrical charge behaves like a small magnet[181]. When an external strong magnetic field is applied, the spins align parallel to the main magnetic field, causing a longitudinal magnetization. This longitudinal magnetization can be flipped over and rotated into transverse magnetization by an RF pulse. The spins will relax back to longitudinal once the RF is retrieved[182]. T1 contrast is commonly enhanced by the gadolinium which is strongly paramagnetic due to its seven unpaired electrons. The T2 is the decay of transverse magnetization, and it is independent on the strength of the external magnetic field[181]. The T2 contrast is usually enhanced by ferromagnetic and

superparamagnetic iron oxide nanoparticles which can behave like a small magnet and introduce magnetic fields to hydrogen protons in tissues. Except T1 and T2, the proton density also contributes to the MRI signal intensity and hence image contrast. Based on the primary signal, there are three different MR images, including T1-weighted, T2-weighted, and proton density-weighted (or intermediate-weighted).

The MRI modality is attractive due to its high resolution, unlimited penetration depth, and non-ionization radiation. However, it is limited due to the poor temporal resolution, high cost, and only anatomic information. Therefore, many efforts are made to improve the temporal resolution and retrieve functional, metabolic, or molecular information by MRI[69, 183].

3.1.3. Radiography

Medical radiography uses ionizing electromagnetic radiation, mainly X-rays, to image internal structures. X-rays have high energy and can pass through the human body. In the body, some of the X-rays are absorbed or scattered causing attenuation of the beam. The attenuation is dependent on the tissue density. Tissues of high density and/or high atomic number lead to more X-ray attenuation and show as lighter grey or white on a radiograph. Less dense tissues lead to less X-ray attenuation and show as darker[184]. Although the contrast between soft and bones is high, the contrast between soft tissues is low. To improve the contrast, contrast agents are developed. The most common contrast agents for radiography are based on barium or iodine.

An advanced radiography is CT. CT combines cross-sectional images obtained with the X-rays and produces a grey-scale 3D anatomic image of the subject being scanned[183]. The detected signal is attenuation of X-ray beam related to the tissue density.

expressed in Hounsfield units (HU). In CT, water is assigned an attenuation value of 0 HU; the HU of muscle, bone, fat, and air are 40, 500, -120, and -1000 respectively[184].

CT is a relatively simple imaging modality. It has high spatial resolution and fast acquisition time. Moreover, the penetration depth is unlimited for humans. However, CT involves exposure to high energy radiation, which may cause damages to tissues. And it primarily provides anatomical information only. The sensitivity and contrast between soft tissues are poor.

3.1.4. Optical image

Optical imaging is a relatively straightforward technique. It uses light to visualize cells or tissues, which interact with light by absorption, attenuation, scattering, and transmission. The most common optical imaging techniques include the light microscopy, fluorescence imaging, and bioluminescence imaging. Light microscopy includes bright field, dark field, and differential interference contrast. The incorporation of light microscopy and staining technology provides not only anatomical but also functional information. Fluorescence imaging needs fluorescent entities to produce signals. The fluorescent entities can be proteins, chemical dyes, and quantum dots. Two important properties of fluorescence entity are the excitation/emission spectra and photostability. Quantum dots have broad excitation, narrow and symmetric emission, high quantum yield, high molar extinction coefficient, and good photo and chemical stability, compared to organic dyes[185]. Bioluminescence imaging is based on the light produced by the enzymatic oxidation reaction of luciferase with its substrate. Bioluminescence imaging has a higher signal-to-noise ratio than fluorescence imaging, because bioluminescence imaging doesn't need an excitation light.

The advantages of the optical imaging include low cost, user friendly, good temporal resolution, and multiplex capabilities. However, this image modalities are limited to cell, small animals, and ex vivo studies due to the poor tissue penetration depth. Therefore, the current optical imaging is not suitable for clinical use[180].

3.1.5. US image

Medical US imaging produce cross-sectional images of the body by ultra-high-frequency acoustic waves[184]. The US transducer has a component called piezoelectric crystal, which can transfer electrical signals to acoustic waves or the reverse. The acoustic waves are emitted by the US transducer, travel in the tissues, reflected back to the piezoelectric crystal, and transferred to electrical signals. The reflected acoustic waves are also named echoes, and the ability to reflect sound waves is echogenicity. Different tissues have various echogenicity and produce contrast in the US images. High, low, and no echogenicity are also named as hyperechoic, hypoechoic, and anechoic respectively. Pure fluid reflects is anechoic and shown as black on the US images; gas-filled structures and bones are hyperechoic and shown as white or light grey on the US images. Therefore, gas-filled microbubbles are used as ultrasound contrast agents.

Resolution and penetration depth are highly relevant to the ultrasound frequency. However, a dilemma exists in frequency selection. At high ultrasound frequency, the resolution is improved but the penetration depth is decreased due to the short wavelengths of high frequency ultrasound waves[180].

US imaging has many advantages compared to other imaging modalities. First, US imaging is super safe and therefore can be used for pregnancy examinations. It is because US imaging involves no ionizing radiation. Second, US imaging has good spatial

resolutions, lower to 50 μm which can indentiy subtle differences in the bodies[129]. Third, this imaging modality has excellent temporal resolution, so it is considered as a real-time imaging modality. Fourth, US images offers quantitative information. Fifth, US imaging is easily accessible and affordable. On the other hand, US images mainly offers anatomical information and shows no multiplexing. However, these limitations can be partially overcome by an emerging US based imaging modality – PAI.

PAI transducers emit infrared light but detect acoustic signals and produce images with these acoustic signals[70]. PAI combines the advantages of US imaging and multiplexity and good contrast of optical imaging. Although the penetration depth is compromised, PAI offers more functional information such as oxygenation and deoxygenation[186].

3.1.6. Magnetic particle imaging

Magnetic particle imaging (MPI) is an emerging imaging modality. It measures the magnetic fields generated by magnetic particles and produces tomographic images[187]. This imaging modality needs a tracer, which is usually superparamagnetic iron oxide nanoparticles. MPI emerged in 2001 and is a pretty new technique compared to other imaging modalities.

3.2. Therapeutic methods

Therapeutic methods based on nanoparticles include target delivery of therapeutic molecules, controlled release of therapeutic molecules, and hyperthermia therapy, photodynamic therapy.

3.2.1. Target delivery

Target delivery means selectively delivery of therapeutics to target areas in the body to maximize the therapeutic efficacy and minimize the side effects. Target delivery

is particularly urgent in chemotherapy for cancer treatment. Chemotherapy is accompanied with dramatic side effects and cause huge pain to patients, because the cancer drugs are also toxic to and kill normal tissues. Target delivery can diminish or even eliminate the side effect by only deliver toxic therapeutics to cancer. There are two types of target delivery: passive and active targeting.

Passive targeting takes advantages of the properties of the delivery system and the disease pathology to preferentially accumulate the drug at the site of interest and avoid non-specific distribution[188]. The most famous passive target is enhanced permeability and retention (EPR), which is realized by the hyper-permeable and aberrant newly-formed blood vessels in the tumors. However, the EPR has a strict size requirement for drugs[189]. First, the drugs should be small enough to permeate the aberrant vascular of cancer, but big enough to escape from renal clearance and unable to penetrate through tight endothelial junctions of normal vascular. Nanoparticles can easily achieve the size requirement and fulfill target delivery of small therapeutics such as doxorubicin and paclitaxel. Another passive targeting uses specific stimuli-responsive delivery system that can release the encapsulated cargos only when such stimuli present (refer to the Controlled release).

Active targeting means the drug delivery system will only present at the targeted diseased sites. This system usually needs a special ligand on the surface that can specifically bind to a marker of the diseased cells or tissues. The common disease markers of cancer include folic acid, integrin receptors, HER2, epidermal growth factor receptors, transferrin acceptors, and other peptides[188].

3.2.2. Controlled release

Controlled release refers to the delivery of therapeutic molecules in response to

stimuli or time. The advantages of controlled release include to superior control of drug exposure over time, to assist drug in crossing physiological barriers, to protect drug from premature elimination, and to release drugs to diseased tissues while isolate drugs from normal tissues. Controlled release also increases patient compliance by reducing frequency of administration or providing an easy administration method. The mechanisms of controlled release nanosystems are diverse, including dissolution, partitioning, diffusion, osmosis, swelling, erosion and degradation[190]. Stimuli for controlled release are also versatile[160], including heat[191-194], magnetic field[166, 195, 196], electronic field[197], photo[110, 198, 199], pH[159, 200, 201], redox[202], enzyme[203], and antibody-antigen reaction[204].

3.2.3. Radiation therapy

Radiation therapy, also called radiotherapy, uses ionizing radiation to control or kill malignant cells. This therapy is mostly applied to cancer treatment, because radiation can control cell growth[205]. Ionizing radiation kills cells by damaging their DNA. Radiotherapy is often used together with surgery, chemotherapy, and/or immunotherapy. However, the side effect and aftermath of radiotherapy is unpredictable because radiation may cause harm to the normal tissues[206, 207].

3.2.4. Hyperthermia therapy

Hyperthermal therapy is a heat treatment – using carefully controlled heat for medical purposes[208-210]. There are three different mechanisms for hyperthermia therapy based on the intensity of heat: intensive hyperthermia, moderate hyperthermia, and mild hyperthermia[210, 211].

First, intensive hyperthermia can be used to kill diseased cells, and this method also called thermal ablation. The aimed temperature for thermal ablation is very high, usually

above 50°C. This high temperature will also kill normal cells, and therefore, it can only be administered locally. Also, the temperature and area need to be controlled precisely.

Second, moderate heat (in the range of 40 to 42°C) can damage cells directly, but more important, it make the cells more vulnerable to other therapy. For examples, heated cells are more sensitive to radiation, chemotherapeutic medications, and immunotherapeutic agents. Due to the relatively high temperature and harm to healthy tissues, moderate hyperthermia therapy is usually used for regional, a large part of the body such as an entire organ or limb. It is also combined with radiotherapy or chemotherapy.

Third, mild hyperthermia reaches a temperature close to a naturally high fever, so that the natural immune system may be stimulated. It can also be combined with chemotherapy along with other treatments to boost the patient's immune system. Mild hyperthermia can be applied to the whole body because of the mild heat. However, the efficacy of mild hyperthermia may be diminished by a natural physiological response called thermotolerance.

3.2.5. Photodynamic therapy

Photodynamic therapy (PDT), also called photoradiation therapy, phototherapy, or photochemotherapy. Photodynamic therapy uses light to activate a special photosensitizing agents or nanoparticles to kill cancer cells. This therapy can decrease side effects due to the inactive state of drugs at tissues without light. However, photodynamic therapy cannot treat cancers deep in the body due to the poor penetration of light through skin and tissue. Except commercial photosensitizing agents such as Photofrim®, Levulan®, and Metvixia® cream, gold nanoparticles[212, 213] and graphene/graphene oxide[214] shows great promises in the photodynamic therapy. Moreover, PDT can also be fulfilled with silica

nanoparticles integrated with photon upconverting nanoparticles or photosensitizer, such as porphyrin and [2-devinyl-2-(1-hexyloxyethyl)pyropheophorbide][215-218].

3.2.6. Immunotherapy

Immunotherapy uses the patient's immune system to fight diseases such as cancer. Immunotherapy can be fulfilled either by activating a person's own immune system or dosing the patients with external immune system components. For example, although the immune system has the potential of recognizing and eliminating cancerous cells[219], the poor immunogenicity of patients can not completely remove the tumor cells nor prevent the tumor recurrence. However, the immune system may be boosted by immunotherapy to effectively eliminating tumor cells due to the decreased antigen presentation of tumor cells and down-regulated immune responses of the patients.[220]

3.3. Theranostic and multimodal imageable silica nanoparticles

Theranostic and multimodal imageable nanoparticles are nanoparticles that act as both diagnostic and therapeutic agents. Theranostic nanoparticles are valuable tools for identifying and selecting patients followed by treating selected patients positively. Multimodal nanoparticle contrast agents combine the advantages of different imaging modalities.

In this context, a variety of diagnostic information can be obtained depending on the particle design. For example, theranostic medicines can provide insights into the availability of a molecular target in the tissue, the vascular permeability and retention of the molecule, the drug release from the particle, and the response of the target tissue[221].

Nevertheless, the silica components in these integrated systems play various important roles in stabilizing and protecting the core nanoparticles or dopants. They offer

multiple chemical modification methods and serve as a therapeutic reservoir to achieve target delivery and/or controlling release. For example, coupling fluorophores into silica nanoparticles can diminish the effect of fluorophore photobleaching. Peng et al. developed intracellular pH sensitive nanoparticles that can detect cellular pH from pH 4-7[145]. These nanoparticles are silica nanoparticles doped with two fluorophore sensors. Silica increases the stability and sensitivity of the fluorophores and allows for high quantification and measurement reversibility by diminishing photobleaching of the dyes.

Silica can also decrease the toxicity of nanoparticles that contain toxic components such as heavy metals. Doping functional elements such as lanthanide ions into silica is another useful strategy to make multifunctional nanoparticles. For example, gadolinium (Gd) is a commonly used MRI T1 contrast agent, but it is toxic due to its accumulation in tissues like brain, bone, and kidneys[222]. Silica nanoparticles doped with gadolinium not only improve the MRI contrast but also decrease the toxicity of Gd.

Rieter et al. added a paramagnetic monolayer of silylated Gd complex onto a luminescent $[Ru(2,2'\text{-bypyridine})_3]Cl_2$ core by a water-in-oil reverse microemulsion method[170]. This nanoparticle offers fluorescent and MRI signals due to the $[Ru(2,2'\text{-bypyridine})_3]Cl_2$ core and the Gd in the silica shell. The silica is also conjugated with diethylenetriaminetetraacetate (DTTA), which provides seven binding sites for Gd^{3+} ions to minimize the toxicity of nanoparticles owing to the leaching of Gd^{3+} centers. The nanoparticle is sufficiently small (<50 nm) to be endocytosed by monocyte cells and allows multimodal *in vitro* imaging of the cells. The authors are using this nanoparticle as target-specific contrast agents for optical and magnetic resonance (MR) imaging of rheumatoid arthritis in mice[170].

Our group previously designed a multimodal silica nanoparticle which has a fluorescent, ultrasound, and MRI signal[171]. The ultrasound contrast can increase the contrast of the stem cells and guide the injection of stem cells, and the MRI signal is proportional to the cell numbers, which can be used to track the cell numbers after injection. The nanoparticle was prepared based on the Stöber method including fluorescein isothiocyanate (FITC)-conjugated organosilanes with TEOS; $GdCl_3$ was used for Gd doping. Silica produces ultrasound contrast because it has a high acoustic impedance mismatch with cells and soft tissues. Silica reflects more ultrasound, and thus the silica materials have more ultrasound signal than soft tissues in ultrasound images. The size of these nanoparticles can be tuned, and the ultrasound contrast of these nanoparticles is size dependent. This nanoparticle is used to label and track stem cells to improve stem cell therapeutic efficacy.

Later work developed a theranostic system using this nanoparticle by introducing pores into the silica nanoparticle[114]. The nanoparticles retain the multimodal imaging signals–ultrasound, MRI, and fluorescence. Sectioning transmission electron microscopy (TEM) images show these nanoparticles are located in the cytoplasm of the cell. Moreover, the pores are used to load a prosurvival agent for stem cells and slowly release the insulin-like growth factor (IGF) inside cells. This system increases cell survival up to 40% ($p<0.05$) versus unlabeled cells under *in vitro* serum-free culture conditions.

Sweeney *et al.* used a similar silica nanoparticle doped with gadolinium oxide and conjugated with tetramethylrhodamine-isothiocyanate (TRITC) to improve real-time monitoring and staging of mouse bladder cancer models[223]. They injected murine flanks with MB49 cancer cells, and then injected silica nanoparticles to examine differences in

MRI signal between tumors and bladder epithelium. The integrated silica nanoparticles enhanced both T1 and T2 weighted MRI signals in the tumors, allowing detailed *in vivo* evaluations. The localization of particles helped delineate the tumor's edges, which are usually difficult to detect. This system can potentially be used for theranostic purposes, as therapeutic carriers for anticancer agents, and diagnostic tools for tumor visualization.

Lin et al. developed a theranostic targeting mesoporous silica nanoparticle with multiple imaging modalities by doping and surface conjugation[224]. The nanoparticles are doped with europium (Eu) and Gd ions. These ions introduce fluorescence and magnetism to the mesoporous structure, and thus the nanoparticles can be used as a fluorescent tool. The MRI indicates the location and size of the tumor. The doped nanoparticle is then conjugated with the anticancer drug camptothecin (CPT) by disulfide bonds. This disulfide bond can be cleaved by a high concentration of intracellular glutathione for intracellular controlled release. Moreover, the surface of the nanoparticle is modified with folic acid, which can be used to target most human cancer cells. *In vitro* and *in vivo* studies show that these integrated silica nanoparticles can target, image, and destroy the tumors in mice.

Silica is also highly useful for assistance in functionalizing nanoparticles. Fluorescent and radio-opaque nanoparticles can be used for CT, MRI, and diffuse optical tomography[164]. They have a silica core that is doped with tris(2,2'-bipyridyl) dichlororuthenium(II) hexahydrate. The core is surrounded by a layer of n-(trimethoxysilyl-propyl)ethyldiamine tri-acetic acid trisodium salt that traps paramagnetic Gd^{3+} ions. Finally, the particles are wrapped by an additional silica shell layer containing amine groups on the surface that can be used for functionalization. This multimodal (optical, radiology, CT, and MRI) contrast agent can help in the preoperative diagnosis and

in the intraoperative surgical resection of tumors or other surgical lesions[164].

Mesoporous silica-coated MnO nanoparticles also show great potential as MRI contrast agents for cell tracking[51]. These nanoparticles have a MnO/SiO_2 core shell structure, and the nanoparticles are named as $HMnO@mSiO_2$ nanoparticles where the symbol @ usually means inside. The innate r_1 relaxivity of MnO provides the MRI signal of the nanoparticle. The silica increases the biocompatibility of MnO core. This nanoparticle can label MSCs *in vivo* and shows intense signals. Moreover, the MRI signal can be detectable 14 days after the injection.

The MnO/SiO_2 core shell structure can also be used for a theranostic and multimodal imaging system. Choi et al. embedded MnO/SiO_2 core/shell nanoparticles into porous poly(propylene fumarate) (PPF) scaffolds and used the MRI signal change to monitor the release of nanoparticles from the PPF scaffold surface. The anti-cancer drug doxorubicin (DOX) was loaded on the surface of the MnO/SiO_2 NPs by electrostatic interaction between the drug with the negatively charged porous silica surface[225]. Additionally, the porous silica shell can also enhance the water- dispersibility of the core and minimize the leakage of the core ions. Moreover, silica shell prevents the aggregation between MnO nanocores and therefore increases the dispersity of MnO nanocores.

Monaco et al. synthesized a core-shell $Fe_3O_4@SiO_2@Au$ nanosystem coated with 11-(4-mercaptobenzamido) undecanoate, poly(lactic-co-glycolic acid)-b-PEG-NH_2, and folic acid[226]. This nanosystem provides *in vivo* targeting capabilities and MRI-PA dual imaging signals. The combination of MRI and PAI offer mutual benefits—it overcame the depth and resolution limits of PAI and the temporal resolution of MRI. The MRI signal is produced by iron oxide while the PA signal is produced by the gold shell. The multilayer

nanoparticles are then embedded in the so-called polymeric micelles to improve their biocompatibility[226]. The researchers then conjugated folic acid on the polymeric micelle surface to get a water-soluble nanocarrier that actively targets folate receptors that are often overexpressed in solid tumors. Their final system is highly biocompatible and can be manipulated to build other targetable nanostructures.

Mesoporous silica shells can also improve the performance of gold nanorods (AuNRs) in biomedical applications. AuNRs show great potential in multiple imaging modalities and therapies including CT, PA, PDT, and PTT. However, AuNRs have a low drug loading capacity and suffer from clustering, aggregation, and shape deformation. Zhang et al. fabricated a mesoporous silica shell coated AuNRs and loaded doxorubicin to the nanoparticle. These particles enable imaging, chemotherapeutics, and hyperthermia within a single nanoparticle platform for cancer treatments[227]. The silica forms a protective layer outside the AuNRs and prevents them from aggregation. The silica-coated nanorod showed stable surface plasmon resonance. In addition, the release of doxorubicin from the nanoparticle can control the pH and near infra-red laser. Moreover, the system can kill cancer cells by photothermal therapy. These properties make this nanoplatform a potential candidate for new therapeutic modalities such as image-guided drug delivery, hyperthermia, and combination therapy.

Kircher et. al. synthesized novel nanoparticles for MRI, photoacoustic, and Raman imaging in brain tumors[228]. These triple-modality contrast agents are used to delineate detailed brain tumor margins to remove more tumor tissue. These contrast agents are created with a 60-nm gold core, a Raman-active layer, a silica shell, and a gadolinium coating. These nanoparticles are highly sensitive and detectable in the picomolar range for

all three modalities. In addition, it was shown that particles injected intravenously accumulated within the brain tumor but not in the adjacent healthy tissue, which allows for a noninvasive brain tumor delineation. This nanoparticle-based triple-modality contrast agent offers more accurate brain tumor imaging and resection.

Other than the functions mentioned above, Chen et al. also found that the silica shell can amplify the photoacoustic intensity of gold nanorods[165]. The group studied the relationship between photoacoustic signals and heat transfer properties in silica coated AuNRs. They found that the additional silica layer acted as a signal amplifier by reducing interfacial heat resistance between gold and a range of solvents. The addition of a silica layer 0-20 nm thick increased photoacoustic signal by up to 3-fold, peaking at 20 nm thickness. The addition of a silica layer to AuNRs appears to be a beneficial way to increase their utility as contrast agents for PAI.

3.4. Monitoring the release of therapeutic molecules

The real-time monitoring capabilities of molecules can provide an abundance of physiological and pathological information of the patients. Theranostic devices with integrated real-time monitoring abilities are emerging and offer more feedback on treatment. Integrated silica nanoparticles also show great potential in the field for real-time monitoring of molecules.

The silica component is an ideal cargo carrier. In 2005, Gruenhagen et al. monitored adenosine triphosphate (ATP) release from MCM-41 silica nanoparticles[229]. ATP was used as a model cargo and the release mechanism was studied through the use of ATP-activated luciferase, which produces bioluminescent signal with ATP exposure. Due to the capability of real-time monitoring for cargos during release, the authors found the release kinetics of

encapsulated molecules can be controlled by changing the capping molecules.

Lai et al. (2013) reported a versatile fluorescence resonance energy transfer (FRET)-based drug delivery system[111]. These nanosystems consist of a coumarin-labeled cysteine tethered mesoporous silica nanoparticles as the drug carrier and a FITC-β-cyclodextrin (CD) as redox-responsive molecular gate blocking the pores. A FRET donor-acceptor pair of coumarin and FITC was integrated within the pore-unlocking event. The presence of glutathione (GSH) in the environment of the particle provokes a redox response, unblocking the particle's pores and releasing the encapsulated drugs. The extent of drug-release can be controlled by the ratio of FITC-β-CD to GSH and monitored by pathological cell viability and FRET signals.

Lai et al. developed a polypeptide-wrapped mesoporous silica coated multicolor up-conversion nanoparticle (UCNP@MSN) as a drug delivery system. This is advantageous because the drug release can be monitored in real-time[230]. They functionalized the system with zinc-dipicolylamine analogue (TDPA-Zn^{2+}) and wrapped it with polypeptides to entrap the loaded drug–DOX. The TDPA-Zn^{2+} and polypeptide layer caused DOX to quench the ultraviolet (UV) emission upconverted from incoming NIR by the upconversion nanoparticles. ATP displaced the peptides because it has a higher binding affinity with TDPA-Zn^{2+}. When ATP displaced the peptides, DOX was released through the open pores of the particles. The release can then be monitored through ratiometric changes in luminescence resonance energy transfer (LRET). The authors also showed that this system could be further functionalized with receptors like folic acids to distinguish different diseases.

Liu et al. synthesized an NIR-triggered nanosensor that monitors drug-release by

using upconverted luminescence and MRI simultaneously[231]. The nanosensor is composed of UCNPs surrounded by a mesoporous silica shell as well as doxorubicin and azobenzene to create a FRET donor-acceptor pair with UCNP. They found that under NIR exposure, drugs loaded into the particles were released, which led to a steady increase in MRI and upconverted luminescence signals. DOX quenched the upconverted emission from UCNPs, and its release increased the upconverted luminescence signal intensity. The loaded drug also made it less likely for water molecules to bond with Gd^{3+} ions. When DOX was released, water from the surrounding environment diffused into the particle and interacted with Gd^{3+}. This increased the T1 MRI signal intensity.

The silica component can also act as fixative for small molecules to offer contrast for monitored drugs. Wang et al. conjugated Stöber silica nanoparticles with methylene blue to monitor the blood concentration of heparin in real time[33]. Methylene blue is an FDA approved dye and it shows thermal expansion when it absorbs infrared light, which is also known as photoacoustic signal. The authors showed that heparin could increase the photoacoustic signal of methylene blue, and moreover, the signal increase is proportional to the concentration of heparin within the clinical dosage range. Silica nanoparticles were used to immobilize the methylene blue and prevent this dye from diffusing into the circulation. Silica adsorbs methylene blue through electrostatic forces, and the surface charge of the silica nanoparticles affects the sensitivity of detection. Thiol modified silica nanoparticles are more sensitive than non-modified ones. PAI is based on ultrasound imaging. PAI inherits the real-time imaging performance and the signal is stable over time. Therefore, this method can monitor the heparin concentration changes without waiting for long time. This system can also detect low molecular weight heparin, which is not

detectable by the conventional method—activated partial thromboplastin time (aPTT).

Though the real-time monitoring capabilities of molecules can provide abundant of physiological and pathological information of the patients as well as feedback for treatments, the development of such devices is still in its nascent stage because of the limitations of real-time imaging modalities. Therefore, more efforts are needed for real-time imaging modalities.

4. Conclusions and prospective

Silica is critical for integrated nanoparticles and offers great potential in theranostic, multimodal imaging, and real-time monitoring for molecules. Silica nanoparticles are easily made and tuned to various morphologies. They also show great biocompatibility and tunable degradability. Silica nanoparticles themselves can be used for drug delivery and ultrasound imaging contrast agents. Moreover, silica nanoparticles can be easily combined with other inorganic and/or organic components, which offers more features. Integrated silica-based nanoparticles can be used in nuclear imaging, MRI, radiography, optical imaging, ultrasound imaging, and magnetic particle imaging. The integrated particles can also be used in target delivery, controlled release, radiation therapy, hyperthermia therapy, photodynamic therapy, and immunotherapy. Extensive research has shown the great potential of integrated silica nanoparticles in theranostic and multimodal imaging.

Despite the huge number of studies on silica-based integrated nanoparticles for applications in bio-imaging and drug delivery, they have not made a significant impact in the clinic yet. The only silica-based integrated nanoparticle close to FDA approval are C-dots, which exhibit positron emission tomography (PET) and optical dual-modality imaging[232]. More studies are needed to improve their colloidal stability, optimize

biodistribution, and customize biodegradation to promote the translation of these nanomedicines. Moreover, similar to all the other nanomedicine systems, increasing the targetability of integrated silica nanoparticles is critical to their translation with respect to manufacturing, cost, toxicity, and imaging and therapeutic efficacy—targetability of nanoparticles affects the actual drug dose at the desired location[233].

We have summarized recent work that used integrated silica nanoparticles to monitor biomolecules. However, most of the systems are based on fluorescence, which is limited for *in vivo* and clinical study because of poor penetration depth of light. Therefore, developing new real-time imaging modalities with high penetration depth is necessary. Ultrasound imaging and photoacoustic imaging are techniques with both real-time capability and increased penetration depth[234]. However, the field is still premature due to the lack of designs for combining ultrasound/photoacoustic contrast agents with other functional materials. We expect that more integrated nano-designs will be studied to offer theranostic systems that also provide real-time feedback *in vivo*.

5. Acknowledgement

The text of Chapter 1, in part, is a reprint of the material as it appears in "Multifunctional nanomedicine with silica: Role of silica in nanoparticles for theranostic, imaging, and drug monitoring" by Fang Chen, Ghanim Hableel, and Jesse V. Jokerst, Journal of colloid and interface science, 2018. The dissertation author was the primary researcher of this paper.

Chapter 2.

Discoid silica nanoparticles as a novel ultrasound contrast agent for stem cell imaging

1. Introduction

Stem cells are promising in regenerative medicine as a treatment for heart diseases, diabetes, alopecia, and neurodegenerative diseases[86-89, 235, 236]. However, the long-term efficacy of stem cells is relatively low perhaps in part due to poor cell viability after implantation and a lack of cell retention in the treatment area[237]. These issues are partially due to mis-injection of stem cells or injection into highly fibrotic tissues[238, 239]. Fortunately, mis-injection can be prevented by real-time imaging guidance to ensure sufficient cell delivery[240] to the desired locations. Ultrasound imaging[114, 241-245] in particular has shown significant potential in imaging stem cell therapy because of its high temporal resolution relative to the gold standard of magnetic resonance imaging (MRI)[240, 246]. Ultrasound is also more affordable than alternative strategies such as MRI, positron emission tomography (PET), and computed tomography (CT). However, the use of ultrasound in stem cell imaging/tracking is limited by the low contrast of these cells above the adjacent tissue[247]. While Doppler imaging[248], elastography[249], and thermoacoustic techniques[250] have all been validated to improve contrast, novel ultrasound contrast agents are also active area of research[36, 251-253].

Silica nanoparticles are an effective *in vivo* ultrasound contrast agent[102, 114, 242, 254-256]. They can efficiently label stem cells because of their nano-scale size, stability[114], and biocompatibility[119, 257, 258]. Moreover, silica particles are multi-functional[134, 259, 260] with a tunable morphology[261, 262], and these modifications in nanoparticle shape can markedly increase the echogenicity of the individual silica nanoparticles[102]. Gd-tagged silica nanoparticles can also offer multimodal imaging with clear biodegradation[114, 242]. Other work has used rattle-type mesoporous silica nanospheres to create multiple

convex/concave interfaces to increase the ultrasound contrast[102], and silica microbubbles synthesized via polystyrene templates have been used for contrast-enhanced ultrasound[263]. In this study, we combine these advances and report a completely novel silica nanoparticle with a concave mesoporous structure to enhance ultrasound signal. The discoid silica nanoparticles (DSN) have a shape surprisingly reminiscent of exosome extracellular vesicle, and therefore they are also named exosome-like silica nanoparticles (ELS). The DSN improve the ultrasound contrast of cells by increasing not only the echogenicity of the nanoparticles but also their affinity to stem cells.

2. Methods

2.1. Chemicals

Hexadecyltrimethylammonium bromide (CTAB, ≥99%), ammonium hydroxide (NH_4OH), tetraethyl orthosilicate (TEOS, ≥99%), bis(triethoxysilyl) ethane (BTSE), bis(3-trimethoxysilyl-propyl)amine (TSPA, 90%), Pluronic P123, hydrochloric acid, mesitylene, and fluorescein isothiocyanate (FITC) were purchased from Sigma Aldrich Inc. Sodium hydroxide (NaOH, ACS), ammonium fluoride, and ammonium nitrate (NH_4NO_3, ACS) were purchased from Fisher Scientific, Acros, and Marcon respectively. Ultrapure agarose was obtained from Life Technologies. The (3-aminopropyl)triethoxysilane (APTES) was purchased from MP Biomedicals. Ethanol was purchased from VWR. All chemicals were used as received without any further purification processes. The water was Millipore grade with a resistivity larger than 18.2 MΩ·cm at room temperature unless specified.

2.2. Synthesis of silica nanoparticles

We synthesized discoid silica nanoparticles with emulsion template method and

two silica sources—BTSE and TSPA. First, 0.4 mmol CTAB, 0.085 ml 26% ammonia solution, 0.6 mmol decane, and 0.4 mmol dimethylhexadecylamine (DMHA) were mixed in 150 ml water. The mixture was then sonicated in a water bath at 50℃ for 2 h followed by emulsification using an ultrasonic cell disruptor (20 KHz, 600 W; Bilon92, Shanghai) at ambient temperature for a total of 30 min. The prepared white emulsion was transferred to an oil bath at 50℃ and then stirred at 700 rpm for 30 min. After that, 2.5 mL of ethanol solution containing 4 ml of silica sources was added slowly. The mixture was stirred for 60 min and then allowed to stand at room temperature for 12 h. After the surfactant-containing nanoparticles were spun down at 20,000 rpm, the solid products were washed thrice with 1 wt% NaCl in methanol for 30 min in sonication bath to remove the template. The discoid silica nanoparticles were centrifuged, washed, and then dispersed in deionized water. The effect of the ratio between BTSE and TSPA on the morphologies of discoid silica nanoparticles was also studied, and the studied ratios of BTSE:TSPA included 5:0, 4:1, and 3:2. All discoid silica nanoparticles used for ultrasound imaging and cellular work were done at a BTSE:TSPA ratio of 3:2.

The Stöber silica nanoparticles were made according to the Stober method[95], and the size was tuned by slightly changing the quantity of ethanol, water, ammonia, and/or TEOS. Specifically, aliquots of NH_4OH (1, 1.8, 2.2, 2.8, and 4.4 ml) and water (4.2 or 5 ml) were added to 50 ml ethanol. The mixture was stirred for 5 minutes before adding 3.5 or 4.2 ml TEOS, and then stirred for another 2 hours. The temperature was maintained at 30℃ throughout the procedure. Then, the Stöber silica nanoparticles was centrifuged and washed with ethanol thrice, followed by drying in 50℃ oven.

The MCM-41 mesoporous silica nanospheres were prepared by CTAB-templated,

base-catalyzed condensation reaction of TEOS [264]. First, 40 mg CTAB were dissolved in 96 ml water and then preheated to 80℃ while stirring. Then, 0.7 ml 2 M NaOH were added to the solution while stirring and continued stirring for 30 minutes at 80℃. We added 1.4 ml TEOS to the mixture and stirred it gently for 2 hours. The product was then filtered and rinsed with water and ethanol twice, and finally calcined in a furnace at 600℃ for 5 hours.

The mesocellular foam silica nanoparticles were synthesized in aqueous hydrochloric acid using P123 as a template and mesitylene as a micelle expander according to the literature[103, 265] with minor modifications. First, 2.43 g P123 were added into 90 mL 1.6 M HCl in an Erlenmeyer flask at room temperature, followed by adding 400.8 mg CTAB, 24.4 mg ammonium fluoride, and 1.6 ml mesitylene. The mixture was stirred at room temperature for 2 hours and then added 5.5 ml TEOS dropwise under vigorously stirring. The mixture was stirred for another 5 minutes after the addition of TEOS. The reaction was allowed to incubate at 38℃ overnight, and then the particles were centrifuged and rinsed with ethanol and water thrice. Particles were dried and calcined at 600℃ for 5 hours.

The four silica nanoparticles were conjugated with FITC to study the interaction between silica nanoparticles and cells. An amino-silane conjugate of the dye was first made by mixing 1 mg dye and 100 μl APTES in 1 ml ethanol with overnight rotation under room temperature. Then the mixture was divided evenly into 4 tubes with 4 mg Stöber silica nanoparticles, MCM-41 mesoporous silica nanospheres, mesocellular foam silica nanoparticles, and discoid silica nanoparticles, and rotated overnight. The products were washed thrice with ethanol, dried, and stored in dark for later use.

2.3. Characterization

Transmission electron microscopy (TEM) images of silica nanoparticles were taken with a JEOL JEM-1200 EXII operating at 120 kV or JEM-2100F operating at 210 kV. Size distributions were analyzed by TEM images as well as nanoparticle tracking analysis (NTA, LM10, Malvern) with a 532 nm laser. The particle-concentrations for 1 mg/ml of Stöber silica nanoparticles, MSC, mesocellular foam silica nanoparticles, and discoid silica nanoparticles solutions were also determined by NTA with camera level at 14 and detect threshold at 5. The four particle solutions were diluted 100- to 10,000-fold prior to analysis and studied with NTA before and after 30 minutes of sonication in bath (KENDAL ultrasonic cleaner, Model 928, Power 60W). The N_2 adsorption-desorption isotherms at 77 K were measured on a Micrometitics Tristar 3000 system. Zeta potentials of the four types of nanoparticles were measured in 50% PBS via DLS (Zetasizer, Malvern). Inductively coupled plasma optical emission spectrometer (ICP-OES, Optima 3000DV, Perkin Elmer) was used to quantify the number of silica nanoparticles endocytosed by cells after sonication in 10 N NaOH.

2.4. Cell culture, labelling, and cytotoxicity assay

We seeded human mesenchymal stem cells (hMSCs, Lonza, PT-2501) in a T75 flask at 5000 cells/cm^2 in growth media (Lonza, PT-3001). These cells were labelled with 8 ml 250 μg/ml silica nanoparticles in fresh cell culture media without any transfection agents. The cells were then incubated under standard conditions for 7.5 hours. We washed the cells with sterile PBS to ensure all the free silica nanoparticles were removed. Cells were then detached by adding 2 ml of TrypLE Express (Life technologies). We scanned these labelled cells with ultrasound both *in vitro* and *in vivo*. Additionally, we treated

hMSCs and also ovarian cancer cells (OV2008, Thermo Fisher Scientific) with silica nanoparticles of different concentrations (0 to 1000 μg/ml) and studied the cell viability by using CellTiter 96® AQueous One Solution cell proliferation assay (MTS, Promega). After incubation with silica nanoparticles for 4 hours, 20 μl of the assay reagent was pipetted into the samples in 100 μl of growth media. This was allowed to incubate under standard conditions. After 4 hours, we transferred 80 μl of the sample solutions to a new plate and read the absorbance at 490 nm. Epifluorescence microscopy used an Evos microscope (Life Technologies) and Hoechst 33342 (NucBlue® Live ReadyProbes® Reagent, Thermo Fisher Scientific) for nuclear staining.

2.5. *In vitro* phantom preparation and ultrasound imaging

All the *in vitro* ultrasound imaging was performed in agarose phantoms. Agarose was added to water at 1% and boiled with stirring and then keep warm at 60°C. The agarose solution was then mixed with nanoparticle solutions or cell solutions at a ratio of 1 to 1. To avoid the aggregation of nanoparticles, the nanoparticle solutions were sonicated in water bath for 30 minutes prior to mixing with agarose, and then the mixture was vortexed. The cell solutions were vortexed both before and after mixing with agarose too. We quickly and carefully pipetted 250 μl mixture into the well of 96-well plate or agarose phantom. A blank control was also made with 0.5% agarose solution for all experiments. The solidified samples were covered with fresh 1% agarose for protection. Ultrasound imaging used a VEVO 770 high-resolution *in vivo* micro-imaging system with transducers (VisualSonics) RMV-706 at 40 MHz and RMV-710B at 25 MHz. The imaging parameters were 100% power, 71 Hz frame rate for RMV-710B, and 34 Hz frame rate for RMV-706. The distance between the imaging transducer and phantom was maintained throughout the scan. At least

five fields of views (FOVs) for each sample were collected.

2.6. *In vivo* ultrasound imaging

All animal studies were performed in accordance with IACUC S15050 at University of California, San Diego. Human mesenchymal stem cells were incubated together with 250 μg/ml discoid silica nanoparticles in growth media for four hours. Then, the free particles were removed by washing with PBS thrice. The labelled cells were detached, spun down, resuspended, and then counted by hemocytometer. The pellets with 1, 0.4, 0.2, 0.05 million cells were resuspended in 150 μl of 50:100 media:matrigel and injected subcutaneously into nude mice with a 28.5 gauge catheter. Images were obtained by 3-D mode and conditions include a 40 MHz transducer at 0.0076 mm per step.

2.7. Data analysis

Data means, standard deviations, and p values were calculated in Microsoft Excel 2016. Unless otherwise noted, all error bars represent the standard deviation. A two-tailed Student's t-test was used for significance and p values<0.05 were considered to be significant. TEM particle sizes of nanoparticles were analyzed with ImageJ 1.48v[266]. For irregular particles, the Feret diameter was adopted. Ultrasound signals were also analyzed by ImageJ 1.48v. Specifically, B-mode ultrasound images were first exported from the ultrasound scanner as 8-bit images. Then, we drew a region of interest (ROI) inside the sample and managed it with ROI manager in the ImageJ. We measured the mean gray value of the same ROI in at least five different fields of views (FOVs) per sample by ImageJ 1.48v and then calculated mean and standard deviation of the mean gray values for each FOV, which ranged from 0 to 255. Detection limits were calculated at 3 standard deviations above the mean of the background signal.

2.8. Calculations for the density of MCM-41 mesoporous silica nanospheres

$$\mathbf{N v \rho = W} \qquad \text{Equation 2.1}$$

W–Total weight of nanoparticles; N–Total number of nanoparticles; v–Volume of one nanoparticle; ρ–Density of one nanoparticle.

$$\frac{N_1 v_1 \rho_1}{N_2 v_2 \rho_2} = \frac{W_1}{W_2} \qquad \text{Equation 2.2}$$

Both MCM-41 mesoporous silica nanospheres and Stöber silica nanoparticles are spheres. Therefore, when the total weight of Stöber silica nanoparticles and MCM-41 mesoporous silica nanospheres are the same, equation 2 can be converted to:

$$\frac{\rho_1}{\rho_2} = \frac{N_2}{N_1}\left(\frac{D_2}{D_1}\right)^3 \qquad \text{Equation 2.3}$$

NTA measurements indicated that there are (76.9 ± 3.2) $\times 10^{10}$ and (17.6 ± 1.4) $\times 10^{11}$ for 1 mg/ml of Stöber silica nanoparticles and MCM-41 mesoporous silica nanospheres. The average size of Stöber silica nanoparticles and MCM-41 mesoporous silica nanospheres are 160 nm and 154 nm. Therefore, the density of Stöber silica nanoparticles is 2.04 times of MCM-41 mesoporous silica nanospheres. It is noteworthy that equations 2.1-2.3 only fit for spheres.

2.9. Calculations for the nanoparticles/cell

NTA measurements indicated the number of particles in a 1 mg/mL sample was (76.9 ± 3.2) $\times 10^{10}$, (17.6 ± 1.4) $\times 10^{11}$, (12.8 ± 1.6) $\times 10^{11}$, and (13.7 ± 0.3) $\times 10^{11}$ particles/ml for Stöber silica nanoparticles, MCM-41 mesoporous silica nanospheres, mesocellular foam silica nanoparticles, and discoid silica nanoparticles, respectively. The Si content in Stöber silica nanoparticles-, MCM-41 mesoporous silica nanospheres-, mesocellular foam silica nanoparticles-, and discoid silica nanoparticles-labeled hMSCs were 0.40, 0.05, 0.75,

and 1.11 ng/cell determined by ICP-OES. We converted the mass of Si to NPs first according to the NPs formula. Then, the number of NPs/cell was calculated by multiplying number of nanoparticles in 1 mg/ml solutions by mass of NPs per cell. The nanoparticles formulas and calculated nanoparticles/cell are listed in **Table 2.1**.

Table 2.1. NTA and ICP-OES results, particles formulas, and calculated NPs/cell.

Particles	SSN	MSN	MCF	DSN or ELS
Concentration of NPs in 1 mg/ml solutions ($\times 10^{10}$ NPs/ml)	76.9	176	128	137
Si (ng/cell)	0.40	0.05	0.75	1.11
NPs formula	SiO_2	SiO_2	SiO_2	$SiO_{1.5}C_{1.8}N_{0.2}$
Si:NPs	0.47	0.47	0.47	0.37
NPs (ng/cell)	0.86	0.11	1.60	3.02
Number of NPs/cell (million)	0.66	0.19	2.05	4.14

3. Results and discussion

3.1. Synthesis and characterization of discoid silica nanoparticles

We fabricated discoid silica nanoparticles via an emulsion soft-template method (**Figure 2.2A)**. The soft templates were an oil-in-water emulsion made of hexadecyltrimethylammonium bromide (CTAB) (green), dimethylhexadecylamine (DMHA) (cyan), and decane (yellow) (step 1). The silica sources were then added to the emulsion and allowed to condense on the surface of the CTAB via an ammonia catalyst (step 2). After extracting the templates in a methanolic sodium chloride solution, the products were lyophilized (step 3). Electron microscopy images illustrate the shape and size similarities between the discoid silica nanoparticles and exosomes (**Figure 2.2 B, C, and F**). When we studied the nanoparticles with TEM (**Fig. 2.2**) we found that nanoparticles have morphology remarkably reminiscent of exosomes—small extracellular

vesicles (30-150 nm) secreted by cells. Like exosomes, discoid silica nanoparticles have a unique curvature and cup-like discoid shape. This shape offers a double scattering/reflection interface to increase echogenicity[102].

During the fabrication, the silica source is critical to forming the exosome-like structure. Three common silica sources, tetraethyl orthosilicate (TEOS), bis(triethoxysilyl) ethane (BTSE), and bis(3-trimethoxysilyl-propyl) amine (TSPA) were investigated. We found TEOS is too stiff and brittle to produce discoid silica nanoparticles (data not shown). However, discoid silica nanoparticles were formed with the co-condensation of BTSE and TSPA. The BTSE offered a rigid framework for the particles, and TSPA allowed the nanoparticles to collapse by changing the overall stiffness—a hollow rigid sphere formed with only BTSE (**Fig. 2.2D**) and no particles formed with only TSPA (**Fig. 2.2G**). This role of TSPA is consistent with Lin et al. who found that TSPA could change the overall stiffness of silica shell and render them more elastic to form silica microbubbles[267]. Discoid silica nanoparticles prepared with different ratios of BTSE and TSPA are shown in **Figure 2.2 E** (4:1) and **F** (3:2) with yields of 37.2% and 35.7%, respectively.

While most silica nanoparticles are negatively charged due to the presence of hydroxyl groups, the discoid silica nanoparticles have positively charged amine groups embedded in the framework. This results in a positive nanoparticles surface charge to improve affinity with the negatively charge cell surface via a charge-dependent mechanism literature[268]. The zeta-potential of final silica products (nanoparticles or gel) changed with the fraction of TSPA and was the highest at 40% TSPA (~30 mV; **Figure 2.2H**). The discoid silica nanoparticles made with 40% TSPA were also the largest (~140 nm; **Figure 2.2H**), and a preliminary study showed that larger nanoparticles have more echogenicity

(Fig. S2) Therefore, discoid silica nanoparticles made with 40% TSPA were characterized and selected for stem cell imaging. We found the sonication output power and sonication time during the emulsion as well as the incubation time didn't influence the discoid silica nanoparticles size.

Porous discoid silica nanoparticles with a mean diameter of ~140 nm was prepared with 40% TSPA. The size of the discoid silica nanoparticles was analysed with both TEM and nanoparticle tracking analysis (NTA). Both size distributions are shown in **Figure 2.2I**. The average TEM size is 138 nm for the discoid silica nanoparticles (N=298). Additionally, a small peak near 500 nm in the NTA size distribution might indicate aggregation. The discrepancy between TEM and NTA size distributions is because that NTA measures the hydrodynamic size of the particles and nanoparticles forms aggregations in water. Unlike other biomedical applications[269, 270], the aggregation is preferred in the stem cell tracking because aggregations of nanoparticles inside the cells increase the ultrasound signal[242]. The N_2 adsorption-desorption isotherms of discoid silica nanoparticles indicated the existence of mesopores on the discoid silica nanoparticles (**Figure 2.2H**). The BJH pore volume and desorption pore size of discoid silica nanoparticles were determined empirically to be around 1.79 cm^3/g and 5.4 nm (**Figure 2.2H inset**); the BET surface area of discoid silica nanoparticles was 694 m^2/g.

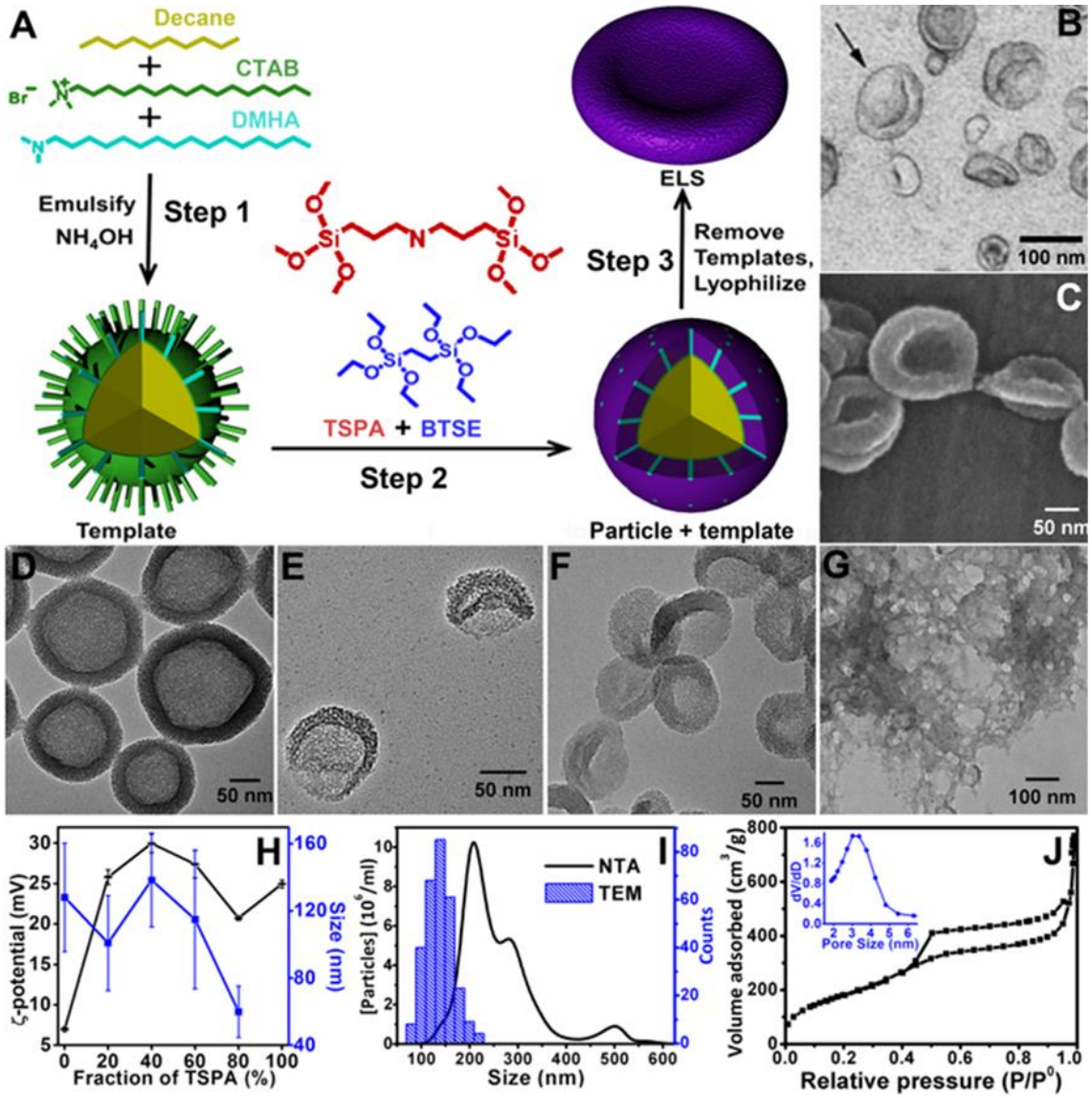

Figure 2.2. Novel discoid silica nanoparticles around 140 nm were prepared via an emulsion template method. (A) Schematic of the discoid silica nanoparticles fabrication and morphology. TSPA (red) changed the overall stiffness of silica shell and render them more elastic[267] to form the discoid silica nanoparticles. (B) TEM image of exosomes (black arrow; adapted with permission from reference[271]). (C) SEM image of typical discoid silica nanoparticles indicates the similarity of shape and size between discoid silica nanoparticles and exosomes. (D-G) TEM images of silica products made with (D) 0%, (E) 20%, (F) 40%, and (G) 100% TSPA (red). Hollow spheres were obtained when no TSPA was added (D); a silica gel was formed with only TSPA (G). (H) Zeta-potential and TEM size distribution of silica nanoparticles synthesized with different fractions of TSPA indicated that the 40% TSPA samples were the largest and had the most positive surface charge, and these samples were used for subsequent analysis and cell tracking. (G) Size distributions of discoid silica nanoparticles synthesized with 40% TSPA. NTA showed a larger mode size than TEM because NTA measures the hydrodynamic size of discoid silica nanoparticles and nanoparticles form aggregations in water. (H) N_2 adsorption-desorption isotherms of discoid silica nanoparticles made with 40% TSPA indicated the existence of mesopores on the discoid silica nanoparticles. The BJH desorption pore size of the discoid silica nanoparticles is 5.4 nm (inset). Reprinted with permission from RSC[32].

3.2. Echogenicity of discoid silica nanoparticles

We analysed the echogenicity versus particle size, porosity/density, surface area, pore structure, and shape of silica nanoparticles with discoid silica nanoparticles and three classical silica nanoparticles including the Stöber silica nanospheres (SSN)[95], the MCM-41 mesoporous silica nanospheres (MSN)[98], and the mesocellular foam silica nanoparticles (MCF)[103].

3.2.1. Effect of particles' size on the echogenicity of Stöber silica nanoparticles

According to the literatures[272, 273] and our studies, the ultrasound signal can be affected by particle size (**Figure 2.3**). Echogenicity of Stöber silica nanoparticles with different sizes (**Figure 2.3**) were measured at identical particle counts. The ultrasound intensity plateaus at 358 nm and declines when the size is 492 nm. The 358 nm Stöber silica nanoparticles have ultrasound signal that is 64.8%, 69.5%, and 36.7% higher than the 260 nm particle and 18.9%, 20.5%, and 22.9% than the 492 nm particles at 1.25×10^{10}, 2.5×10^{10} and 5×10^{10} particles/ml, respectively ($p<0.0005$) (**Figure 2.3C**).

Echogenicity of all Stöber silica nanoparticles increased with concentrations, but the linearity of ultrasound signal as a function of concentration is different. The R^2 values are 0.993, 0.999, 0.998, 0.952, and 0.932 for Stöber silica nanoparticles of 60, 160, 260, 358, and 492 nm, respectively (**Figure 2.3D**). The signal for the 358 nm and 492 nm particles at 5×10^{10} particles/ml drops compared to the linear fitting (**Figure 2.3D**).

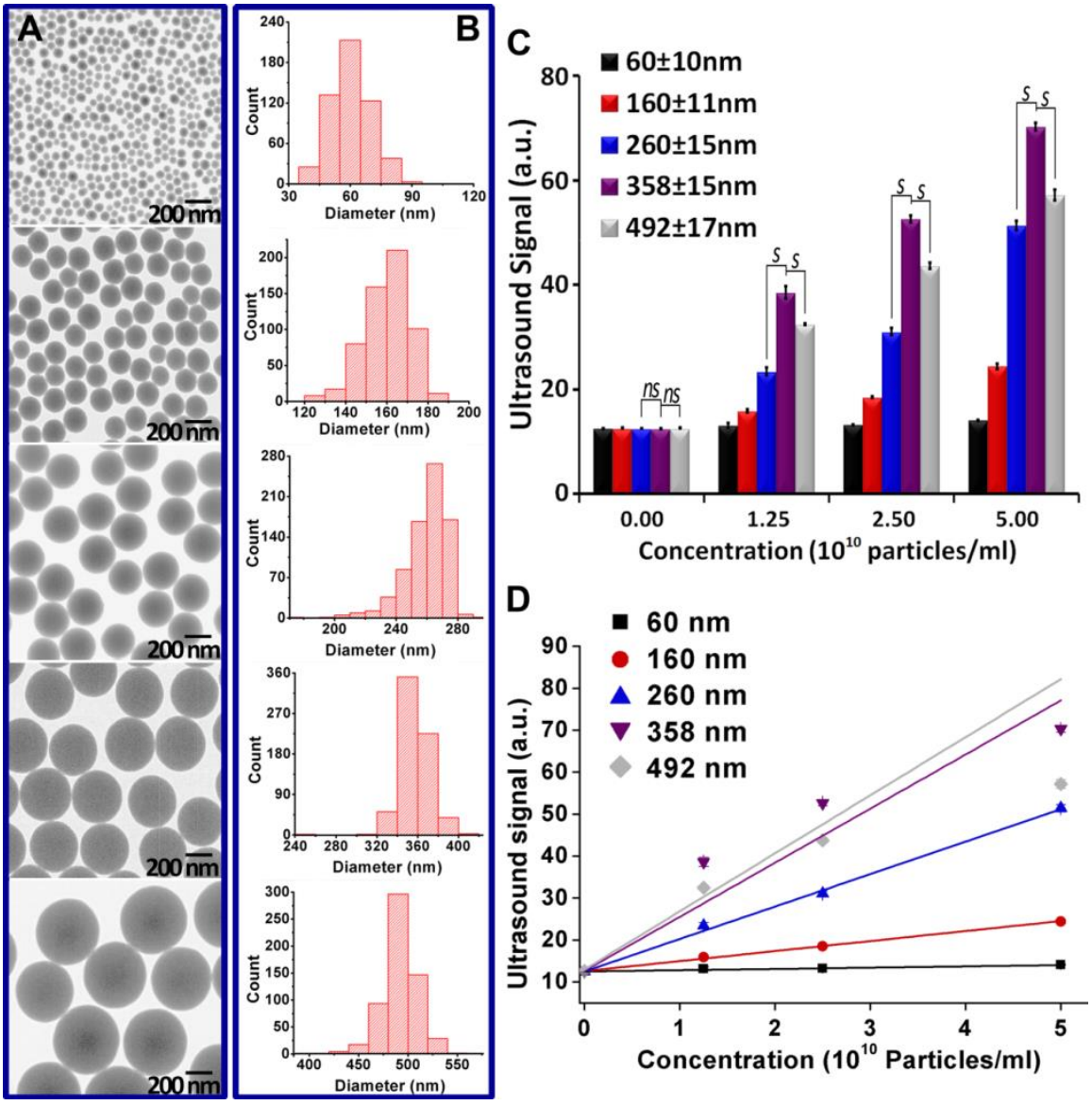

Figure 2.3. Ultrasound intensity as a function of size. (A) TEM images and (B) size distributions of Stöber silica nanoparticles with different sizes. (C) Ultrasound signal of Stöber silica nanoparticles changes with size and particle concentration. The samples were scanned in an agarose phantom at 40 MHz. (ns: non-significant; s: significant). The ultrasound contrast increases as a function of Stöber silica nanoparticles size, but then reaches a plateau at 358 nm and declines at 492 nm. The 358 nm Stöber silica nanoparticles produce more signal than 260 nm and 492 nm nanoparticles ($p<0.0005$). Ultrasound intensities of all five Stöber silica nanoparticles increase with particle-concentrations. (D) The linear relationship between ultrasound signal and particle-concentrations. The R-square values suggest that the most linear behavior occurs with particles smaller than 260 nm. Error bars represent the standard deviation of five replicate measurements. Reprinted with permission from RSC[32].

3.2.2. Effect of ordered 2D pores/channels on the ultrasound signals

We compared the ultrasound signal of similar sized Stöber silica nanoparticles and MCM-41 mesoporous silica nanospheres (**Figure 2.4**) at identical particle-concentrations to determine the impact of the channels on acoustic signals. **Figure 2.4** shows the ultrasound images and processed data of Stöber silica nanoparticles and MCM-41 mesoporous silica nanospheres at the same particle-concentrations scanned at 40 MHz. As expected, both nanoparticles have increased signal as a function of concentration. The ultrasound signals of Stöber silica nanoparticles at 2.5×10^{12}, 5.0×10^{12}, 1.0×10^{13} and 2.0×10^{13} particles/ml are 38%, 48%, 36% and 38% higher than that of MCM-41 mesoporous silica nanospheres. Moreover, echogenicity of MCM-41 mesoporous silica nanospheres was lower than that of Stöber silica nanoparticles at all the measured concentrations. Porosity greatly increased the surface area, and the BET surface area of Stöber silica nanoparticles is more than 10 times lower than that of MCM-41 mesoporous silica nanospheres[264, 274, 275]. However, even though larger surface area may bear more air nanobubbles, the increased surface area in MCM-41 mesoporous silica nanospheres didn't improve its echogenicity. Additionally, both particles were suspended in Millipore water without any degas procedures. Therefore, we may conclude that the echogenicity of silica nanoparticles is hardly attributed to air nanobubbles on their surfaces.

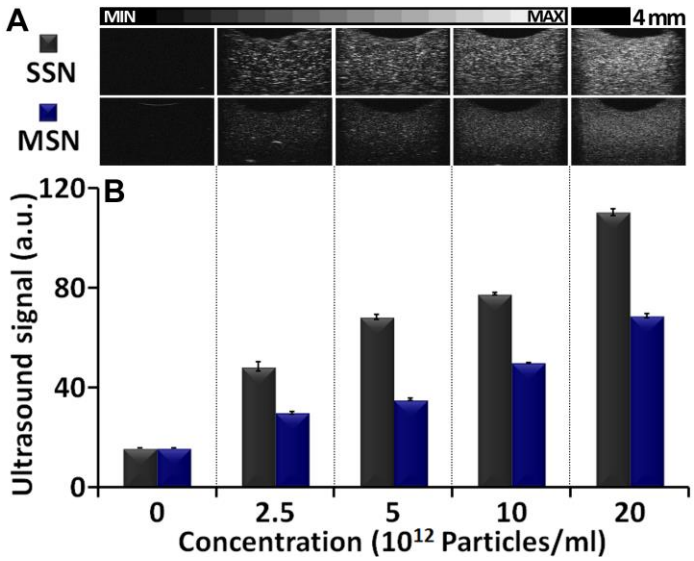

Figure 2.4. Effect of 2D pores/channels on ultrasound signal. (A) Ultrasound images and (B) ultrasound intensity of Stöber silica nanoparticles and MCM-41 mesoporous silica nanospheres scanned at 40 MHz. Both the ultrasound images and image processing indicate that the nonporous Stöber silica nanoparticles produce higher ultrasound contrast than porous MCM-41 mesoporous silica nanospheres. Error bars represent the standard deviation of five replicate measurements. Reprinted with permission from RSC[32].

Instead, the negative effect of pores on the MCM-41 mesoporous silica nanospheres may be attributed to two mechanisms. First, pores can decrease density of particles and thereafter reduce the impedance (production of density and velocity) mismatch between nanoparticles and their surroundings and eventually decrease the echogenicity of MCM-41 mesoporous silica nanospheres. As shown in **Figure 2.5**, the echogenicity of Stöber silica nanoparticles was about 11% to 48% (the difference was concentration dependent) higher than that of MCM-41 mesoporous silica nanospheres. In addition, the density of the MCM-41 mesoporous silica nanospheres was about 50% lower than Stöber silica nanoparticles because more of their volume is empty space. We conclude that the lower signal is because the MCM-41 mesoporous silica nanospheres have a lower impedance mismatch (product of density and velocity) with their surroundings and thus less echogenicity than Stöber silica nanoparticles.

Second, the ordered and penetrating 2D channels on the MCM-41 mesoporous silica nanospheres (**Figure 2.5**) may have decreased the effective backscattering interfaces and therefore weakened the echogenicity. The effect of porous structure on echogenicity is discussed in the next section.

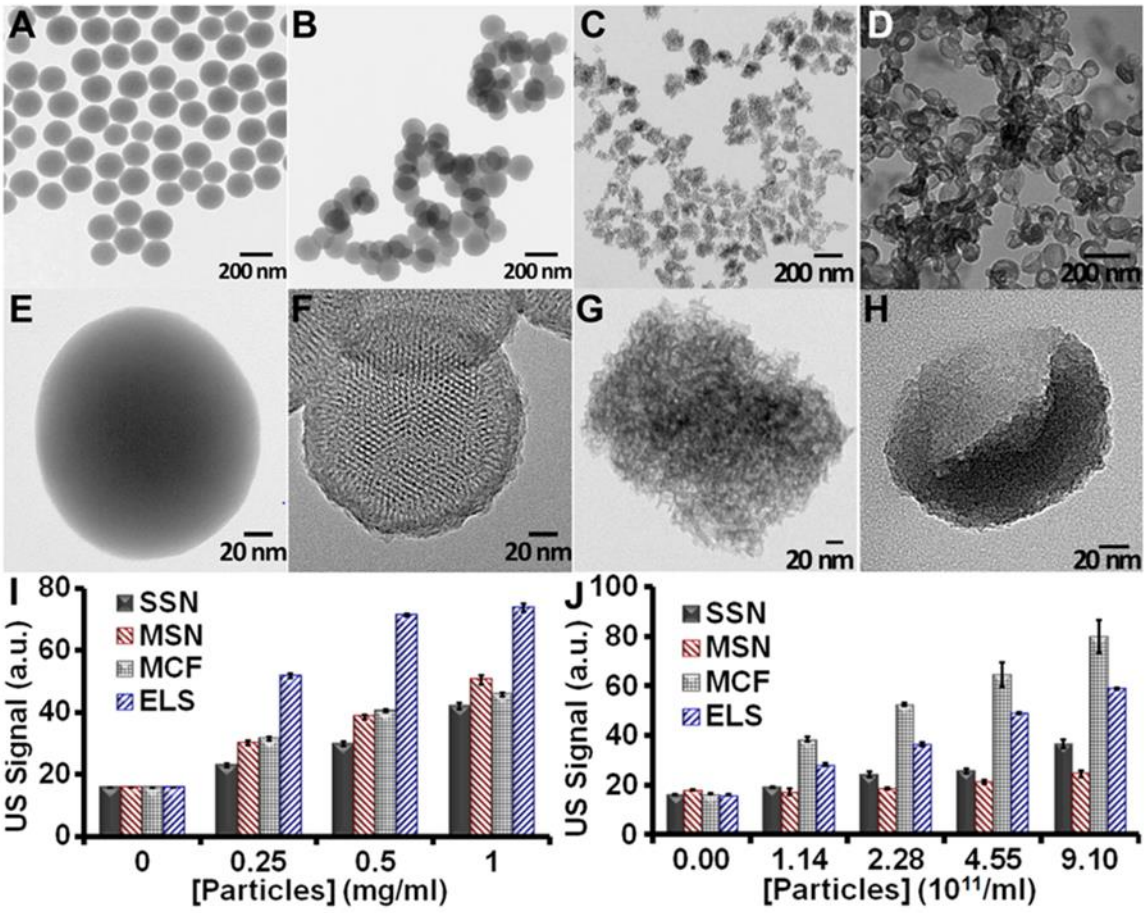

Figure 2.5. TEM images of SSN (A, E), MSN (B, F), MCF (C, G), and DSN (or ELS) (D, H). Both SSN and MSN are spherical, while MCF and DSN have flatter surfaces. HRTEM images (E-H) show that all particles except SSN are porous. The MSN have ordered and penetrating 2D channels, while the MCF and DSN have disordered and non-penetrating pores. (I, J) *In vitro* echogenicity of the four silica nanoparticles. All scans used 40 MHz with concentrations determined on (I) weight basis and (J) particle basis. Error bars represent the standard deviation of five replicate measurements. * represents $p < 0.05$, unpaired Student's t-test. Reprinted with permission from RSC[32].

3.2.3. Echogenicity of discoid silica nanoparticles

Morphologies of all nanoparticles are shown in **Figure 2.5**. The average TEM sizes of Stöber silica nanoparticles, MCM-41 mesoporous silica nanospheres, mesocellular foam silica nanoparticles, and discoid silica nanoparticles was 160 nm, 154 nm, 125 nm, and 138 nm respectively. The NTA size also indicated that the mesocellular foam silica nanoparticles was the smallest followed by discoid silica nanoparticles, MCM-41 mesoporous silica nanospheres, and Stöber silica nanoparticles (**Figure 2.6**).

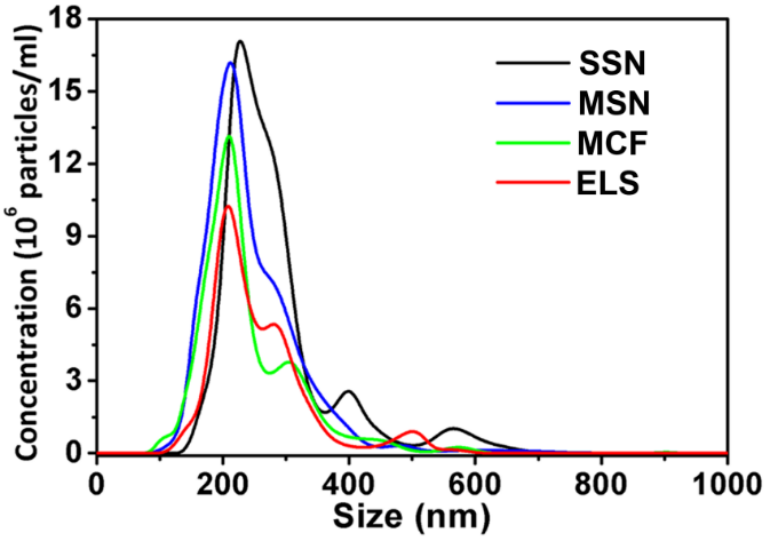

Figure 2.6. NTA size distributions of Stöber silica nanoparticles, MCM-41 mesoporous silica nanospheres, mesocellular foam silica nanoparticles, and discoid silica nanoparticles. Size distribution of nanoparticles suspensions sonicated in water bath for 30 minutes before the NTA measurement. The hydrodynamic radii of Stöber silica nanoparticles, MCM-41 mesoporous silica nanospheres, mesocellular foam silica nanoparticles, and discoid silica nanoparticles are 246, 208, 202, and 208 nm respectively. Reprinted with permission from RSC[32].

The discoid silica nanoparticles exhibited the strongest echogenicity among four nanoparticles at identical mass concentrations (**Figure 2.5**). The ultrasound signal of discoid silica nanoparticles at 0.25, 0.5, and 1 mg/ml was 2.25-, 2.39-, and 1.76-fold of that of Stöber silica nanoparticles; the signal was 1.72-, 1.85-, and 1.46-fold of the ultrasound signal of MCM-41 mesoporous silica nanospheres; and it was 1.64-, 1.76-, and 1.62-fold

of that of mesocellular foam silica nanoparticles. The theoretical LOD of discoid silica nanoparticles (3 standard deviations above background) was 0.77 μg/ml; this value was 7.10, 3.56, and 2.61 μg/ml for Stöber silica nanoparticles, MCM-41 mesoporous silica nanospheres, and mesocellular foam silica nanoparticles, respectively. The higher echogenicity of discoid silica nanoparticles could allow a lower nanoparticle dose to produce the same ultrasound contrast and may therefore increase the biocompatibility. When compared at identical particle numbers, the mesocellular foam silica nanoparticles showed the highest signal (discoid silica nanoparticles were second highest; **Figure 2.5**).

The BJH pore volume of discoid silica nanoparticles were determined empirically to be 1.79 cm^3/g, and that of MCM-41 mesoporous silica nanospheres and mesocellular foam silica nanoparticles were reported to be 2.23 and 1.73 cm^3/g[265]. Correspondingly, the echogenicity of mesocellular foam silica nanoparticles and MCM-41 mesoporous silica nanospheres was the highest and the lowest among three porous silica nanoparticles (**Figure 2.5**). Additionally, the porosity of discoid silica nanoparticles is higher than mesocellular foam silica nanoparticles, and there are more discoid silica nanoparticles than mesocellular foam silica nanoparticles when their mass concentrations are the same. This may explain why echogenicity of the discoid silica nanoparticles was slightly lower than that of mesocellular foam silica nanoparticles with the same particle numbers, but it was higher than the echogenicity of mesocellular foam silica nanoparticles with the same mass concentrations (**Figure 2.5**).

TEM images show that both mesocellular foam silica nanoparticles and discoid silica nanoparticles have pores, but these are disordered and do not penetrate deep into the nanoparticle cores as in the MCM-41 mesoporous silica nanospheres (**Figure 2.5**). This

suggests that the ultrasound waves are unlikely to be transmitted, but are rather more likely to be backscattered. We conclude that discoid silica nanoparticles and mesocellular foam silica nanoparticles have more effective backscattering interfaces[102] introduced by disordered and non-penetrating 3D pore structure and that this is responsible for their increased echogenicity. Both mesocellular foam silica nanoparticles and discoid silica nanoparticles have higher echogenicity than Stöber silica nanoparticles (**Fig. 2.5**). The echogenicity of the mesocellular foam silica nanoparticles was 100%, 117%, 152%, and 118% higher than that of the Stöber silica nanoparticles; the echogenicity of the discoid silica nanoparticles was 46%, 51%, 91%, and 61% higher than that of Stöber silica nanoparticles. This indicated that the effective backscattering interfaces played a more important role in improving the echogenicity than impedance mismatch.

Therefore, the echogenicity of silica nanoparticles could be increased by introducing irregular external surfaces, double convex/concave external surface, disordered non-penetrating 2D pore structure, and/or disordered 3D pore structures that create multiple concave and convex structures to produce backscatter[102].

3.3. Biocompatibility and affinity of discoid silica nanoparticles to stem cells

We characterized the labelling and cytotoxicity of the discoid silica nanoparticles with human mesenchymal stem cells (hMSCs). All silica nanoparticles were incubated separately with the hMSCs under the same conditions without any transfection treatments. We evaluated the impact of discoid silica nanoparticles on hMSC metabolism and viability by MTS, and EthD-III assays (**Figure 2.7**). MTS assay (well-known assays for detecting the cell metabolism) indicated no decrease on cell metabolism between the cells with no discoid silica nanoparticles and those up to 1000 μg/ml. For comparison, the other three

classical silica nanoparticles were also biocompatible at a dosage up to 1 mg/ml (**Figure 2.8**) similar to the literature[114, 242].

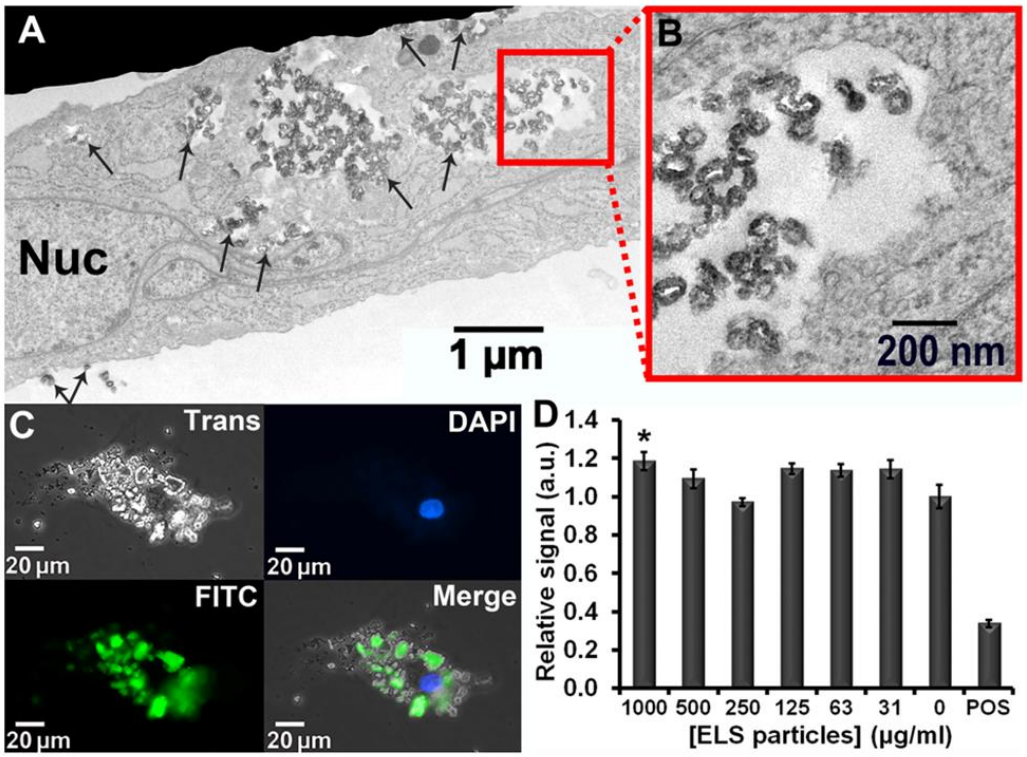

Figure 2.7. hMSCs labeling and cytotoxicity of DSN (or ELS). (A) TEM images of DSN-labeled hMSCs indicated aggregation of DSN inside the cells. DSN located both inside and on the cells. Arrows indicate the DSN, and Nuc indicates nucleus. (B) Higher magnification TEM image indicated that the DSN retained the unique curvature after entering the hMSCs. (C) Epifluorescence microscopy with hMSCs nucleus in blue and DSN fluorescently tagged in green. The majority of DSN were specifically bound to the hMSCs. (D) Cytotoxicity of DSN to hMSCs was determined by MTT and EthD-III assays. MTT assays indicate no decrease on DSN-labeled cell metabolism. "POS" indicated positive control of hMSCs with cytotoxic agent. (Data presented as mean with standard deviations; *represents $p < 0.05$, unpaired Student's t-test). Reprinted with permission from RSC[32].

TEM images show that discoid silica nanoparticles entered the cells and were contained in endosomes (**Figure 2.8, Figure 2.9**). High resolution TEM imaging clearly showed the unique curvature and discoid shape of discoid silica nanoparticles inside the hMSC (**Figure 2.8**); most discoid silica nanoparticles were aggregated in the cytosol. Other

TEM images illustrated clusters on both the cell interior and periphery indicating endosomal uptake of discoid silica nanoparticles (**Figure 2.10**). Epifluorescence microscopy showed that the majority of discoid silica nanoparticles (green via fluorescein label) were bound to the hMSCs (**Figure 2.8**) similar to Stöber silica nanoparticles, MCM-41 mesoporous silica nanospheres, and mesocellular foam silica nanoparticles (**Figure 2.11**).

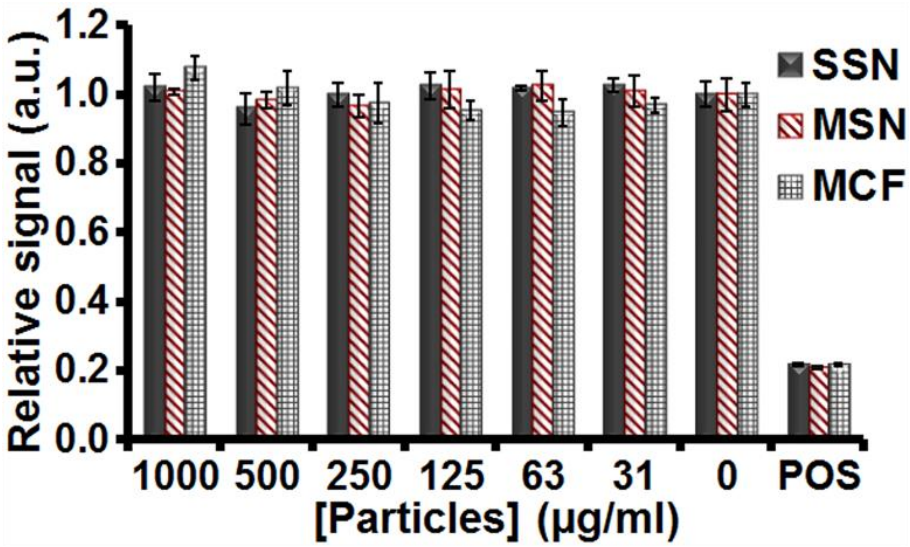

Figure 2.8. Cytotoxicity of SSN, MSN, and MCF. MTS assay indicated SSN, MSN, and MCF were nontoxic even up to 1 mg/mL. Reprinted with permission from RSC[32].

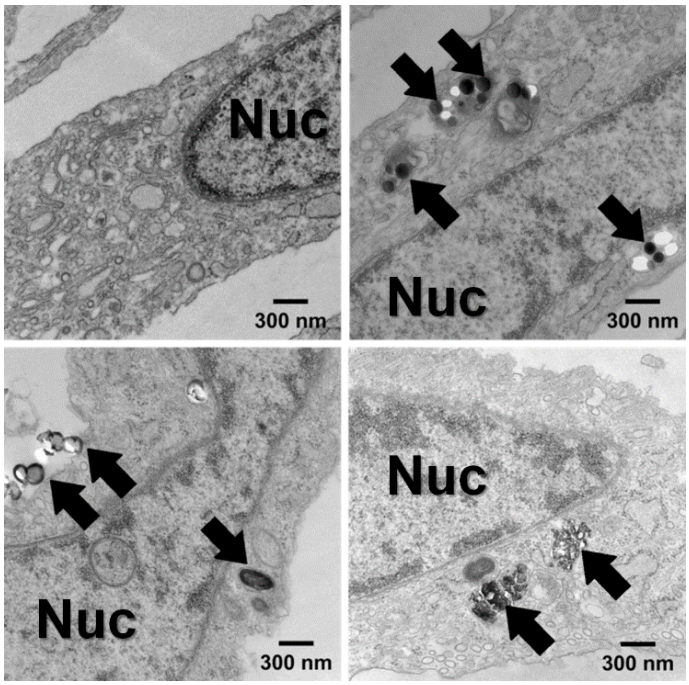

Figure 2.9. TEM images of (A) unlabeled hMSCs, (B) SSN-, (C) MSN-, and (D) MCF-labeled cells indicate all silica nanoparticles can be endocytosed by hMSCs without transfection reagents. All the cells were incubated under the same conditions except that different types of silica nanoparticles were used. Nuc stands for the nucleus, and the arrows indicate the silica nanoparticles. Reprinted with permission from RSC[32].

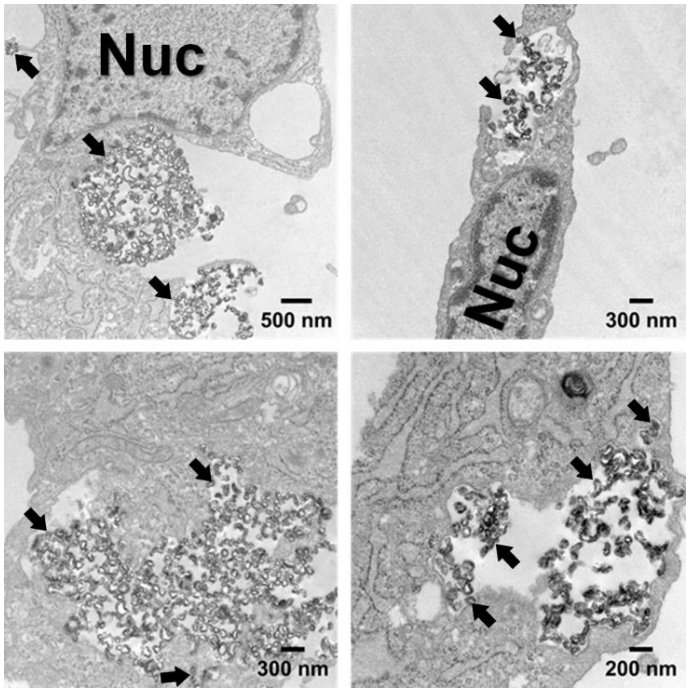

Figure 2.10. TEM images of DSN-labeled hMSCs indicate the endosomal uptake of the DSN. No transfection reagents were used. Nuc stands for the nucleus, and the arrows indicate the DSN. Reprinted with permission from RSC[32].

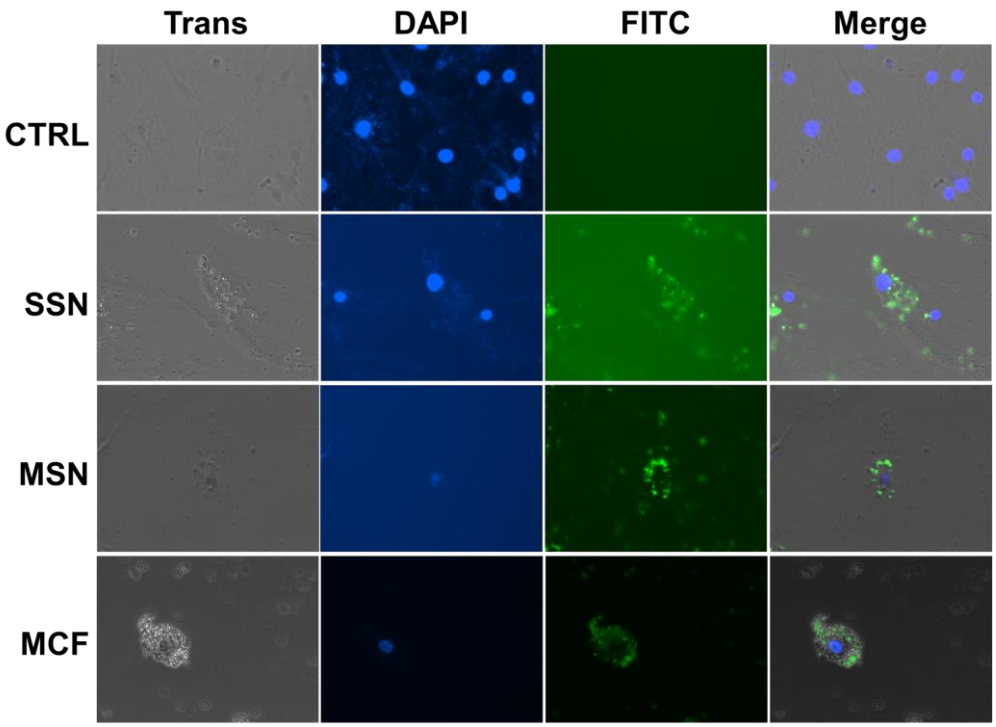

Figure 2.11. Epifluorescence images with hMSCs nucleus in blue and silica nanoparticles fluorescently tagged in green. The overlay images indicate most of the silica nanoparticles were specifically bound to the hMSCs. Reprinted with permission from RSC[32].

Next, we quantified the numbers of silica nanoparticles per vesicle inside hMSCs observed by TEM. The average discoid silica nanoparticles, Stöber silica nanoparticles, MCM-41 mesoporous silica nanospheres, and mesocellular foam silica nanoparticles numbers per vesicle were 285, 6, 4, and 30. For a more global analysis, we measured the Si content per cell via ICP-OES after the labelled cells were dissolved in concentrated base. We measured 1.11 ng Si/cell which equals to 4.14 million discoid silica nanoparticles per discoid silica nanoparticles-labelled hMSC. The Si content per cell for discoid silica nanoparticles-labelled hMSCs was 2.8-, 22.2-, and 1.5-times higher than that in Stöber silica nanoparticles-, MCM-41 mesoporous silica nanospheres-, and mesocellular foam silica nanoparticles-labelled hMSCs, respectively. Also, the particle number per cell in

discoid silica nanoparticles-labelled hMSCs was 6.3-, 21.8-, and 2.02-times larger than that in Stöber silica nanoparticles-, MCM-41 mesoporous silica nanospheres-, and mesocellular foam silica nanoparticles-labelled hMSCs, which were 0.66, 0.19, and 2.05 million nanoparticles/cell, respectively (The calculations for nanoparticles/cell were based on the ICP-OES and NTA data). We rationalize that these differences were due to the differences in surface charge. Zeta-potentials of discoid silica nanoparticles, Stöber silica nanoparticles, MCM-41 mesoporous silica nanospheres, and mesocellular foam silica nanoparticles were +30.0 mV, -38.7 mV, -32.0 mV, and -23.1 mV, respectively. The unique positive charge on a silica particle seen here via the novel TSPA chemistry is what facilitates this increased cell labelling.

3.4. Discoid silica nanoparticles increasing ultrasound contrast of stem cells

The echogenicity of discoid silica nanoparticles-labelled hMSCs was increased versus unlabelled cells and cells labelled with other silica nanoparticles. After the hMSCs were incubated with nanoparticles for four hours at 250 μg/ml, an agarose phantom with the same cell number was scanned with ultrasound at both 25 and 40 MHz. B-mode ultrasound image of discoid silica nanoparticles-labelled hMSCs was much brighter than unlabelled hMSCs with the same cell number with both frequencies (**Figure 2.12**). We then analyzed the mean gray value of these ultrasound images using five different FOVs for each sample with ImageJ software[266]. The discoid silica nanoparticles increased the echogenicity of hMSCs by 3.63-fold. While all four silica nanoparticles increased the echogenicity of hMSCs (**Figure 2.12)**, the discoid silica nanoparticles increased it the most. Moreover, the echogenicity improvement was related to the nanoparticles endocytosed/bound by cells (**Figure 2.12**).

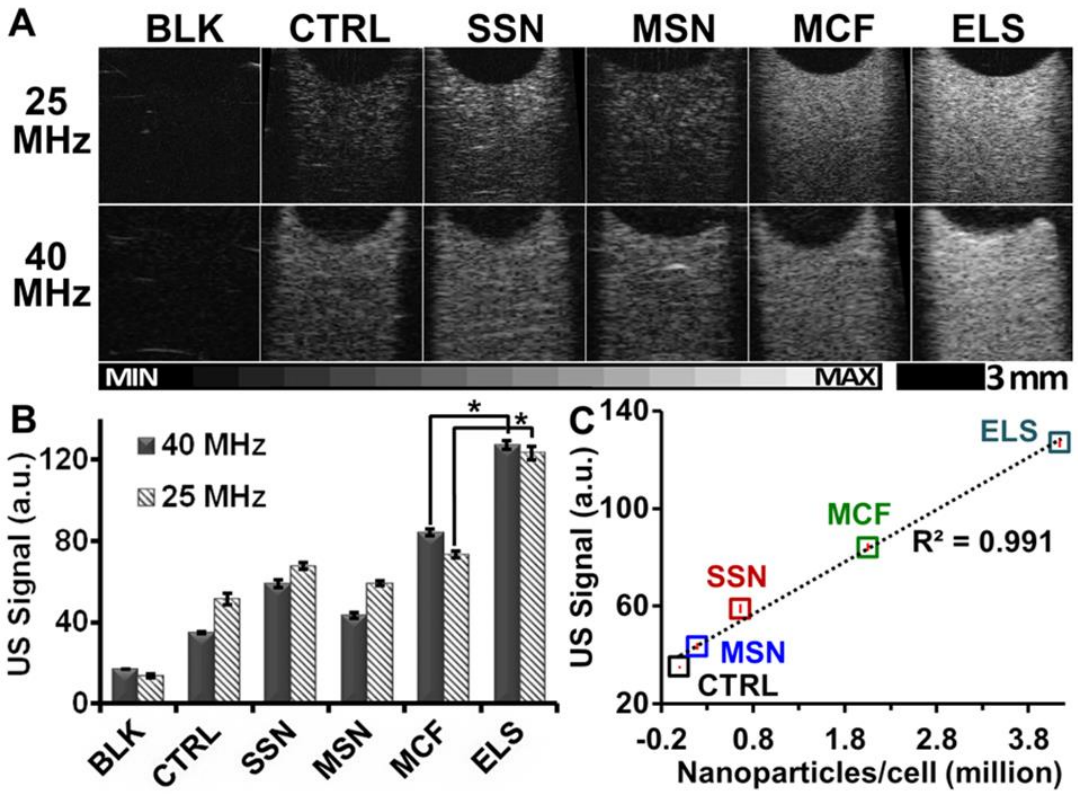

Figure 2.12. DSN significantly increased the echogenicity of hMSCs. Cells were incubated with different types of silica nanoparticles under identical conditions. The labeled cells with the same number were then scanned with ultrasound. Both ultrasound images (A) and ultrasound intensity analysis (B) show that DSN increase the echogenicity of hMSCs. The signal of DSN labeled cells was 3.63-fold of unlabeled cells. Other silica nanoparticles including SSN, MSN, and MCF also increased the echogenicity of hMSCs but not as strong as the DSN. The differences in ultrasound signals between DSN- and MCF-labeled cells were significant. (C) The ultrasound signals (40 MHz) of cells were positively related to the nanoparticles endocytosed by or bound to the hMSCs. The average nanoparticles/cell was determined by ICP-OES after the cells were incubated in different nanoparticles with the incubation conditions. Reprinted with permission from RSC[32].

We then modified the Stöber silica nanoparticles, MCM-41 mesoporous silica nanospheres, and mesocellular foam silica nanoparticles with the APTES, incubated these modified nanoparticles with hMSCs, and then compared the hMSC ultrasound signal to the cells labelled with unmodified nanoparticles. APTES-modified mesocellular foam silica nanoparticles remarkably increased the ultrasound signal of hMSCs than unmodified mesocellular foam silica nanoparticles; APTES-modified MCM-41 mesoporous silica

nanospheres slightly increased the ultrasound signal of hMSCs than unmodified MCM-41 mesoporous silica nanospheres; while APTES-modified Stöber silica nanoparticles did not increase the ultrasound signal of hMSCs compared to the unmodified Stöber silica nanoparticles. This result may be because of the difference in zeta potential after modification. We checked the zeta potential of the modified and unmodified Stöber silica nanoparticles, MCM-41 mesoporous silica nanospheres, and mesocellular foam silica nanoparticles. The APTES-modification increased the zeta potential of mesocellular foam silica nanoparticles to +21.2 mV, that of MCM-41 mesoporous silica nanospheres to + 10.6 mV, and that of Stöber silica nanoparticles to only +3.65. According to the literature[268], silica nanoparticles uptake by hMSCs can be regulated by a threshold of positive surface charge. Moreover, even compared to the APTES-modified nanoparticles, the discoid silica nanoparticles still had the highest ultrasound signal (**Figure 2.13**). These results indicate that the high ultrasound contrast of discoid silica nanoparticles labelled hMSCs derived from both the high ultrasound signal and high cells uptake of the discoid silica nanoparticles.

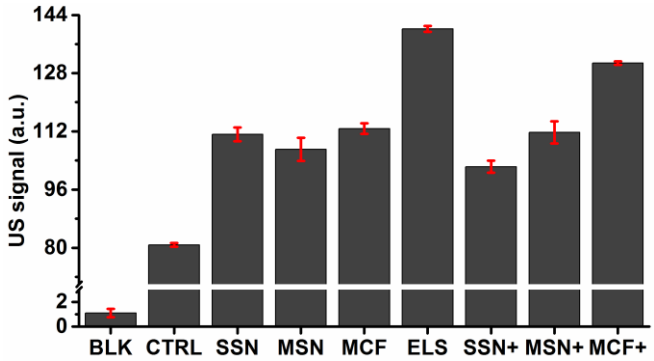

Figure 2.13. Ultrasound signal of unlabeled hMSCs (CTRL) and hMSCs labeled with SSN, MSN, MCF, DSN, amine modified SSN (SSN+), amine modified MSN (MSN+), and amine modified MCF (MCF+). The modification increased the cell labeling efficiency of MCF significantly and that of MSN slightly, while the same modification does not increase the cell labelling efficiency of SSN. However, the DSN still have the highest cell labelling efficiency even compared to the APTES-modified nanoparticles. Reprinted with permission from RSC[32].

The discoid silica nanoparticles also increased the *in vivo* echogenicity and ultrasound sensitivity of hMSCs. The discoid silica nanoparticles-labelled hMSCs were subcutaneously injected with a matrigel carrier into nude mice. PBS and unlabelled cells were also injected as controls. *In vivo* ultrasound images demonstrated significant increase of echogenicity of transplanted discoid silica nanoparticles-labelled stem cells compared to unlabelled cells (**Figure 2.14**). Discoid silica nanoparticles increased the *in vivo* echogenicity of hMSCs 3.3-fold times with 200,00 cells (**Figure 2.14**). Therefore, the discoid silica nanoparticles increased the sensitivity of stem cells via ultrasound. The theoretical limit of detection (LOD) of discoid silica nanoparticles labelled hMSCs was 475 cells—nearly 50-fold higher than the LOD of unlabelled cells.

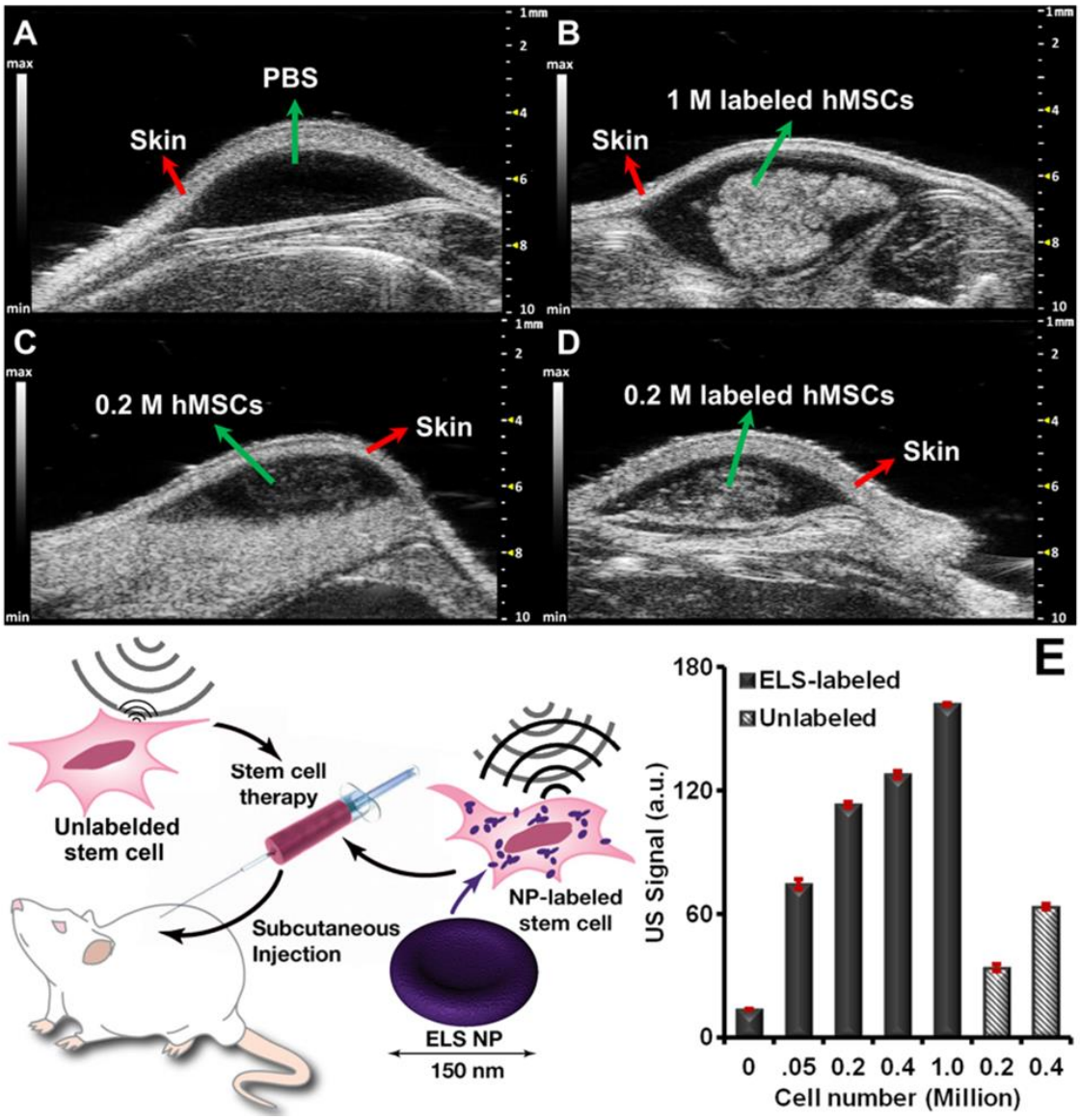

Figure 2.14. *In vivo* ultrasound images and quantification of cells echogenicity. *In vivo* ultrasound images of (A) PBS, (B) 1 million DSN-labeled hMSCs, (C) 0.2 million unlabeled hMSCs, and (D) 0.2 million DSN-labeled hMSCs. (E) Quantification of *In vivo* echogenicity of hMSCs shows ultrasound signal of both unlabeled and DSN-labeled cells were cell number dependent. Bars stands for standard deviation. The LOD of DSN labeled and unlabeled hMSCs was 475 and 21,364 cells respectively. Reprinted with permission from RSC[32].

4. Conclusions

In summary, discoid silica nanoparticles increased both the *in vitro* and *in vivo* echogenicity of stem cells via strengthened particle echogenicity as well as improved cell

labelling efficiency. The incorporation of TSPA—an elastic silica source containing an amine group—to the discoid silica nanoparticles not only provide the exosome-like shape but also increases the zeta-potential, which increases the cell uptake. The unique curvature and discoid shape provide more effective ultrasound backscattering interfaces to enhance the ultrasound contrast of individual discoid silica nanoparticles nanoparticle. This novel discoid silica nanoparticles nanoparticle increases the cell contrast and enables real-time cell tracking/imaging by affordable ultrasound. Noticeably, for stem cell treatment, injected cells tend to die because of hostile environment[276, 277]. As mesoporous silica nanoparticles have been demonstrated to load and control release various drugs[264, 278, 279], the discoid silica nanoparticles could also be loaded with prosurvival reagents[280-282] to increase the cell viability. In addition, these discoid silica nanoparticles are easily chemically modified. While we labelled them with fluorescein here, they could also be coated with a radionuclide or a gadolinium ion for multimodal imaging.

5. Acknowledgement

The text of Chapter 2, in part, is the reprint of the material as it appears in "Exosome-Like Silica Nanoparticles: A Novel Ultrasound Contrast Agent for Stem Cell Imaging" by Fang Chen, Ming Ma, Junxin Wang, Fang Wang, Shixiong Chen, Eric R. Zhao, Anamik Jhunjhunwala, Sean Darmadi, Hangrong Chen, Jesse V. Jokerst, Nanoscale, 2017. The dissertation author was the primary researcher of this paper.

Chapter 3.

Biocompatibility of silicon carbide nanomaterials and their application in stem cell long-term imaging/tracking via photoacoustic and photoluminescence imaging

Chapter 3.1 Cellular toxicity of silicon carbide nanomaterials as a function of morphology

1. Introduction

Silicon carbide (SiC) is temperature tolerant, radiation resistant, and chemically inert[283, 284]. SiC is a wide bandgap semiconductor with high breakdown electric field strength, high saturated electrons' drift velocity and a high thermal conductivity[285]. Due to these unique electrical properties, SiC has become a promising bio-sensor for a variety of medical applications[286-288] including glucose sensing[289], DNA detection[290], and neural probing[291]. SiC is also used to coat medical devices and implants due to its excellent strength, small density (in comparison with metals), stability, and chemical inertness[292].

SiC nanomaterials also have highly strong and stable luminescence[293, 294]. Versus organic dyes and fluorescent proteins, SiC nanomaterials have a higher quantum yield, lower photobleaching, and more stable fluorescence. Cubic symmetric SiC (3C-SiC) nanoparticles have intense photoluminescence in the visible spectral range in aqueous solutions[295]. These SiC nanoparticles maintain their uniform dispersity and luminescent properties in aqueous solutions after storage in air for over 7 months[296]. SiC nanowires with an oxidized layer have recently shown markedly enhanced optical emission from organic photosensitizers resulting in efficient energy transfer[288]. SiC nanomaterials are also more biocompatible than quantum dots because SiC does not release heavy metal ions to the surrounding biological environment[297].

The strong luminescence and nano-scale size make SiC nanomaterials great candidates for labeling and tracking live cells[65, 286, 298]. Botsoa *et al.* demonstrated that 3C-SiC nanoparticles can enter 3T3-L1 fibroblasts with no toxicity after one week of

incubation[286]. The photoluminescence of 3C-SiC nanoparticles enables cell-tracking using fluorescence imaging. SiC nanowires (SiCNWs) can also enter epithelial cells, breast cancer cells, and normal human dermal fibroblasts[284]. These studies highlight the significant potential of SiC nanoparticles (SiCNPs)[286] and SiCNWs[299, 300] including a role in cell tracking to understand the fate of stem cells and to improve the efficacy of stem cell therapy[69].

However, it is critical to understand the cytotoxicity of nanomaterials, including SiC, before using them for cell tracking. Previous work showed that macrophages, fibroblasts, and osteoblast-like cells have a dose-dependent toxicity response to both alpha- and 3C-SiC with no measurable toxicity below 0.1 mg/mL[301]. Cacchioli *et al.* proved the cytocompatibility of the SiCNWs to epithelial cells, breast cancer cells, and normal human dermal fibroblasts by analyzing cell proliferation, cell cycle progression, and oxidative stress[284]. However, Mzyk *et al.* showed that SiC nanoparticles prepared by plasma activated chemical vapor deposition were toxic to mouse fibroblasts[302].

These controversies have limited the translation and development of SiC nanomaterials for medical applications. Such controversies arise from the complexity of factors that affect the cytotoxicity of nanomaterials. Unlike nanoparticles that are intrinsically toxic because they contain and release heavy metal ions[303, 304], SiC nanomaterials could have great biocompatibility because they contain low amounts of toxic elements—silicon, carbon, and oxygen (due to surface oxidation). However, the cytotoxicity of nanomaterials also depends on dosage, morphology, structure, and surface properties[116, 119, 284, 305] besides their elemental compositions[306].

For example, Napierska *et al.* found that the cytotoxicity of monodisperse silica

nanoparticles in human endothelial cells are size-dependent: The smaller silica nanoparticles showed higher cytotoxicity than larger particles[117]. The shape of nanomaterials is another factor that affects their cytotoxicity. Silver nanowires have a significant antimicrobial activity but low cytotoxicity to human cells versus silver nanoparticles[307]. Crystallinity also affects cytotoxicity. Zhang *et al.* found that crystalline silica particles induced apoptosis and generated toxic reactive oxygen species (ROS) while amorphous silica nanoparticles are generally biocompatible[119]. The same group also found that the toxicity of amorphous silica nanoparticles depends on the concentration of hydroxyl groups on their surface and the potential to generate ROS[119].

Although there have been previous studies on the cytotoxicity of SiC-based nanomaterials[64], there are very few reports with human mesenchymal stem cells (hMSCs). Mesenchymal stem cells (MSCs) have a great capacity for self-renewal while maintaining their multipotency, therefore, MSCs have been widely investigated as regenerative medicine. To understand the toxicity of nanomaterials to hMSC is important to develop nanomaterials for hMSCs tracking as well as to understand the complex toxicity of nanomaterials before *in vivo* applications. We present here a careful study on the differences in cytotoxicity between SiCNWs and SiCNPs to hMSCs *in vitro*. Our study focuses on the cytocompatibility of different shapes of SiC nanomaterials and how that affects the metabolism, viability, adhesion, proliferation, migration, oxidative stress, and differentiation ability of hMSCs. We also compared the cytotoxicity of SiCNWs to hMSCs and a breast cancer cell line.

2. Methods

2.1. SiC nanomaterials synthesis and characterization

The SiC nanowires (SiCNWs) were synthesized in a polymer pyrolysis chemical vapor deposition (PPCVD) route similar to our previous report[299]. The polymethylsilane (PMS) used in this work was provided by the National University of Defense Technology (Changsha, China) [308]. Briefly, 4.0 g PMS was mixed well with 5.0 g activated carbon fine powder (100 mesh, with a BET surface area of 390 m^2/g) in a ceramic boat (30 mm × 60 mm) to make a slurry, followed by pushing the slurry into the center of a tubular corundum furnace (Φ 41 mm, 1200 mm in length). A cleaned graphite substrate (30 mm × 50 mm) was placed at downstream of the slurry. The furnace was heated to 1300℃ at 10℃/min with ultra-high-purity argon atmosphere at 5mL/min. The samples were maintained under these conditions for 3 h, and then allowed to cool to room temperature naturally. Finally, a large amount of a cotton-like nanowires was found covering the graphite substrate. We collected the nanowires and then grinded them in a ball mill for 0.5h. The SiC nanoparticles were purchased from US Research Nanomaterials, Inc (#US2161 and #US2022). Both SiC nanoparticles and nanowires were sterilized by heating to 600℃ for 2 hours before cell labeling. SEM images of SiC nanomaterials were taken using an FEI Quanta FEG 250 SEM at an accelerating voltage of 5 kV (Zeiss, Germany). EDX spectra were performed at an accelerating voltage of 20 KV. TEM images were performed on a JEOL 1200 EX II with a Gatan Orius 600 camera.

2.2. Cell culture and labeling

The hMSCs were purchased from Lonza and were used between passage 2 and 10. The growth media were also purchased from Lonza. The seeding density is around 5,000

cells/cm^2 unless specified. Cells were passaged when they reached about 90% confluence with TrypLE Express (Life Technologies) with about 5-8 days between each passage. Labeling with SiC nanoparticles or nanowires was performed without any exogenous transfection agents. The SiC nanomaterials were added to media and allowed to incubate for 4 hours. The adherent cells were washed three times with excessive PBS before detachment or other treatment.

2.3. SEM and EDX sample preparation

Cells were cultured in 6-well plate until 80% confluence and then incubated with 1 ml of 50 µg/mL SiC nanoparticles or nanowires for 4 hours. Cells without any nanomaterials were used as control. After 4 hours, cells were washed with sterilized PBS thrice, detached, isolated from the media, and then resuspended and kept in 500 µL 0.1% glutaraldehyde in PBS for 30 minutes. We then centrifuged and resuspend the cells in PBS. Drops of cells were added onto sterile plastic slides. The cells were immersed in 0.1% glutaraldehyde again for 60 minutes right after the drops were dried in the air. We then transferred the plastic slides carefully to 0.5% glutaraldehyde and left them in the solution for 1h. After that, the cells were dehydrated through a series of alcohols and hexamethyldisilazane (Sigma Aldrich) then critical point dried with liquid CO_2 (Tousimis AutoSamdri 815A, USA). Samples were then sputter coated with an iridium layer using a coating device (Emitech K575X Sputter Coater). SEM images were taken using an FEI Quanta FEG 250 SEM at an accelerating voltage of 5 kV (Zeiss, Germany). EDX spectra and mapping were performed at an accelerating voltage of 20 KV.

2.4. Differentiation experiments

Low passage number (≤ 6)) MSCs were used for differentiation experiments and

done at least in duplicate. Cells were plated and incubated as described above. Stained cells were imaged with a bright field microscopy (Keyence BZ-9000, Germany).

For osteogenic inducted differentiation, standard media was replaced with osteogenic media (hMSC Osteogenic BulletKit, Lonza PT-3002) after the cells were labeled with SiC nanomaterials. Standard media was used for non-induced cells. The media for both induced and non-induced cells was changed every 2-3 days. Once week after the non-induced unlabeled cells reached 100% confluence, all cells were fixed with 70% ethanol on ice for one hour and then stained with freshly made 2% Alizarin Red in water for 7 minutes followed by water washes until no excess stain was removed. Dissolving the colored complex in 10% acetic acid and measuring the optical density at 402 nm quantitated the degree of osteogenesis.

For the adipogenic protocol, standard media was replaced with adipogenic induction media (hMSC Adipogenic BulletKit, Lonza PT-3004) after the cells were labeled with SiC nanomaterials. The cells were then incubated in maintenance media and induction media for 2-3 days alternatively. Once week after the non-induced unlabeled cells reached 100% confluence, all cells were fixed in 10% formalin for 45 minutes and washed with water then 60% isopropanol. Oil red O (Sigma Aldrich) was used to stain the adipogenic cells. The stain solution is freshly made by adding 18 mL water to 27 mL of 3 mg/mL Oil Red O in isopropanol followed by filtration after 10 minutes. The cells were allowed to stain for 5 minutes and then washed with water.

2.5. Cell metabolism, viability, and oxidative stress

Cell metabolism was studied after labeling hMSCs with SiC nanomaterials using CellTiter 96® AQueous One Solution cell proliferation assay (MTS, Promega). After co-

incubated with SiC nanomaterials for 4 hours, 20 µL of the assay reagent was pipetted into the samples in 100 µL of growth media. This was allowed to incubate under standard conditions for 4 hours. We then transferred 80 µL of the sample solutions to a new plate and read the absorbance at 490 nm on a spectrophotometer (SpectraMax M5, Molecular Devices). Cell viability was studied with calcein AM cell viability assay kit (Biotium). Labeled cells were incubated with 100 µL of the reagent assay (containing 2 µM calcein AM) for around 1 hour and then the fluorescence was read at 517 nm with an excitation at 494 nm on a spectrophotometer (SpectraMax M5, Molecular Devices). Quantitative ROS measurement was performed by staining cells with 2',7'-dichlorofluorescin diacetate (DCFDA, Sigma Aldrich) assay. H_2O_2-treated cells and nontreated cells were routinely included as positive and negative controls, respectively. The fluorescence intensity was read at 530 nm with an excitation at 485 nm on a spectrophotometer (SpectraMax M5, Molecular Devices).

2.6. Cell adhesion, proliferation, and migration

For cell adhesion assessment, we detached unlabeled and SiC-labeled hMSCs and then seeded them at the same initial density onto plates. Twenty-four hours after seeding, the non-adherent cells were removed by aspirating the media and washing with PBS. Attached cells were then harvested, counted, and then quantified as a percentage of the initial seeding number. For cell proliferation, we repeated these above procedures 1, 3, and 6 days after seeding. The cell numbers on day 3 and 6 were normalized to day 1. For cell migration ability assessment, cells were labeled in 6-well plate when reached to around 60% confluence. Cells were allowed to grow overnight after remove the free nanomaterials. Then, a gap among cells were created by scraping cells away with a pipette

tip. The gap was imaged repeatedly with light microscopy over 3 weeks. Cells inside and outside the gap on the microscope images were counted with ImageJ.

2.7. Surface marker and cytokine secretion analysis

Cluster of differentiation proteins CD73 (clone: REA804), CD90 (clone: REA897), and CD105 (clone: 43A4E1) on hMSCs were evaluated by flow cytometry (FACSCanto 2, BD Biosciences). The following fluorophores-conjugated monoclonal antibodies and corresponding isotypes were used (Miltenyi Biotec): CD73-PE, CD90-FITC, and CD105-APC. For cytokine secretion analysis, cells were incubated in fresh growth media for 48 hours after labeling. Then the cell media was collected, and cytokines in the media were analyzed with a human inflammation MAP® v.1.0 profile (Myriad RBM).

2.8. RNA isolation and RT-PCR analysis

The total amount of cellular RNA was extracted from cells in two T25 flasks when the confluence reached to 90%, using GeneJet RNA Purification Kit (Thermo Scientific, #K0731). RNA was quantified by using a NanoDrop 2000 (Thermo Scientific). One microgram of total RNA was reverse transcribed and quantitative PCR was performed. Samples were normalized to EF1α, and the ratio change to unlabeled cells was calculated.

3. Results and discussion

3.1. characterization and surface modification of SIC nanomaterials

We synthesized SiCNWs by polymer pyrolysis chemical vapor deposition[299]. The SiCNWs were grown on clean graphite. To remove the potential impurities from graphite, the products were calcined at 600℃ in air for 2 hours. The SiCNPs were made by chemical vapor deposition. We also calcined these SiCNPs at 600℃ in air for 2 hours.

The SiCNPs are 78.8 ± 18.0 nm (abbreviated as SiCNP80, n = 200) and 603.2 ± 97.6 nm (abbreviated as SiCNP600, n = 179) by TEM, respectively. The width of the SiCNW were 82.3 ± 12.4 nm (n=199). Their morphologies and elemental analysis data are shown in **Figure 3.1**. The Pt and Ir arise from the coatings used for scanning electron microscopy (SEM). Elemental analysis showed a small peak for oxygen in the SiC nanomaterials, which indicates oxidation of the surface of SiC nanomaterials similar to the literature[284]. The oxidized layer can be modified with functional moieties. In this study, all SiCNPs and SiCNWs were modified with (3-aminopropyl) triethoxysilane-conjugated fluorescein isothiocyanate (FITC); and green fluorescence overlaps with their intrinsic luminescence (**Figure 3.2**). This indicates that we can modify the SiC nanomaterials with targeting molecules for specific cell imaging.

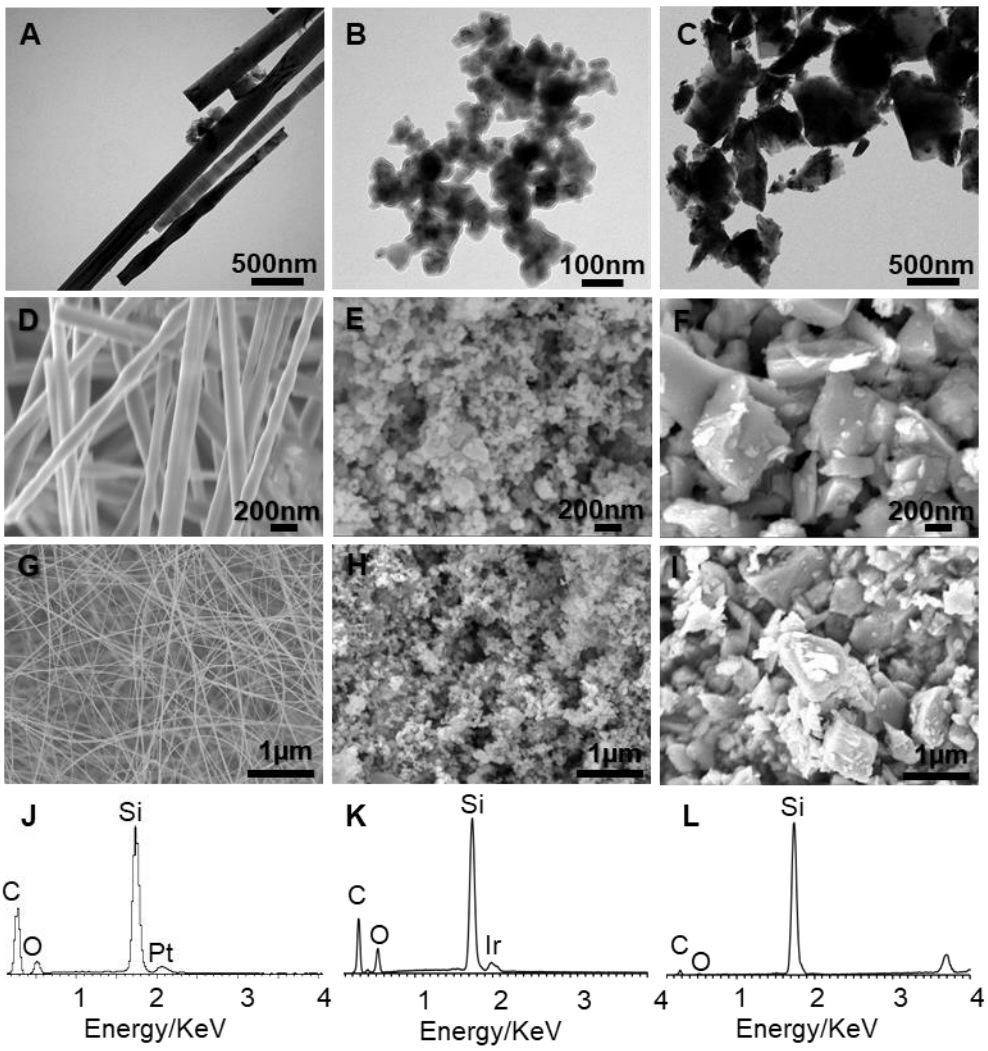

Figure 3.1. Characterization of SiC nanomaterials. TEM images of SiCNW (A) and SiCNP with an average size of around (B) 80 nm (SiCNP80) and (C) 600 nm (SiCNP600). SEM images of (D, G) SiCNW and (E, H) SiCNP80 and (F, I) SiCNP600. The width of SiCNW is around 80 nm. EDX spectra of (J) SiCNW, (K) SiCNP80, and (L) SiCNP600 show the presence of silicon, carbon, and oxygen. The oxygen in the EDX spectra is due to the oxidation of the SiC nanomaterials surface. The Pt and Ir stem from the coatings for SEM sample preparation. Reprinted with permission from Elsevier[309].

3.2. Labeling hMSCs with SiC nanomaterials

Next, we used these materials to label stem cells because stem cell labeling with exogenous contrast agents is a common method to track cells and may improve the efficacy of stem cell therapy[64, 69, 171, 310]. We incubated hMSCs with SiCNWs, SiCNP80, and

SiCNP600 for four hours. The free nanoparticles were washed away with three rounds of sterile PBS. The SiC nanomaterials showed fluorescent signals in both FITC and Texas Red channels. We can use this signal to track the location of hMSCs under a fluorescence microscope (**Figure 3.2**).

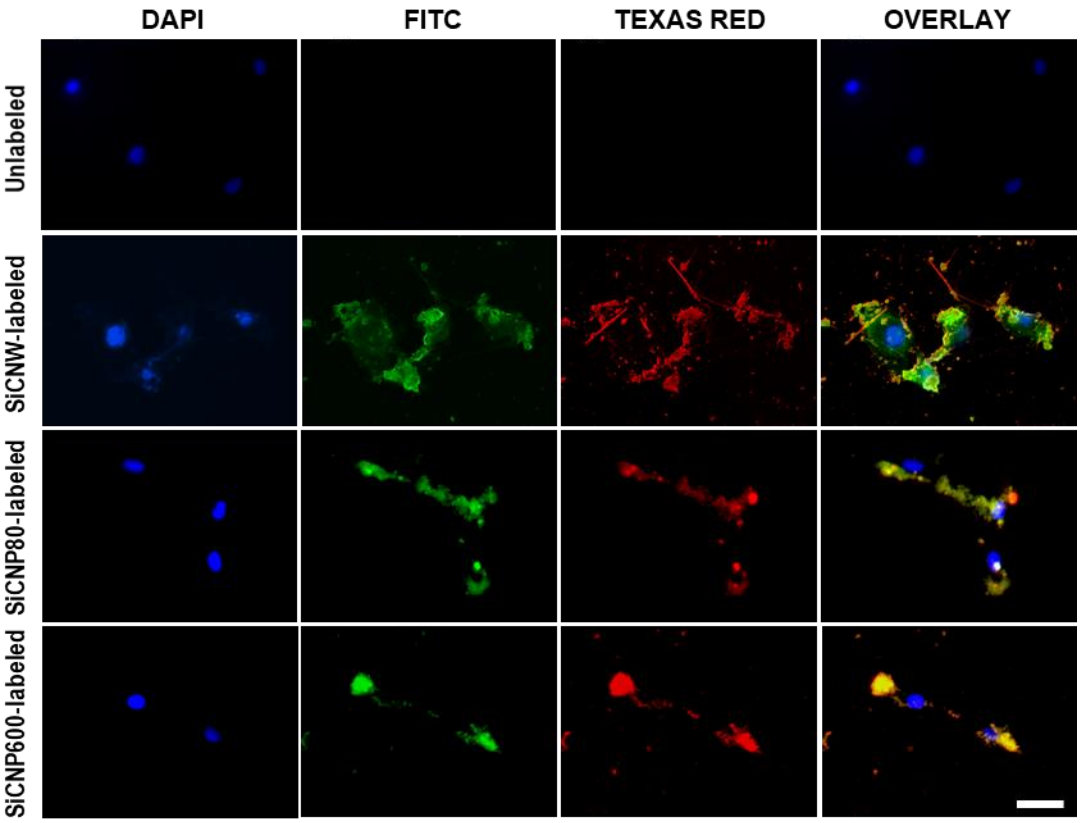

Figure 3.2. Labeling hMSC with FITC-conjugated SiC nanomaterials. FITC was conjugated onto the oxidized surface of SiC nanomaterials through silane. Fluorescence of FITC (green) overlaps with the photoluminescence of SiC nanomaterials (red) approves the SiC surface oxidization and modification. Blue fluorescence is from hMSC nucleus stained with NucBlue®. All the SiC nanomaterials can label hMSCs. The scale bars are 50 μm. Reprinted with permission from Elsevier[309].

Next, untreated cells and all three SiC-treated hMSCs were imaged with SEM and analyzed with energy dispersive X-ray spectra (EDX) (**Figure 3.3**). **Figure 3.3 A-D** show unlabeled hMSCs as well as those labeled with SiCNP80, SiCNP600, and SiCNWs. The

area in the red dotted rectangles is enlarged in **Figure 3.3 E-H** and provides more details on the cells' surface morphology. Non-treated hMSCs are covered by microvilli and small vesicles similar to other reported SEM images[311]. A Si peak is seen for the SiCNPs- and SiCNWs-labeled hMSCs but not control hMSCs (**Figure 3.3 I-L**). EDX mapping of cells also shows that the SiC-labeled hMSCs have Si all over the cells while control cells have negligible Si signals. (**Figure 3.4**). The SiC nanomaterials on cell surface have been removed before sampling, and the Si signal is thus derived from the SiCs that enter the cells at an accelerating voltage 20 KV. The SiCNWs-labeled hMSCs have a wire-like structure protruding from the membrane (**Figure 3.3H**), which could be microvilli for adhesion or tunneling nanotubes[312]. EDX mapping proves that most of these wire-like structures are SiCNWs because they contain silicon as indicated by the green arrows (**Figure 3.4**). One wire-like structure is broken into two parts and does not contain silicon (red arrow), and it is very likely to be a microvillus or tunneling nanotube.

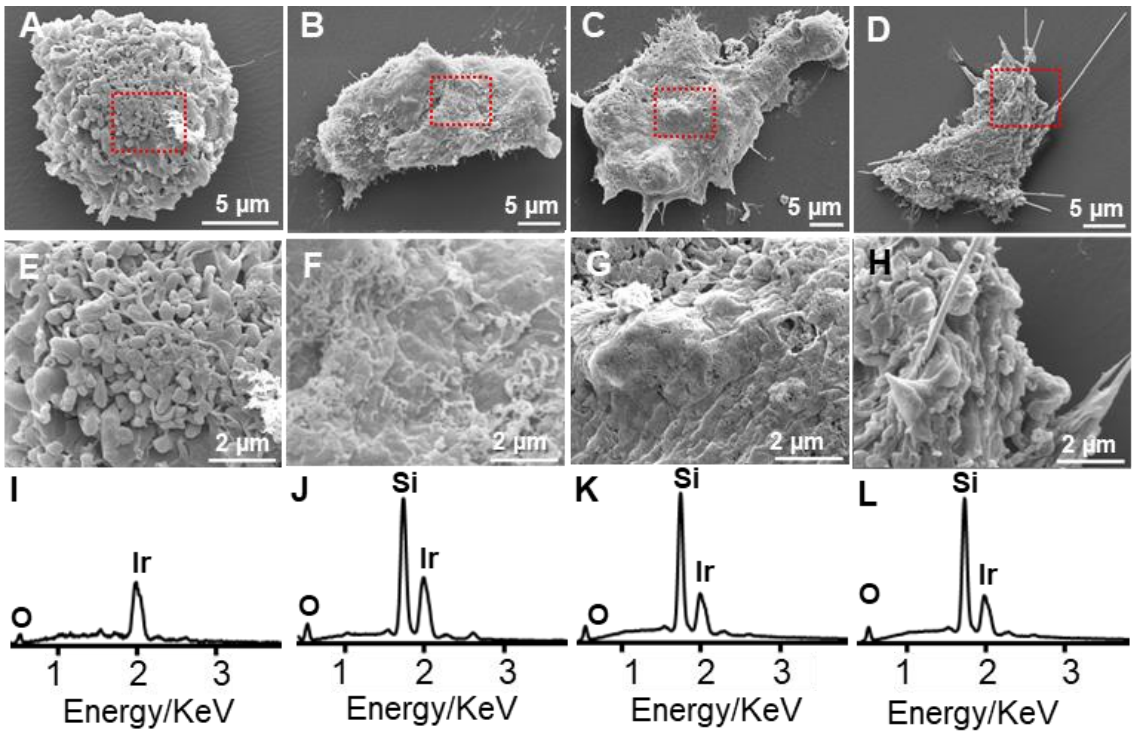

Figure 3.3. SEM and EDX of hMSCs. SEM images of (A) unlabeled hMSCs, (B) hMSCs labeled with SiCNP80, (C) SiCNP600, and (D) SiCNWs. Images (E-H) are enlarged areas from the rectangular in (A-D) respectively. EDX spectra of (I) unlabeled hMSCs, (J) hMSCs labeled with SiCNP80, (K) SiCNP600, and (L) SiCNWs. Cells labeled with SiC nanomaterials show a Si peak while the unlabeled hMSCs has no Si peak. Iridium peaks are due to the coatings for SEM sample preparation. Reprinted with permission from Elsevier[309].

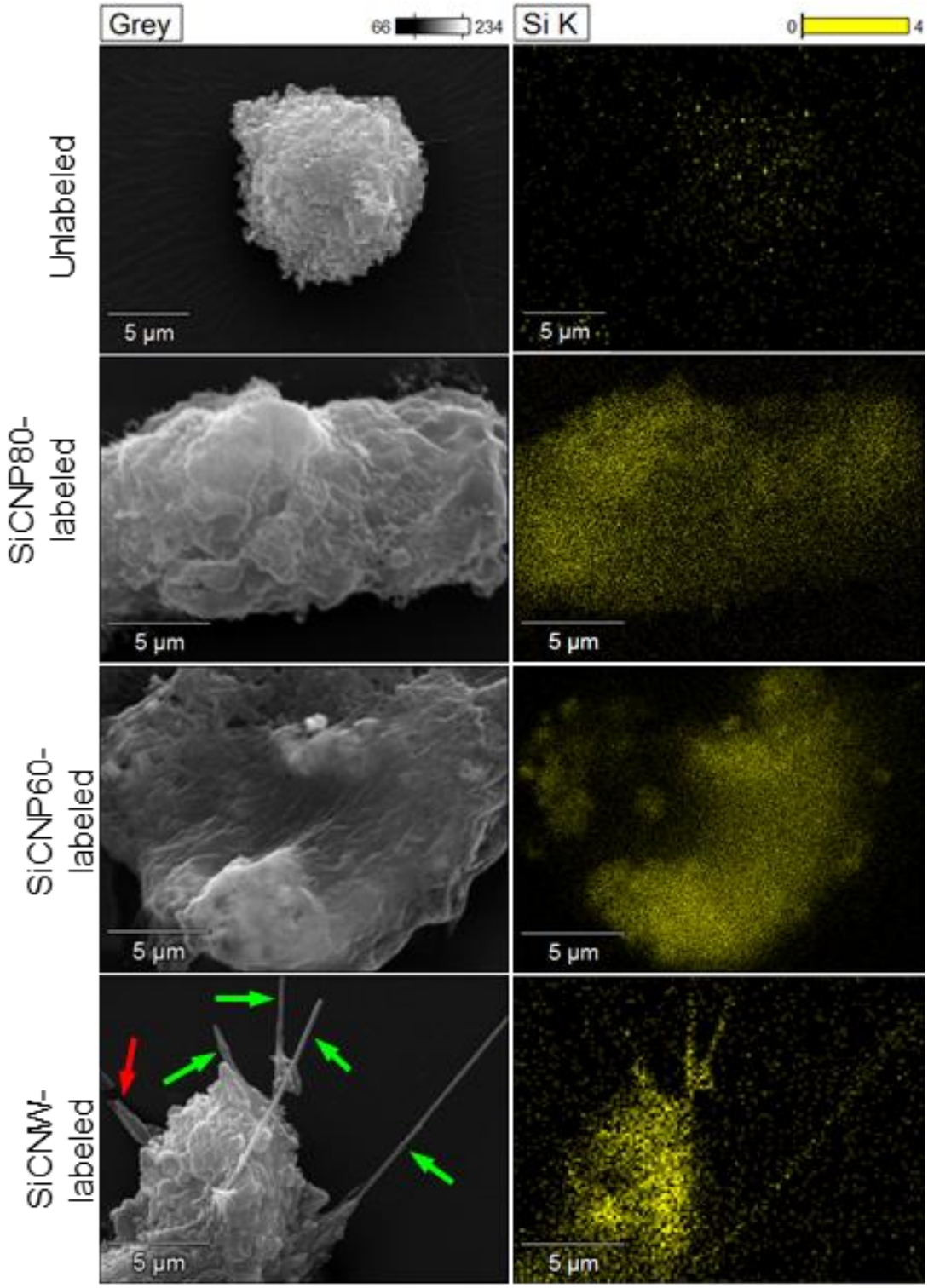

Figure 3.4. EDX mapping of unlabeled and SiC-labeled hMSC show the presence of Si on the cells. The background Si on unlabeled hMSC is from hexamethyldisilazane during drying. The red arrow indicates the microvilli that does not contain silicon, and green arrows indicate the SiCNW. SiCNP80 and SiCNP600 mean SiC nanoparticles with an average size of 80 nm and 600 nm, respectively. SiCNW means SiC nanowires. Reprinted with permission from Elsevier[309].

3.3. Cytocompatibility of SiC nanomaterials

Knowing that these SiC nanomaterials can enter hMSCs and track the stem cell location under fluorescence microscopy, we next investigate the impact of SiC nanomaterials on hMSCs metabolism, viability, oxidative stress, adhesion and proliferation, migration, and pluripotency.

We found that SiCNWs-labeled hMSCs have similar effects on the metabolism, viability, and oxidative stress as SiCNPs-labeled and unlabeled hMSCs. The metabolic activity was studied with an MTS [3-(4,5-dimethylthiazol-2-yl)-5-(3-carboxymethoxyphenyl)-2-(4-sulfophenyl)-2H-tetrazolium]. SiC nanomaterials up to 400 μg/mL did not cause a significant decrease in the cellular metabolism of hMSCs versus unlabeled cells (**Figure 3.5A**). The cell viability was also studied with a calcein AM assay. The results showed no decrease in cell viability for all three SiC nanomaterials from 0 to 400 μg/mL after hMSCs were incubated with the nanomaterials for 4 hours (**Figure 3.5B**).

The oxidative stress was measured with a 2',7'-dichlorofluorescin diacetate ROS assay (details are included in the Supporting Information). Cells exposed to 100 μg/mL of SiC nanomaterials for 4 hours produced low levels of ROS regardless of the morphology of SiC nanomaterials (**Figure 3.5C**). All three assays discussed above were performed within 24 hours after the 4 hours of labeling with SiC nanomaterials. Therefore, we may conclude that SiCNWs has a similar short-term effect on hMSCs as both SiCNP80 and SiCNP600. The SiC nanomaterials have no acute cytotoxicity to hMSCs within 0 to 400 μg/mL. However, that was not the case for long-term viability studies.

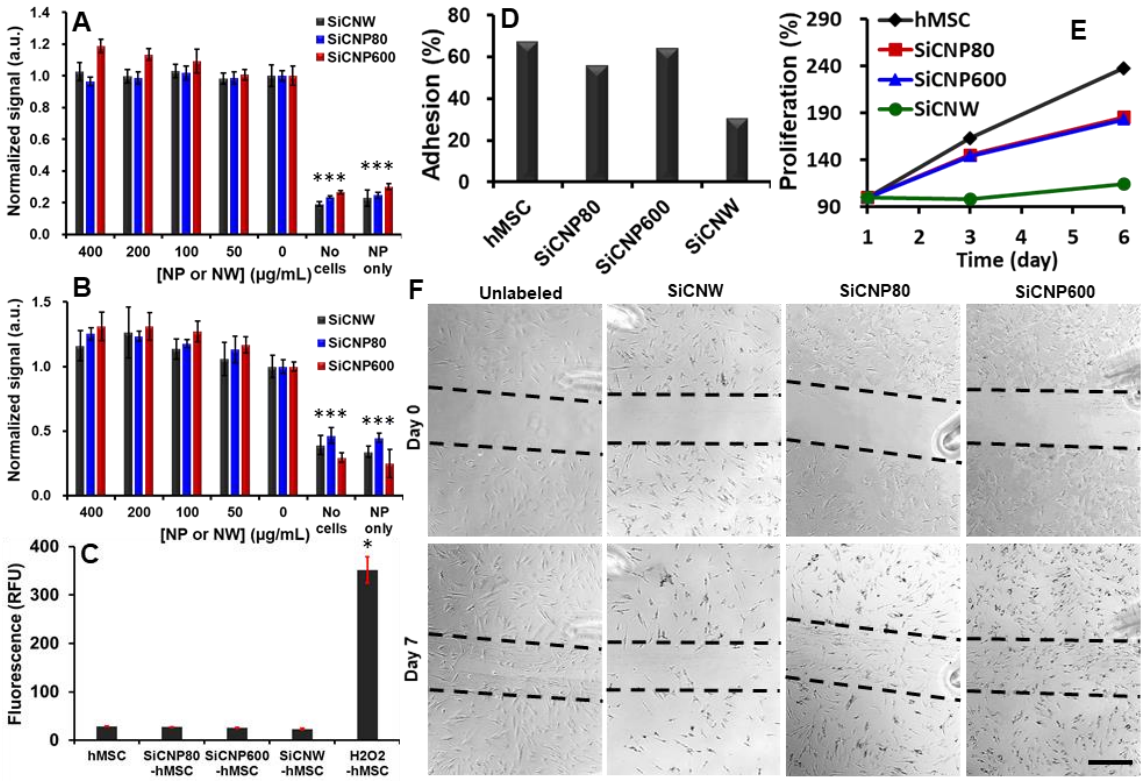

Figure 3.5. Influence of SiC on hMSCs viability, oxidative stress, adhesion, proliferation, and migration ability. (A) The MTS assay showed no significant decrease in cellular metabolism at any combinations of materials and concentrations (up to 400 μg/mL) ($p > 0.05$). (B) A calcein AM cell viability assay shows no significant decrease in viability at any concentrations from 0-400 ug/mL ($p > 0.05$). (C) SiC labeling did not generate intracellular reactive oxygen species. (D) SiCNWs decreased the adhesion ability of hMSCs by more than 50%. (E) SiCNWs greatly decreased proliferation of hMSCs. (F) Migration assay shows hMSCs can migrate after labeling with SiCNWs and SiCNPs. However, there are much less cells in the scratched area on the seventh day in hMSC labeled with SiCNWs than the other three cells. Scale bar is 500 μm. Dashed black lines are added to guide the eye. *** represents $p < 0.005$ compared to hMSC groups, unpaired Student's t-test. Standard bars present standard deviations at least four replicates. Reprinted with permission from Elsevier[309].

For adhesion and proliferation assays, hMSCs were exposed to SiC nanomaterials (0.1 mg/mL) and then detached and re-plated, similar to procedures as stem cell therapy. Approximate 67%, 56%, 64%, and 31% of unlabeled, SiCNP80-, SiCNP600-, and SiCNW-labeled hMSCs adhered to the flask 24 hours after the seeding (**Figure 3.5D**). This indicates that SiCNP80 and SiCNP600 decreased the adhesion ability by 17% and 4%,

respectively, but the SiCNWs decreased the adhesion ability of hMSCs by 54%. Long-term proliferation studies were performed 3 and 6 days after re-plating. The proliferation rate of SiCNW-labeled hMSCs on days 3 and 6 relative to day 1 are 98% and 115% respectively. The SiCNWs-labeled hMSCs had a proliferation rate that was 65% and 123% lower than the unlabeled hMSCs on day 3 and 6, while both SiCNP80- and SiCNP600-labeled hMSCs had a proliferation rate that was less than 20% and around 50% lower than the unlabeled hMSCs on day 3 and 6, respectively (**Figure 3.5E**).

We also performed a migration assay to evaluate the long-term viability of SiC-labeled hMSCs. The original cell density for all four groups was approximately 5,000 cells/cm^2. Cells were removed with a pipet tip, and the hMSCs were allowed to migrate for seven days. One week later, the cell density in the scratched area of unlabeled and SiCNPs-labeled hMSCs were around 5,400 cells/cm^2 and it was only about 1,800 cells/cm^2 for SiCNWs-labeled hMSCs (**Figure 3.5F**).

These data showed that SiCNWs were more toxic to hMSCs than SiCNPs at identical labeling concentrations. To confirm that the toxic effect is not because of impurities or endotoxins in the SiCNWs, we performed a control experiment by checking the impact of SiCNWs on cancer cell lines. Similar to prior reports[284], SiCNWs do not affect the viability, proliferation, and migration ability of cancer cells. Resazurin assay shows the cell viabilities of SiCNW-labeled OV2008 and MCF-7 are over 95% even when the feeding concentration of SiCNWs is up to 0.4 mg/mL (**Figure 3.6A**). The proliferation rate of SiCNW-labeled MCF-7 is around 97.7%, 96.3%, 99.6%, and 95.6% to that of unlabeled MCF-7, respectively (**Figure B**). Unlabeled and SiCNWs-labeled MCF-7 were plated at a density around 100,000 cells/cm^2 on the first day for migration assay. Three

days later, the cell density in the scratched area for unlabeled and SiCNWs-labeled MCF-7 increased from 0 to 286,207 and 289,796 cells/cm^2 respectively (**Figure 3.6C**). Additionally, the SiCNWs can label breast cancer cells and track these cells under fluorescence microscopy (**Figure 3.7)**.

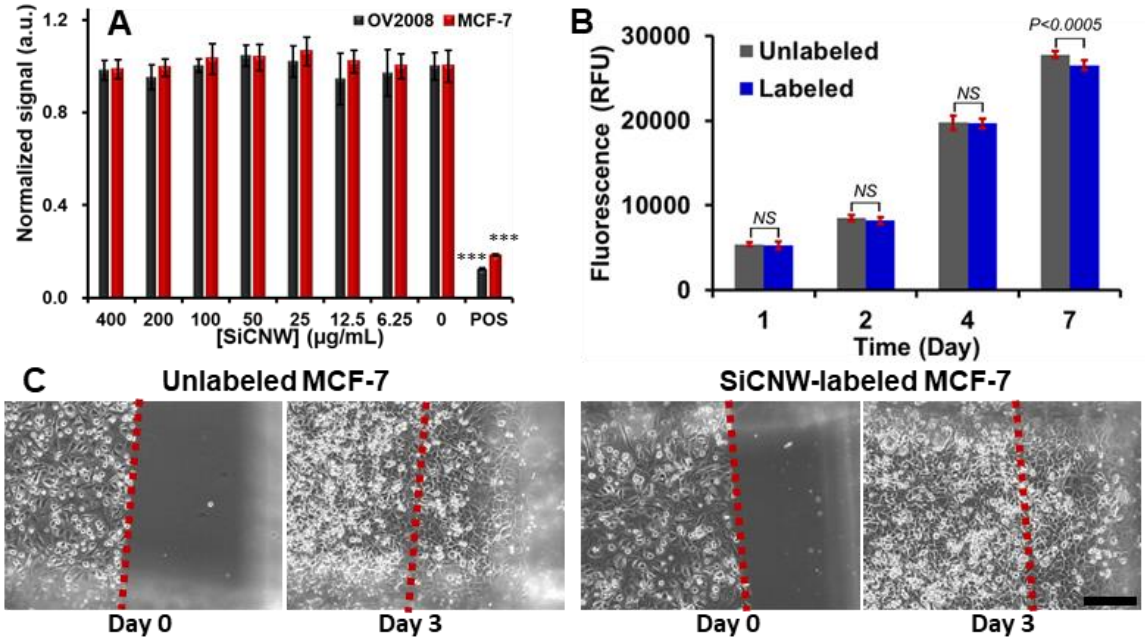

Figure 3.6. Influence of SiC on Cancer cells. (A) Viability assay shows that the SiCNWs do not decrease cell viability in both OV2008 and MCF-7 at concentrations up to 400 μg/mL. (B) Proliferation study shows that SiCNW has negligible effect on the proliferation of MCF-7. (C) Migration assay shows the MCF-7 can migrate after labeled with SiCNW. Scale bar presents 200 μm. Reprinted with permission from Elsevier[309].

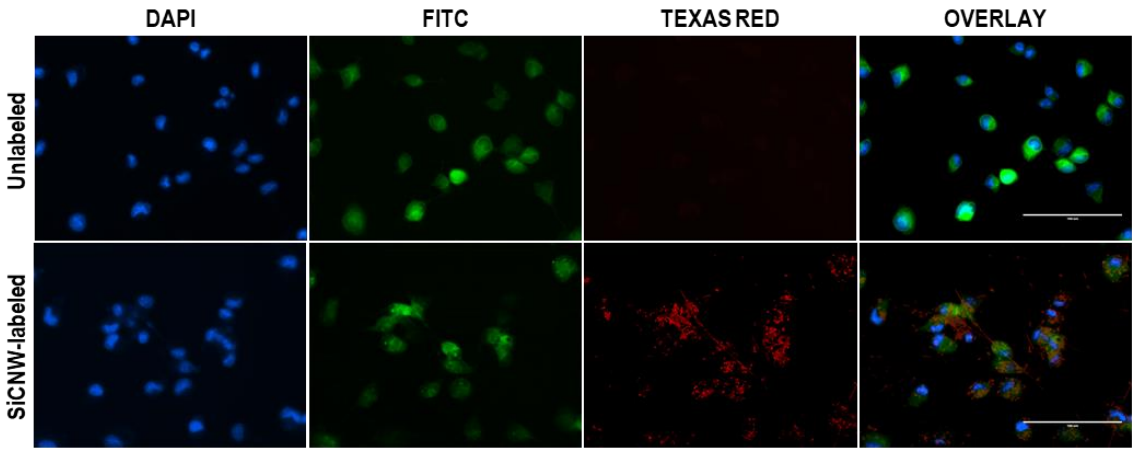

Figure 3.7. Labeling MCF-7 with SiC nanomaterials. Blue fluorescence is from hMSC nucleus stained with NucBlue®, green is from the GFP on the MCF-7, and the red is from the photoluminescence of SiC. The scale bars are 100 μm. Reprinted with permission from Elsevier[309].

3.4. Effects of SiC nanomaterials on functionality of hMSC

In regenerative medicine, stem cells are often expected to differentiate and replace cells in damaged tissues[54], which makes it critical that nanomaterial labels do not interfere with hMSC multipotency. Thus, we studied the impact that these SiC nanomaterials had on hMSC multipotency—we found that the effect is morphology-dependent. The SiCNP80 and SiCNP600 do not affect the potency of hMSC, while SiCNWs prevent hMSCs from differentiating into osteogenic and adipogenic cell types (**Figure 3.8**). The hMSCs were first exposed to SiCNPs or SiCNWs at 100 μg/mL for 4 hours and then treated with normal media, osteogenic induction media, or adipogenic induction media. Calcium deposits were detected by Alizarin Red S staining and fatty lipid vacuoles were stained red by Oil Red O staining three weeks later. Microscopy images show the presence of SiC nanomaterials in hMSCs even after three weeks (**Figure 3.8**). The SiCNP600- and SiCNP80-labeled cells differentiated into both osteogenic and adipogenic lineages similar to control (unlabeled) hMSCs (**Figure 3.8**). However, cells labeled with SiCNWs failed to differentiate into

osteocytes or adipocytes even after treatment with differentiation induction media (**Figure 3.8**). We also quantified the degree of osteogenesis by dissolving the color compounds and measuring optical density. The SiCNWs-labeled hMSCs could not be differentiated into osteogenic lineages (**Figure 3.9**).

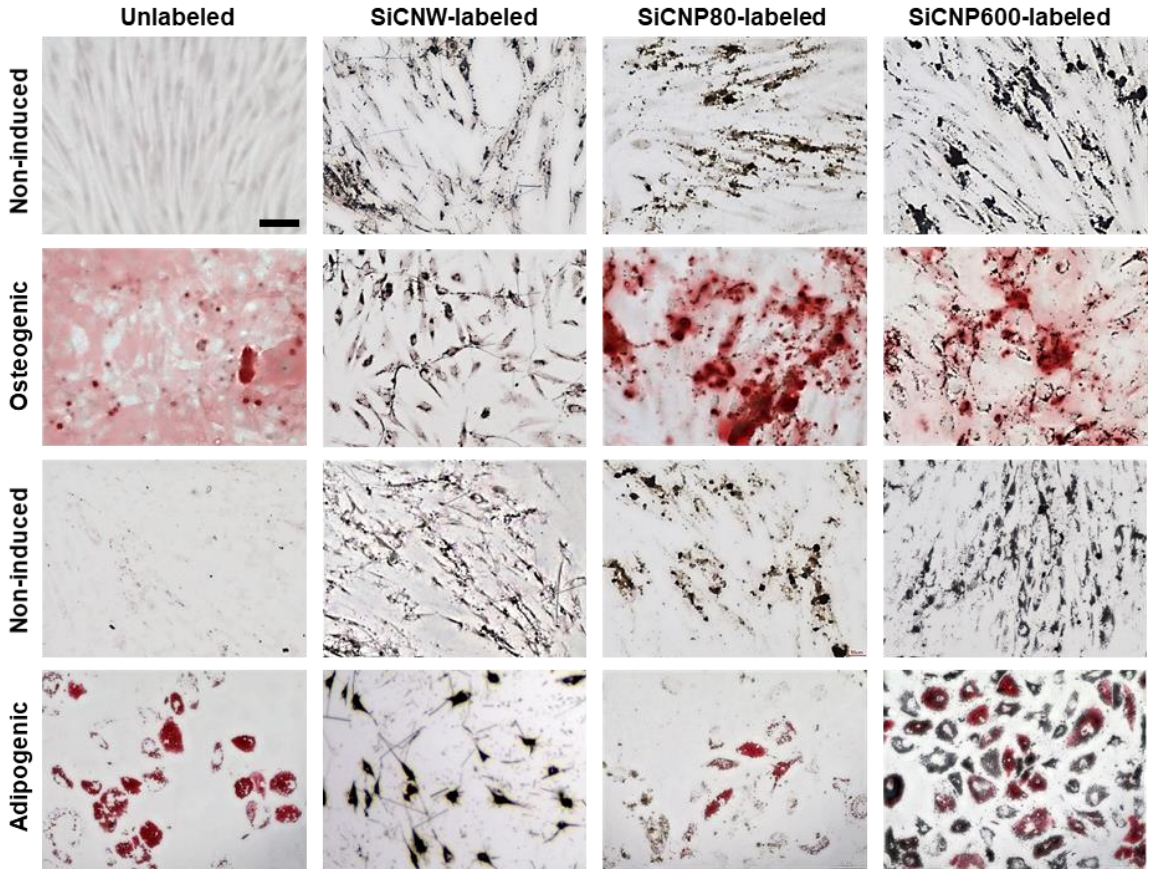

Figure 3.8. hMSCs pluripotency is retained after labeled with SiCNPs but not SiCNWs. Photomicrographs were obtained three weeks after labeling with SiC nanomaterials, and these images clearly showed the presence of SiC nanomaterials in hMSCs even after three weeks. The first two rows were labeled with Alizarin Red S to detect osteogenic cells; the bottom two rows were labeled with Oil Red O to detect adiopenic cells. Non-induced cells did not have adipogenesis or osteogenesis. Unlabeled cells could be induced to either osteocytes or adipocytes. Cells labeled with SiC nanoparticles could also differentiate, but the SiCNWs-labeled cells did not differentiate. All images have the same magnification and the scale bar in the upper-left image presents 100 µm. Reprinted with permission from Elsevier[309].

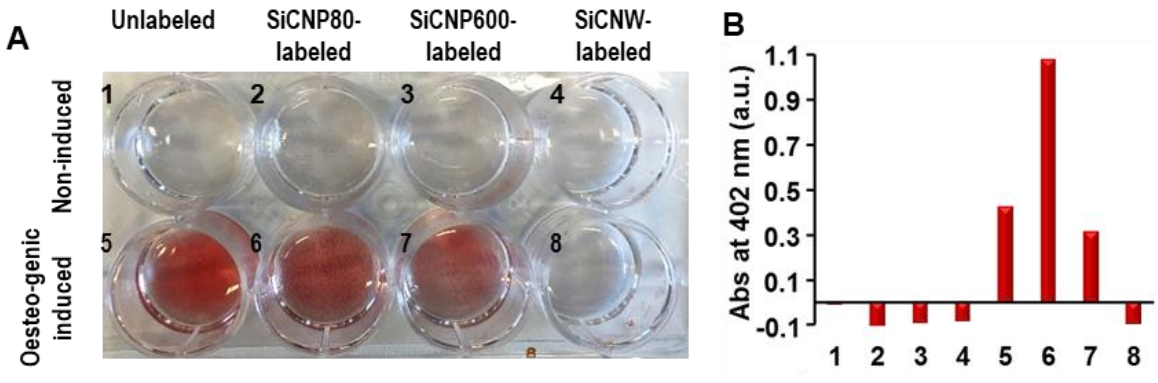

Figure 3.9. Quantification of the degree of osteogenesis by optical absorbance. (A) Photograph of osteogenic induced hMSCs are stained with Alizarin red, an indicator for calcific deposition by cells of an osteogenic lineage. Only SiCNW treated hMSCs shows no color change, which indicates the SiCNW prevent the hMSC from differentiating to osteocytes. (B) The red component in the wells are dissolved in 10% acetic acid, and the absorbance at 402 nm was read. 1-8 correspond to the wells in (A). Reprinted with permission from Elsevier[309].

3.5. Effects of SiC nanomaterials on phenotypes of hMSC

To understand the mechanism by which SiCNWs dysregulate hMSCs, we studied the phenotypes, cytokine secretion, and gene expression levels of SiCNWs-labeled hMSCs versus unlabeled and SiCNPs-labeled hMSCs. Surface marker proteins (or cluster of differentiation) of hMSCs—CD73, CD90, and CD105—were analyzed with flow cytometry (**Figure 3.10A**). Around 67.9%, 52.7%, and 62.5% of SiCNWs-labeled hMSCs remained positive for the CD73, CD90, and CD105 respectively, while over 96% of SiCNP80- and SiCNP600-labeled hMSCs retained these three markers. It is well-accepted that hMSCs should be CD73, CD90, and CD105 positive[313-315]. The CD105 antigen, also known as endoglin, serves as a receptor for the growth and differentiation factors Transforming growth factor beta 1 (TGF-β1) and 3 (TGF-β3)[316]. CD73 is a membrane-bound enzyme that catalyzes the conversion of adenosine monophosphate to bioactive adenosine at neutral pH[317]. CD90 is an activation-associated cell adhesion molecule[318]. The

SiCNWs-labeled hMSCs have similar morphology to neurons under microscope (**Figure 3.11**). In conclusion, the SiCNWs decreased immunophenotype of hMSCs as well as stemness, while SiCNP80 and SiCNP600 have less impact.

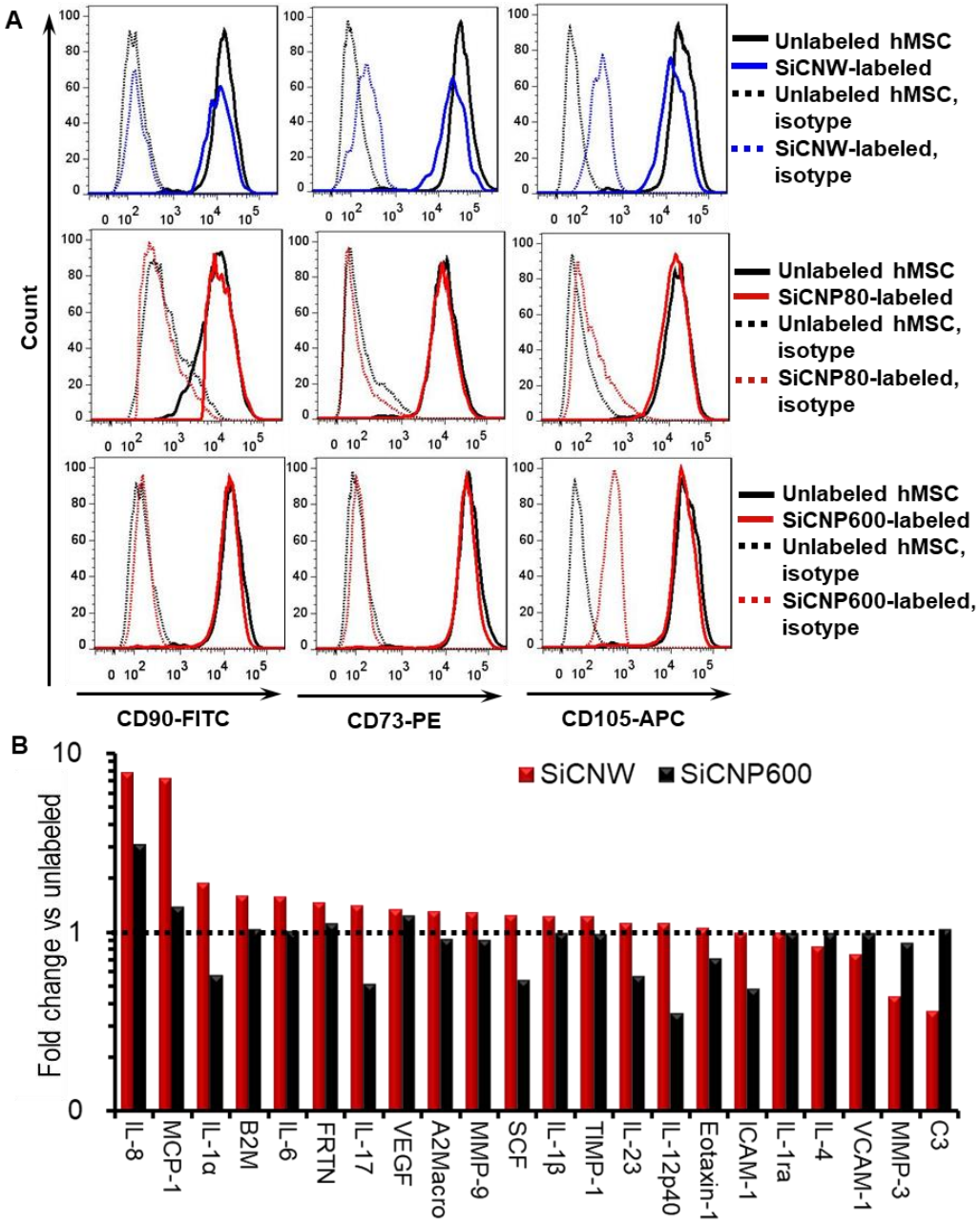

Figure 3.10. Molecular changes of hMSC labeled with SiC nanomaterials. (A) Phenotypes on the surface of SiC-labeled hMSCs. Less SiCNWs-labeled hMSCs remained positive for the CD73, CD90, and CD105 when compared to SiCNP80- and SiCNP600-labeled hMSCs. Unlabeled cells were used as a control and treated with the same antibodies. IgG conjugated with FITC, PE, and APC were used as isotypes. (B) Cytokines secreted by hMSC after labeled with different SiC nanomaterials. SiCNWs-labeled hMSCs secreted 7.2 and 7.8 times more of MCP-1 and IL-8 than unlabeled hMSCs, and they secreted MMP-3 and C3 less than half of unlabeled cells. MCP-1 and IL-8 are pro-inflammatory cytokines. C3 is important to activate the complement system and MMPs play an important role in promoting the differentiation, angiogenesis, proliferation, and migration of hMSCs. SiCNWs have more impact on MCP-1, IL-8, MMP-3, and C3 secretion than SiCNPs600, which may cause the differences in cytotoxicity to hMSCs between the SiCNW and SiCNPs. Reprinted with permission from Elsevier[309].

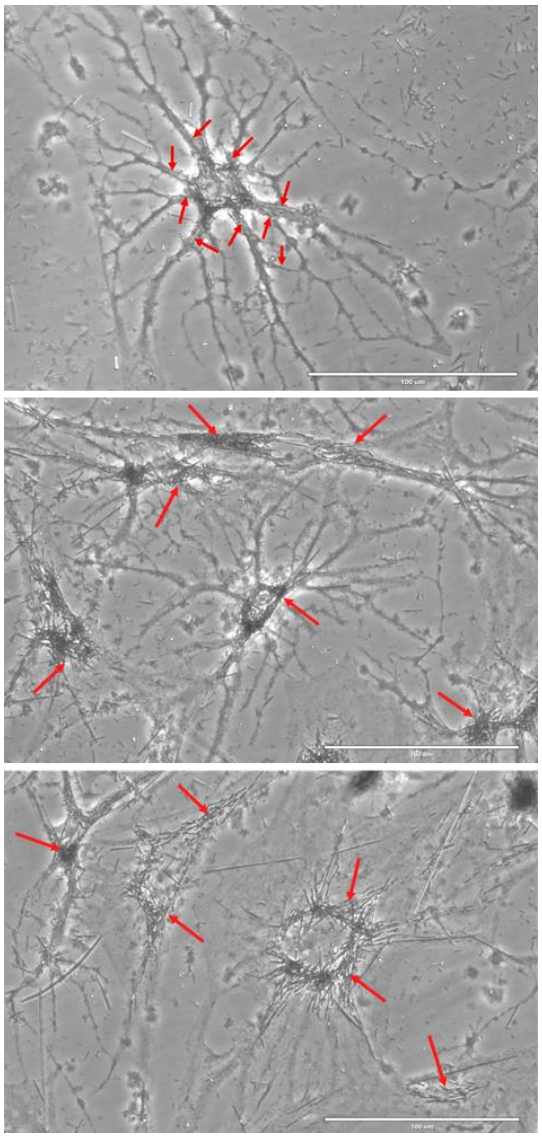

Figure 3.11. Bright field image of SiCNW-labeled hMSC. Red arrows indicate SiCNWs that are along with cell antennas. Scale bars are 100 µm. Reprinted with permission from Elsevier[309].

3.6. Effects of SiC nanomaterials on genes expression of hMSC

We next investigated the gene expression levels in SiCNWs- and SiCNP600-labeled and unlabeled hMSCs via real-time polymerase chain reaction (RT-PCR). The genes of interest included: 1) senescence-associated genes: cyclin-dependent kinase inhibitors CDKN1A (P21), CDKN2A (p16) and CDKN2B (p15), P53. 2) proliferation-

related genes: cyclin-dependent kinase 4 (CDK4), MKi67, and CDK1. 3) adipose-specific genes: lipoprotein lipase (LPL), peroxisome proliferator-activator receptor-gamma2 (PPARG). 4) bone-specific genes: alkaline phosphatase (ALP), bone sialoprotein (BSP). 5) cartilage-specific genes: aggrecan (AGN), and collagen type II alpha 1 (COL2A)[319-321]. The housekeeping gene elongation factor-1α (EF1α) monitored RNA loading. The fold changes of gene expression in SiCNWs-labeled hMSCs versus unlabeled cells for all studied genes are within 200%, and the changes are similar to SiCNP600-labeled hMSCs (**Figure 3.12**). Therefore, the cytotoxicity of SiCNWs to hMSCs is unlikely due to the changes of gene expression in hMSCs.

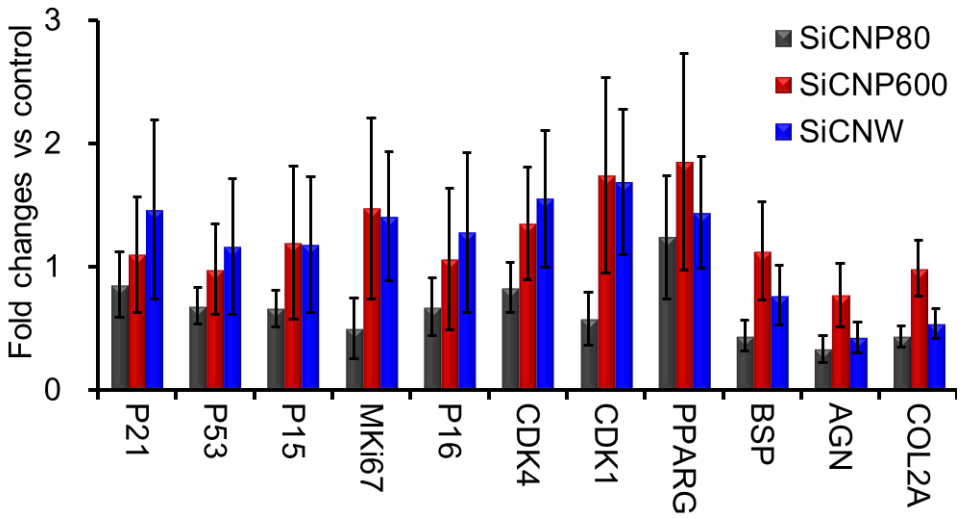

Figure 3.12. Molecular changes of hMSC labeled with SiC nanomaterials. Representative gene expression of all the SiC-labeled cells were within one-fold of unlabeled hMSC. Error bars presents standard errors of 3 replicates. Reprinted with permission from Elsevier[309].

3.7. Effects of SiC nanomaterials on cytokine secretion of hMSC

We evaluated cytokine secretion from unlabeled and labeled hMSCs because the cytokines can explain nanoparticle immunotoxicity[122]. Secretome analysis of SiCW- and

SiCNP600-labeled and unlabeled hMSCs showed that 23 of the 46 analyzed proteins were detectable in cell culture media. Cytokine concentrations from the SiCNWs-labeled cells were within one-fold (50%-200%) of unlabeled hMSC except for complement protein 3 (C3), matrix metalloproteinase-3 (MMP-3), monocyte chemotactic protein 1 (MCP-1), and interleukin-8 (IL-8) (**Figure 3.10B**). SiCNWs-labeled hMSCs secreted 7.2 and 7.8 times more of MCP-1 and IL-8 than unlabeled hMSCs. In comparison, the SiCNP600-labeled hMSCs secreted 1.4 times more MCP-1 and 3.1 times more IL-8 compared to unlabeled hMSCs.

Both MCP-1 and IL-8 are pro-inflammatory cytokines. MCP-1 is a key chemokine that regulates migration and infiltration of monocytes/macrophages[322], and IL-8 is a chemokine that plays a key role in the activation of neutrophils and their recruitment to the site of inflammation[122]. Gerszten et. al. found that both MCP-a and IL-8 can trigger the adhesion of monocytes onto monolayers[323]. SiCNWs-labeled hMSCs increased secretion of IL-8 and MCP-1 likely to improve the cells adhesion and migration ability undermined by SiCNWs as shown by the adhesion and migration studies[122]. These increased IL-8 and MCP-1 levels might prevent hMSCs from differentiating because IL-8 and MCP-1 could inhibit adipocyte differentiation[324].

SiCNWs-labeled hMSCs secreted MMP-3 and C3 levels less than half that of unlabeled hMSCs (**Figure 3.10B**). C3 plays a central role in the activation of the complement system, and C3 deficiency causes susceptibility to bacterial infection[325, 326]. MMPs play an important role in promoting the differentiation, angiogenesis, proliferation, and migration of hMSCs[327]. Specifically, MMP-3 is responsible for remodeling the extracellular matrix, which is necessary for wound repair, organismal growth and

development, and mediation of immune response[328]. SiCNWs can be internalized by cells through direct penetration[284], and the SEM images of SiCNWs-labeled hMSCs (**Figure 3.3D&H, Figure 3.4**) also show SiCNWs protruding hMSCs membranes. Moreover, clusters of SiCNWs can penetrate hMSCs membrane and puncture the cell membrane, which may lead to undesired exchange between hMSCs and the environment (**Figure 3.13**). Thus, a deficiency in MMP-3 could hinder wound repair mechanisms. The SiCNP600-labeled hMSCs had MMP-3 and C3 levels that were 88% and 105% that of unlabeled hMSCs, respectively.

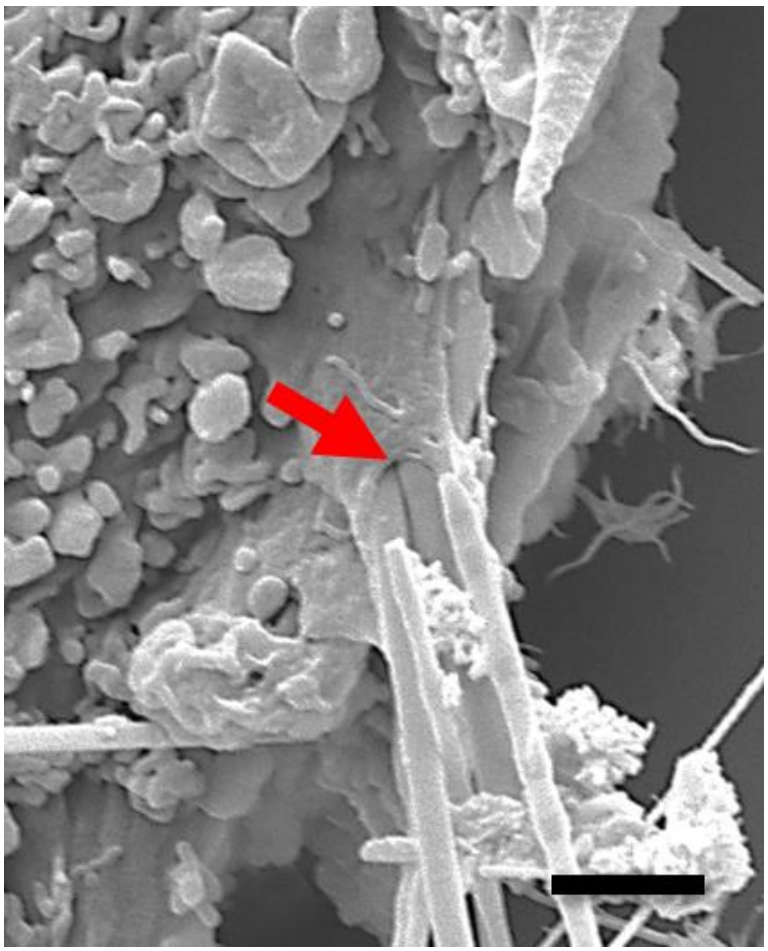

Figure 3.13. Magnified SEM image of SiCNW-labeled hMSC. Red arrow indicates the slot on cell membrane caused by a cluster of SiCNWs. Scale bar is 1 μm. Reprinted with permission from Elsevier[309].

4. Conclusion

Here, we have provided a comprehensive analysis on the impacts of SiC nanomaterials to hMSCs in terms of metabolic activity, viability, oxidative stress, adhesion, proliferation, migration, pluripotency, phenotype, gene expression levels, and cytokine secretion (all procedures are described in the Supporting Information). Our results indicate that the cytotoxicity of SiC nanomaterials to hMSCs is shape-dependent—SiCNWs is toxic to hMSCs but SiCNPs (both 80 nm and 600 nm) show no toxicity at the same labeling concentration.

Therefore, SiCNPs have great potential as optical contrast agents for hMSCs tracking—they have stable and strong luminescence[293, 294] but also good cytocompatibility to hMSCs. However, the SiCNWs were shown to be toxic to hMSCs 24 hours after labeling. The SiCNWs adversely affect hMSCs adhesion, proliferation, migration ability, multipotency, phenotypes, and cytokine secretion. Importantly, SiCNWs should not be used with hMSCs because of the negative impact they have on hMSCs ability to differentiate into the osteogenic and adipocytic lineages[329, 330]. The toxic effect of SiCNWs to hMSCs may be due to the excessive production of pro-inflammatory cytokines MCP-1 and IL-8 and deficiency in MMP-3 and C3.

Chapter 3.2 Silicon carbide nanoparticles as a photoacoustic and photoluminescent dual-imaging contrast agent for long-term cell tracking

1. Introduction

Silicon carbide (SiC) materials are used as dental implants, bone prosthetics, coronary heart stents, and brain-machine interfaces devices.[331] Bulk silicon carbide materials are biocompatible, durable, resilient, and inert. Thus, they are often used as coatings for biomedical devices to prevent leakage of ions and/or reduce biofouling.[301] The emergence of silicon carbide nanomaterials two decades ago has resulted in several novel biomedical applications like cell imaging.[283]

Silicon carbide quantum dots have been used as photoluminescent probes for cell imaging. For silicon carbide, the word photoluminescence more accurately describes the luminescent property than fluorescence due to the delayed emission time.[332] Silicon carbide quantum dots have strong photoluminescence due to their highly improved radiative recombination rates in such small clusters—only few nanometers. Botsoa *et al.* reported using silicon carbide quantum dots with a cubic symmetry crystalline structure (β-SiC) to image living 3T3-L1 fibroblast cells via fluorescence microscopy.[286] Fan *et al.* synthesized β-SiC quantum dots via electrochemical etching and used these quantum dots to label human fetal osteoblast cells.[333] Zakharko *et al.* demonstrated that the silicon carbide quantum dots could label fibroblast cells and the photoluminescence of these quantum dot-labeled cells could be greatly enhanced via localized plasmons.[334] Beke *et al.* showed that silicon carbide quantum dots made by chemical etching could image live neuron cells via two-photon microscropy.[335]

In addition, sub-micron silicon carbide nanoparticles (SiCNPs) could also enter and

visualize cells via nonlinear photoluminescence signals.[336, 337] For example, Rogov *et al.* labeled 3T3-L1 fibroblast cells with 3C-SiC nanoparticles larger than 100 nm and then imaged the labeled cells with nonlinear microscopy.[336] Boksebeld *et al.* used folate-modified 3C-SiC nanoparticles with a diameter of 150 nm to label cancer cells *via* multi-photon microscope.[337] The non-centrosymmetric crystalline structure and relatively large diameter (associated with a large two-photon absorption cross-section) of SiC nanoparticles provided an intense emission peak. Previously, we demonstrated the ability of silicon carbide nanoparticles of approximately 80 nm and 600 nm to track human mesenchymal stem cells (hMSCs) via photoluminescence.[309]

While many studies have shown the utility of silicon carbide nanoparticles for *in vitro* cell imaging, there is little evidence that these nanoparticles can be used for *in vivo* cell tracking—perhaps because photoluminescence has poor tissue penetration depth.[54] This poor penetration of photons limits the use of silicon carbide nanomaterials in cell therapy applications that require *in vivo* tracking of transplanted cells. Photoacoustic imaging is an emerging technique combining the contrast and spectral tuning of optical imaging and high temporal and spatial resolution of acoustic imaging.[33, 338] The improved penetration depth of photoacoustic imaging over optical and fluorescent imaging gives it an advantage for *in vivo* systems.[70] Here, we show for the first time that the silicon carbide nanoparticles generate photoacoustic signals and can track cells *in vivo*.

In this work, we used silicon carbide nanoparticles to track mesenchymal stem cells. Mesenchymal stem cells are a promising regenerative medicine but their retention is poor.[32] It is important to track long-term the injected cells—including the cell location, cell numbers, and cell fate.[339] Silicon carbide nanoparticles have great potential in tracking

mesenchymal stem cells due to their biocompatibility.[309] Here, we compared the photoluminescence and photoacoustic intensities of silicon carbide nanoparticles with three sizes. Then, we used the one with the strongest photoluminescence and photoacoustic intensities to label and track stem cells. This nanoparticle can image mesenchymal stem cells *in vitro via* fluorescence microscopy and, moreover, track stem cells *in vivo via* photoacoustic imaging. Both the photoluminescence and photoacoustic signals of this nanoparticle in mesenchymal stem cells are stable for over 10 days. The photoluminescence of this silicon carbide nanoparticle in mesenchymal stem cells were seen even when the cells differentiated to adipocytes and osteocytes.

2. Methods

2.1. Nanoparticle characterization

Silicon carbide nanoparticles of different sizes were purchased from US Research Nanomaterials Inc. (US2161, US2022, and US2011) and were calcined at 600oC for 2 hours before use as described previously.[309]

Particle sizes were analyzed with TEM images that were taken on a JEOL1400-Plus with a Gatan Orius 600 camera. High resolution TEM (HRTEM) images were obtained via a FEI Tecnai F20 operated at 200 kV, and the element mapping was performed in this electron microscope in STEM mode. STEM images and EDX spectra were taken on a HD-2000 STEM (Hitachi) and Quantax EDS (Bruker) at an accelerating voltage of 200 kV. X-ray diffraction (XRD) patterns were scanned on a Rigaku Miniflex XRD unit operating at 40 kV and 40 mA using Cu Kα radiation ($\lambda = 1.5418$ Å) with a 2θ step size of 0.02° within 20-80°. Zeta potential was measured via a Malvern Zetasizer ZS90.

Absorbance spectra of SiCNPs (20 μg/mL) were obtained with a UV-vis microplate

reader (SpectraMax M5, Molecular Devices). Photoluminescence spectra of SiCNPs suspended in water (20 μg/mL) were examined with the same UV-vis microplate reader under the time-resolved fluorescence mode. To maximize the signal intensity, the integration time was set to 1.5 ms and 100 flashes were recorded per read. Photoluminescence spectra were also recorded via a customized fiber-coupled spectrometer (Princeton Instruments). A layer of SiC nanoparticles were added on glass slide, dried, and then excited by 325 nm or 442 nm UV light (~10 mW) at an angle of ~45° relative to the sample plane. The emission spectra were collected through a 20x objective and recorded by the fiber-coupled spectrometer. A 450 nm long pass filter was applied in front of the spectrometer when the particles were excited by 442 nm light using the same optical setup laser.

Photoacoustic scans were obtained using a Vevo LAZR from Visualsonics.[54] SiCNP samples were resuspended in water at a concentration of 1 mg/mL. Samples were then loaded into polythene tubing and scanned with an array photoacoustic transducer (LZ250, Visualsonics, Inc.) operating at 25 MHz center frequency. The photoacoustic spectra between 680 nm and 970 nm were scanned with a step size of 5 nm. To determine the limit of detection by photoacoustic imaging, SiCNPs were resuspended in water at different concentrations (100, 50, 25, 10, 5, and 0 μg/mL) and scanned with a wavelength at 725 nm. The limit of detection was defined as the concentration that had a signal intensity at 3 standards deviations above the mean.

2.2. Cell culture

Human mesenchymal stem cells (hMSCs, cat #: PT-2501) and cell culture media (cat #: PT-3001) were purchased from Lonza. Human MSCs from passage 2-10 were used.

Mouse mesenchymal stem cells (mMSCs, cat #: MUBMX-01001) were purchased from Cyagen. Mouse MSCs were used between passages 8-12 and were cultured with Dulbecco's Modified Eagle Medium (DMEM) from Gibco supplemented with 10% fetal bovine serum (Sigma) and 1% antibiotic-antimycotic (Thermo Fisher Scientific). Cell media was replaced every 2-3 days. Cells were grown to 80-90% confluency. For passage and usage, cells were detached with 0.25% Typsin-EDTA (Gibco), then centrifuged at 1,000 rpm for 5 minutes, resuspended, and counted by hemocytometer.

For labeling condition studies, hMSCs were plated into a 6-well plate and grown until fully confluent. Then, 2 mL of SiCNPs suspensions in cell media at concentrations of 0, 50, 100, and 200 μg/mL were added to each well separately. After a specific incubation time (1, 4, or 8 hours), cells were washed with PBS thrice to remove free nanoparticles and then collected. The cell labeling capacity was then quantified by thermogravimetric analysis (TGA) and photoacoustic imaging independently. TGA experiments were performed with approximately 400,000 cells resuspended in 20 μL of Millipore water using a Perkin-Elmer STA 6000 Simultaneous Thermal Analyzer. The labeled cells were heated from 25 to 600℃ at a heating speed of 10℃/min and then held at 600℃ for 2 hours. SiCNPs were also analyzed by TGA as a positive control. For photoacoustic imaging, labeled cells were dispersed in a 1:1 warm mixture of PBS: agarose (1%), added in to polyethene tubes, cooled, and then scanned.

The cytotoxicity of SiCNP620 to mesenchymal stem cells was studied by plating cells into a 96-well plate at a density of 5,000 cells/well. Cells were incubated with SiCNP620 suspensions at different particle concentrations—400, 200, 100, 50, 25, and 0 μg/mL. Positive controls included 400 μg/mL SiCNP600 and media only. Eight replicates

were tested. After 48 hours, an 3-(4,5-dimethylthiazol-2-yl)-5-(3-carboxymethoxyphenyl)-2-(4-sulfophenyl)-2H-tetrazolium (MTS) (Promega) assay was performed by adding 100 μL of a 1:10 v/v MTS:media solution to each well. The cells with MTS reagent were incubated for four hours. Next, to avoid any interferences of nanoparticles on the absorbance, 70 μL of supernatants from each well were transferred to a new plate, and the absorbance was read at a wavelength of 490 nm.

The effect of SiCNP620 on the proliferation of mesenchymal stem cells was also studied. Cells were plated in a 96-well plate at a density of 3,000 cells/well and then incubated with SiCNP620 suspensions at different particle concentrations—400, 200, 100, 50, 25, and 0 μg/mL for different durations—1, 2, 3, and 4 days. Positive controls included 200 μg/mL SiCNP600 and media only. Eight replicates were tested for each concentration and duration. At each time point, a Resazurin (Sigma-Aldrich) assay was performed by adding 100 μL of a 1:10 v/v Resazurin:media solution to each well, followed by incubation for 4 hours. We then transferred 70 μL of the supernatant from each well to clean wells and read the fluorescence at an excitation of 550 nm and emission of 585 nm.

2.3. *In vitro* photoluminescence imaging of cells

Photoluminescence imaging was conducted via EVOS fluorescence microscope with a Texas Red channel, which corresponds most closely to the emission wavelength of SiC. SiCNP620-labeled (50 μg/mL of SiCNP620, incubated 4 hours) and unlabeled cells were plated separately in a 6-well plate. Cell morphology was then recorded with photoluminescence imaging on different days for three weeks. Cells plated in other wells were treated with adipogenic or osteogenic induction media for three weeks. The morphology changes were recorded with bright field and photoluminescence imaging.

2.4. *In vivo* cell tracking by photoacoustic imaging

All animal studies were carried out in accordance with the regulations set by the Institutional Animal Care and Use Committee (IACUC) of the University of California, San Diego. Unlabeled mMSCs and SiCNP620-labeled mMSCs were detached, counted, resuspended in PBS, and kept in ice. Subcutaneous injections were performed by mixing the cell solution and cold Matrigel (Corning) at a 1:1 v/v ratio. Then, 100 μL of the mixture was injected subcutaneously into the mouse and immediately scanned with a photoacoustic transducer (LZ250, Visualsonics, Inc.) operating at 25 MHz center frequency. The photoacoustic scans were also performed 3, 7, and 14 days after the injections.

3. Results and discussion

Silicon carbide nanoparticles with three different sizes were synthesized via plasma chemical vapor deposition by US Research Nanomaterials, Inc (US2011, US2022, and US2161). The average size of these nanoparticles was 33±12 nm, 78±16 nm, and 624±94 nm based on their TEM images (**Figure 3.14 a-d**), which were subsequently labeled as SiCNP30, SiCNP80, and SiCNP620. Additionally, SiCNP30 and SiCNP80 are more circular than SiCNP620: the circularity of SiCNP30, SiCNP80, and SiCNP620 were 0.90 ± 0.03, 0.89 ± 0.13, and 0.61 ± 0.09. All three SiCNPs were negatively charged in water, where the pH lies above the isoelectric point of 3C-SiC.[340] The zeta potentials of the nanoparticles from smallest to largest were -19.0, -25.3, and -30.7 mV. According to Chung *et al.*, the differences in zeta potential of these SiCNPs would have insignificant effects on their cell uptake.[268]

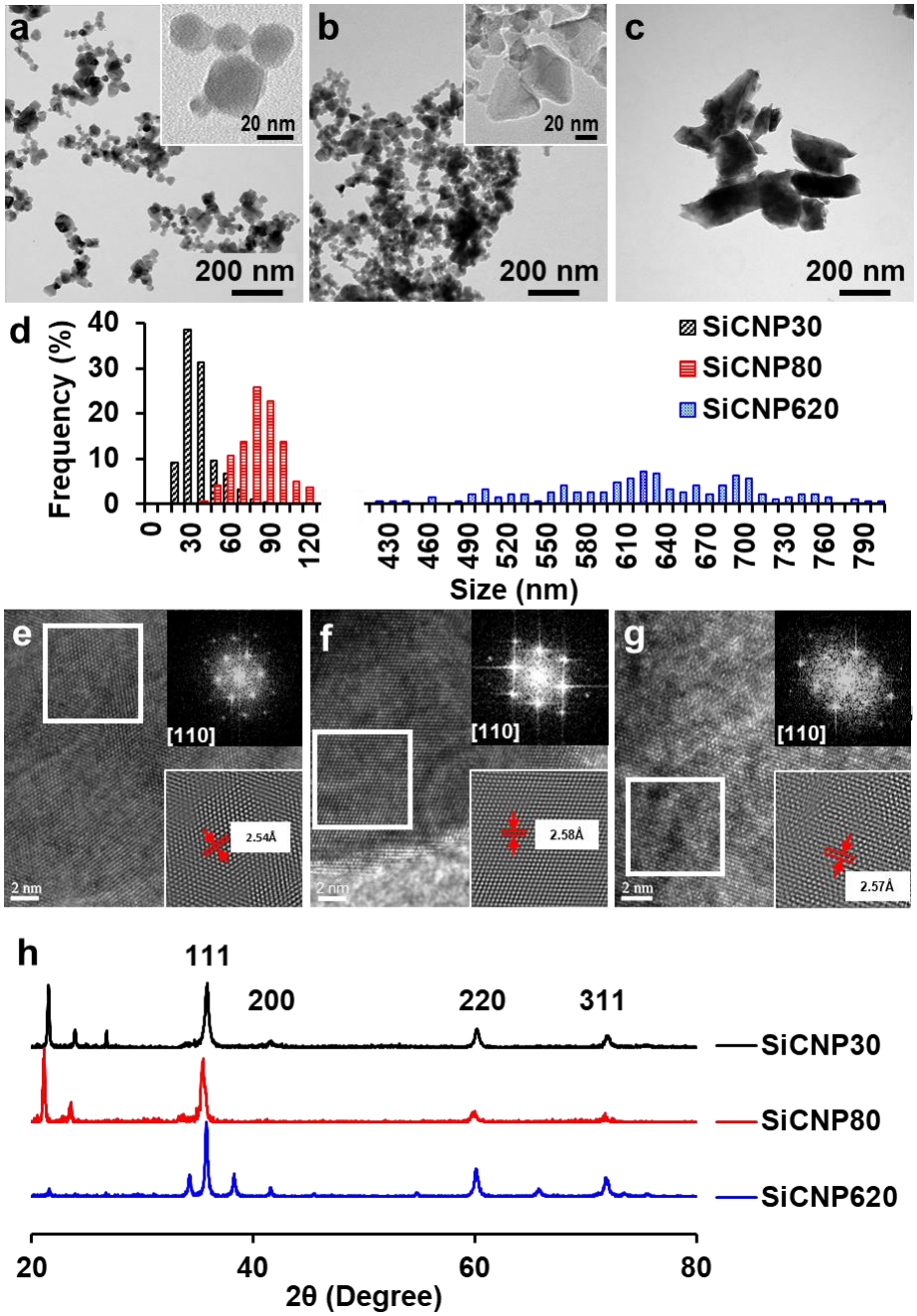

Figure 3.14. TEM images of SiCNPs with average sizes of (a) 30 nm, (b) 80 nm, and (c) 620 nm. The circularity of SiCNP30, SiCNP80, and SiCNP620 were 0.90 ± 0.03, 0.89 ± 0.13, and 0.61 ± 0.09. (d) TEM size distributions of SiCNPs. High resolution TEM images and fast Fourier transformation patterns of (e) SiCNP30, (f) SiCNP80, and (g) SiCNP620 show a typical diffraction pattern of a cubic crystal structure along the [110] zone axis. The measured lattice spacing of the (111) plane for the three types of silicon carbide particles are 2.54Å, 2.58Å and 2.57Å, respectively. (h) X-ray diffraction spectra of all SiCNPs show peaks around 2θ of 35.77°, 41.54°, 60.2°, and 72.04°, which corresponds to the SiC(111), SiC(200), SiC(220), and SiC(311) peaks of cubic 3C-SiC (powder diffraction file card 96-901-8857).

We characterized the crystal structure of these nanoparticles in more detail to confirm that these particles have similar crystalline structure. The fast Fourier transform patterns in the high resolution TEM images are typical diffraction patterns for a cubic crystal structure along the [110] zone axis. The measured lattice spacing of the (111) plane for the three nanoparticles are 2.54Å, 2.58Å and 2.57Å, respectively (**Figure 3.14 e-g**). Those measured spacings are close to the standard values of powder diffraction file card 96-900-8857. X-ray diffraction spectra of all SiCNPs show peaks around 2θ 35.77°, 41.54°, 60.2°, 72.04°, and 75.79°, which corresponds to the SiC(111), SiC(200), SiC(220), SiC(311), and SiC(222) peaks of cubic 3C-SiC (PDF 96-901-8857) (**Figure 3.14h**). 3C-SiC, or β-SiC polytype, is the most thermodynamically stable polytype and has the lowest thermal conductivity.[341] The other peaks match with SiO_2 peaks (powder diffraction file card 96-412-4080, 96-900-0779, 96-901-4487) and are likely due to the glass sample holder.

After confirming the crystal structure of these particles, we investigated the effect of size on light absorption and photoluminescence. SiCNPs (20 μg/mL) showed size-dependent light absorption (**Figure 3.15a**). The absorbance spectra of SiCNP30 and SiCNP80 showed that their absorbance decreased with increasing wavelength, which are similar to the absorbance of 3C-SiC nanocrystals smaller than 10 nm. The sharper decrease in absorbance of SiCNP30 than SiCNP80 may indicate more quantum-confinement events in the smaller SiCNPs.[333] Remarkably, SiCNP620 has a very broad absorbance peak at 560 nm (2.2 eV) corresponding to the bandgap of bulk 3C-SiC. The increased absorbance intensity of SiCNP30 and SiCNP80 in the short wavelength range may be due to the high contribution of Rayleigh scattering for smaller particles. The scattering effect diminishes

with increasing wavelength, explaining the gradual decline in absorbance intensity.

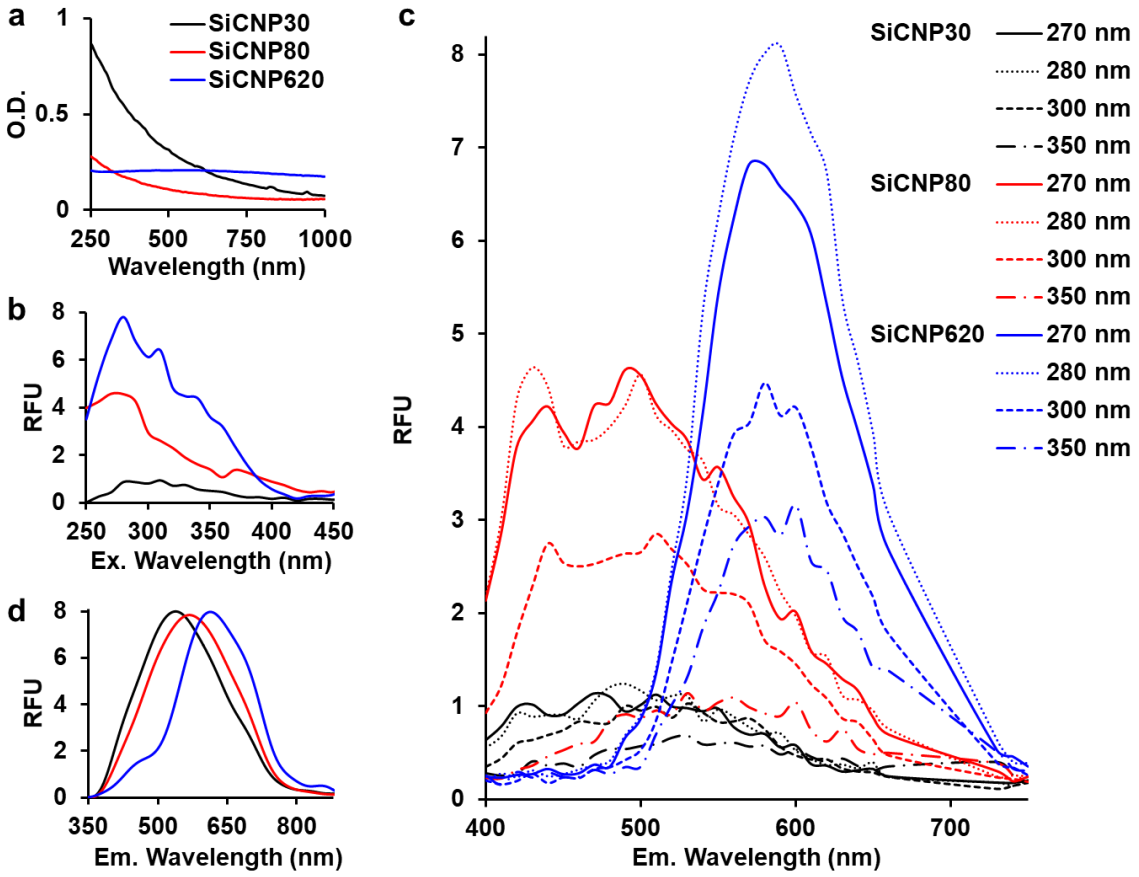

Figure 3.15. Optical properties of all SiCNPs. (a) Absorbance spectra of SiCNP suspensions. (b) Excitation spectra (emission 540 nm) and (c) emission spectra at varying excitation wavelengths of SiCNP suspensions. (d) Emission spectra of dry SiCNPs using a laser excitation source of 325 nm. The intensities were normalized. Black, red, and blue represent SiCNP30, SiCNP80, and SiCNP620, respectively.

The photoluminescence of all SiCNPs were examined at varying excitation and emission conditions. The excitation spectra of 2 mg/mL SiCNPs in water were studied at emission 540 nm with a UV-vis microplate reader (SpectraMax M5, Molecular Devices). The excitation peaks of SiCNP30, SiCNP80, and SiCNP620 were around 280 nm, and the intensity increased with increasing particle size (**Figure 3.15b**). The emission spectra of these SiCNPs suspensions were scanned with excitations at 270, 280, 300, and 350 nm

(**Figure 3.15c**). SiCNP620 showed the highest photoluminescence intensity among all SiCNPs. The photoluminescence of SiCNP620 was approximately 2-fold of SiCNP80 and 8-fold of SiCNP30 when the excitation wavelength was 280 nm. The emission spectra of dry SiCNPs were also studied with a 10-mW laser (325 nm). The emission peaks of SiCNP30, SiCNP80, and SiCNP620 were 538 nm (2.3 eV), 568 nm (2.2 nm), and 614 nm (2.0 eV), respectively (**Figure 3.15d**), indicating a red-shift of photoluminescence as the particle size increases.

The photoluminescence mechanisms of silicon carbide nanoparticles is complicated and remain controversial.[342] The photoluminescence of silicon carbide nanoparticles can be linear and non-linear. The linear photoluminescence may be produced by quantum confinement effect in the small features[343] or the amorphous fractions of silicon carbide nanoparticles and the Si-O bonds on the surfaces. This might be one reason for the stronger photoluminescence of SiCNP620 than SiCNP30 and SiCNP80, because SiCNP620 showed the lowest circularity—0.6 compared to 0.9 of SiCNP 30 and SiCNP80. Second, the non-linear photoluminescence can be second-harmonic generation or two-photon excitation fluorescence (photoluminescence is used in this paper because it more accurately describes the luminescent property than fluorescence due to the delayed emission time.[332]).[336, 337] A larger diameter is favored for the non-linear photoluminescence because the two-photon absorption cross-section is larger.[337] This might be another reason for the strongest photoluminescence of SiCNP620 among the three nanoparticles.

Next, we compared the photoacoustic properties of these silicon carbide nanoparticles. The photoacoustic spectra show that all particles had a broad wavelength signal at a concentration of 1 mg/mL in water (**Figure 3.16a**). The nanoparticles were then

scanned at a fixed wavelength of 725 nm, and SiCNP620 had the highest photoacoustic intensity (**Figure 3.16b**). The photoacoustic intensity of SiCNP30 and SiCNP80 were 23% and 82% of that of SiCNP620, respectively (**Figure 3.16c**). Hence, we conclude that the photoacoustic intensity increased with increasing particle size. This is expected because the absorbance of near-infrared light by SiCNP620 was higher than both SiCNP30 and SiCNP80 (**Figure 3.15a**) and particles with a larger cross-section, provided that the material and light fluence are the same, will have a greater photoacoustic signal.[344, 345] Interestingly, the largest nanoparticle had both the strongest photoluminescence and photoacoustic intensity. Photoluminescence and photoacoustic intensity are typically inversely related due to competing radiative and non-radiative decay pathways when the light absorbance is constant.[346] However, we see here that both photoluminescence and photoacoustic signal increase with increasing size, which was very likely due to the increased light absorption by larger particles (**Figure 3.15a**).

We also studied the relationship between nanoparticle concentration and photoacoustic signal with the SiCNP620 because SiCNP620 showed the highest photoacoustic signals. The photoacoustic intensity of SiCNP620 was linearly dependent on the particle concentration (**Figure 3.16d**). The limit of detection of SiCNP620 was measured to be 10 μg/mL.

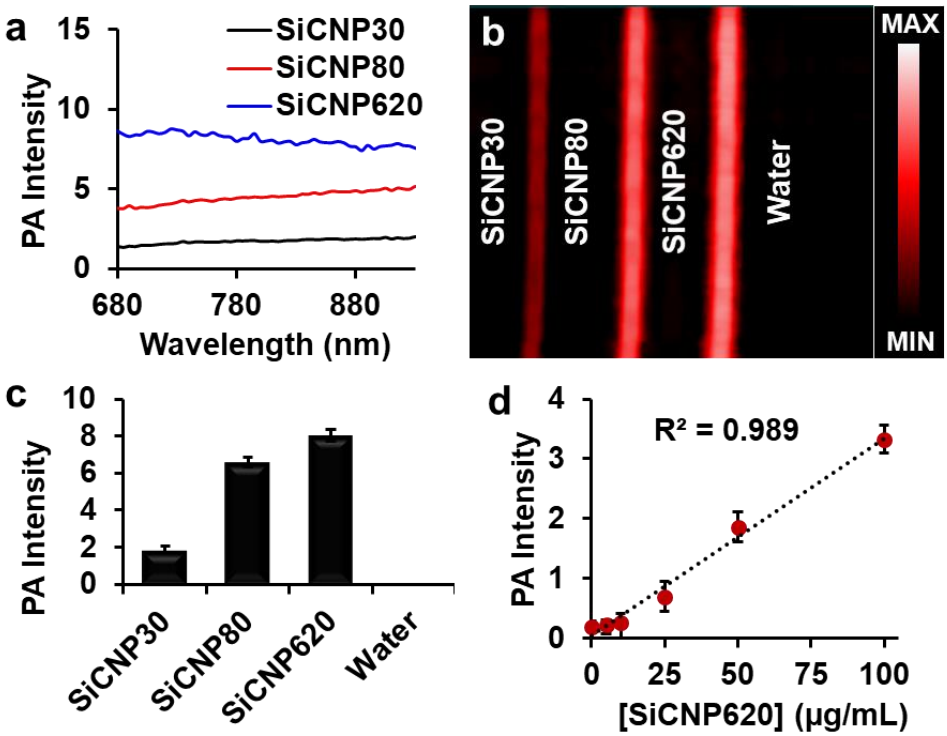

Figure 3.16. Photoacoustic properties of SiCNPs. (a) Photoacoustic spectra, (b) photoacoustic image and (c) corresponding quantification of photoacoustic intensity at 725 nm. (d) Photoacoustic signal of SiCNP620 was linearly dependent on the particle concentration. The limit of detection of SiCNP620 was found to be 10 μg/mL. Error bars are standard deviations of 5 regions of interests.

Given the strongest photoluminescence and photoacoustic signals of SiCNP620 among the three SiCNPs, we used SiCNP620 for stem cell imaging and tracking. We first studied the cytotoxicity of SiCNP620 to mouse mesenchymal stem cells at different concentrations *via* a 3-(4,5-dimethylthiazol-2-yl)-5-(3-carboxymethoxyphenyl)-2-(4-sulfophenyl)-2H-tetrazolium, or MTS, assay (Promega). No significant decrease in cell viability was found when the SiCNP620 concentration was smaller than 400 μg/mL (**Figure 3.17a**). Moreover, the SiCNP620-labeled cells showed a similar growth rate compared to unlabeled cells at labeling concentrations of 50-200 μg/mL (**Figure 3.17b**).

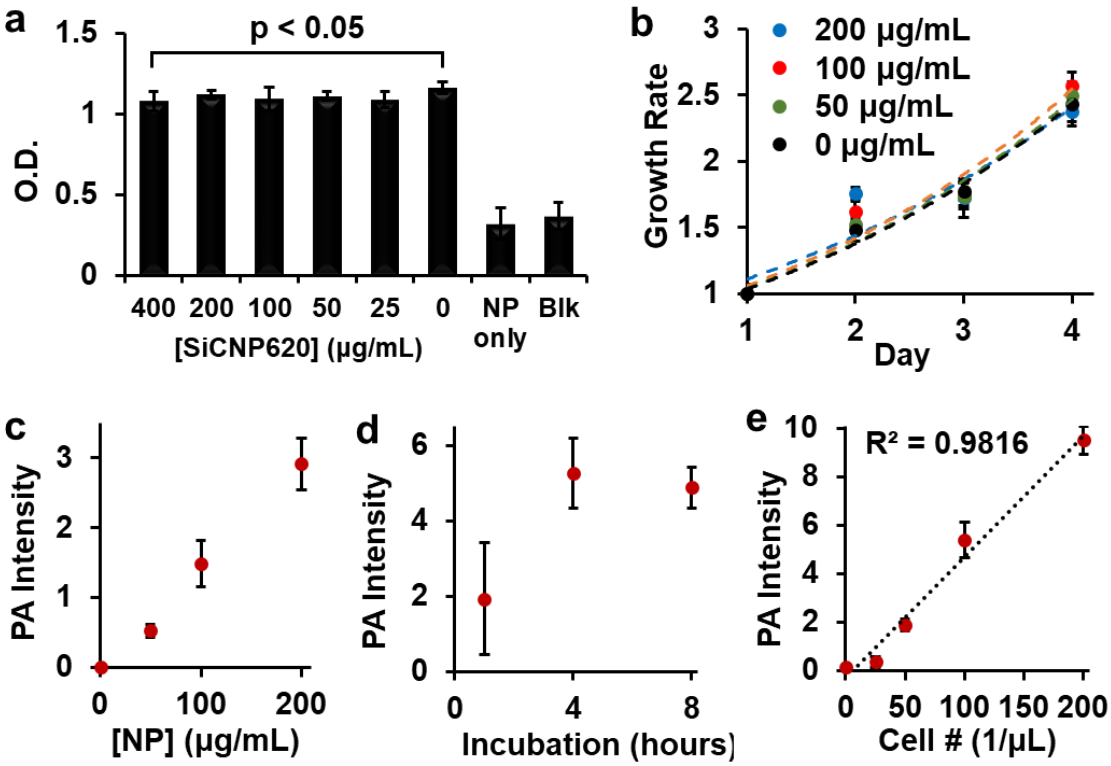

Figure 3.17. Biocompatibility and labeling conditions of SiCNP620 in MSCs. (a) No significant decrease in cell viability was seen for labeling concentrations smaller than 400 μg/mL. (b) Cells labeled with SiCNP620 at different concentrations showed similar growth rates to that of unlabeled cells. Error bars are standard deviations of 8 replicates. (c) A linear relationship is seen between labeling concentration and photoacoustic signal for four hours of labeling. (d) For a labeling concentration of 50 μg/mL, a labeling time of four hours was optimal. (e) Photoacoustic intensity was linearly dependent on the concentration of SiCNP620-labeled cells (50 μg/mL, 4 hours incubation), and the limit of detection was 37 cells/μL. Error bars are standard deviations of 5 measurements.

Then, we studied the labeling ability of SiCNP620 to mouse mesenchymal stem cells. The overall labeling capacity which is the average number of nanoparticles entered a cell was evaluated with photoacoustic imaging. The labeling concentration and incubation time affected the labeling capacity. The photoacoustic signal increases with increasing labeling concentration (**Figure 3.17c**), and a labeling time of 4 hours was found to be optimal (**Figure 3.17d**). Cell labeling capacity was also quantified with thermogravimetric analysis. At labeling concentrations of 50 μg/mL and 200 μg/mL, the

cell labeling capacity were 1.87 and 6.88 ng SiCNP/cell, occupying 0.25% and 0.93% of the cell volume, which was higher than reported for silica nanoparticles.[171] For all future experiments, stem cells were labeled with a particle concentration of 50 μg/mL unless otherwise specified. There was a linear relationship between photoacoustic intensity and the number of SiCNP620-labeled cells (50 μg/mL) (**Figure 3.17e**), and the limit of detection of these labeled cells was approximately 37 cells/μL.

The SiCNP620-labeled mesenchymal stem cells were visible under a fluorescence microscope using a Texas Red filter cube (the excitation is 585 nm and the emission is 624 nm). Unlabeled cells showed no photoluminescence signal (**Figure 3.18**). The photoluminescence of SiCNP620 was stable and the labeled stem cells showed strong photoluminescence signals even 11 days after labeling, suggesting the ability of SiCNP620 for long-term imaging and tracking of stem cells. Unlabeled and SiCNP620-labeled mesenchymal stem cells were treated with adipogenic and osteogenic induction media. The SiCNP620-labeling did not affect stem cell differentiation. Moreover, SiCNP620 could track mesenchymal stem cell-derived adipocytes and osteocytes (**Figure 3.18**). Interestingly, for the adipogenic induced cells, the SiCNP620 could enter and therefore track the lipid vesicles as well.

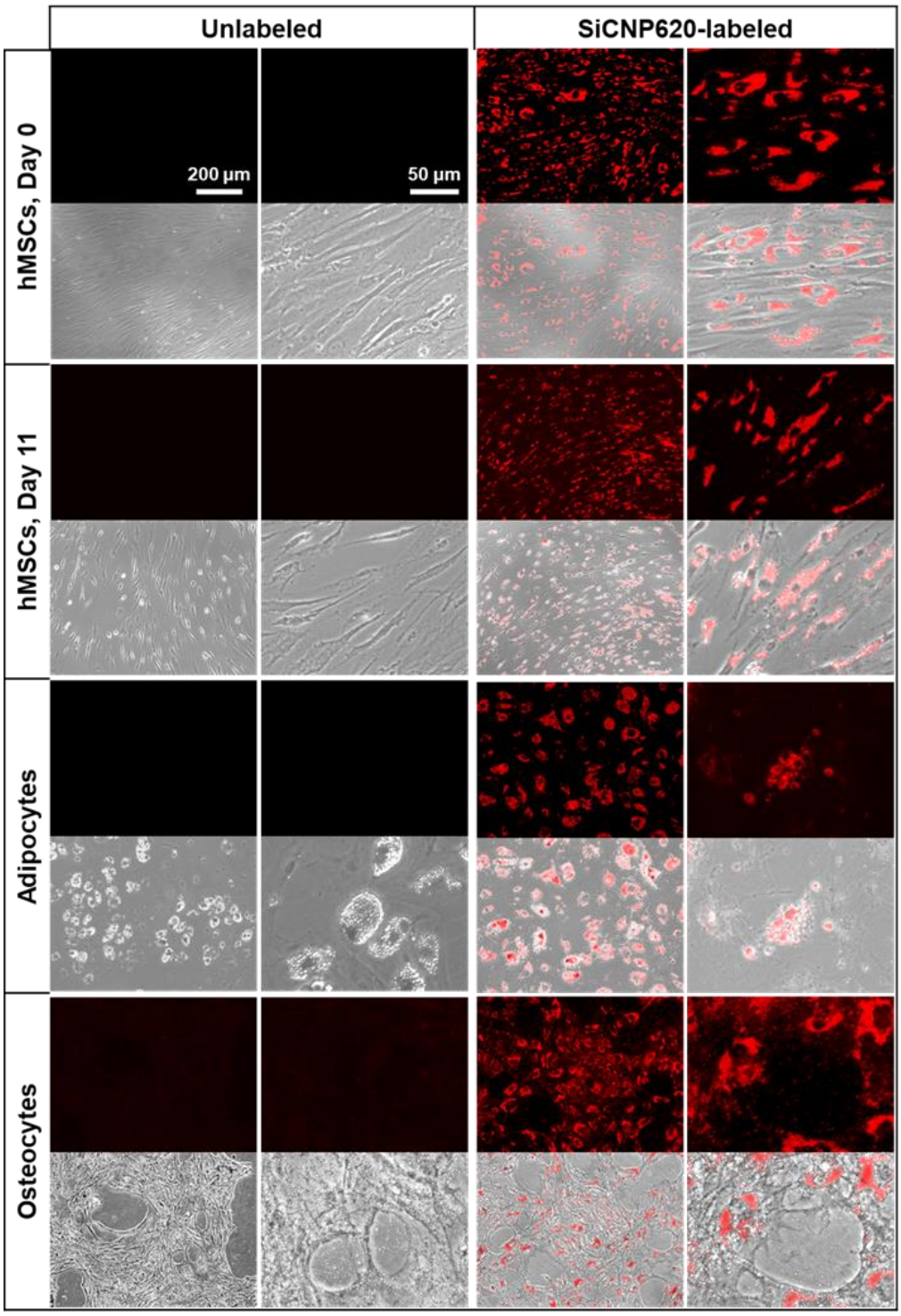

Figure 3.18. Fluorescence image (top) and its overlay with bright field image (bottom) of unlabeled and SiCNP620-labeled cells. SiCNP620-labeled mesenchymal stem cells are still visible under fluorescence microscope 11 days after labeling, indicating the long-term cell imaging ability of SiCNP620. In addition, adipocytes and osteocytes differentiated from SiCNP620-labeled mesenchymal stem cells still show photoluminescence three weeks after labeling.

To demonstrate the potential of these particles for *in vivo* cell tracking, we subcutaneously injected SiCNP620-labeled mouse mesenchymal stem cells into a nude mouse and scanned the cells with photoacoustic imaging. **Figure 3.19a** shows the photoacoustic spectra of injected cells. The photoacoustic intensity from 680 to 730 nm was decreased compared to the photoacoustic spectra of SiCNP620 only (**Figure 3.16a**), which may be due to the reduced tissue penetration of shorter wavelengths compared to the longer wavelengths. As a result, all cell implants were scanned in 3-dimensions at 770 nm. The photoacoustic intensity increased as the labeled cell concentration increased and then saturated when the cell concentration reached 20,000 cells/μL (**Figure 3.19b-c**). The *in vivo* limit of detection of SiCNP620-labeled cells was 7,800 cells/μL. Unlabeled cells showed no photoacoustic signal even at a high cell concentration. Continuous monitoring of the cell implants showed that we could still track SiCNP620-labeled cells for 14 days after injection via photoacoustic imaging (**Figure 3.19d**).

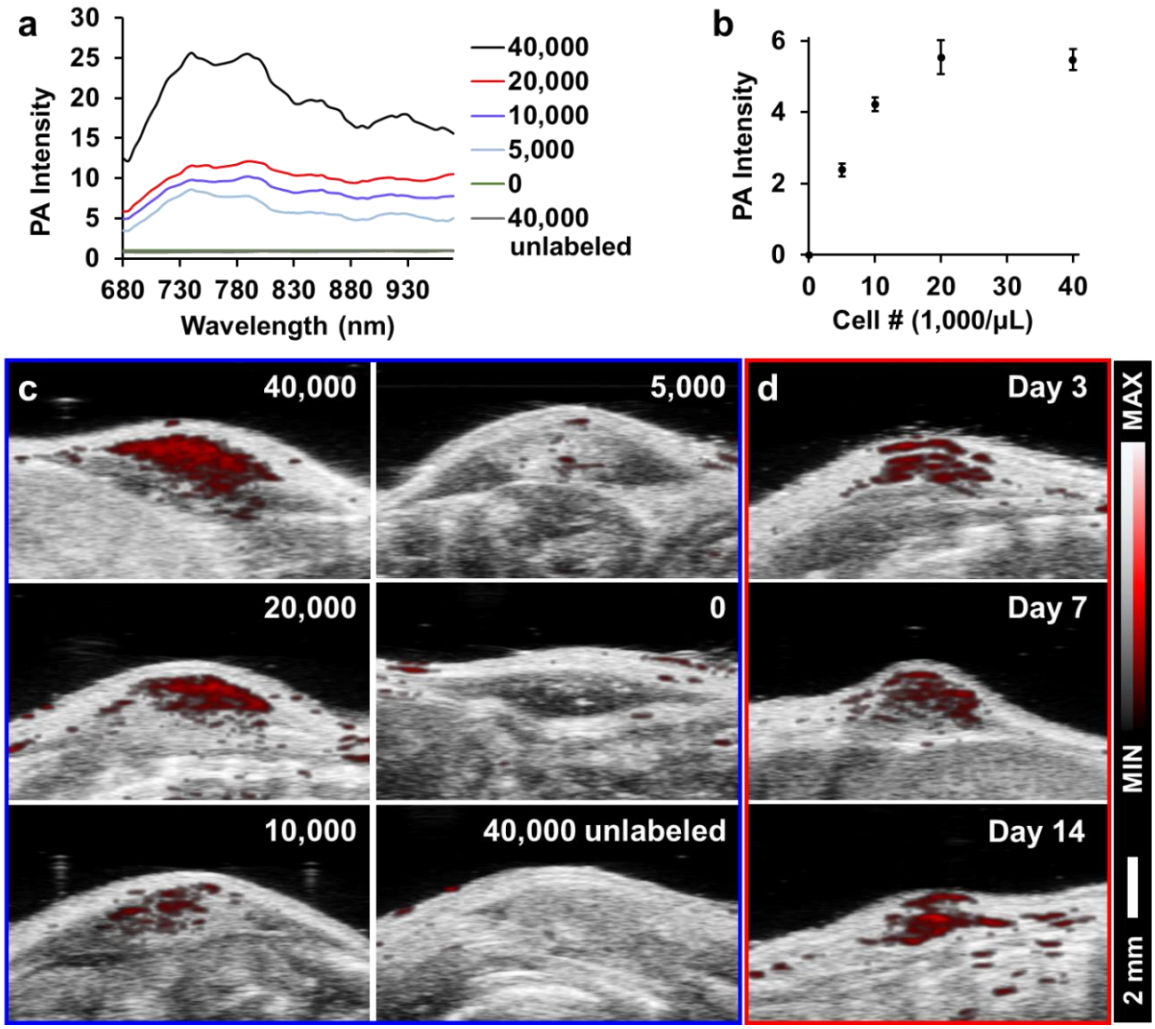

Figure 3.19. Tracking SiCNP620-labeled mesenchymal stem cells *in vivo*. (a) Photoacoustic spectrum of labeled MSCs implanted at varying cell concentrations. Labels represent injection concentrations in cells/μL. (b) Quantified photoacoustic intensity of injected SiCNP620-labeled cells at a wavelength of 770 nm. Error bars are standard deviations of 5 ROIs. (c) Photoacoustic and ultrasound overlay images of the injections. (d) Long-term tracking of the 20,000 cells/μL implant shows that cells are still visible over a period of 14 days.

4. Conclusion

Long-term cell tracking is important to understand cell fate post-injection and provides insight for subsequent treatment. In this paper, we report for the first time that SiCNPs have intrinsic photoluminescent and photoacoustic signals, which enable SiCNPs

to image cells *in vitro* and track cells *in vivo*. The SiCNPs were capable of long-term tracking of stem cells even after differentiation due to stable and strong luminescence. These nanoparticles showed excellent biocompatibility and labeling capacity for mesenchymal stem cells. Thus, SiCNPs are promising for long-term stem cell imaging and tracking.

Future work involves understanding the mechanisms of photoacoustic excitation and optimizing the photoacoustic intensity of SiCNPs by surface modification. Coating with additional silica or etching could potentially change the photoacoustic intensity by reducing the thermal interfacial resistance between the nanoparticle and surrounding medium.[165] Ongoing work will be quantifying cells and monitoring the cell fate *in vivo* with photoacoustic imaging. The ability of these nanoparticles to track differentiated stem cells and other cells will also be performed in our next steps.

5. Acknowledgement

The text of Chapter 3, in part, is the reprint of the material as it appears in "Cellular toxicity of silicon carbide nanomaterials as a function of morphology" by Fang Chen, Gongyi Li, Eric R. Zhao, Jingting Li, Ghanim Hableel, Jeanne E. Lemaster, Yuting Bai, George L. Sen, Jesse V. Jokerst, Biomaterials, 2018, and "Silicon carbide nanoparticles as photoacoustic and photoluminescent dual-imaging contrast agent for long-term cell tracking" by Fang Chen, Eric R. Zhao, Tao Hu, Yuesong Shi, Donald J. Sirbuly, Jesse V. Jokerst, to be published, 2019. The dissertation author was the primary researcher of both papers.

Chapter 4.

Adsorption and desorption behaviour of organosilica nanoparticles with an intrinsic secondary amine: an efficient and reusable carrier for drugs

1. Introduction

Mesoporous silica nanoparticles are made from surfactant templates and offer high surface areas[139, 347]. They can be routinely made on the gram scale and are commercially available. Mesoporous silica nanoparticles have great potential in drug delivery vehicles[114, 264, 279], transfection vectors[348], and imaging agents[36, 102, 349]. They also have promising utility in adsorption due to their high surface area and facile/tunable adsorption-desorption characteristics via surface coating. Indeed, mesoporous silica nanoparticles have been modified with amine groups to adsorb anionic molecules[350-353] or carboxylate groups to adsorb cationic molecules[354, 355].

However, these surface modification approaches do not take full advantages of the high surface area of mesoporous silica nanoparticles because the surface functionalization does not cover the entire nanoparticle surface[356]. Moreover, these functionalized amine groups are unstable[357, 358]. These two limitations can be overcome by integrating amine groups directly into the nanoparticle frame[32], and amines are an efficient binding site for anionic drugs[359]. In this paper, we designed and fabricated organosilica nanoparticles (OSNP) with intrinsic secondary amine groups and then tested their adsorption mechanism and capabilities using phenol red, methylene blue, rose Bengal, and rhodamine B as model drugs.

The adsorption studies demonstrated that the neutral OSNP could adsorb either anionic or cationic molecules by tuning the surface charge of the material via pH. At neutral pH, the OSNP bound negatively charged molecules selectively from a mixture of positively and negatively charged molecules. Moreover, the OSNPs have a relatively high adsorption capacity within several minutes and could be reused at least 10 times without any decrease

in adsorption capacity. We applied the Langmuir and Freundlich isotherm models and calculated the pseudo-first-order and pseudo-second-order adsorption kinetic constants.

2. Methods

2.1. Chemicals

Hexadecyltrimethylammonium bromide (CTAB, ≥99%), ammonium hydroxide (NH_4OH), bis(triethoxysilyl) ethane (BTSE), bis(3-trimethoxysilyl-propyl)amine (TSPA, 90%), dimethylhexadecylamine (DMHA), rhodamine B, sodium chloride, decane, and hydrochloric acid were purchased from Sigma Aldrich Inc. Phenol red was from Acros Organics. Methylene blue and rose bengal disodium were purchased from the Fisher Scientific. Ethanol was purchased from VWR. Methanol was provided by Alfa Aesar. Millipore water with a resistivity larger than 18.2 MΩ·cm was used unless specified otherwise.

2.2. Organosilica nanoparticles synthesis

The OSNP synthesis used organosilicate precursors. First, we mixed 0.4 mmol CTAB, 0.085 ml 26% ammonia solution, 0.6 mmol decane, and 0.4 mmol DMHA in 150 ml water. The mixture was sonicated in a water bath at 50^{o}C for 3 hours, emulsified with an ultrasound probe for 30 minutes, and then stirred at 50^{o}C for 30 minutes. In a separate tube, the TSPA and BTSE were mixed in ethanol and then sonicated in a water bath for 30 minutes. The OSNP properties were tuned by adjusting the ratio of TSPA to BTSE. The TSPA percentages were 0, 20, 40, 60, 80, and 100% with a 0.40 mL total volume of TSPA and BTSE. The silica mixture was then slowly added to the emulsified solution of CTAB. The final mixture was stirred for an additional 2 hours at 50^{o}C followed by standing

overnight at 50^{o}C. The mixture was then centrifuged, washed with 1% NaCl in methanol thrice, washed with ethanol thrice, and resuspended in water.

2.3. Characterization

The OSNP were imaged with a JEOL JEM-1200 EXII transmission electron microscope (TEM) operating at 120 kV. A JEM-2100F operating at 210 kV was also used for some samples. The hydrodynamic radius and zeta potential were measured with a Zetasizer from Malvern via dynamic light scattering (DLS). The N_2 adsorption-desorption isotherms at 77 K were measured on a Micrometitics ASAP 2020 system. FT-IR spectrum was performed on a Spectrum Two™ spectrometer from PerkinElmer. The nitrogen in the OSNP was analyzed using a Perkin Elmer CHN analyzer. Solid-state ^{29}Si NMR spectra were recorded using a Bruker AMX-600 spectrometer. X-ray photoelectron spectroscopy (XPS) analysis was performed using a Kratos Axis Ultra DLD instrument with monochromatic Al (Ka) radiation. The data were analyzed using Casa-XPS software, and two different components were fit to the N 1s signals. The energy difference between these components was fixed at 1.8 eV[360]. An inductively coupled plasma optical emission spectrometer (ICP-OES, Optima 3000DV, Perkin Elmer) was used to quantify the loss of OSNP during desorption. The pH was measured with a Milwaukee MW 102 pH/Temp Meter. All absorbance measurements used a SpectraMax M5 spectrophotometer from Molecular Devices.

2.4. Adsorption studies

Adsorption was done at pH 7 with 80% TSPA nanoparticles at room temperature unless otherwise specified. First, 5 mg of OSNP with different compositions, zeta potential, and surface areas were added separately to 1 mL of 0.5 mg/ml (1.33 mM) phenol red. Upon

mixing, the tubes were vortexed, reacted overnight, and then the supernatants were collected after centrifugation.

To study the influence of pH on the adsorption capacity 100 µL samples at various pH 1 to 13 were added to 100 µL of 0.5 mg/ml (1.33 mM) phenol red with vortex. These solutions were then added to 100 µL of Millipore water containing 2 mg of OSNP. This was allowed to stand for 10 minutes before supernatant collection.

Ionic strength was tuned with NaCl. NaCl solutions of different ionic strength were created and then mixed with 4 mg/ml (10.63 mM) phenol red at a ratio of 2:1. The mixtures were then added separately to 40 mg/ml OSNP solutions at a ratio of 3:1. The final mixtures were vortexed, allowed to stand for 30 minutes, and then the supernatant was collected.

To study the effect of dye concentration, phenol red at 0 to 5 mg/ml (13.29 mM) were prepared, and then 2 mg of OSNP were added to 200 µL of each solution. The mixtures were vortexed, reacted for 30 minutes, and then the supernatant was collected for absorbance spectroscopy.

We then studied the effect of adsorbent dosage. The 30 µL of OSNP aqueous solutions from 0 to 80 mg/ml were mixed with 240 µL of 0.1 mg/ml (0.27 mM) phenol red and 90 µL of 0.01 M HCl solution. These mixtures were vortexed and reacted for 30 minutes before supernatant collection for absorbance spectroscopy.

To test the reusability of OSNP on phenol red adsorption, 0.5 mg/ml (1.33 mM) phenol red was mixed with a pH 2 solution of OSNPs at a volume ratio 1:1. The OSNP were added to these phenol red solutions for 5 minutes. The supernatant was then collected via centrifugation. The particles were rinsed with water once to remove free dye and then treated with 300 µL of 0.0167 M NaOH for 5 minutes to detach the phenol red from the

OSNP. We collected the supernatant and then washed the pellets with water. These procedures were repeated 10 times.

For the selective adsorption of anionic dye, phenol red (0.04 mM or 0.4 mM) and methylene blue (0.04 mM or 0.4 mM) were mixed at three molar ratios: 10:1, 1:1, and 1:10. Then OSNP (80% TSPA) were added and allowed to adsorb dyes for 5 minutes before collection of supernatants.

To understand the adsorption mechanisms, we compared the OSNP absorption of phenol red, rose bengal, methylene blue, and rhodamine B. The 1.4 mg of OSNP made of 80% TSPA were added to 0.1 ml pH 7 or pH 13 solutions. Then, 0.1 ml 0.2 mM of phenol red, rose Bengal, rhodamine B, and methylene blue were added to both solutions separately. The mixtures were vortexed, reacted for 5 minutes, and centrifuged.

Finally, we studied the adsorption kinetics and isotherms. The OSNP were added to phenol red solution at a ratio of 0.5 mg OSNP: 0.1 ml dye. The dye concentration varied from 0.015 mg/ml (0.04 mM) to 2 mg/ml (5.31 mM). The mixture was vortexed, allowed to react for 5, 10, 20, 40, 60 minutes or 2.5, 5, 10, 24, and 73 hours. The supernatant was then collected by centrifugation. For the isotherm study, OSNP aqueous solutions at different concentrations were made; 100 µL of each solution was then mixed with 100 µL of 5 mg/ml (13.29 mM) phenol red. These mixtures were vortexed and allowed to react for 30 minutes before supernatant collection.

2.5. Adsorption data analysis

The absorbance spectra of phenol red vary with pH. Under basic conditions, there is a peak at 557 nm, while at pH < 7.5 the absorbance shifts to ~425 nm. For consistency, we used the 557 nm peak and diluted the standards and the samples with 0.1 M NaOH prior

to spectral analysis. The absorbance spectra were then read, and the absorbance at 557 nm was used to quantify the phenol red concentration. The adsorption capacity was calculated as the milligram or millimole of dye immobilized on the nanoparticles per gram of nanoparticles. A standard curve of phenol red was made for each day. The means, standard deviations, and standard errors were calculated with Microsoft Excel.

3. Results and discussion

We prepared an inherently cationic mesoporous silica nanoparticle, which shows relatively high and fast adsorption to phenol red. First, we characterized the material's physical properties and binding capabilities. We then performed several control experiments to understand the mechanism of binding. Finally, we quantified the binding via kinetic and isotherm studies.

3.1. Nanoparticle synthesis and characterization

Six organosilica samples were made with different volume fractions of TSPA, i.e., the percentage of TSPA relative to BTSE and TSPA. This fraction was changed from 0% to 100%. The product made with 100% TSPA was macroscopic and is not a nanoparticle (**Figure 4.1**). The other samples were less than 150 nm. The 0, 20, 40, 60, and 80% OSNP were 128 nm, 101 nm, 136 nm, 106 nm, and 59 nm, respectively (**Figure 4.1**). This size change may be due to the amine in the TSPA (inset, **Figure 4.2**)—these groups can catalyze the reaction between silanes to form siloxane bonds and accelerate the hydrolysis/polymerization[361]. This fast hydrolysis and polymerization prevents the diffusion of precursors and makes it difficult to generate large particles[99]. Typical yields were 47%, 36%, 37%, 74%, 93%, and 101% for the 0, 20, 40, 60, 80, and 100% TSPA batches. The higher yield at higher TSPA concentrations might be because of the catalytic

property of TSPA for the hydrolysis/polymerization[361].

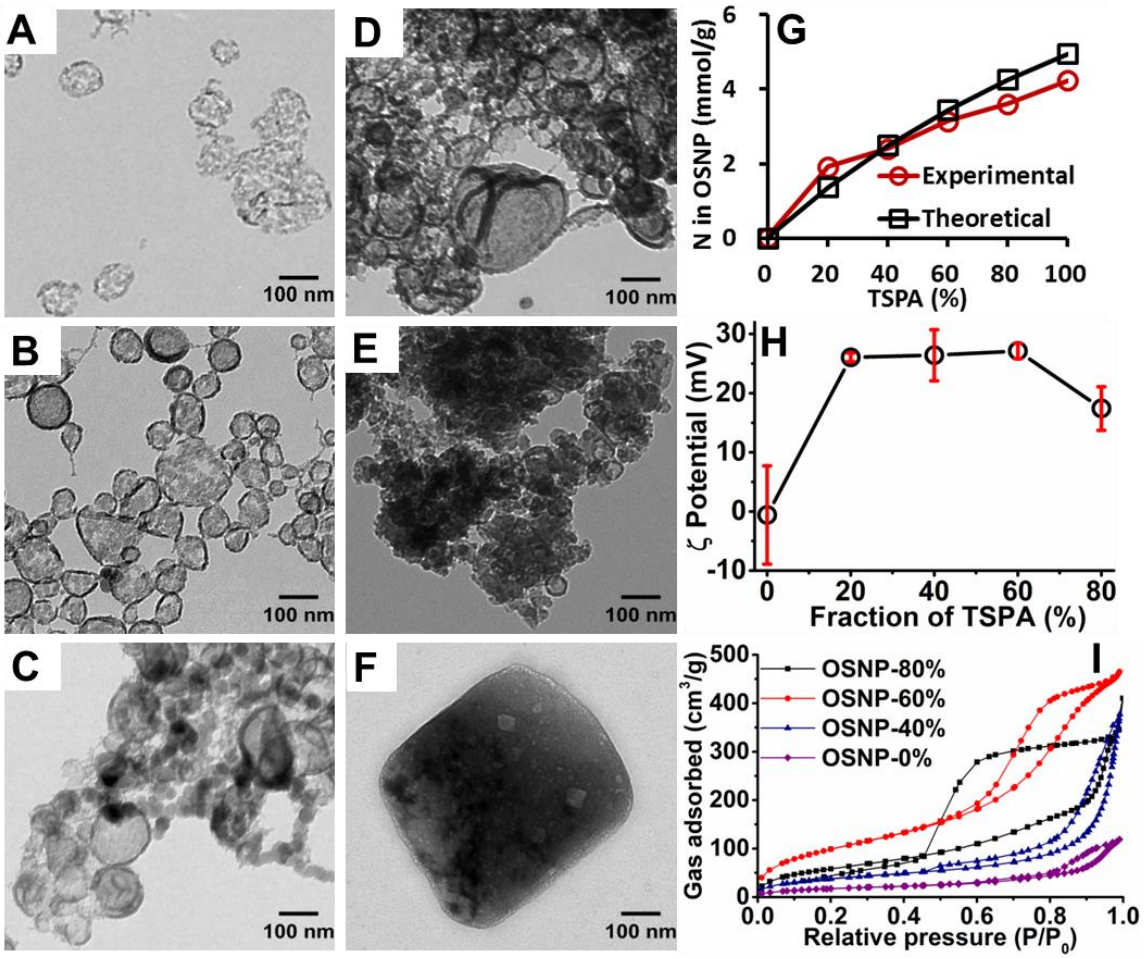

Figure 4.1. Characterization of the organosilica products. The organosilica products were prepared with TSPA and BTSE at different ratios. Panels (A-F) are TEM images of OSNP with different initial quantities of TSPA (0, 0.08, 0.16, 0.24, 0.42, and 0.4 mmol, respectively, corresponding to 0%, 20%, 40%, 60%, 80%, and 100% (v/v) of TSPA over total silica sources). (G) The amount of nitrogen in the OSNP increases as the TSPA fraction increases. (H) Zeta-potential of OSNP made with different fraction of TSPA shows a more positive surface charge as more TSPA is incorporated into the nanoparticle. Error bars in panel H represent the standard deviations of 6 measurements. (I) N_2 adsorption-desorption isotherms of OSNP made with different fractions of TSPA indicate the mesoporous structure of OSNP. Reprinted with permission from ACS[3].

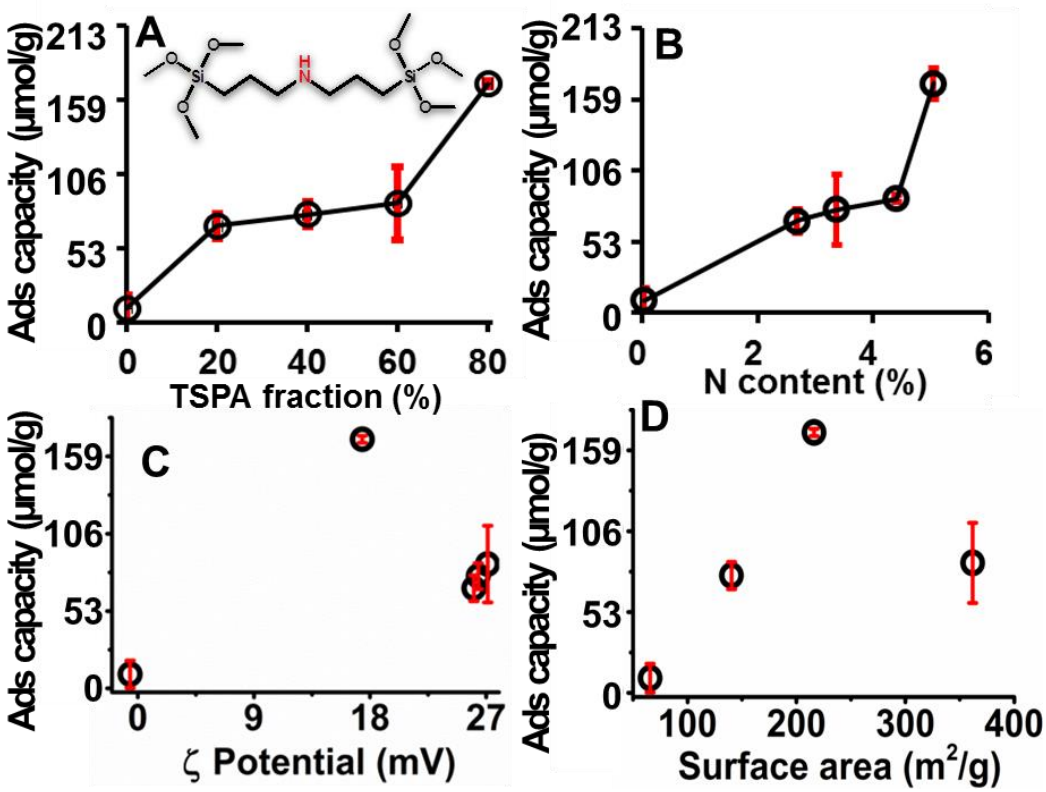

Figure 4.2. Phenol red adsorption capacity of OSNPs. Capacity changes with (A) TSPA, (B) nitrogen content, (C) zeta potential, and (D) BET surface area. Of the four parameters, the adsorption capacity is only positively dependent on the TSPA and nitrogen content. Error bars represent the standard error for more than 3 measurements (RT, t=16 hr, 5 mg OSNP, 0.5 mg/ml or 1.33 mM phenol red). Samples with more positive zeta-potential sequestered more phenol red, but no further increase in adsorption capacity when the zeta potential was over 20 mV. The adsorption capacity increased up to a surface area of 220 m^2/g and then decreased with increasing surface area. Reprinted with permission from ACS[3].

The condensation of OSNP made with 80% TSPA was examined with solid state NMR. The OSNP is composed of 54.4% T^3 and 27.1% T^2 species[362] (**Figure 4.3**). Washing with a NaCl/methanol solution effectively removed the templates as confirmed by FT-IR spectroscopy: the absorbance peaks at 2925, 2857, and 1462 cm^{-1} disappeared after washing (**Figure 4.4**), which correspond to the asymmetric, symmetric stretching, and bending vibrations of the C-H bonds in decane and CTAB[363].

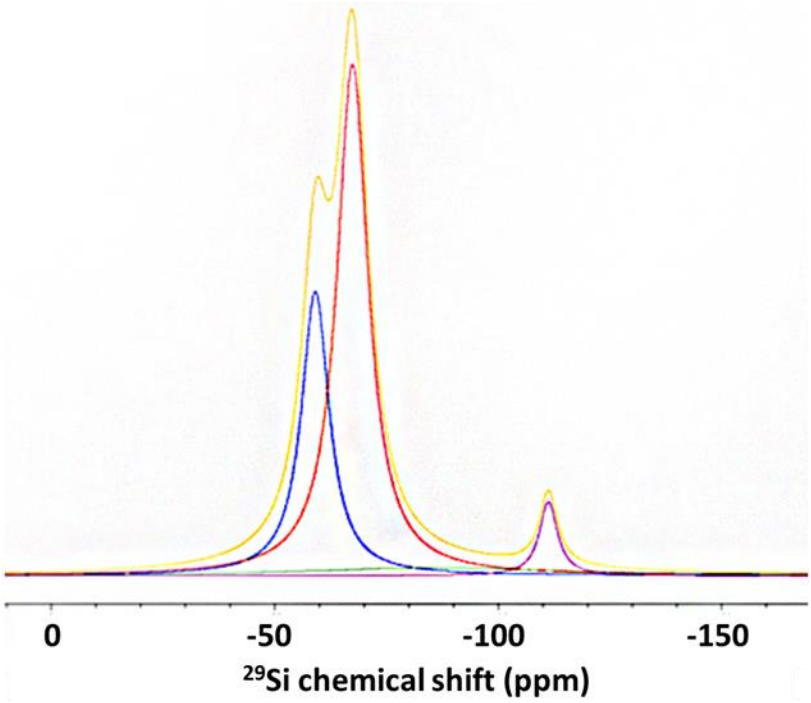

Figure 4.3. Solid state NMR of the OSNP made of 80% TSPA (yellow). The nanoparticle contains 27.1%, 54.4%, and 18.3% of T^2 (-59 ppm, blue), T^3 (-68 ppm, red), and Q^4 (-112 ppm, purple) species. Reprinted with permission from ACS[3].

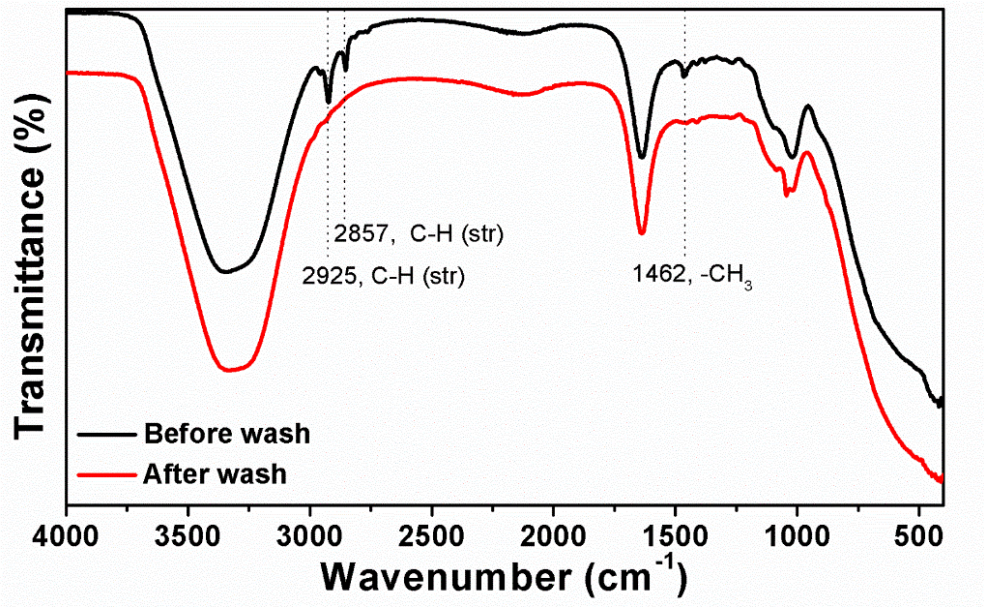

Figure 4.4. Template removal efficiency by NaCl/methanol solution. The FT-IR absorbance peak at 2925, 2857, and 1462 cm^{-1} disappeared after washing with NaCl/methanol solution.The 2925, 2857, and 1462 cm^{-1} peaks correspond to the asymmetric, symmetric stretching, and bending vibrations of the C-H bond. Reprinted with permission from ACS[3].

The nanoparticle composition affects the amine content, zeta potential, and surface area of the products. The nitrogen content in the organosilica made of 100%, 80%, 60%, 40%, 20%, and 0% TSPA were 4.23, 3.60, 3.14, 2.40, 1.92, and 0.03 mmol/g. The result showed the amount of nitrogen was positively dependent on the TSPA added (**Figure 4.1**). The zeta became more positive with increasing TSPA and plateaued between 20% and 60%—higher TSPA concentrations (80%) had slightly lower zeta value (**Figure 4.1**). On the other hand, the surface area and pore volume increase as the TSPA fraction increases from 0% to 60% and then decrease at 80% TSPA (**Figure 4.1**). The BET surface areas of 0%, 40%, 60%, and 80% TSPA OSNPs were 66, 140, 362, and 216 m^2/g. Their BJH pore volumes were 0.18, 0.58, 0.74, and 0.64 cm^3/g. All samples have a type IV isotherm with a hysteresis loop at $P/P_o > 0.5$ indicating a mesoporous structure.

3.2. Optimization and evaluation of phenol red adsorption capacity

The adsorption capacity is dependent on the TSPA fraction and the amine content. As show in **Figure 4.1**, the OSNP composition changes the amine content, zeta potential, and surface area. However, the adsorption capacity only increased as the TSPA and nitrogen (amine) content increased (**Figure 4.2**). The TSPA-containing nanoparticles removed 7- to 18-fold more dye than TSPA-free control nanoparticles. The most efficient removal occurred at 80% TSPA fraction. However, there was no such trend between adsorption capacity and zeta potential or surface area (**Figure 4.2**). More positive OSNP (over +20 mV) sequestered more phenol red from the solution, but further increase in zeta potential did not increase dye sequestration. The adsorption capacity increased with surface area and reached a maximum near 220 m^2/g; it then decreased with increasing surface area.

Next, we studied the effect of pH, ionic strength, dye concentration, and adsorbent

dosage on the adsorption capacity (**Figure 4.5**). Wastewater can have a variety of pH values. For example, the pH of tannery waste water varies between 2.0 and 12.8 during different operations[364]. Thus, it is important for a remediation tool to work under a broad range of pH values. The pH is particularly important because it affects the surface charge of the adsorbents (**Figure 4.5**) and dye ionization (**Figure 4.5**). The adsorption capacity of OSNP toward phenol red was stable from pH 2 to 11 (**Figure 4.5**) but changed dramatically at pH 1.2, 11.6, and 12.5.

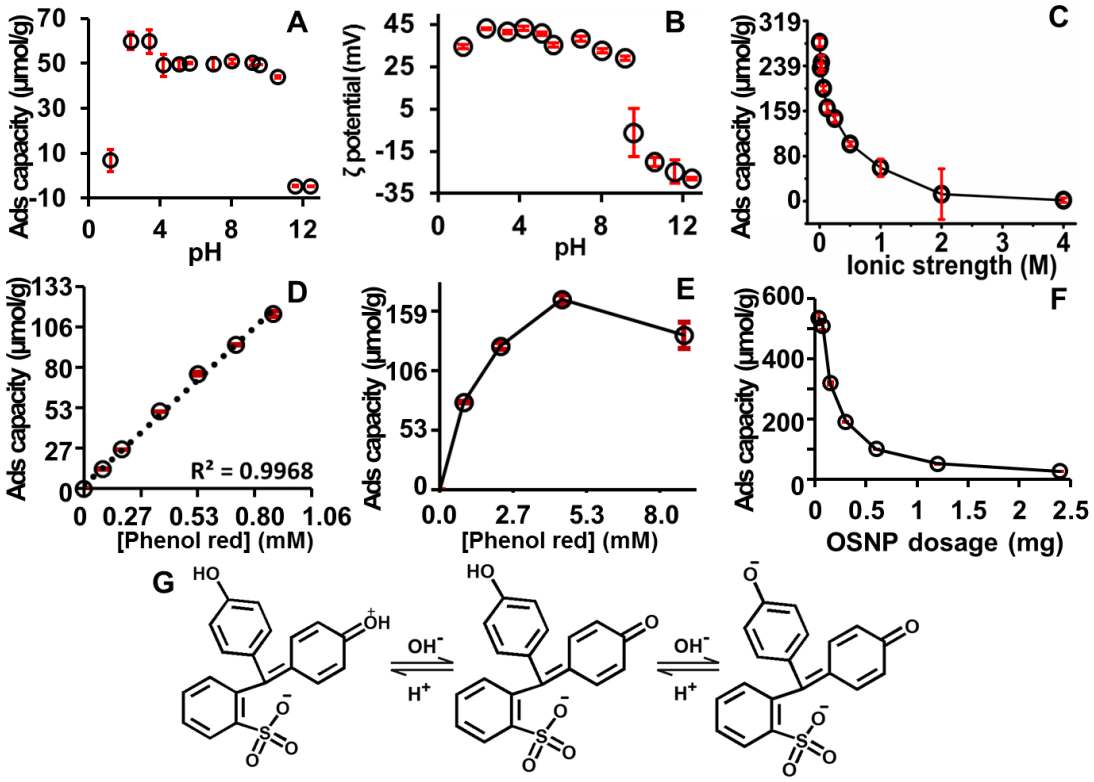

Figure 4.5. Effect of pH, ionic strength, dye concentration, and adsorbent dosage on phenol red adsorption capacity of OSNP. (A) The absorption capacity was reduced at extreme basic (pH > 11) or acidic (<2) conditions. (B) OSNP is positive at pH 8.1, and it becomes negative at pH 9.6. (C) Adsorption capacity decreased as the ionic strength increased to 1 M and then decreased slowly as the ionic strength further increased. (D) The adsorption capacity was linearly dependent on the dye concentration when it is low. Panel (E) shows that the absorption capacity increased as the dye concentration increased and reached a peak at 1.67 mg/ml (4.4 mM), which then decreased as the concentration further increased to 3.3 mg/ml (8.8 mM). (F) The adsorption capacity decreased as the dosage of adsorbent increased. Error bars represent the standard deviation. (G) The structure of phenol red changes as the pH changes. The first acid dissociation constant is 1.2 and the second dissociation constant is 7.7. Reprinted with permission from ACS[3].

The poor adsorption capacity at pH 1.2 is likely due to a structural change in phenol red (**Figure 4.5**). At low pH (< 1.2), the phenol red is zwitterionic[365] and it is difficult for the phenol red to be adsorbed by the OSNP through electronic attraction forces. In addition, more than 70% of the amines on the OSNP are protonated at pH 1 as shown by XPS compared to only ~24% at pH 2 (**Figure 4.6**); hence, hydrogen bonding is difficult at pH 1. On the other hand, OSNP at pH 12 or 13 cannot adsorb any phenol red due to the electrostatic repulsion forces between the negative OSNP and the deprotonated negative phenol red (**Figure 4.5**).

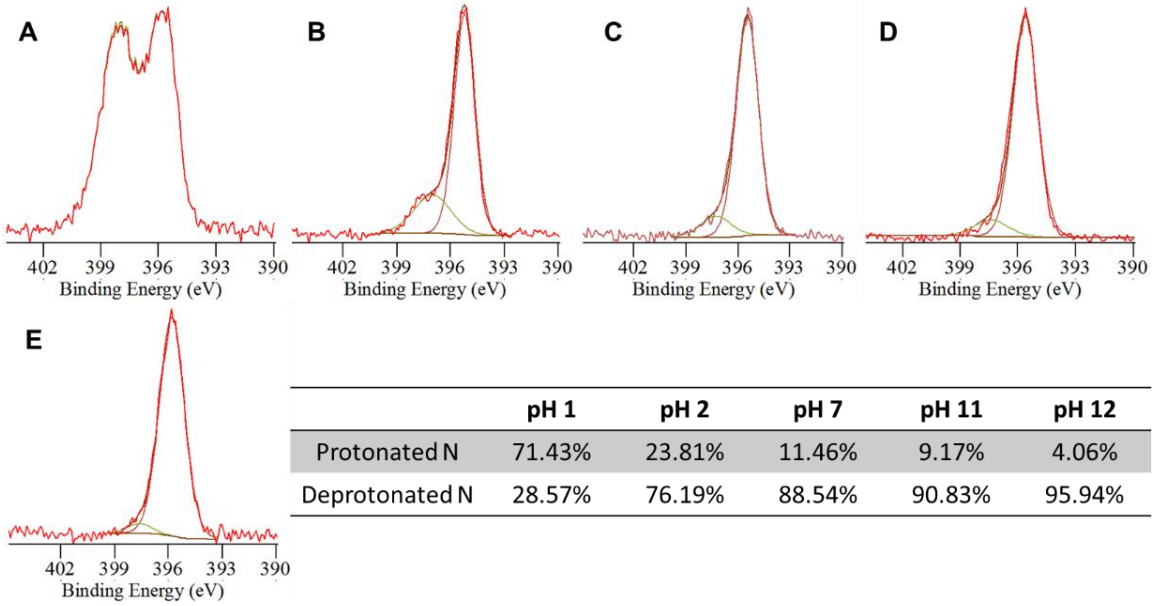

	pH 1	pH 2	pH 7	pH 11	pH 12
Protonated N	71.43%	23.81%	11.46%	9.17%	4.06%
Deprotonated N	28.57%	76.19%	88.54%	90.83%	95.94%

Figure 4.6. XPS spectra. N1s spectra of the OSNP made of 80% TSPA at (A) pH 1, (B) pH 2, (C) pH 7, (D) pH 11, and (E) pH 12. The protonated N is in green while the deprotonated N is in red. There is more protonated nitrogen in more acidic solutions. The table shows the percentage of protonated and deprotonated N1s. Reprinted with permission from ACS[3].

Ionic strength is another important parameter in regulating the adsorption of charged moieties because it can compete with the dye or adsorbents in the solution. To understand the effect of ionic strength on the adsorption capacity of the OSNP, the ionic

strength was adjusted with NaCl to a broad range from 0 M to 4 M. **Figure 4.5** shows that the adsorption capacity decreased as the ionic strength increased from 0 to 0.5 M, and then decreased slowly as the ionic strength further increased to 4 M, which indicates the adsorption mechanism may be due to the electrostatic interactions.

The effect of dye concentration was studied from 0 to 0.33 mg/ml (0.88 mM) because typical effluent dye concentrations are 0.001 mg/ml to 0.25 mg/ml[366]. The adsorption capacity is linear with the phenol red concentration (**Figure 4.5**), but plateaus near 2 mg/ml (5.31 mM) (**Figure 4.5**) because the active binding sites on the nanoparticles become saturated at high dye concentrations.

We studied the effect of adsorbent dosage (0, 0.038, 0.075, 0.15, 0.3, 0.6, 1.2, and 2.4 mg) on the adsorption capacity. The capacity increased with decreasing adsorbent dose (**Figure 4.5**). Remarkably, the adsorption was performed at RT, pH ≈ 2.6, 0.067 mg/ml (0.177 mM) phenol red; the maximum adsorption reached to almost 201 mg/g (0.53 mmol/g) at adsorbents dosage of 37.5 µg.

3.3. Selective adsorption of anionic dye

We tried to extract phenol red from a mixture of phenol red and methylene blue. The OSNP adsorbed only phenol red (> 95%) even at phenol red:methylene blue ratios of 1:10 and 1:1 (**Figure 4.7**); no methylene blue was adsorbed. At phenol red:methylene blue of 10:1, around 84% of phenol red and 5% of MB was adsorbed (**Figure 4.7**). The inset shows the color change of each dye and their mixtures before and after adsorption. The OSNP turned pink after exposure to phenol red suggesting that the OSNP are basic. The color differences in the insets between the dyes are due to the concentration changes (**Figure 4.7**).

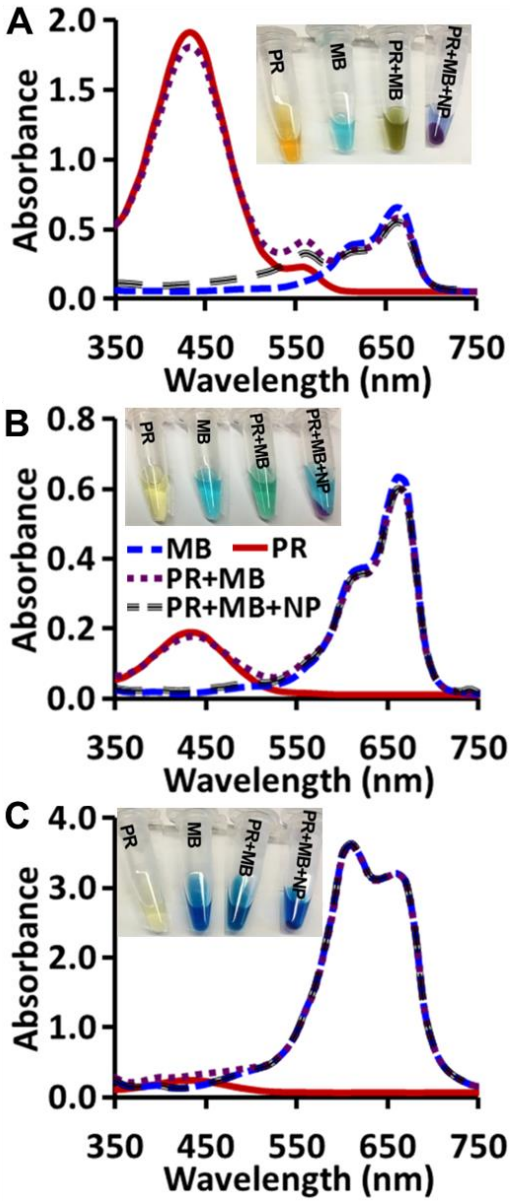

Figure 4.7. Selective adsorption of anionic dye. Absorbance of phenol red, methylene blue, and their mixture before and after addition of OSNP at different phenol red:methylene blue ratios. (A) 10:1, (B) 1:1, and (C) 1:10. The inset images show that the OSNP turned pink after being added to the mixture indicating the basic nature of the OSNP. The absorbance spectra of the supernatants show only adsorption for phenol red but not methylene blue. Reprinted with permission from ACS[3].

3.4. Reusability of the OSNP

Reusability is a critical property of adsorbents due to cost and environment

concerns. To achieve good reusability, desorption should be easy and release active sites for re-adsorption. In this study, the phenol red was adsorbed by the OSNP in acidic solution, followed by desorption in NaOH (0.017 M) solution. **Figure 4.8** shows the significant change of supernatant after adsorption in acidic dye solution and after washing with 0.017 M NaOH. The OSNP turned from white to pink after phenol red adsorption, and turned back to white after washing with NaOH solution (**Figure 4.8**).

The adsorption/desorption was performed 10 time. The dye removal efficiency is 97.7%, 99.4%, 99.5%, 99.4%, 99.2%, 99.3%, 98.9%, 98.6%, 98.4%, and 98.1% from cycle 1 to 10 (standard deviation of 0.62%); the corresponding average dye recovery efficiency are around 77.4%, 79.6%, 78.1%, 82.2%, 78.3%, 77.6%, 80.0%, 77.0%, 79.2%, and 79.9% (standard deviation of 1.6%) (**Figure 4.8**). The zeta potential of the OSNP after adsorption and desorption is also "recyclable". The zeta potential of OSNP increased after adsorption of phenol red, and returned to baseline after desorption (**Figure 4.8**). The changes in the zeta potential were consistent between cycles. This indicates that the dye removal and recovery were stable for at least 10 cycles.

ICP-OES was used to measure the silicon loss during desorption with NaOH. The accumulative loss of OSNP after 10 cycles is around 0.65% (**Figure 4.8**). The average OSNP loss per cycle is 0.065%, which means the OSNP will be depleted after more than 1500 cycles. However, the adsorption capacity was not diminished due to this loss of OSNPs. This might be because additional intrinsic amine groups are found throughout the OSNP, i.e., there will be new binding sites on the surface even when the original binding sites are partially lost.

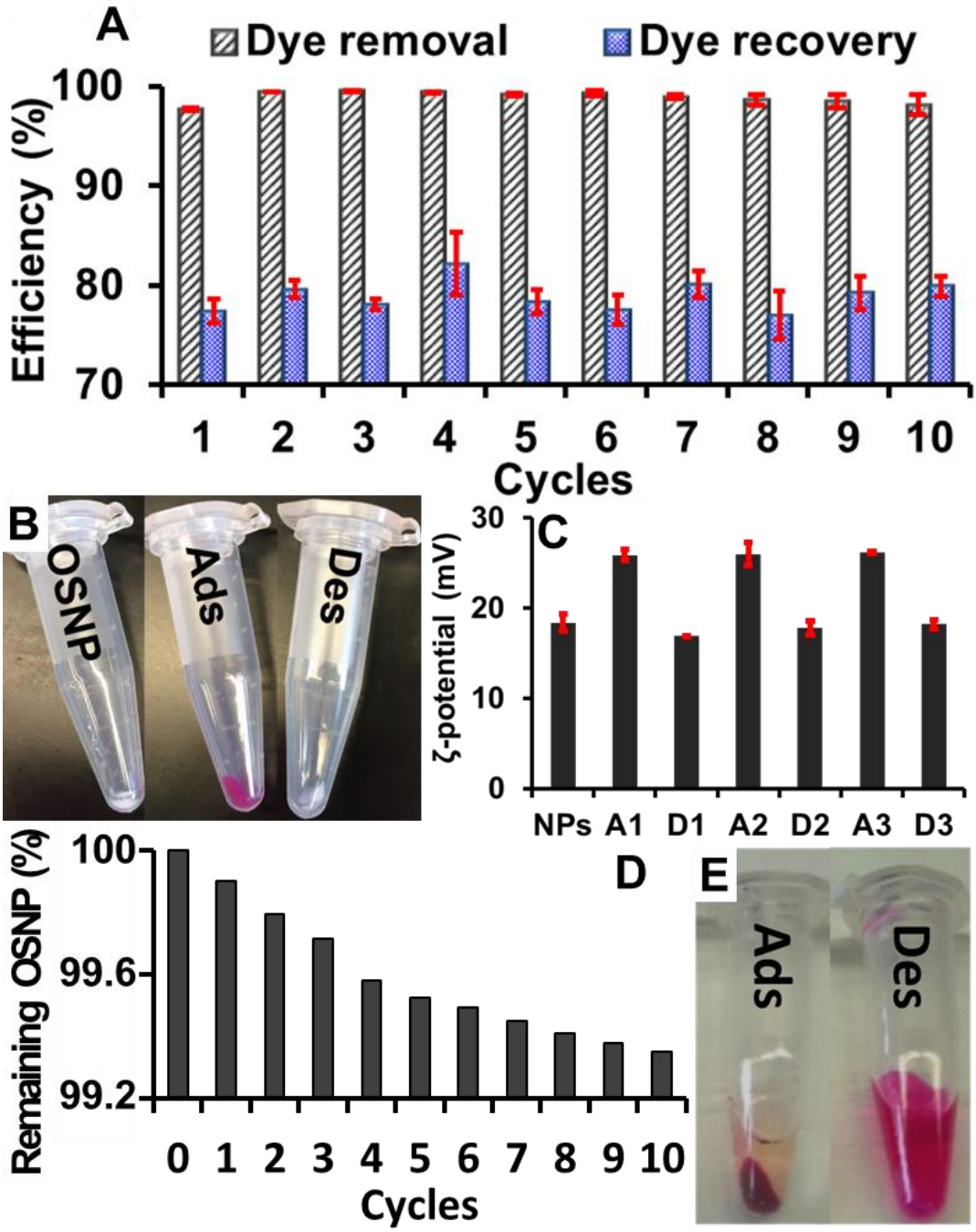

Figure 4.8. Reusability of OSNP for dye adsorption. (A) The OSNP can be reused for phenol red adsorption (t=5 min, pH=2 treatment, RT, 0.25 mg/ml or 0.66 mM phenol red, 2 mg of OSNP). Error bars represent the standard deviation for 3 measurements. (B) The OSNP changed from white to pink after addition to phenol red solutions and centrifugation due to adsorption (Ads.), but they became white again after base treatment due to dye desorption (Des.). (C) Change of zeta potential after dye adsorption and recovery of zeta potential after dye desorption. NPs represents the original OSNP; A1, A2, and A3 represents NPs after adsorption in cycles 1, 2, and 3; D1, D2, and D3 represents NPs after desorption in cycle 1, 2, and 3. (D) The accumulative loss of loss in the first 10 cycles. (E) The color of supernatant after desorption was more intense than after adsorption indicating a high adsorption and desorption efficiency. Reprinted with permission from ACS[3].

Moreover, the CHN analysis indicated that there were 7.2 μmol of nitrogen binding sites per 2 mg of OSNP (**Figure 4.1**), and for each reuse cycle there were 0.13 μmol of phenol red bound to 2 mg OSNP (**Figure 4.8**). Therefore, even under the worst-case scenario in which each nitrogen can participate in only one binding event, the OSNPs could still be reused more than 50 times.

3.5. Adsorption mechanism

We hypothesized that the adsorption of phenol red by OSNP is due to both electrostatic attraction as well as hydrogen bonding. The amine groups can form a strong hydrogen bond (29 kJ/mol) with the hydroxide on phenol red[367]. To verify our hypothesis, we compared the adsorption of OSNP to four dyes including methylene blue, rhodamine B, phenol red, rose bengal (**Figure 4.9**) with acid dissociation constants (pKa) of 3.8[368], 3.7[369], 7.7[365], and 4.7[370], respectively.

At pH 7, nearly all phenol red and rose bengal were adsorbed, but not the methylene blue or rhodamine B (**Figure 4.9**). At pH 7, methylene blue is positive, phenol red[365] and rose bengal are negative, rhodamine B is zwitterionic and the OSNP is positive (**Figure 4.5**). Phenol red and rose bengal are attracted by the OSNP, while methylene blue is repelled by the OSNP. At pH 13, the OSNP is negative (**Figure 4.5**), and the adsorption behavior changed dramatically: only a small amount of phenol red and rose bengal were adsorbed, but nearly all methylene blue is adsorbed. Thus, we conclude that electrostatic forces are the primary adsorption mechanism because much more negative phenol red were adsorbed compared to zwitterionic rhodamine B at pH 7, when both of them can form hydrogen bonding with the amine on the OSNP.

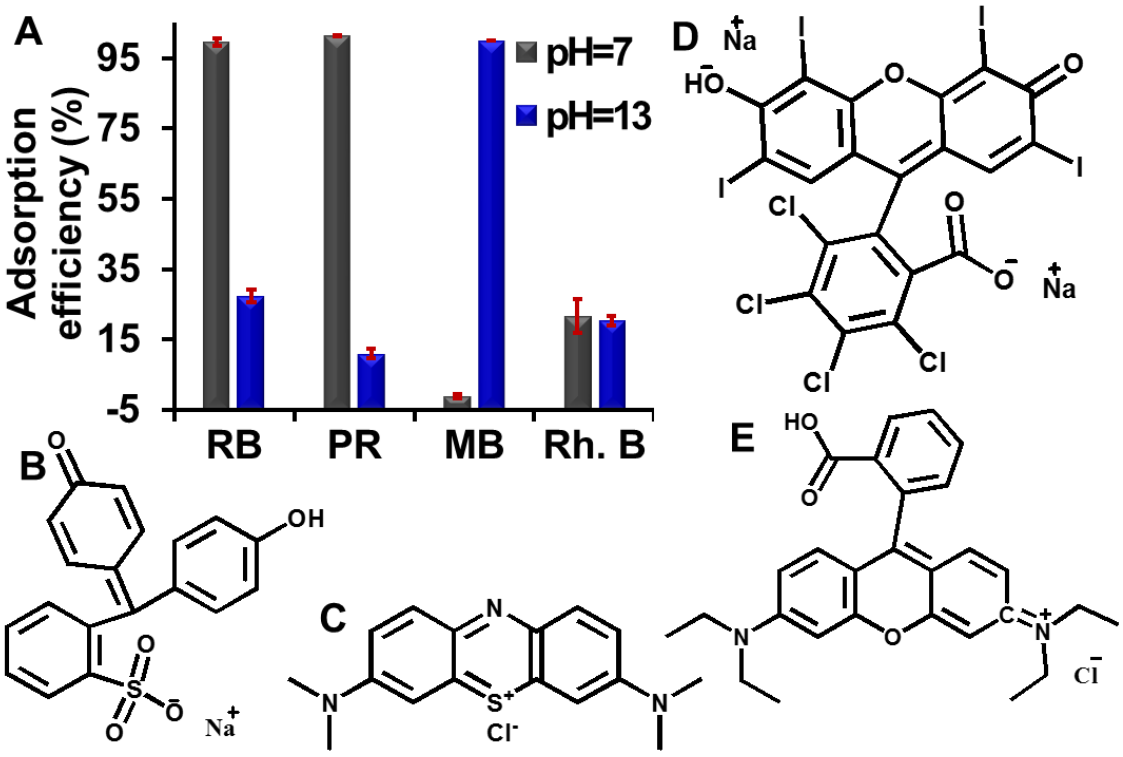

Figure 4.9. Adsorption mechanism. (A) Adsorption of OSNP to four dyes, including (B) phenol red (PR, pKa=7.7[365]), (C) methylene blue (MB, pKa=3.8[368]), (D) rose bengal (RB, pKa=4.7[370]), and (E) rhodamine B (Rh. B, pKa=3.7[369]). Positive OSNP (at pH 7) has a high adsorption to negative RB and PR, a low adsorption to zwitterionic Rh. B, and no adsorption to positive MB; while the negative OSNP (at pH 13) has a high adsorption to MB, small adsorption to RB, PR, and Rh. B. Reprinted with permission from ACS[3].

To further confirm the contribution of hydrogen bonding, we compared the adsorption of rose bengal and phenol red at 0.3 mM at pH 7, when only phenol red can form hydrogen bonds with the OSNP. The results showed about 97.5% of phenol red and 94.9% of rose bengal were adsorbed. Therefore, we found that the amine loading level is the most important factor governing dye adsorption. The mechanism of adsorption is mainly electrostatic forces and hydrogen bond arising from the amine groups on the OSNP.

3.6. Kinetics

The adsorption of phenol red happened immediately upon contact, and the

adsorption efficiency is related to the initial dye concentrations. When the dye concentration is equal to or smaller than 0.08 mg/ml (0.21 mM), about 100% of the dye is adsorbed within 5 minutes (**Figure 4.10**). At other concentrations, the dye adsorbed within the first 5 minutes. This is over 85% of the dye adsorbed within the first hour. We also performed a long-term adsorption at 0.5 mg/ml (1.33 mM). The results showed that most adsorption occurred within the first 30 minutes; more dye can be sequestered slowly over the subsequent 3 days (**Figure 4.10**).

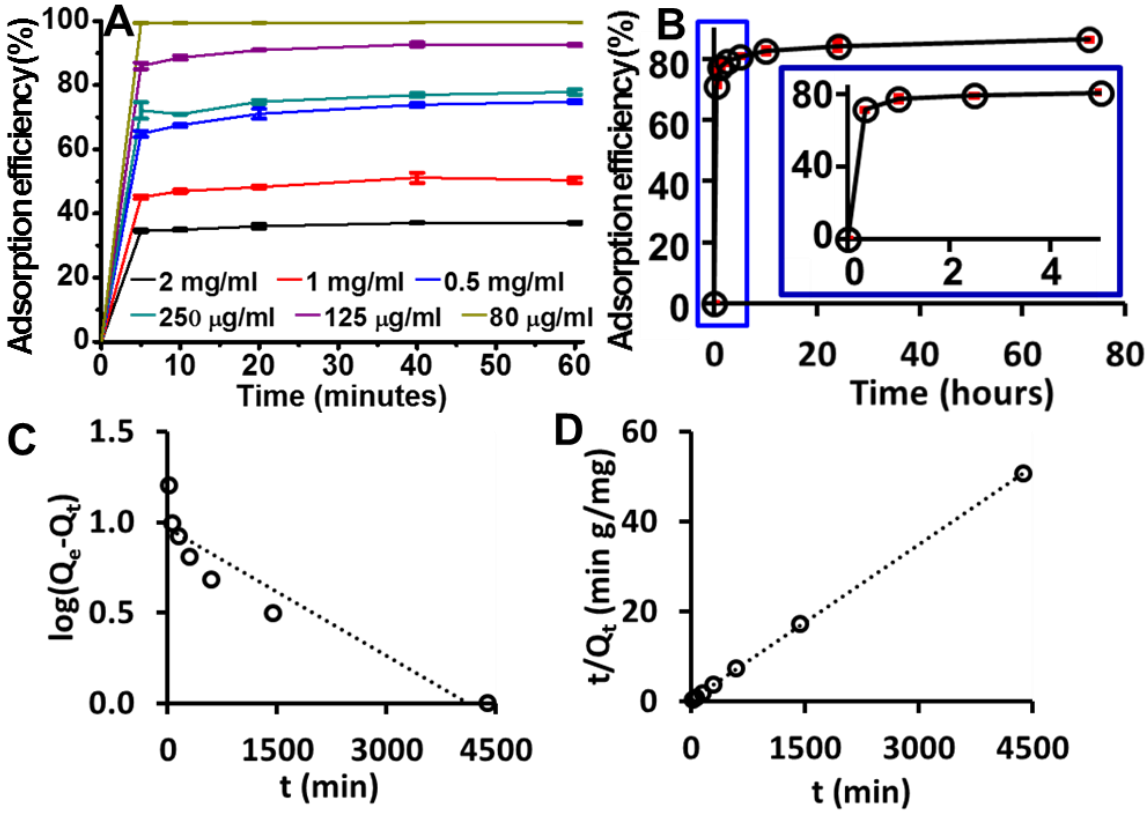

Figure 4.10. Adsorption kinetics. (A) Short-term adsorption efficiency of phenol red by OSNP is different when the dye concentration changes. The adsorption efficiency decreases as the dye concentration increases. (B) Long-term adsorption when the dye concentration is 0.5 mg/ml (1.33 mM) (pH=7, RT, 0.75 mg of OSNP). The inset shows the PR adsorption within the first 5 hours. Most adsorption happened within the first 30 minutes. More dye can be sequestered slowly over the subsequent 3 days. Error bars represent the standard deviations for 3 measurements. Plots based on (C) pseudo-first-order and (D) pseudo-second-order adsorption models show that the pseudo-second-order adsorption model is a better fit for the phenol red adsorption. Reprinted with permission from ACS[3].

To evaluate the rate and mechanism of mass transfer of phenol red from liquid phase to the OSNP surface, pseudo-first-order and pseudo-second-order kinetics models were investigated to understand the mechanism of phenol red sorption onto the OSNP. The pseudo-first-order model was summarized by Lagergren[371] as seen in equation 4.1. The pseudo-second-order rate equation was described by McKay and Ho[372] and is shown in equation 4.2.

$$\log(Q_e - Q_t) = \log Q_t - \left(\frac{K_1}{2.303}\right) \quad \text{Equation 4.1}$$

$$\frac{\mathrm{t}}{\mathrm{Q_t}} = \frac{1}{K_2 {Q_e}^2} + \frac{1}{Q_e}\mathrm{t} \quad \text{Equation 4.2}$$

Here, Q_e and Q_t are the adsorption capacities (mg/g) at equilibrium and at time t; K_1 (1/min) and K_2 (g/mg min) are the rate constants. **Figure 4.10** shows the graphs plotted based on two kinetics models, and **Table 4.11** summarizes the values of Q_e, K_1, K_2, and R^2. The results show that the adsorption of phenol red is better described by the pseudo-second-order kinetics model, which indicates that the rate limiting step involves chemisorption of the adsorbate onto the adsorbent[353].

Table 4.11. Parameters of pseudo-first-order and pseudo-second-order kinetics for the adsorption of phenol red on the OSNP. Reprinted with permission from ACS[3].

Kinetic models	Q_e	K_1	K_2	R^2
Pseudo-first-order	87.24 mg/g (0.23 mmol/g)	0.19 min^{-1}	-	0.9597
Pseudo-second-order	83.21 mg/g (0.22 mmol/g)	-	0.0033 g/mg min (1.24 g/mmol min)	0.9959

3.7. Isotherms

Adsorption isotherms are valuable tools to assess the distribution of solute between the solid and liquid phases, and the adsorption isotherm parameters reflect the adsorption

capacity and energy change during adsorption[373]. We applied both Langmuir and Freundlich isotherm models to the phenol red-OSNP system (**Figure 4.12**).

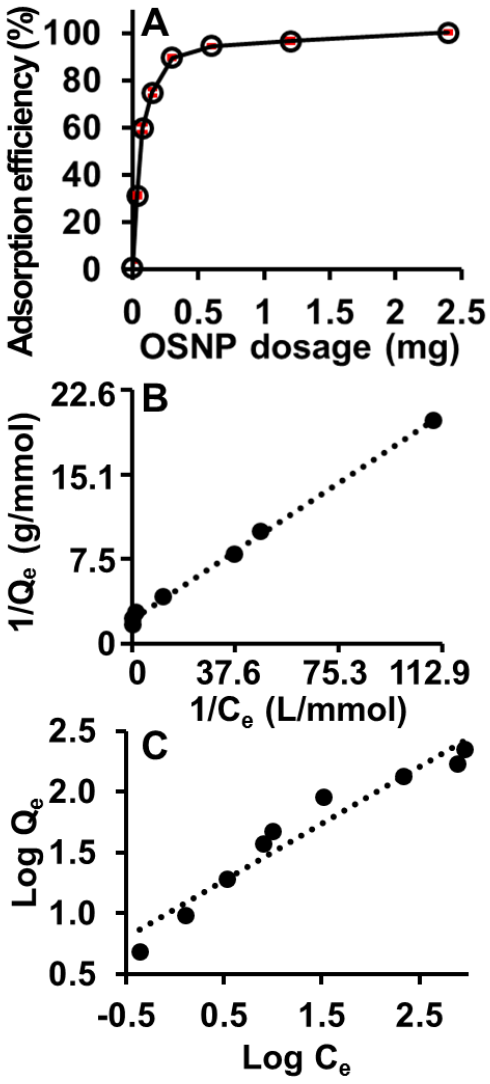

Figure 4.12. Effect of adsorbent dosage on phenol red removal efficiency and adsorption isotherms. (A) The adsorption increased as the OSNP amount increased. Error bars represent the standard deviation of 3 measurements. (B) Langmuir adsorption isotherms shows a linear plot (R^2=0.9977), which indicates that the adsorption of phenol red is a monolayer and occurs at specific homogeneous sites within the adsorbent. (C) The Freundlich adsorption isotherms are less linear with R^2=0.9392 compared to the Langmuir adsorption. Reprinted with permission from ACS[3].

We studied the isotherms by change the adsorbent dosage (0, 0.038, 0.075, 0.15, 0.3, 0.6, 1.2, and 2.4 mg). The total amount of adsorbed dye increased with the dose of

adsorbent and reached almost 100% with 2.4 mg OSNP (**Figure 4.11**) because there were more active sites for adsorption.

The Langmuir adsorption isotherm[11, 373] assumes that adsorption occurs at specific homogeneous sites within the adsorbents and forms a monolayer on the homogeneous surfaces. The linear form of the Langmuir equation is:

$$\frac{1}{Q_e} = \frac{1}{Q_m} + \frac{1}{bQ_mC_e} \qquad \text{Equation 4.3}$$

Here, Q_e is the amount of adsorbate adsorbed per unit mass of adsorbent (mg/g), C_e is the equilibrium concentration of the adsorbate (mg/L), Q_m (mg/g) is the theoretical maximum adsorption capacity, and b (L/mg) is the energy of adsorption. Another important Langmuir constant is separation factor (R_L), which is defined by equation 4.4:

$$R_L = \frac{1}{bC_o+1} \qquad \text{Equation 4.4}$$

Where C_o (mg/L) is the initial adsorbate concentration. The separation factor is related to the feasibility of the adsorption including unfavorable (R_L>1), linear (R_L=1), favorable (0<R_L<1), and irreversible (R_L=0)[374].

The Freundlich adsorption isotherm[375, 376] is an empirical equation based on the assumption that adsorption process occurs at heterogeneous surfaces having different available binding sites with unequally energies of adsorption. Therefore, this isotherm indicates that the adsorption is not a monolayer and the adsorption sites with greater affinity are occupied first. The Freundlich model is given by the relation:

$$\text{Log } Q_e = \text{Log } K_f + \frac{1}{n}\text{Log } \mathrm{C_e} \qquad \text{Equation 4.5}$$

Where K_f is the Freundlich constant, corresponding to adsorption capacity; and 1/n is the heterogeneity factor—a parameter for adsorption intensity and surface heterogeneity.

The favorable range of $1/n$ is between 0 and 1[377].

Figure 4.11 fit the Langmuir and Freundlich isotherms to the phenol red-OSNP systems, respectively. The calculated parameters are shown in **Table 4.13**. The linear relationship between $1/Q_e$ and $1/C_e$ indicates that the Langmuir isotherm holds for the phenol red-OSNP system (**Figure 4.11**). The linear relationship between $1/Q_e$ and $1/C_e$ also explained why the adsorption capacity increased when the dye concentration increased (**Figure 4.10**). Both Langmuir and Freundlich models indicated the favorable adsorption of phenol red by the OSNP. In addition, the adsorption of phenol red by the OSNP is better estimated by the Langmuir isotherm than the Freundlich.

Table 4.13. Langmuir and Freundlich isotherms parameters for the adsorption of phenol red on OSNP. Reprinted with permission from ACS[3].

	Parameters	Values
Langmuir	Q_m	175.44 mg/g (or 0.46 mmol/g)
	b	0.04 L/mg (or 15.05 L/mmol)
	R_L	0.26
	R^2	0.9977
Freundlich	K_f	10.74 mg/g (or 0.03 mmol/g)
	$1/n$	0.47
	R^2	0.9392

The theoretical maximum Langmuir adsorption capacity was calculated to be 175.44 mg/g (0.47 mmol/g). The adsorption capacity of the OSNP to phenol red is higher than most reported natural or synthetic adsorbents. We compared the theoretical Langmuir maximum adsorption capacity of the OSNP for phenol red with other reported adsorbents for phenol derivatives and found that the OSNP were better than 67 of 77 reported adsorbents including both commercial and non-commercial sources derivatives[375, 376, 378, 379].

4. Conclusions

An organosilica nanoparticle with intrinsic active binding sites for drug adsorption was synthesized and characterized. The binding property of the OSNP primarily depends on the amount of amine groups on the nanoparticles. The OSNP made with 80% TSPA has the highest adsorption capacity. The OSNP adsorbs molecules through electrostatic attraction and hydrogen bonding. The OSNP can adsorb either anionic or cationic molecules by changing the particle zeta potential. Taking advantage of this unique adsorption property, we demonstrated the OSNP can extract phenol red from its mixture with methylene blue. We believe the OSNP can also be used for similar species including in drug delivery or imaging agents.

Using phenol red as a model drug, we found the experimental maximum drug adsorption is over 200 mg/g (0.53 mmol/g), and the theoretical maximum adsorption is around 175 mg/g (0.47 mmol/g). The adsorption efficiency can reach 100% at room temperature and neutral pH when the phenol red concentration equals the typical concentration in cell culture media. Adsorption occurred within 5 minutes. The Langmuir model was a better fit than the Freundlich model. Moreover, the OSNP can be reused for over 10 cycles without diminishing the adsorption and desorption efficiencies.

In a summary, the high yield, high adsorption capacity, and excellent reusability highlight the utility of OSNPs for environmental remediation, drug delivery, and carriers for imaging agents. The results highlight that OSNPs with amine groups are an effective adsorbent material. They have fast adsorption, high removal efficiency, high adsorption capacity, tunable adsorption ability for different molecules, and reusability.

5. Acknowledgement

The text of Chapter 4, in part, is the reprint of the material as it appears in "Organosilica Nanoparticles with an Intrinsic Secondary Amine: An Efficient and Reusable Adsorbent for Dyes" by Fang Chen, Eric R. Zhao, Taeho Kim, Junxin Wang, Ghanim Hableel, Philip J.T. Reardon, Soundaram J. Ananthakrishna, Tianyu Wang, Santiago Arconada-Alvarez, Jonathan C. Knowles, Jesse V. Jokerst, ACS Applied Materials & Interfaces, 2017. The dissertation author was the primary researcher of this paper.

Chapter 5.

Increases efficacy of stem cell therapy via triple-functional inorganic nanoparticles

1. Introduction

Cardiovascular disease remains a leading cause of death[380] in part because human hearts have a limited regeneration capacity.[381] Consequently, many efforts have been made to regenerate/repair cardiac tissue *via* stem cells.[330, 382-385] Mesenchymal stem cells (MSCs) are particularly promising due to their abundance, potent proliferation, and multi-lineage differentiation capacity, and expressing of paracrine factors.[386, 387] There are three main mechanisms by which MSCs improve cardiac function: endogenous stem cell recruitment, replacement of apoptotic cells, and secretion of paracrine factors to increase proliferation and reduce inflammation.[171]

Unfortunately, stem cell therapy is limited by mis-injection into highly fibrotic tissues,[388] poor cell survival due to ischemia and inflammation,[330, 389] and low cell retention in cardiac tissue.[276] We and others[114, 171, 390, 391] have used nanoparticles as imaging agents,[171] drug delivery vehicles,[114] and/or scaffolds[390] to improve stem cell therapy. Although various nanoparticles have shown potential in stem cell tracking,[171] pro-survival,[114] or manipulation,[391-394] translation has been limited by the niche utility of each particle type. Therefore, a hybrid multi-functional nanoparticle that can simultaneously track cells, deliver therapeutic drugs, and retain cells is highly desired.[395]

This work combines imaging, drug delivery, and cell directing capabilities into a single triple-function silica-iron oxide nanoparticle (SIO). This nanoparticle can guide cell injection in real-time, track cells by multi-modal imaging, increase viability, and increase cell retention by magnet-manipulation (**Figure 1)**. We have previously reported that mesocellular foam silica nanoparticles (MCF) could significantly increase the ultrasound contrast of human MSCs (hMSCs).[32] Here, we show that this foam-like structure can also

offer sustained release of cargo to increase the survival of hMSCs. The same system can be coated with superparamagnetic iron oxide nanoparticles (SPIO) for MRI imaging or manipulation of cells with an external magnet. The resulting product—called SIO here—increased the efficacy of stem cell therapy and improved heart function in a murine model of myocardial infarction. We also then evaluated its toxicity and the mechanism of myocardium repair.

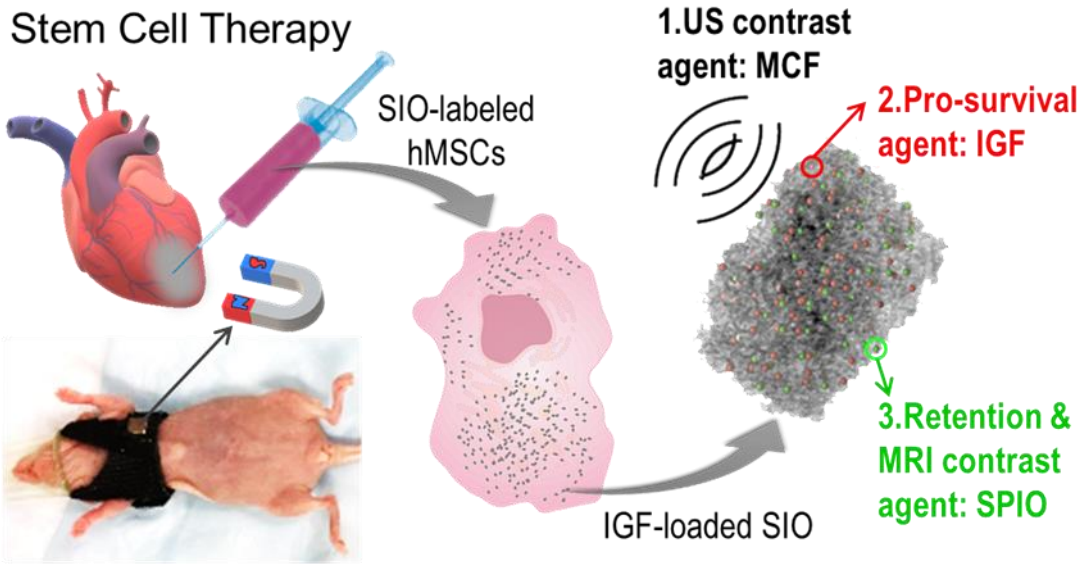

Figure 5.1. Schematic of treatment approach with multi-functional silica-iron oxide nanoparticles (SIO). The SIO increase ultrasound (US) and magnetic resonance imaging (MRI) contrast of human mesenchymal stem cells (hMSCs). They can also increase cell retention *via* the iron oxide nanoparticles embedded in the silica and an external magnet. Moreover, the SIO improve cell viability with sustained release of insulin-like growth factor (IGF).

2. Methods

2.1. Materials

Poly(ethylene glycol)-block-poly(propylene glycol)-block-poly(ethylene glycol) (P123), hexadecyltrimethylammonium bromide (CTAB), mesitylene, tetraethyl

orthosilicate (TEOS), iron (II) chloride hexahydrate, and ammonium hydroxide were purchased from Sigma-Aldrich. Hydrochloric acid (HCl) was purchased from J.T. Baker. Ammonium fluoride (NH_4F) was purchased from Acros Organics. Iron (III) chloride tetrahydrate was purchased from Fisher Chemical.

2.2. MCF nanoparticles fabrication

MCF were fabricated *via* a combination of micelle-templated sol-gel[103] and sonication-gradient centrifugation methods.[137] First, HCl (90 mL, 1.6 M) was added to P123 (2.4 g) and stirred until the polymer was fully dissolved. Then, CTAB (400 mg), NH_4F (25 mg), and mesitylene (1.6 mL) were added followed by stirring at 700 rpm for 2 hours. Next, TEOS (5.5 mL) was added dropwise with stirring at 1000 rpm followed by another 5 minutes of stirring. The mixture was then allowed to stand without stirring at 38°C for 18 hours. The products were collected and washed three times with ethanol followed by calcination (in a KSL-1100X furnace by MTI Corporation) at 600°C for 5 hours. To make MCF and optimize their size distribution, calcined particles were ground, sonicated for 2 hours, and then centrifuged at 500 rpm for 5 minutes. The supernatant was collected and centrifuged at 1000 rpm for 5 minutes. Again, the supernatant was collected and centrifuged at 8000 rpm. Optimized MCF in the pellet were collected, lyophilized, and stored for later use.

2.3. SIO synthesis

SIO were made by growing SPIO onto the MCF *in situ*. First, Millipore water (resistivity > 18.2 ohms) (1 mL) deoxygenated by N_2 bubbling was added to MCF (120 mg). Next, iron (III) chloride tetrahydrate (432 mg) and iron (II) chloride hexahydrate (159 mg) were added to the mixture. The vials were sealed, and N_2 was bubbled through once

more followed by sonication for 5 minutes. Then, the catalyst sodium hydroxide (12 mL, 0.5 M) was added dropwise under vigorous stirring followed by stirring for another hour at room temperature. The nanoparticles were collected and centrifuged at 10,000 rpm for 10 minutes. Free iron oxide nanoparticles, which were small and stayed in the supernatants, were removed by removing the supernatants. The pellet was then suspended and washed with Millipore water. The centrifugation and washing process were repeated twice more.

2.4. Characterization

TEM images were taken on a conventional TEM (JEOL1400-Plus). High resolution imaging was conducted on HRTEM (FEI Tecnai F20) operated at 200 kV. The objective lens astigmatism of HRTEM (FEI Tecnai F20) was corrected by using a standard carbon grating replica with Au/Pd particles. The ring in the live FFT pattern of the amorphous carbon film was tuned to be nearly perfect round, which indicates the reducing of astigmatism. Based on this corrected objective lens parameters (deflection currents), the SIO TEM samples were subsequently loaded and characterized. The elemental mapping of the SIO was performed on this HRTEM in scanning TEM (STEM) mode. During the optimization of reaction conditions, Z-contrast images and EDX spectra were taken on a STEM (Hitachi HD-2000) equipped with EDS detector (Bruker Quantax) at an accelerating voltage of 200 kV.

DLS measurements were obtained using a Malvern ZS 90, Malvern Instruments. The absorbance was measured over time on a UV-vis spectrometer (SpectraMax from Molecular Devices) for colloidal stability evaluation. The nitrogen adsorption-desorption analysis was done at 77 K on a Micromimetics ASAP 2020 system. Magnetic hysteresis loops were measured by sweeping the field from -7 T to 7 T at 300 K on a Quantum Design

MPMS3 superconducting quantum interface device (SQUID) magnetometer.

2.5. IGF loading and release from SIO

IGF was loaded to SIO by mixing SIO (16 mg) and IGF (100 µL, 1 µg mL^{-1}) in Millipore water and stirring in an ice water bath in the dark for 18 hours. The particles were then centrifuged at 8,000 rpm for 5 minutes followed by washing with water thrice. The supernatant was collected, and the amount of IGF remaining in the supernatant were measured by BCA assay. The loading capacity and efficiency were then calculated based on this result. A negative control was performed without nanoparticles. The IGF-loaded SIO were then lyophilized, refrigerated, and used within 7 days.

For the release study, IGF-loaded SIO (2 mg) were suspended to PBS (100 µL) preheated to 37°C. The release system was sealed and rotated in a 37°C oven. At designated time points, the nanoparticles were centrifuged at 14,000 rpm for 5 minutes, and the supernatant was collected. The pellet was then resuspended in fresh preheated PBS (100 µL).

2.6. Cell culture and labeling

The hMSCs (PT-2501, Lonza) were seeded at 5,000 cells cm^{-2} in mesenchymal stem cell growth media (PT-3001, Lonza) in an incubator with standard cell culture conditions. Cells used for SIO biocompatibility experiments were between passage 2 and 6. Cells used for MRI and ultrasound imaging were between passage 6 and 10. Cells for animal injections were passage 5 with the same lot number. Media was changed every 3-4 days and cells were passaged every 5-8 days at around 90% confluence using Trypsin-EDTA (0.25%, Gibco). All cells were labeled without transfection agents, and unless otherwise specified, the labeling was performed by incubating the cells with nanoparticles

(200 μg mL^{-1}) for 4 hours in a standard incubator unless specified. Labeled cells were then washed thrice with sterile PBS to remove free particles.

2.7. SIO labeling conditions and half-life in hMSCs

To optimize SIO labeling conditions, we performed two experiments that varied the labeling concentration and the labeling time. For the first experiment, cells were labeled with 0, 100, 200, 400, and 800 μg mL^{-1} of SIO for four hours. For the second experiment, cells were labeled for 1, 2, 4, 6, 16, and 24 hours at 200 μg mL^{-1}. Cells were then detached, counted, and analyzed for iron content by ICP-OES. To determine the half-life of SIO in hMSCs, we labeled cells at a concentration of 200 μg mL^{-1} for four hours. Then, we plated 50,000 cells into four T25 flasks. On days 0, 1, 4, 7, and 14, cells were analyzed by ICP-OES for iron content.

2.8. Biocompatibility of SIO to hMSCs

Cytotoxicity and proliferation assays were performed with a Resazurin assay (Sigma Aldrich). For cytotoxicity, cells were plated into a 96-well plate at a density of 10,000 cells/well and allowed to adhere for overnight. Then, SIO (200 μL) at varying concentrations were added to the cells. After 72-hour incubation, the media with nanoparticles was removed and cells were washed thrice with PBS. Then, 10:1 v/v media:Resazurin (100 uL) was added to all groups and allowed to incubate for 4 hours. Fluorescence was then measured at excitation and emission wavelengths of 550 and 585 nm, respectively.

For proliferation, unlabeled and SIO-labeled hMSCs were plated at a density of 5,000 cells cm^{-2} in 96-well plates. Viable cell numbers were then detected with the same Resazurin assay on different days. The effect of SIO on hMSCs' viability was further

confirmed with a calcein/EthD-III live/dead cell assay (Biotium). A positive control was created by adding CTAB (10%) to cells and incubating for 4 hours. All groups and an SIO-only control were analyzed with flow cytometry (FACSCanto 2, BD Biosciences).

The effect of SIO on cell differentiation were assessed *in vitro*. Unlabeled and SIO-labeled hMSCs were plated in 6-well plate with approximately 70% confluency. Then the cells were treated with osteogenic and adipogenic induction media (PT-3002 and PT-3004, Lonza) with media changed every 3 days for 3 weeks. To better visualize the differentiation, adipogenic induced cells were stained with Oil Red O (Sigma Aldrich) and osteogenic induced cells were stained with a von Kossa staining kit (Fisher Scientific). Control cells were treated with growth media. Stained cells were then observed with a microscope (BZ-X710, Keyence).

For the scratching/migration assay, cells were plated at a density of 5,000 cells cm^{-2} and allowed to grow overnight. A line was then scratched with a pipet tip leaving a gap between the cells. This area was then marked and imaged daily till the gap was completely refilled by migrating cells.

Phenotypes of hMSCs were detected by flow cytometry. First, unlabeled and SIO-labeled hMSCs were detached, centrifuged, and then resuspended in 100 µL labeling buffer (PBS with 2 mM EDTA and 0.5% BSA) containing 10 µL of each antibodies or isotype controls. The antibodies were CD73-PE (Clone AD2, 130-097-943, lot # 5170202055), CD90-FITC (Clone DG3, 130-097-930, lot # 5170202054), and CD105-APC (Clone 43A4E1, 130-099-125, lot #5170202046) from Miltenyi Biotech, and the isotypes were mouse IgG-PE, mouse IgG-FITC, and mouse IgG-APC (Clone IS5-21F, Miltenyi Biotech).

The effect of SIO on cytokine secretion was studied by detecting cytokines in the

cells culture media. SIO-labeled and unlabeled cells were plated at a density of 5,000 cells cm^{-2} in a 6-well plate and allowed to incubate 48 hours. The media was then collected, and the cytokines in the media were analyzed with a Luminex human 62-plex (Human Immune Monitoring Center, Stanford University).

2.9. Long term pro-survival effect of IGF-loaded SIO

Cells were plated into a 96-well plate at a density of 9,000 cells/well and allowed to grow for 2 days. The media was then replaced with 100 µL incomplete media (MSCBM from Lonza) containing free IGF (200 ng mL^{-1}), free BSA (200 ng mL^{-1}), IGF-loaded SIO (562 µg mL^{-1}), or nothing. Three more control groups were included: cells with growth media (also known as complete media), incomplete media without cells, and IGF-loaded nanoparticles without cells. Viable cell numbers were then detected with the Resazurin assay (the same procedure with the cytotoxicity and proliferation assays) on days 1, 2, 4, and 7.

2.10. Magnet-assisted cell direction and retention

To control the propagation of cells, SIO-labeled cells were detached and resuspended in 5 mL growth media and added to T25 flasks. A magnet was taped on the outside of the cell growing wall (becoming sidewall due to the standing flask) of the flask. Control groups included SIO-labeled cells without an external magnet on the flask and unlabeled cells with an external magnet. The flasks were then put into the incubator overnight. The magnets were removed 2 days later. The area in the magnetic field was observed with a microscope (EVOS, Thermo Fisher Scientific) daily for 4 weeks. The flasks were held vertically except during the microscopic imaging.

We also investigated the cell retention under different shear stresses (7 – 35 dyne cm^{-2}) created with a peristaltic pump. Cells were loaded into the tube (inner diameter 0.86 mm) without passing the squeezing point. A magnet was then placed by the tube and cells were observed under an EVOS microscope. Cells were stained with Qtracker 800 (Thermo Fisher Scientific) for better visualization. Then, the flow direction was reversed, and the cell solution was collected with different flow rates (2.8, 5.2, 8.5, 11.2, 13.0, and 14.6 mL min^{-1}). The cell concentration before and after the experiment were determined with a hemocytometer. Retention was calculated as (cell concentration before - cell concentration after)/cell concentration before.

2.11. *In vitro* or *ex vivo* ultrasound and magnetic resonance imaging

SIO or SIO-labeled hMSCs were suspended in 0.5% hot agarose solution at different concentrations of 0, 0.025, 0.05, 0.1, 0.2, 0.25, 0.4, 0.5, 2.5, and 5 mg mL^{-1} for nanoparticles or 0, 10,000, 50,000, 150,000, 300,000, 600,000 cells/60 µL, injected to a 384-well plate while it is hot, and then cooled down before imaging. Ultrasound imaging of the phantom was performed with a 40 MHz-centered linear transducer (MS550) on a VEVO 2100 system (VisualSonics, Fujifilm). MR imaging was performed on a Bruker 7T magnet with Avance II hardware, equipped with a 72 mm quadrature transmit/receive coil, and using a RAREVTR_T 2 Series pulse sequence in ParaVision version 5.1. For T2 measurements, the following parameters were used: TR = 5000 ms; TE = 12.6, 17.7, 62.8, 87.9, 113.0, 138.1, 163.2 ms; FOV (field of view) = 6.91 × 3.12 cm; slice thickness = 2 mm; and matrix size = 256 × 116. Relaxivities were calculated by linearly fitting plots of 1/T2 (s^{-1}) *versus* Fe ion concentrations (µM).

2.12. *In vivo* retention of SIO

All animal studies were performed in accordance with the Institutional Animal Care and Use Committee (IACUC) at the University of California, San Diego (UCSD). Mice were anesthetized with 1 - 2 % isoflurane. SIO in 50% Matrigel (40 µL of 10 mg mL^{-1}) were injected into the left ventricle myocardium close to the apex with a 31G BD insulin syringe. The injection was guided by ultrasound imaging with a 40 MHz-centered linear transducer (MS550) on a VEVO 2100 system (VisualSonics, Fujifilm) in real-time and assisted by an injection arm came with the VEVO 2100 system. Immediately after the injection, the mouse was cleaned and a magnetic harness was put onto the mouse with the magnet close to the heart apex. The harness was adjusted not to hinder normal movement of the animal, and the mouse was monitored twice daily. For the SIO control group, no magnetic harness was used on the animals. For the magnet control group, animals were put on magnetic harness but no injections. After 7 days, the iron content in hearts were determined with inductively coupled plasma mass spectrometry (iCAP RQ-ICP-MS, ThermoFisher). ICP-MS was used here because the concentration of the elements could be low and ICP-MS is more sensitive than ICP-OES.

2.13. Ischemia/reperfusion surgery

C57B6 (12 weeks old) were anesthetized with a cocktail of ketamine (50 mg kg^{-1}) and xylazine (5 mg kg^{-1}) by i.p. injection for initial induction and then isoflurane (0.75 - 1.5%) for complete induction of anesthesia. Animals were ventilated throughout the entire procedure (PhysioSuite, Kent Scientific Co). With thoracotomy, LAD coronary artery occlusion was performed by tying an 8-0 prolene suture ligature on a piece of 2-0 silk suture. After 60 minutes of ischemia, 20 µL of 1:1 v/v DMEM:Matrigel or the same matrix

containing unlabeled or IGF-loaded SIO-labeled hMSCs (5 million cells mL^{-1}) were injected intramyocardially below the ligation point close to apex. All cells injected were passage number 5 from a same donor. Reperfusion was started by removing the 2-0 silk suture from around the LAD coronary artery. The chest is closed once the mouse is hemodynamically stable.

2.14. Ultrasound imaging-guided intramyocardial injection and echocardiography

For the ultrasound-guided intramyocardial injection, animals were anesthetized with 1 - 2% isoflurane and mounted to a warm animal bed with four contact electrode sensors for electrocardiography. A 40 MHz-centered linear transducer (MS550) on a VEVO 2100 system (VisualSonics, Fujifilm) was adjusted to show parasternal long axis view of heart and align with syringe fixed on a mechanic injection assistant arm.

Animals for echocardiography were anesthetized with 0.25 - 1% isoflurane and underwent echocardiography using a VEVO 2100 ultrasound system (VisualSonics, SonoSite FUJIFILM) with a 40 MHz-centered linear transducer (MS550) as described previously.[54] The heart rate was controlled within 450 and 500 beats per minute. Cardiac function and structure were quantified *in vivo* by 2-dimensional (2D)/speckle-tracking echocardiography by the software VEVO Lab (VisualSonics, Fujifilm). Ejection fraction (EF), global longitudinal strain (GLS), and average peak strain values were determined and calculated as echocardiography-based parameters of LV contractility.

2.15. *In vivo* magnetic resonance imaging

In vivo MR imaging was performed on a MRS4700 scanner with 4.7 T magnet (MR Solutions Ltd, UK). Animals were anesthetized with 1 - 2% isoflurane and immobilized on a mouse holder with a prone position during the scan. Scanning sequence cardiac IR

segmented FLASH was used and the parameters were: TR = 7 ms; TE = 2 - 64 ms; FOV (field of view) = 3.5 × 3.5 cm2; slice thickness = 2 mm; and matrix size = 192 × 192. Electrocardiography and breath rate were gated for the imaging.

2.16. Histology

Postmortem heart and body weights were measured and hematoxylin-eosin-stained heart, lung, liver, and spleen tissue were studied. Cardiac interstitial fibrosis was evaluated on trichrome-stained sections. We quantified six random hearts from each group and each heart was sectioned to 10 μm with every 10th section collected. We analyzed 4 to 13 slices for each group and calculated the percentage of fibrosis with four continuous slices that showed a maximum fibrosis and a coefficient of variation less than 15%. These sections were then scanned with a microscope under 40X magnification. For fibrosis quantification, Fibrosis was calculated by count of blue pixels/count of blue and red pixels. The red and blue pixels were distinguished by changing the color threshold with software ImageJ and the count of these pixels were measured. Color threshold settings for the entire heart (both red and blue pixels) was RGB color space with the Triangle thresholding method. The fibrosis (blue pixels) was quantified with pixels with a hue between 150-195 by the Triangle thresholding method. Heart sections were also stained with iron staining kit from Sigma Aldrich to visualize the SIO. The presence of injected hMSCs in the heart was evaluated by immunostaining for CD73-PE (Clone REA804), CD90-FITC (Clone REA897), and CD105-APC (Clone 43A4E1) from Miltenyi Biotech.

3. Results and discussion

3.1. SIO nanoparticles synthesis, optimization, and characterization

SIO were made by growing SPIO *in situ* on MCF without any surface modification (**Figure 5.2a**). The MCF were chosen because they showed good ultrasound contrast to cells and great potential as a nano-container or reactor due to their relatively big pore size.[32, 396, 397] The MCF were fabricated *via* a bottom-up sol-gel micelle-templating.[103] These silica particles became smaller and monodisperse after 8.5 hours sonication (**Figure 5.3**).[137] The MCF we used to make SIO were 383±167 nm (n=570), and the diameter of the MCF pores were 16.6±3.6 nm (n=589) stacked in 3-dimensions (**Figure 5.4**).[103] These relatively large pores allow MCF to be reactive sites and be loaded with proteins.

To make silica and iron oxide hybrid nanoparticles, we first tried to load SPIO directly to the MCF. This method is straightforward, but the pre-formed SPIO blocked the pores (**Figure 5.5**). This could lead to decreased drug loading. Thus, we developed an *in situ* growth method to achieve the goals: the SPIO were grown on both the externl surfaces and pore walls of MCF to form SIO. First, the MCF were dispersed in a solution of $FeCl_3$ and $FeCl_2$ in an ultrasonic bath. Liquid catalyst-alkaline solution was added into this suspension with stirring, and iron oxide nanoparticles formed gradually on the surface and in the pores of MCF (**Figure 5.2a**). The MCF and liquid reactants were mixed well, so iron oxide nanoparticles could grow throughout the MCF instead of blocking the pores. The *in situ* growth method uses MCF as nano-reactors, which avoids the formation of large iron oxide nanoparticles because of the size confinement of the silica pores.[397]

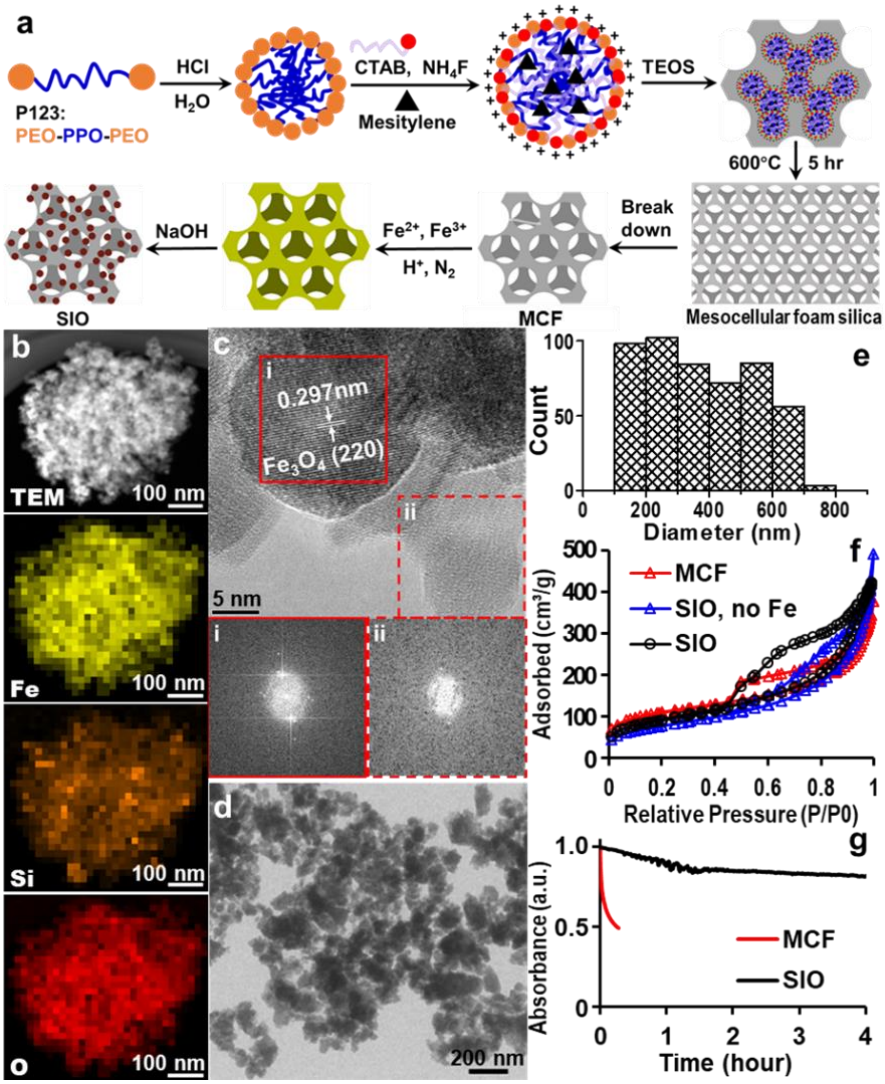

Figure 5.2. SIO synthesis, optimization, and characterizations. (a) Schematic synthesis of SIO. SPIO were grown *in situ* on calcined MCF prepared by a micelle-templated sol-gel method. (b) TEM image and EDX element mapping of a representative SIO. The mapping shows that the iron is well dispersed in the MCF. (c) HRTEM analysis indicates the presence of both crystal and amorphous regions. The lattice spacing of panel i is about 2.97Å, which agrees well with the lattice spacing of (220) planes of cubic Fe_3O_4. Below the HRTEM image, the fast Fourier transformation (FFT) patterns confirm the crystalline and amorphous features of panels i and ii. The amorphous structure is typically found in silica nanoparticles made with low-temperature sol-gel method,[103] sonication, and gradient centrifuge.[137] (d) Low magnification TEM image of multiple SIO show that SIO were irregularly shaped. (e) TEM size distribution of the SIO. The average size of SIO is 380 nm. The diameter is the average of Feret and MinFeret measured by ImageJ. Feret diameter is the longest distance between any two points along the selection boundary, also known as the maximum caliper. MinFeret diameter is the shortest longest distance between any two points along the selection boundary. (f) Nitrogen adsorption-desorption analysis indicates that both MCF and SIO were mesoporous. We also tested a product with catalyst but no iron precursors (SIO, no Fe). Increased pore volume and pore size in this product indicates the dissolution of silica during *in situ* growth. (g) Deposition of SPIO increased the colloidal stability of SIO compared to the MCF. The absorbances were normalized to the first time point.

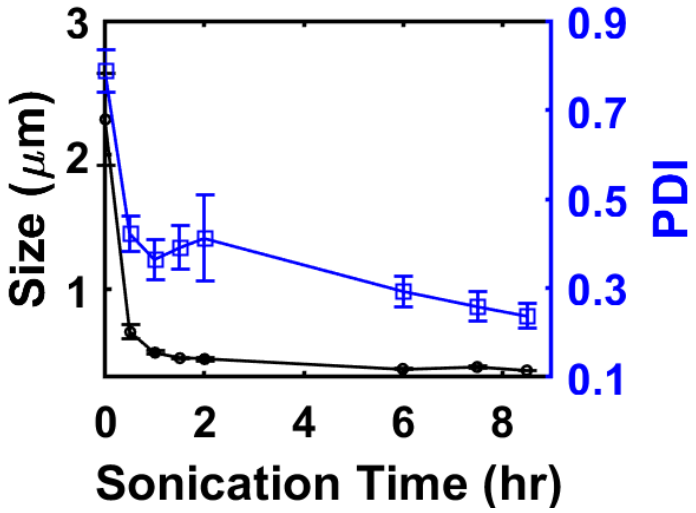

Figure 5.3. Size and PDI of MCF. Both average DLS size and polydispersity index of MCF decrease with increasing sonication time. The error bars represent the re standard deviation of three measurements.

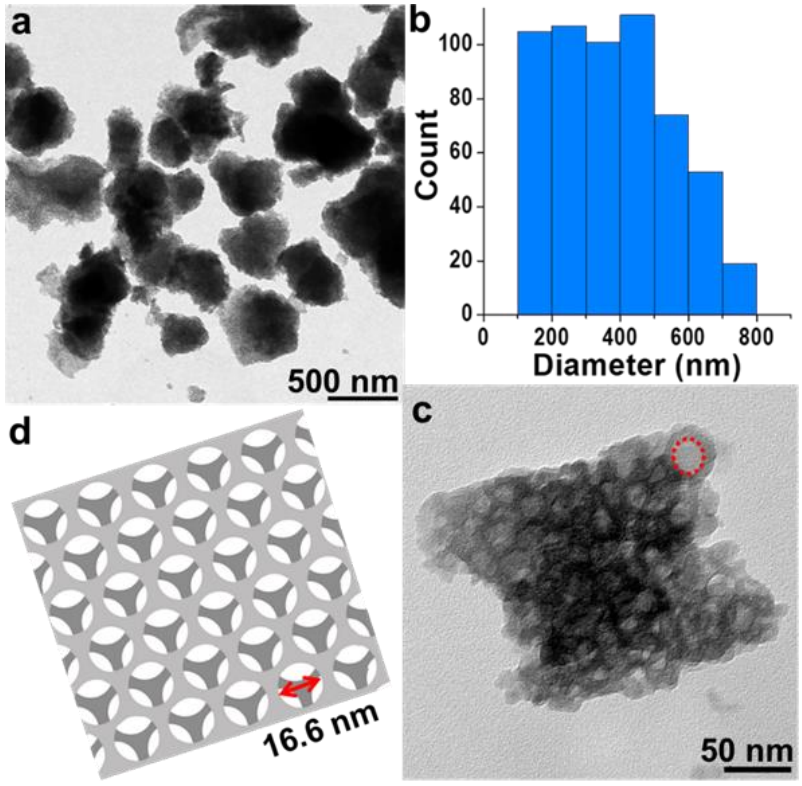

Figure 5.4. Characterization of optimized MCF. (a) TEM image and (b) size distribution (n=570) of MCF sonicated for 8.5 hours. The diameter is the average of Feret and MinFeret measured by ImageJ. Feret diameter is the longest distance between any two points along the selection boundary also known as the maximum caliper. MinFeret diameter is the shortest longest distance between any two points along the selection boundary. (c) Higher magnification TEM image shows the 3-dimensional porous structure of MCF. (d) Schematic illustration of MCF porous structure.[103]

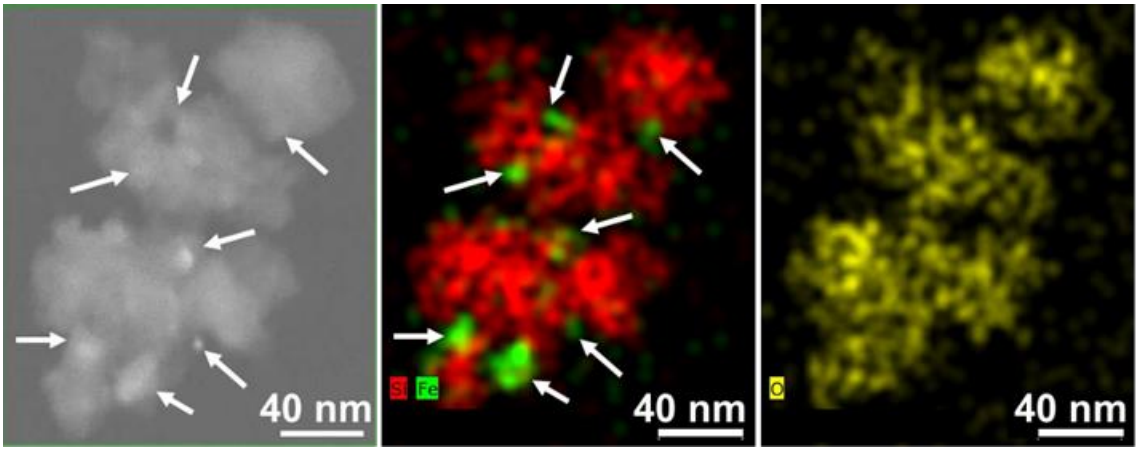

Figure 5.5. STEM image and EDX mapping of product made by loading pre-formed SPIO into MCF. Grey is the Z-contrast image. Red is silicon, green is iron, and yellow is oxygen. The white arrows indicate the SPIO blockades.

Next, we optimized the conditions for *in situ* growth of SPIO. The SPIO growth needs alkali as a catalyst, but the silica can be dissolved by the alkali. The alkali concentration, type of cationic ions in the alkali, temperature, and reaction time are all important for iron oxide formation and the silica dissolution. A lower pH and lower temperature decrease the extent of silica dissolution in alkali. Sodium ions and prolonged reaction time increases the magnetite crystal size, which increases the saturation magnetization.[398] Removing oxygen also improves the SPIO magnetization.[399] We investigated these factors and concluded that the optimal growth occurred at 1 hour of reaction at room temperature in the presence of 0.5 M NaOH and nitrogen protection.

The products made with the optimized reaction conditions showed a good dispersity of iron in the MCF (**Figure 5.6**). Energy-dispersive X-ray (EDX) mapping of a typical SIO showed that the iron was dispersed together with silicon and oxygen throughout the entire SIO (**Figure 5.2b**). SIO showed both crystal and amorphous regions under high resolution TEM (HRTEM). The fast Fourier transformation (FFT) pattern in frame i of **Figure 5.2c**

shows crystalline features with a lattice spacing of 2.97Å, which agrees well with the lattice spacing of (220) planes of cubic Fe_3O_4. (2.966 Å on PDF#65-3170). XRD pattern of the SIO matched with the crystal structure of magnetite (PDF# 96-101-1033) (**Figure 5.7**). In addition, this crystal region is a particle rather than a shell, which indicates the SPIO were formed during the *in situ* growth. The FFT from frame ii (**Figure 5.2c**) indicates an amorphous structure typical of silica made with a low-temperature sol-gel method.[119] The distorted white centers of FFT patterns of both crystal and amorphous regions are due to objective stigmatism from magnetite (**Figure 5.2c**).[400]

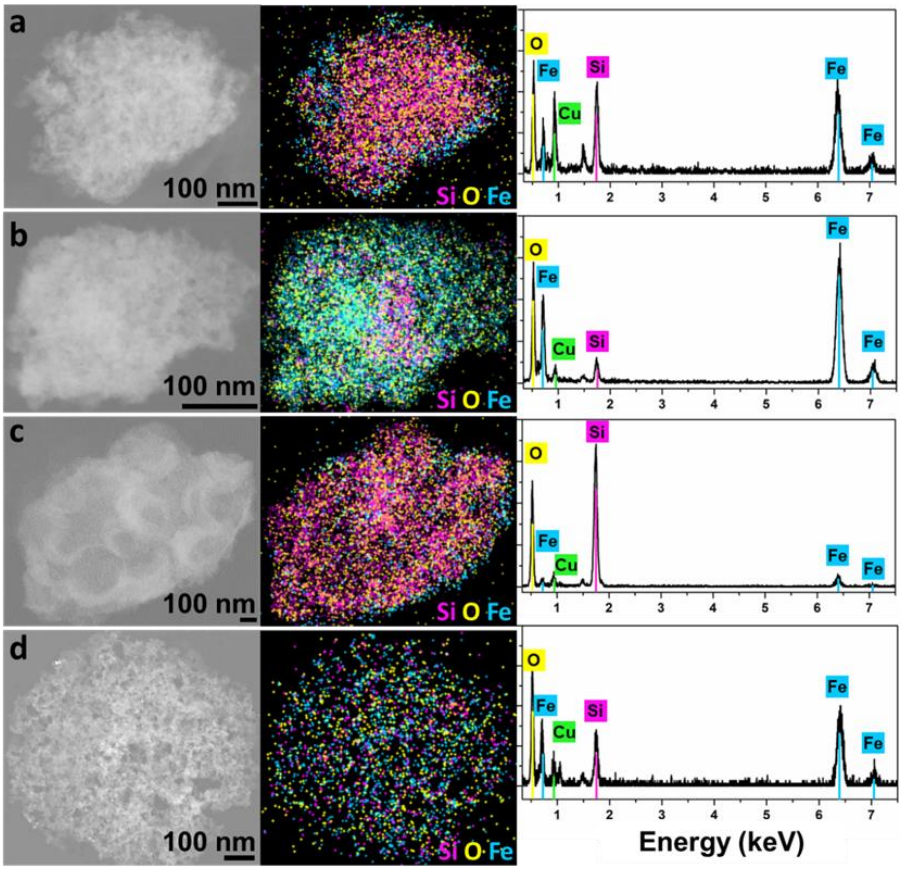

Figure 5.6. EDX mapping and spectra of SIO under different reaction conditions: (A) 0.7 M ammonia, 60 minutes, RT; (B) 0.5 M sodium hydroxide, 10 minutes, 100ºC; (C) 0.5 M sodium hydroxide, 30 minutes, RT; (D) 0.5 M sodium hydroxide, 60 minutes, RT. The last condition was chosen as an optimized reaction condition. Pink, yellow, cyanine, and green indicate silicon, oxygen, iron, and copper, respectively.

The saturation magnetization of the SIO also proved that the iron oxide in the SIO was Fe_3O_4. The saturation magnetization of SIO at room temperature was 52 emu/g (**Figure 5.8**). According to the ICP-MS analysis, the Fe-to-Si mass ratio in SIO was 1.34. Therefore, the saturation magnetization of iron oxide in the SIO was 91 emu/g. The saturation magnetization indicated that the iron oxide in SIO was Fe_3O_4, whose saturation magnetization is 90 emu/g.[401] In addition, the small coercivity (0.1 Oe) and the shape of hysteresis loop (**Figure 5.8**) confirmed that the SIO is superparamagnetic.[402]

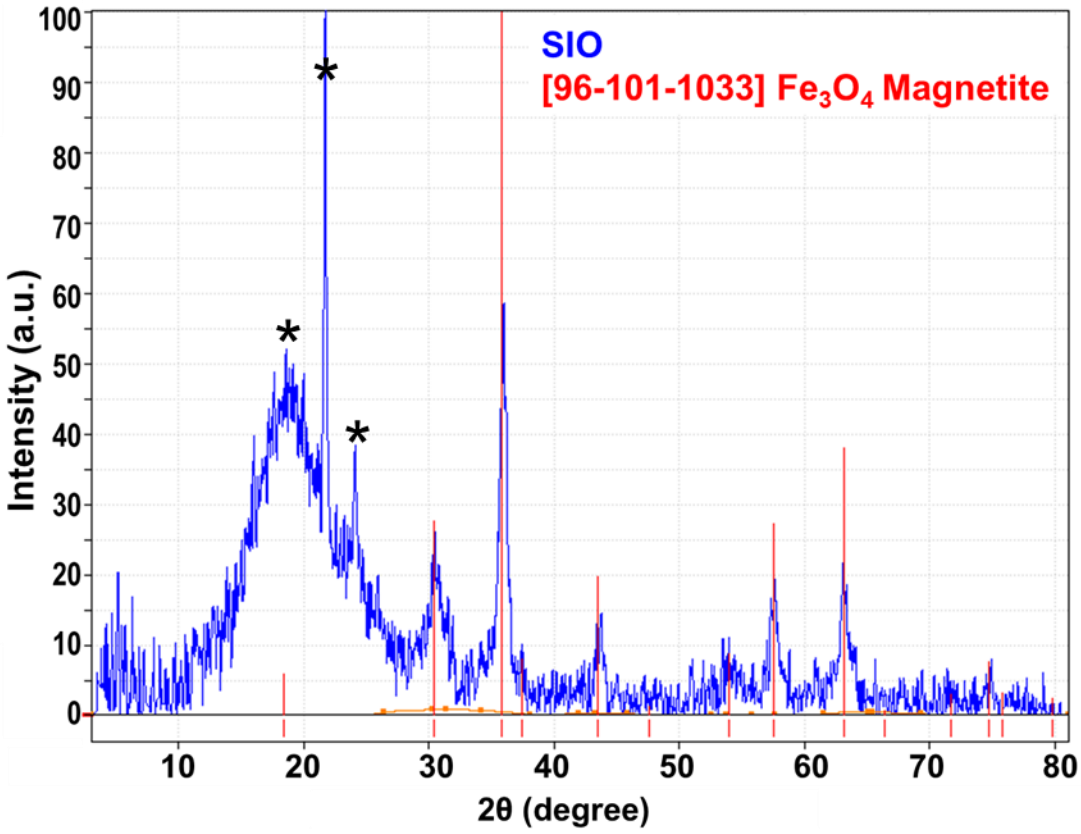

Figure 5.7. Powder X-ray diffraction pattern of SIO (blue) and magnetite from the database (red). Peaks marked with asterisks were from the sample holder.

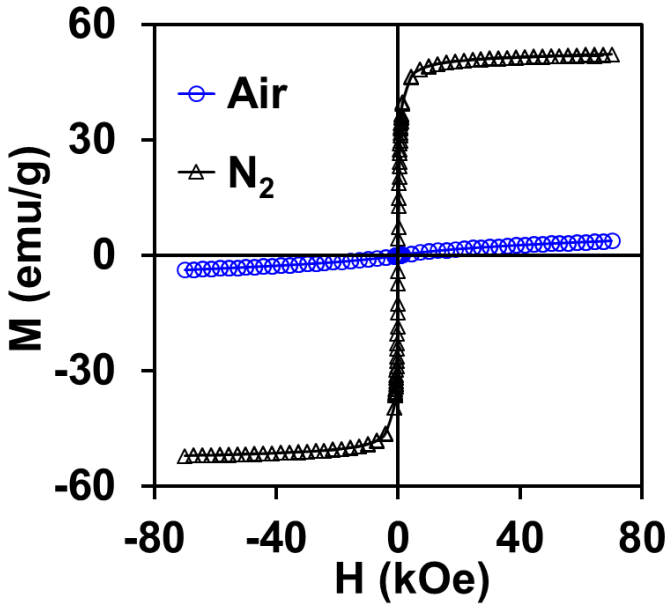

Figure 5.8. Hysteresis loop of SIO. Hysteresis loop indicates that SIO are superparamagnetic. The nitrogen protection during in situ growth of SPIO significantly increased the saturation magnetization of SIO. The measurement temperature was 300 K.

The SIO were irregularly shaped (**Figure 5.2d**), and their size distribution is shown in **Figure 5.2e**. Their average size was 380±166 nm (n=500), which is about the same as the starting MCF due to the balance between silica dissolution and SPIO deposition. The surface area, pore volume, and average pore size of MCF were 394 m^2/g, 0.50 cm^3/g, and 9.2 nm, respectively. With the alkali catalyst but no iron precursors, the pore volume and pore size were increased to 0.741 cm^3/g and 12.2 nm, which suggested dissolution of silica in the presence of the alkali. The surface area, pore volume, and pore size of SIO were respectively 333 m^2/g, 0.62 cm^3/g, and 9.2 nm, indicating the conjugation of SPIO on the MCF (**Figure 5.2f**).

The colloidal stability of SIO was also improved after SPIO-conjugation. The colloidal stability was determined by measuring the absorbance of a nanoparticle suspension in a cuvette over time. As shown in **Figure 5.2g**, only 29% of SIO settled after

24 hours *versus* 49% of MCF settled within 15 minutes at the same concentration. This implies that only 29% SIO settled after 24 hours. The increased colloidal stability may be due to the increased absolute value of zeta potential, which led to stronger electrostatic repulsion between particles. Dynamic light scattering (DLS) results showed that zeta potential of silica nanoparticles increased from -10 mV to 29 mV after deposition of positive SPIO.[403]

3.2. Cell uptake of SIO

Optimized SIO could be taken up by hMSCs without any transfection agents. SIO concentration and incubation time affected the cell uptake capacity. The cell uptake of SIO increased with the SIO labeling concentration ranging from 0 to 800 μg/mL (**Figure 5.9a**). Approximately 21%, 38%, 29%, and 24% of the total nanoparticles were taken up or adhered to the hMSCs when the labeling concentrations were 50, 200, 400, and 800 μg/mL. We chose 200 μg/mL as the labeling concentration in order not to overdose the cells. The cell uptake of SIO reached maximum at 4 hours and decreased slightly afterwards when 200 μg/mL of SIO were used (**Figure 5.9b**). The cell uptake of SIO at 4 hours was 2.19 ± 0.34 ng/cell when the SIO labeling concentration was 200 μg/ml. This labeling condition was chosen for the late experiments unless specified.

The half-life of SIO in MSCs was studied *via* ICP analysis. The results showed that the cell uptake of SIO decreased exponentially *versus* time (**Figure 5.9c**). The half-life of SIO in hMSCs (passage 5) was 6.7 days, which was close to the doubling time of the cells—7.2 days. Therefore, the dilution of SIO in hMSCs may mainly be due to the division of cells.

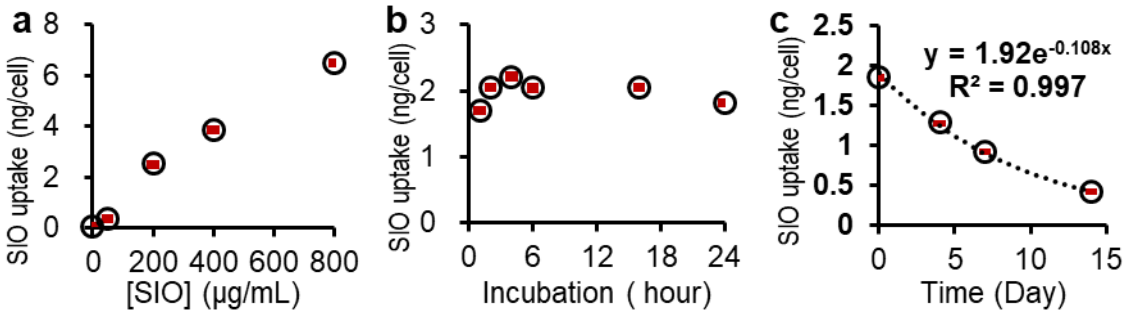

Figure 5.9. Effect of labeling condition and half-life of nanoparticles inside hMSCs. (a) Loaded SIO increased as the incubation concentration of SIO increased. Error bars are standard deviations of six measurements. (b) The incubation time changed the amount of loaded SIO slightly, with a peak at 4 hours. Error bars are standard deviations of six measurements. (c) Loaded SIO decreased as time went, which is likely due to the division of cells. According to the exponential fitting curve, the half-life of SIO in hMSCs was around 6.7 days. Error bars are standard deviations of three replicates.

Cell uptake of SIO was confirmed with transmission and fluorescence microscopy, iron staining, TEM image, and flow cytometry. Most of bright SIO in the transmitted image colocalized with the cells; fluorescence microscopy confirmed the nuclei (blue) and SIO (green) as shown in **Figure 5.10a**. Iron staining studies also showed the colocalization of iron (blue) and cells (pink) in the SIO-labeled cells; while there is no iron in the unlabeled cells (**Figure 5.10b**). TEM image indicates that the SIO were taken up by hMSCs *via* phagocytosis and the SIO maintained their shape (**Figure 5.10c**).[404] Flow cytometry analysis showed that approximately 93% out of 10,000 cells were labeled with SIO after 4 hours of incubation (**Figure 5.10d**).

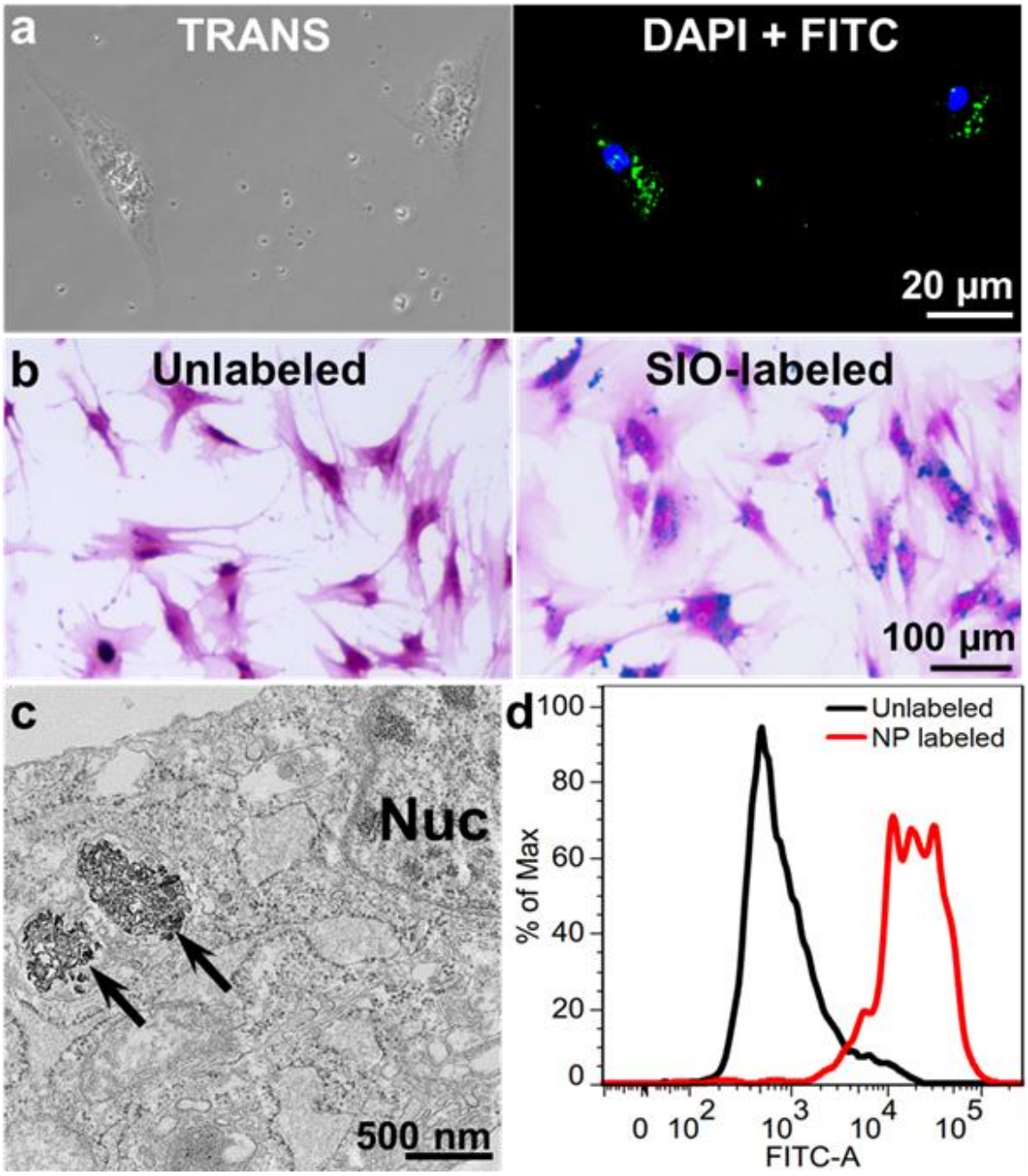

Figure 5.10. SIO enter and label hMSCs. (a) Photomicrographs of SIO-labeled hMSCs show the presence of FITC-conjugated SIO (green) together with hMSC. Blue indicates the hMSC nuclei. (b) Microscope images show unlabeled and SIO-labeled hMSCs stained with potassium ferrocyanide and pararosaniline solutions (iron staining kit from Sigma Aldrich). Blue, pink, and red indicate the presence of iron, cytoplasm, and nuclei respectively. (c) Sectioning TEM image of SIO-labeled hMSC indicates the presence of SIO in cytoplasm. (d) Flow cytometry shows more than 92.5% of hMSCs were labeled with FITC-conjugated SIO (red solid line).

3.3. Biocompatibility of SIO

We next measured the impact of SIO-labeling on hMSCs. A Resazurin assay showed the cell metabolism were 85.3% (p=0.00041) and 98.5% (p=0.65) of unlabeled cells when the SIO-labeling concentration was 2 and 1 mg/ml SIO, respectively (**Figure 5.11a**). This indicates the excellent biocompatibility of the SIO. Cell counting experiments showed that the SIO did not inhibit the proliferation of hMSCs—the doubling time for SIO-labeled and unlabeled hMSCs were 3.6 and 3.7 days, respectively (**Figure 5.11b**). The shorter doubling time here than previous was likely due to the different cell batch and passage numbers. A calcein/ethidium homodimer III live/dead assay showed only 0.4% cell death after SIO-labeling which was negligible compared to the cell death of unlabeled cells, which is 0.2% (**Figure 5.11c**).

The impact of SIO-labeling on phenotypes (CD73, CD90, and CD105)[309] were studied with flow cytometry (**Figure 5.11d**). 30,000 and 10,000 events were run for SIO-labeled and unlabeled hMSCs, and over 4,500 cells were analyzed for all the samples. We gated the fluorescence signals with unlabeled cells, and the gate was set where 99% of unlabeled cells treated with antibodies were included. Results showed that 95.8%, 95.8%, and 97.3% of the SIO-labeled hMSCs maintained the CD73, CD90, and CD105 phenotypes.

SIO-labeled hMSCs retained their multipotency. Unlabeled and SIO-labeled hMSCs treated with adipogenic induction media were both stained red with Oil Red O, which indicates the presence of fatty lipid deposits in both cells. Also, both cells treated with osteogenic induction media were stained black by von-Kossa staining indicating the presence of calcium deposits (**Figure 5.11e**). Therefore, we could conclude that the SIO-

labeling did not affect the adipogenic and osteogenic differentiation capacities of hMSCs.

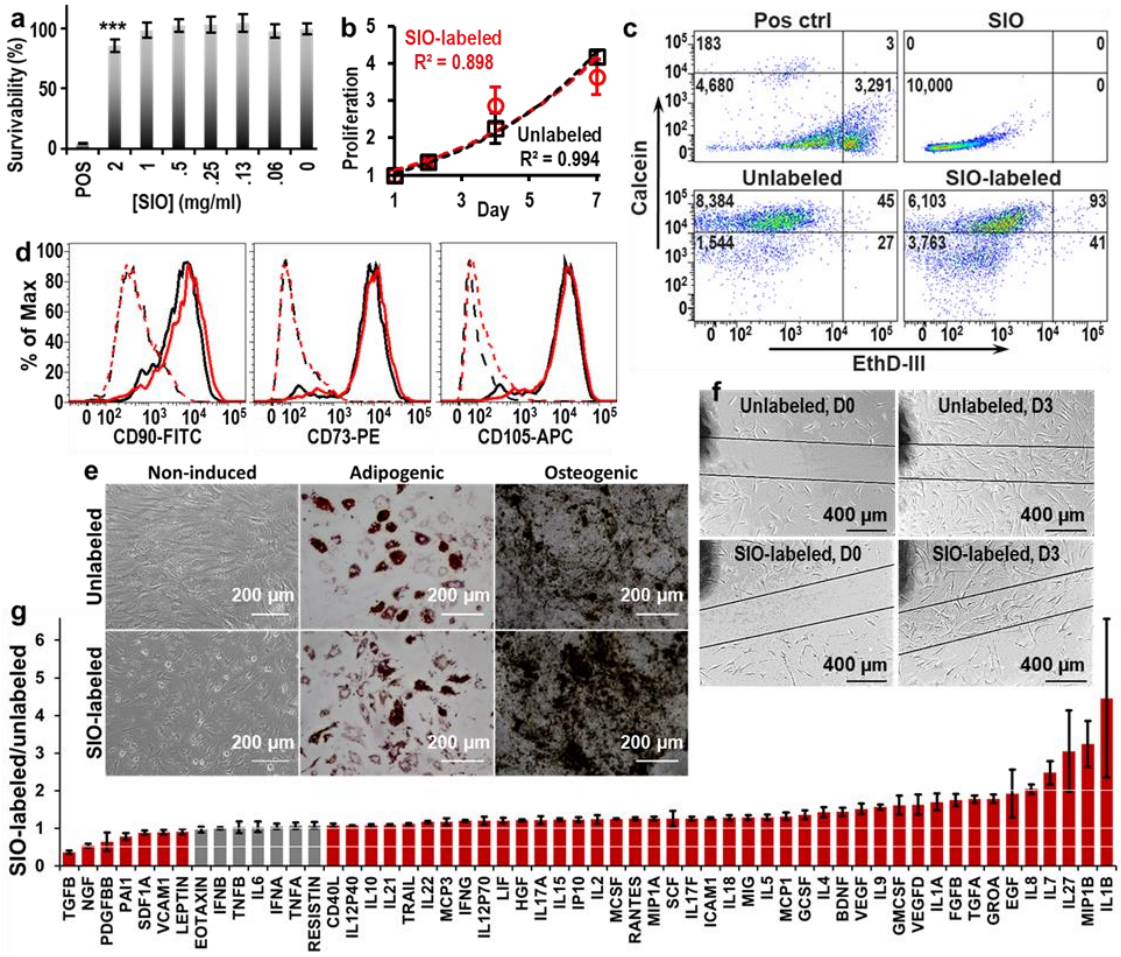

Figure 5.11. Biocompatibility of SIO. (a) A Resazurin assay showed no significant decrease in cell viability at SIO concentrations below 1 mg/ml. Error bars are standard deviations of 6 replicates. *** $p < 0.0005$. (b) The exponentially-fitting curves for proliferation of SIO-labeled and unlabeled hMSCs are similar, and the doubling time for SIO-labeled and unlabeled hMSCs were 3.6 and 3.7 days. Error bars are standard deviations of 8 replicates. (c) Calcein/ethidium homodimer III live/dead assay shows only 0.4% of cells died after labeled with SIO. (d) Flow cytometry showed SIO-labeled hMSCs maintained the phenotypes—CD73, CD90, and CD105. Black and red lines are unlabeled and SIO-labeled hMSCs, respectively. Dashed lines are isotype control with isotype mouse IgG; solid lines are hMSCs stained with specific binding antibodies. (e) SIO-labeled hMSCs maintained their adipogenic and osteogenic differentiation ability. (f) SIO-labeled hMSCs showed normal migration. (g) Fold change of cytokines secreted by SIO-labeled and unlabeled hMSCs. SIO-labeled hMSCs secreted more than 200% of IL1B, IL27, IL7, IL8, and MIP1B and less than 50% of TGFB than unlabeled ones. Grey bars indicate a statistically non-significant ($P > 0.05$) change in expression; red bars indicate significance ($P < 0.05$), two-tailed homoscedastic test. Error bars are standard deviation of four replicates.

The SIO-labeled cells could still move as seen in a migration assay (**Figure 5.11f**). For the unlabeled hMSCs, the cell density in the scratched area on day 3 was approximately 9290 cells/cm^2, which was 147% of the initial cell density in the unscratched area. For the SIO-labeled hMSCs, the cell density in the gap on day 3 was approximately 8871 cells/cm^2 or 143% of the initial cell density in the unscratched area. This result indicated that the SIO-labeling did not inhibit cell migration.

Although SIO-labeling showed no negative impact on metabolism, viability, proliferation, differentiation, phenotypes, and migration ability, it did affect the concentration of multiple cytokines in cell media. Secretome analysis showed a general increase in levels of cytokines with the addition of SIO. Noticeably, 50 out of 56 detected cytokines showed a change less than 1-fold upon the addition of SIO (**Figure 5.11g**). SIO-labeled hMSCs secreted 3.79-fold of IL1B, 2.93-fold of IL27, 2.47-fold of IL7, 2.04-fold of IL8, and 3.18-fold of MIP1B compared to unlabeled ones, and the changes are significant ($p < 0.05$ when two-tailed homoscedastic t-test were used). The addition of SIO led to significant decrease in TGFB secretion (0.36-fold of TGFB secreted by unlabeled hMSCs, $p < 0.05$ with two-tailed homoscedastic t-test) (**Figure 5.11g**).

3.4. Functions of SIO—imaging, sustained release, and cell directing

The *in situ* SPIO-conjugation increased the nanoparticles' colloidal stability, zeta-potential, and saturation magnetization. These properties enable SIO to increase the efficacy of stem cell therapy through triple-functions: enhancement of ultrasound and MRI contrast of cells, sustained release of pro-survival agents to increase cell viability, and magnetic-assisted manipulation of cells to improve retention.

First, SIO have high ultrasound and MRI contrast compared to soft tissues, which

allows guided real-time injection through ultrasound imaging and tracking of SIO-labeled cells *via* MRI.[171, 405] We evaluated the T2-based MRI signal of SIO with spin echo imaging. The LOD of SIO with T2-weighted MRI (7T) was 43.7 μg/mL. The relaxivity per Fe was 32 ±8.8 $mM^{-1}s^{-1}$ similar to commercial agents.[406] *In vivo* MRI also showed a high contrast between SIO and myocardium (**Figure 5.12**). The ultrasound signal of SIO was tested with a 40-MHz transducer, and the LOD was 22.6 μg/mL (**Figure 5.13**). We then labeled hMSCs with SIO and scanned with MRI and ultrasound imaging. SIO increased both MRI and ultrasound contrast of hMSCs (**Figure 5.14a**) and could be used to count cells (**Figure 5.15**) down to 20 cells/μL *via* MRI and 152 cells/μL *via* ultrasound imaging. Therefore, the T2 weighted MRI can exhibit excellent sensitivity for cell tracking that complements the excellent temporal resolution of ultrasound.[407]

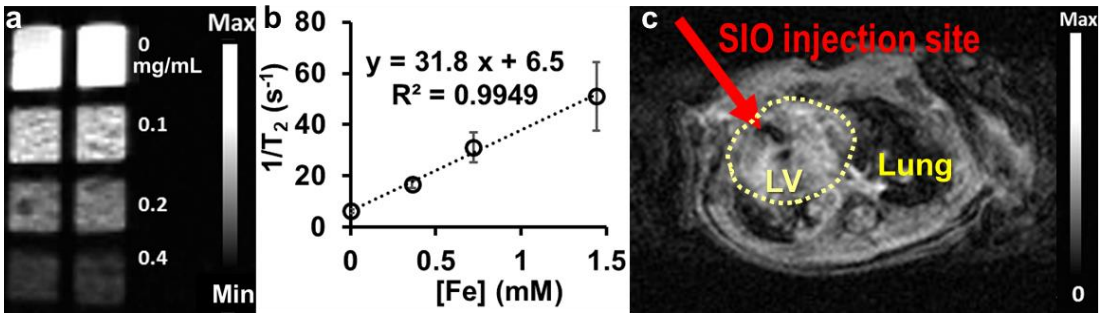

Figure 5.12. MRI contrast of SIO. (a) MRI of SIO in agarose phantom with different concentrations. Two columns are two replicates. The scan was performed with repetition time 5,000 ms and echo time 12.6 ms at 4.7 T. (b) Relaxivity of SIO per Fe was found to be 31.8 $mM^{-1}s^{-1}$. Error bars are standard deviations of two SIO batches. (c) *In vivo* MRI image showed a high MRI contrast of SIO against myocardium.

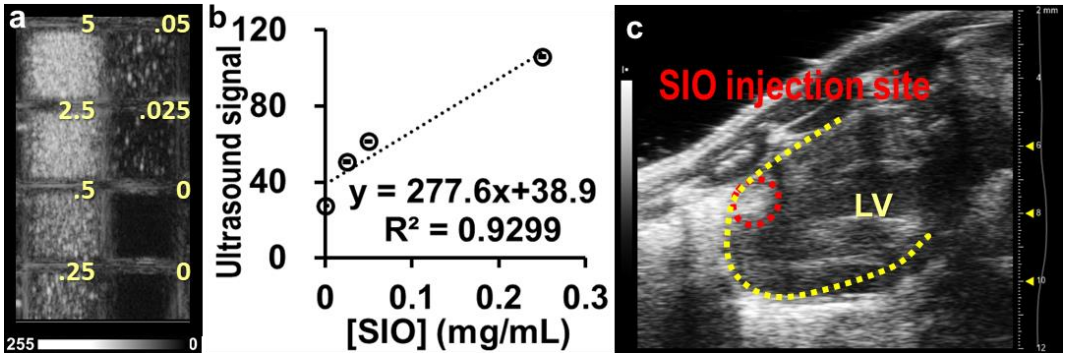

Figure 5.13. Ultrasound contrast of SIO. (a) Ultrasound image of SIO in agarose phantom with different concentrations from 0 to 5 mg/mL. The scan was performed a linear transducer (MS550, VisualSonics) with 40 MHz. (b) Relationship between ultrasound signal and SIO concentration. Error bars are standard deviations of five fields-of-view. (c) *In vivo* ultrasound images showed the contrast of SIO against myocardium.

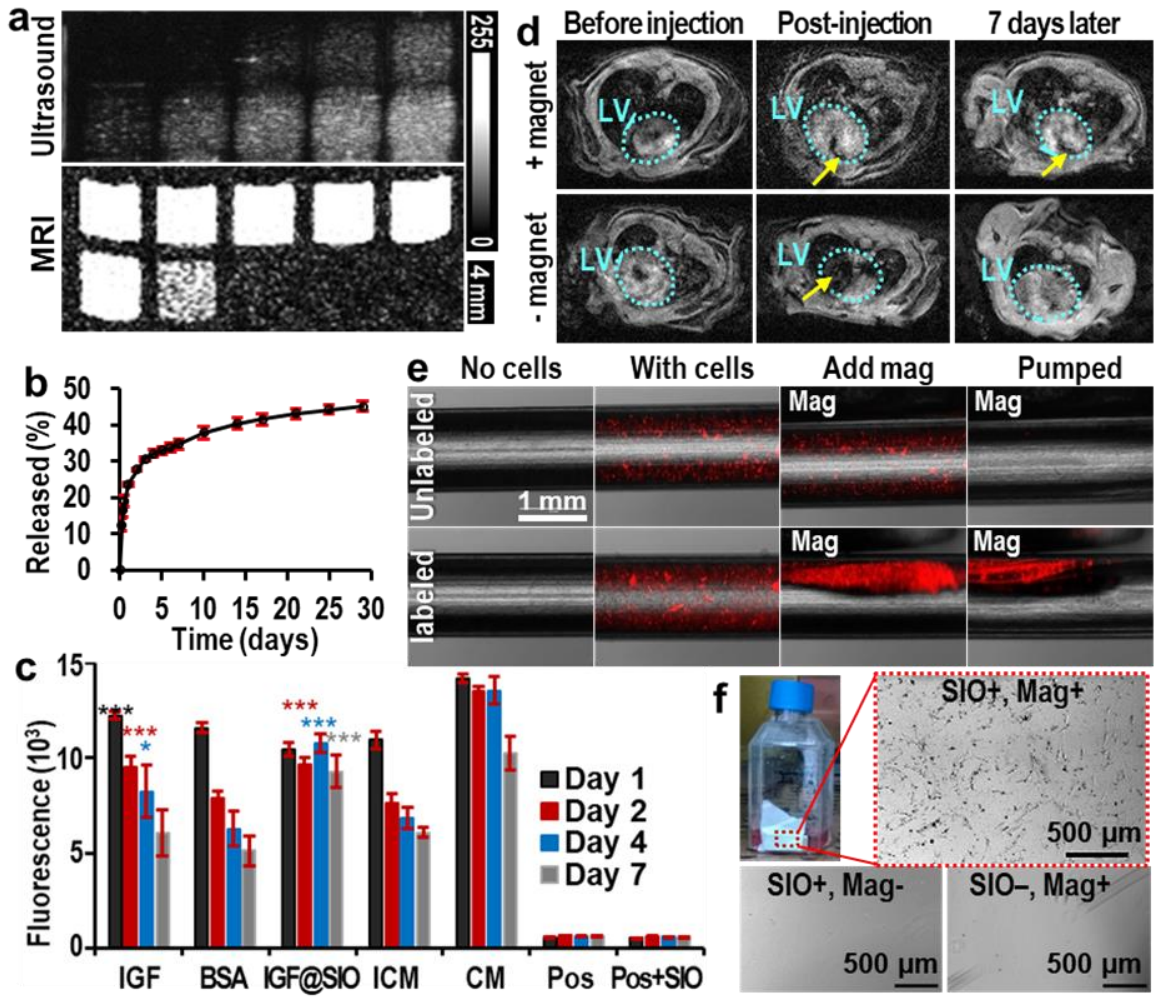

Figure 5.14. Multi-functions of SIO. (a) Ultrasound and T2-weighted MR images of unlabeled (top row, the cell numbers were 0k, 10k, 50k, 150k, and 300k from left to right) and SIO-labeled hMSCs (bottom row, the cell numbers were 10k, 50k, 150k, 300k, and 600k from left to right). These images show the enhancement of both MRI and ultrasound signals of hMSCs after SIO-labeling. MRI was done with a repetition time of 1,400 ms and an echo time of 15 ms at 4.7 T. (b) Cumulative release profile of IGF from SIO. Error bars are standard deviations of triplicates. (c) *In vitro* survival of hMSCs treated with free IGF, free BSA, IGF-loaded SIO (IGF@SIO), incomplete media (ICM), and complete media (CM). No cells and nanoparticles (NP) only groups are control groups with only incomplete media or media containing nanoparticles. Error bars are standard deviations of six replicates. The asterisks show the p-value compared to incomplete media group. * $p < 0.05$, *** $p < 0.0005$. (d) MRI shows the long-term retention of SIO in the left ventricle wall only with presence of magnet. Azure dotted circles show the outlines of left ventricles. Yellow arrows indicate the locations of SIO. (e) Overlay of fluorescence and microscope images show that SIO and magnet could improve the retention of hMSCs in laminar flow with a shear stress at 27 dyne/cm^2. Both cells were stained with fluorescent quantum dots for visualization. (f) Suspended SIO-labeled hMSCs could be directed by an external magnet to the side wall of flask. These attracted cells could adhere to and grow on the side wall. In contrast, no cells would grow on the same location without SIO-labeling or without a magnet.

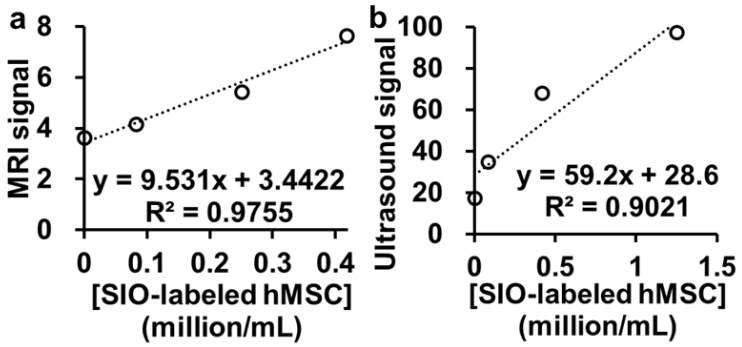

Figure 5.15. MRI and US signal of SIO-labeled hMSCs. (a) MRI signals of SIO-labeled hMSCs in agarose phantom was linearly dependent on cell concentrations. (b) Relationship between ultrasound signals and concentration of SIO-labeled hMSCs in agarose phantom.

The second function of SIO was drug delivery to enhance cell survival.[389, 408] **Figure 5.16** shows that the SIO made with *in situ* growth method kept the high loading capacity of MCF. The loading cargo was a protein—insulin-like growth factor (IGF, 7.6 kDa)—a pro-survival agent that can improve cell viability.[114] The IGF loading capacity of SIO was 7.36 mg/g, and the loading efficiency was over 98% when the IGF-to-nanoparticle mass ratio was 0.0075. The IGF loading capacity of SIO was only 1.2% lower than that of MCF (7.45 mg/g). Both nanoparticles had a similar linear dependence relationship between the loading capacity and IGF-to-nanoparticles ratio (**Figure 5.16**).

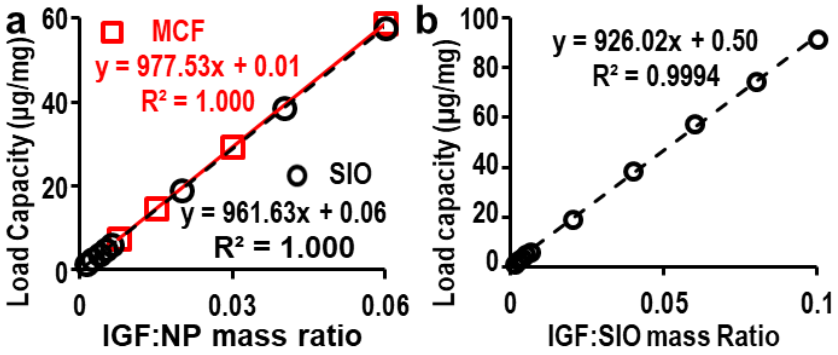

Figure 5.16. Loading capacity of the MCF and SIO. (a) The loading capacities of both the MCF and SIO showed a linear dependence on the mass ratio of IGF:nanoparticles. The loading capacity between these two nanoparticles were similar. (b) Loading capacities of SIO showed a linear dependence on the mass ratio of IGF:nanoparticles within 0 - 0.1.

Moreover, SIO demonstrated better sustained IGF-release ability than MCF. We were unable to detect any release from IGF-loaded MCF within one week *via* a bicinchoninic acid (BCA) assay (**Figure 5.17**). To confirm that we had loaded IGF in the first place, we mixed IGF-loaded MCF with the BCA solution and saw a high concentration of protein. We therefore concluded that MCF was unable to release IGF at detectable concentrations. This is likely due to strong electrostatic forces between the negatively-charged MCF (-10 mV) and positively-charged IGF at neutral pH.[409] On the other hand, SIO were positively-charged (29 mV). We found that IGF-loaded SIO showed sustained release of IGF over one month (**Figure 5.14b**): 23.7%, 34.8%, and 45.1% of the loaded IGF was released on days 1, 7, and 29, respectively.

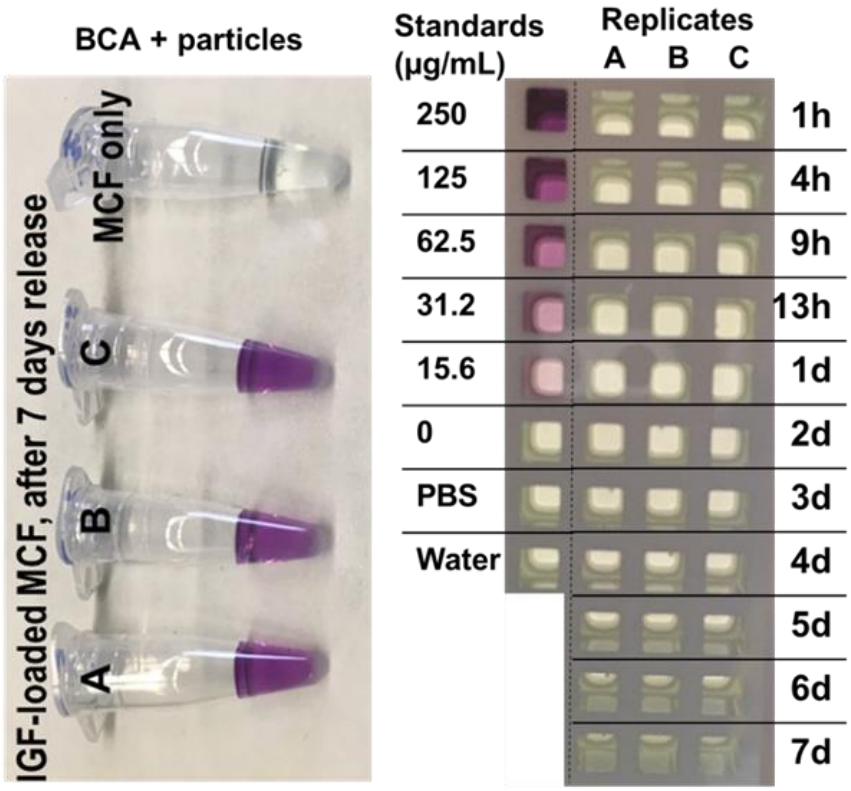

Figure 5.17. No IGF release from IGF-loaded MCF. The BCA assay produces a purple color in the presence of protein. No IGF release was seen from MCF. After one week of incubation, the IGF-loaded MCF turned when stained with the BCA agent (Left), however, no IGF was detected in the release media.

In vitro cell survival assays suggested the released IGF from SIO were still functional as pro-survival agents. hMSCs were treated with IGF-loaded SIO, free IGF, free bovine serum albumin (BSA), incomplete media without FBS (positive control), and complete media (negative control) for one week. To mimic cell transplantation, the cell media were not replaced with fresh media once cells were plated. The comparison between IGF and BSA groups indicated that IGF is a pro-survival agent for hMSCs.[114] Free IGF significantly increased the viability of hMSCs on days 1-4, but not on day 7 (**Figure 5.14c**). IGF-loaded SIO significantly increased the cell viability by 26%, 57%, and 53% on days 2, 4, and 7 *versus* incomplete media underscoring the importance of sustained release. Furthermore, the viability of hMSCs treated with IGF-loaded SIO showed no significant ($p = 0.09$) decrease compared to complete media on day 7 suggesting that the sustained release of IGF from SIO increased the long-term survival of hMSCs.

The third function of SIO was to increase cell retention by magnet-manipulation. We first investigated the retention of SIO with a magnet. First, an *in vitro* retention study showed that SIO stayed in static tissue mimics—0.5% agarose gel[410] attracted by a magnetic field (**Figure 5.18**). An *in vivo* study showed a significantly ($p=0.036$, one-pair, type two t-test) higher SIO retention in the left ventricle wall of mice with magnet after 7 days. Approximately 15% of the SIO were detected in the hearts of mice with magnet ($n=9$), while no SIO were detected in those without magnet ($n=8$). The magnet was embedded in a jacket held close to the apex of mouse as shown in **Figure 5.19**. Seven days after injection, SIO were still visible in the left ventricle by *in vivo* MRI when a mouse was wearing a jacket with an external magnet while most SIO were gone on day 7 compared to post-injection when a mouse was wearing a jacket without magnet (**Figure 5.14d**). These

results suggested that SIO in the rodent myocardium could still be retained by an external magnet.

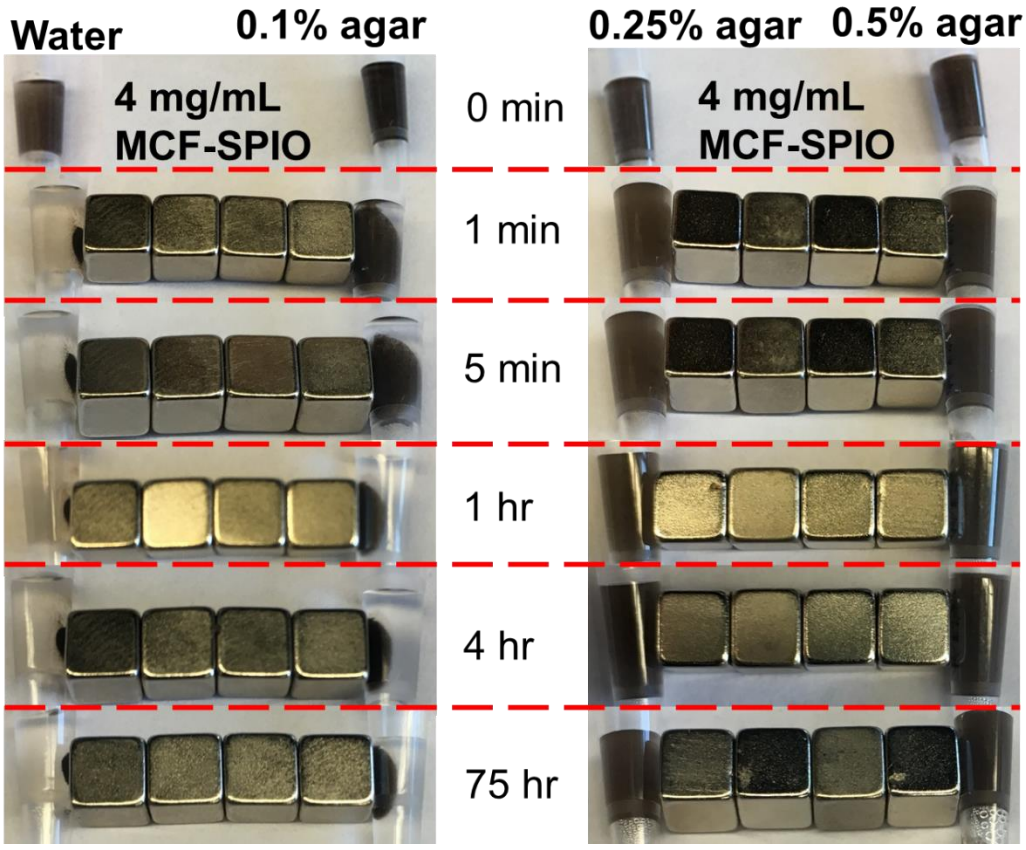

Figure 5.18. Demonstration of SIO retention in mimicking tissues. The maximum pull force of the cubic magnets is about 10 newtons. Almost all the nanoparticles were pulled out from water within one minute and from 0.1% agarose within 1 hour. However, the retention of 0.25% and 0.5% agarose is strong, and the nanoparticles cannot be pulled out by these magnets. The 0.5% agarose gel has a similar mechanical properties as soft tissues.[410]

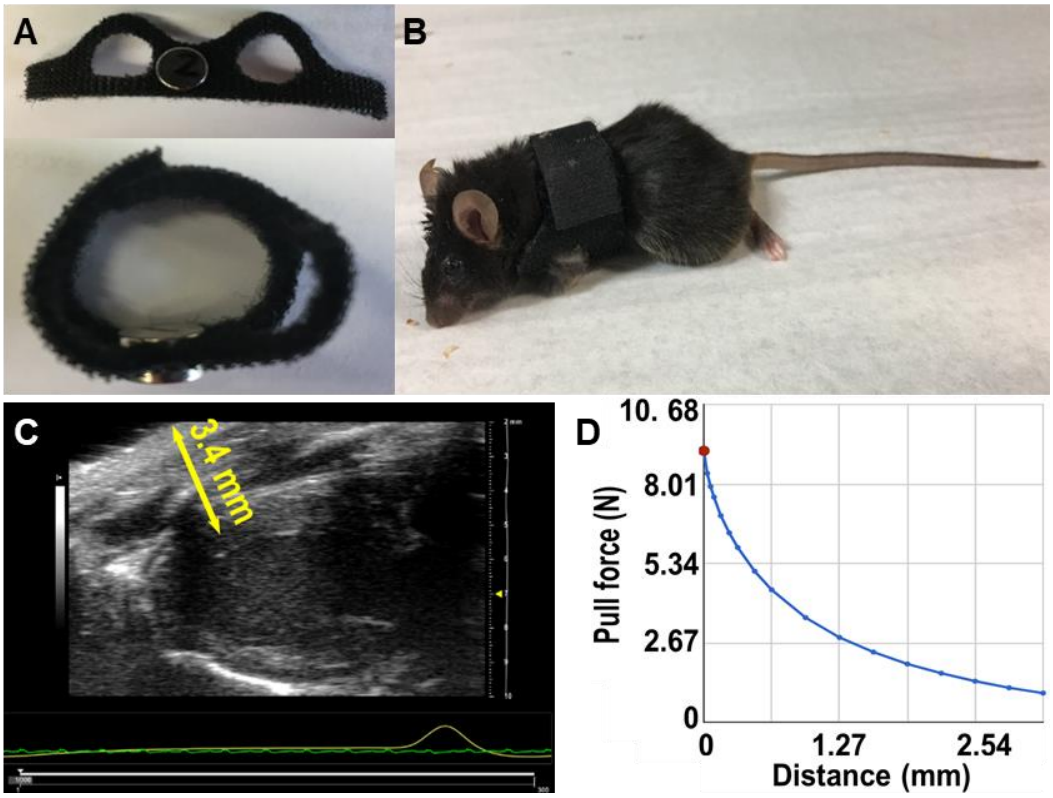

Figure 5.19. *In vivo* study of SIO retention at mouse heart apex by external magnet harness. (a) Design of the magnetic harness. Total weight of each harness is controlled within 10% of the mouse body weight. (b) Mouse wearing a magnetic harness. (c) Ultrasound image indicates the distance between the magnet and apex is approximately 3.4 mm. (d) The pull force of the magnet as a function of distance (adopted from K&J Magnetics).

Next, we studied the effect of SIO-labeling on cell retention by a magnet. The magnet-enhanced retention of SIO also increased the retention of SIO-labeled hMSCs. The retention of SIO-labeled hMSCs was 58.14% when the shear stress was 27 dyne/cm^2 (**Figure 5.14e**), which is higher than the mean wall shear stress of left ventricle of both mice and humans.[411] However, all unlabeled hMSCs were removed under the same conditions. We also quantitated the retention of cells *versus* shear stress from 7 to 35 dyne/cm^2 and found that the retention of SIO-labeled hMSCs decreased as the shear stress increased (**Figure 5.20**). The cell retention was approximately 85% when the shear stress was 12.8 dyne/cm^2, which is the mean wall shear stress in the human left ventricle.[412]

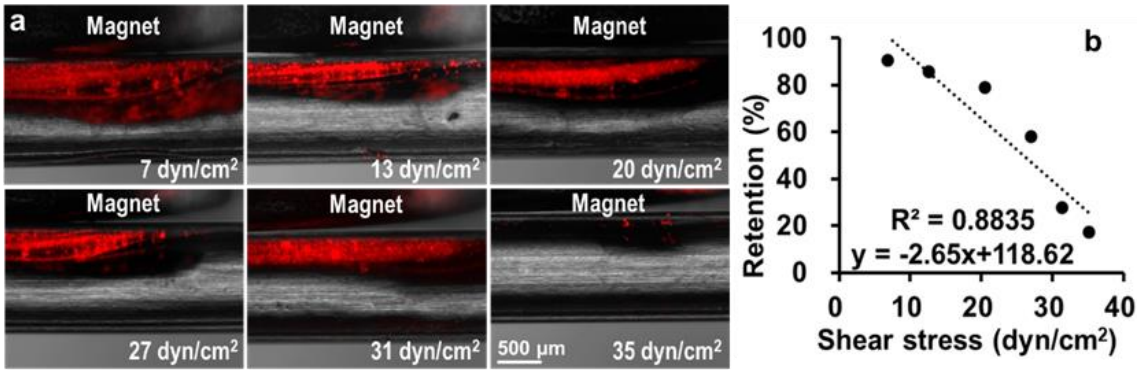

Figure 5.20. Retention of SIO-labeled hMSCs versus shear stress. (a) Overlay of fluorescence and microscope images show the retention of SIO-labeled hMSCs with the presence of magnet in laminar flow with a range of shear stress 7 - 35 dyn/cm^2. The mean wall shear stress in left ventricle of human is 12.8 dyn/cm^2.[412] Cells were stained with fluorescent quantum dots for visualization. (b) Retention of SIO-labeled hMSCs was dependent on the shear stress.

Further studies showed that suspended SIO-labeled hMSCs could overcome gravity and be attracted by an external magnet to the flask side wall. These attracted cells could adhere to and grow on the side wall. The cells density of SIO-labeled hMSCs with an external magnet was approximately 5,850 cells/cm^2; otherwise, the cell densities were 0 cells/cm^2 (**Figure 5.14f**). After being attracted and adhered to the side wall, the SIO-labeled hMSCs could continue growing on the side wall without the magnet (**Figure 5.21**).

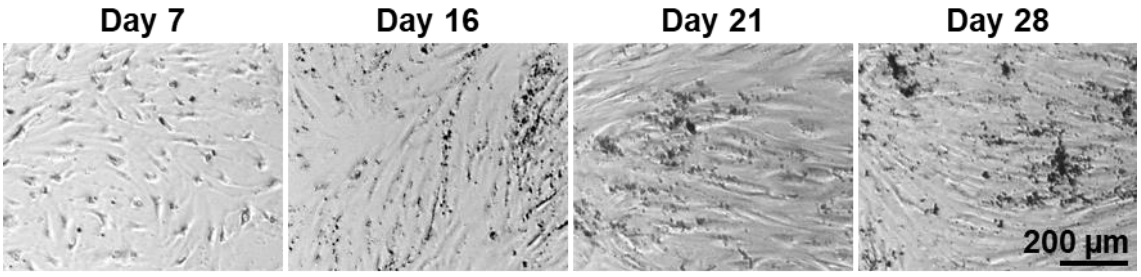

Figure 5.21. Growth of SIO-labeled hMSCs on the side wall of a flask. The SIO-labeled cells were attracted by an external magnet and started to adhere on the side wall of flask on the first day. The cells continued growing after removal of the magnet.

3.5. SIO-labeled hMSCs improve left ventricular function

In vivo experiments used the murine ischemia/reperfusion model in four groups: healthy control, negative control (no treatment), hMSC treatment, and IGF-loaded SIO-labeled hMSC treatment. The study timeline is shown in **Figure 5.22a**. Animals from the latter three groups received a 60-minute ischemia by left anterior descending (LAD) coronary artery ligation followed by intramyocardial injection with 20 μL media, 0.1 million hMSCs, or 0.1 million IGF-loaded SIO-labeled hMSCs and followed by reperfusion. Echocardiography[413] was used to evaluate the cardiac function on days 7, 30, and 60 after the surgery.

The treatment with stem cells were confirmed with immunofluorescence images. Only animals treated with stem cells, both unlabeled and SIO-labeled, showed the presence of CD73-PE, CD90-FITC, and CD105-APC (**Figure 5.22b**) in their left ventricles. In addition, iron staining, *ex vivo* MRI, and H&E staining showed that SIO only presented in the hearts from SIO-labeled hMSCs (**Figure 5.22 c, d**). Moreover, the intramyocardially injection of hMSCs and SIO-labeled hMSCs did not change the pathology of other organs and showed no toxicity (**Figure 5.23**).

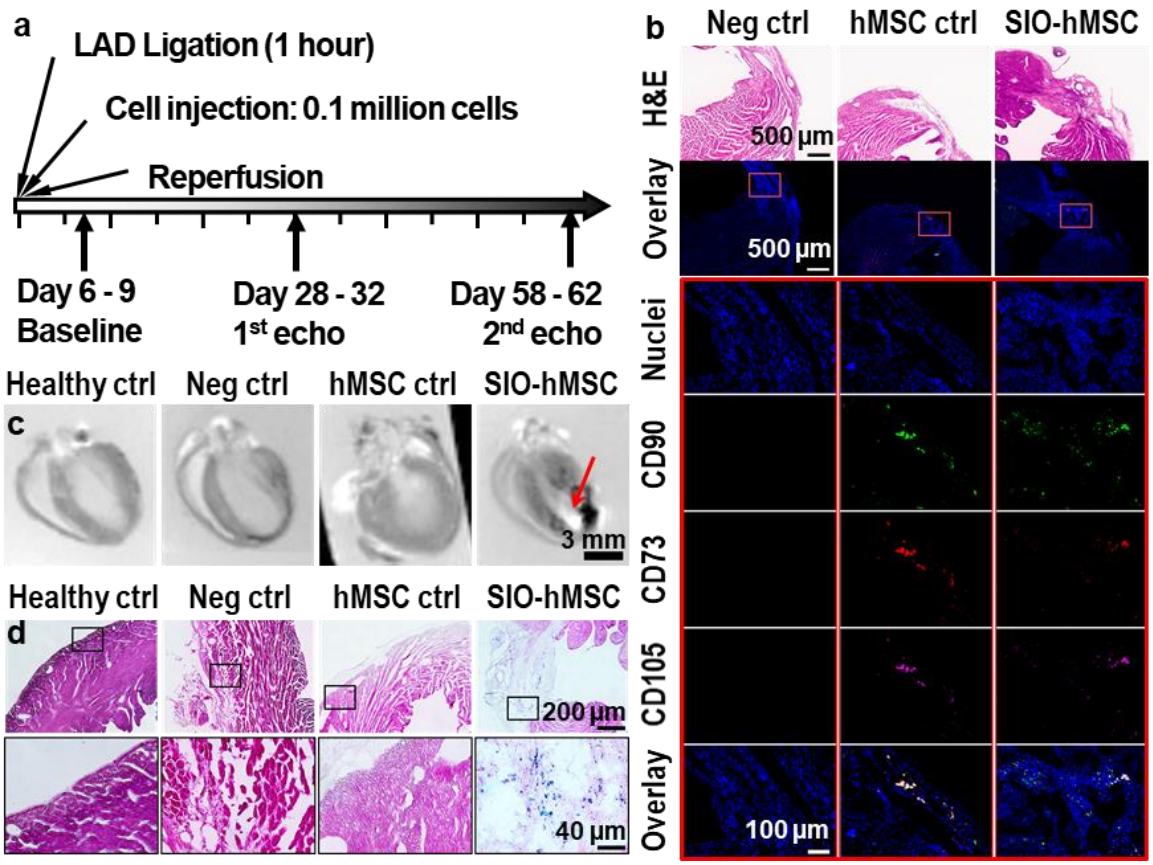

Figure 5.22. Timeline and confirmation of treatments in myocardium after 60 days. (a) Timeline for surgery, treatment, and echocardiograph. Hearts were collected and sliced more than 60 days after injection of hMSCs. (b) H&E staining (first row) and immunofluorescence (second row) images of heart slice from injured groups. The third to seventh rows show higher magnification images of the outlined regions (highlighted with red rectangles) from the second row. The results indicated the presence of hMSCs' phenotypes CD73, CD90, and CD105 in heart slices from both hMSC control and IGF-loaded SIO-labeled hMSCs. (c) *Ex vivo* MRI showed the presence of SIO (pointed by red arrow) only in the IGF-loaded SIO-labeled hMSCs treatment group. (d) Iron staining of heart slices from each group. Iron was stained blue, myocardium cells were stained dark pink, and fibrosis was stained light pink. The result shows the presence of iron only in IGF-loaded SIO-labeled hMSCs treatment group.

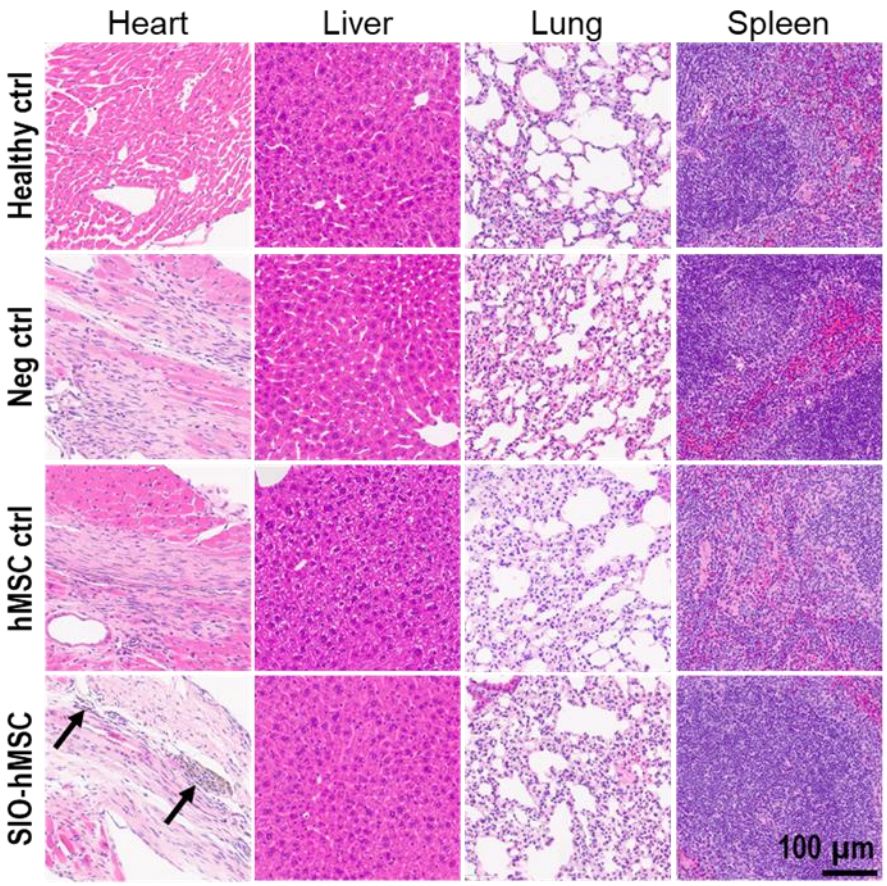

Figure 5.23. H&E staining of organs from four groups. Arrows point at brown segments which indicate the presence of SIO. No observable differences were found in liver, lung, and spleen among the four groups.

Echocardiography showed that unlabeled hMSCs decreased heart function on day 60 compared to the baseline. The hMSC control group had a decrease (-15%) in the mean LVEF on day 60 (**Figure 5.24a**); and the mean change in LVEF of hMSC control group were -17% on day 60 and nonsignificant compared to the negative control group (**Figure 5.24b**). This outcome is inconsistent with other reports, however, inconsistent outcome of stem cell therapy in treating myocardial infarction is common in the pre-clinical and clinical trials.[386] The inconsistency in outcomes with MSCs between studies may be due to the cell dosage, routes of administration, donor variance, culture expansion, and

immunogenicity.[414, 415] For example, most reported clinical trials with allogenic MSCs caused no significant changes in the LVEF while most autologous MSCs increased the LVEF.[416]

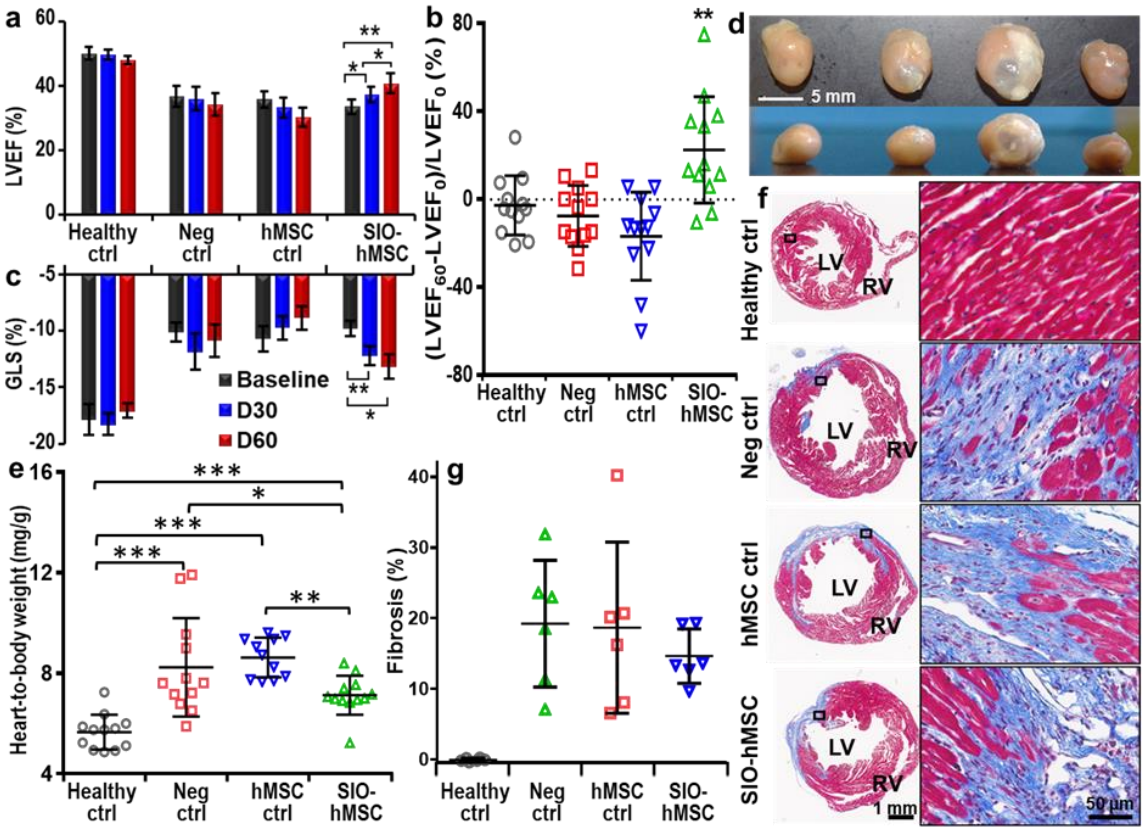

Figure 5.24. SIO-labeled hMSCs improved heart functions and decreased cardiomegaly. (a) Comparison of mean LVEF among four groups (n=12) from baseline, day 30, and day 60. IGF-loaded SIO-labeled hMSCs significantly increased LVEF and absolute value of GLS on both day 30 and 60 compared to the baseline. Error bars are standard errors (n=12). * $p < 0.05$, ** $p < 0.005$. (b) Change of LVEF on day 60 from baseline for individual subjects. Error bars are standard deviations (n=12). ** $p < 0.005$ (two-tail and type two t-test was used). (c) Mean global longitudinal strain (GLS) of each group (n=12) from baseline, day 30, and day 60. (d) Photos show frontal view (top row) and transverse view (bottom row) of a representative heart from each group. (e) Mean heart-to-body weight ratio of each group. Error bars are standard errors (n=11 for hMSC ctrl group and 12 for the other three groups). * $p < 0.05$, ** $p < 0.005$, *** $p < 0.0005$. (f) Representative heart slices stained with trichrome staining from each group. Blue indicates fibrosis and red indicates myocardium. RV: right ventricle. (g) Quantitative analysis for fibrosis. Error bars are standard deviations for six animals.

On the other hand, IGF-loaded SIO-labeled hMSCs significantly improved the heart functions of mice with ischemia-reperfusion injuries. First, IGF-loaded SIO-labeled hMSC injection significantly improved the left ventricular ejection fraction (LVEF) of diseased mice (**Figure 5.24a**). There were no significant differences between baseline LVEF among the diseased groups, which suggested the injuries were created equally. The increases in mean LVEF were 11% and 21% on days 30 and 60, respectively. Changes in LVEF from baseline for individual animals in each group were also analyzed. Only 2 of 12 animals from the IGF-loaded SIO-labeled hMSC treatment group had a decrease in LVEF on day 60 compared to day 30, but this occurred in 6 of the 12 animals for the other three groups (**Figure 5.25**). The mean change in LVEF of labeled hMSCs treatment group on day 60 were 22%, which increased significantly compared to the negative control group.

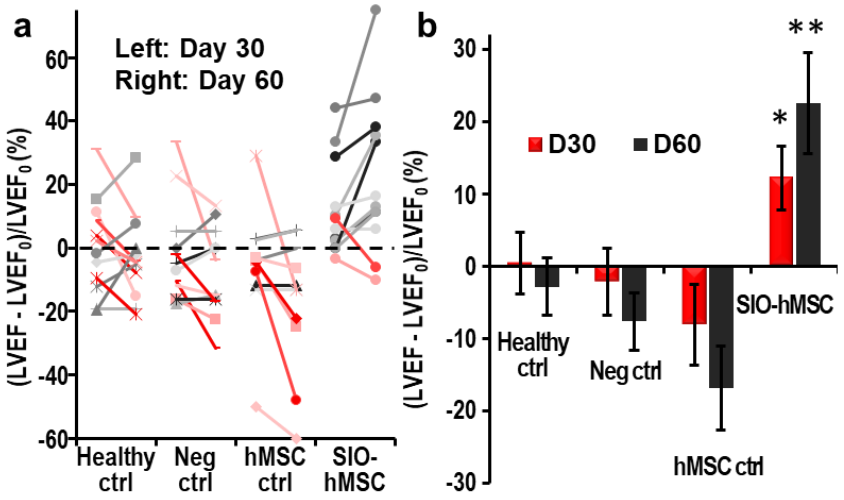

Figure 5.25. Change of LVEF for individual animals. (a) Change in LVEF from baseline for individual subjects (n=12 for all four groups). Grey and red indicates the increase and decrease of ΔLVEF on day 60 compared to day 30. (b) Mean change in LVEF of each group show that the IGF-loaded SIO-labeled hMSC had significantly improved heart function compared to the other groups on both day 30 and 60. The asterisks showed the significance in change compared to negative control group. Error bars are standard errors (n=12). * $p < 0.05$, ** $p < 0.005$ (two-tail and type two t-test was used).

IGF-loaded SIO-labeled hMSCs also significantly increased the global longitudinal strain (GLS)—an index of left ventricular (LV) systolic dysfunction.[417] There were no significant differences between baseline GLS among the diseased groups. The increase in GLS on day 30 and 60 was 24% and 34% compared to the baseline (**Figure 5.24c**). We also analyzed radial strain by dividing LV myocardium to 49 nodes (**Figure 5.26**). Animals treated with IGF-loaded SIO-labeled hMSCs had an increased average radial strain in the nodes close to the apex on day 60 compared to day 30.

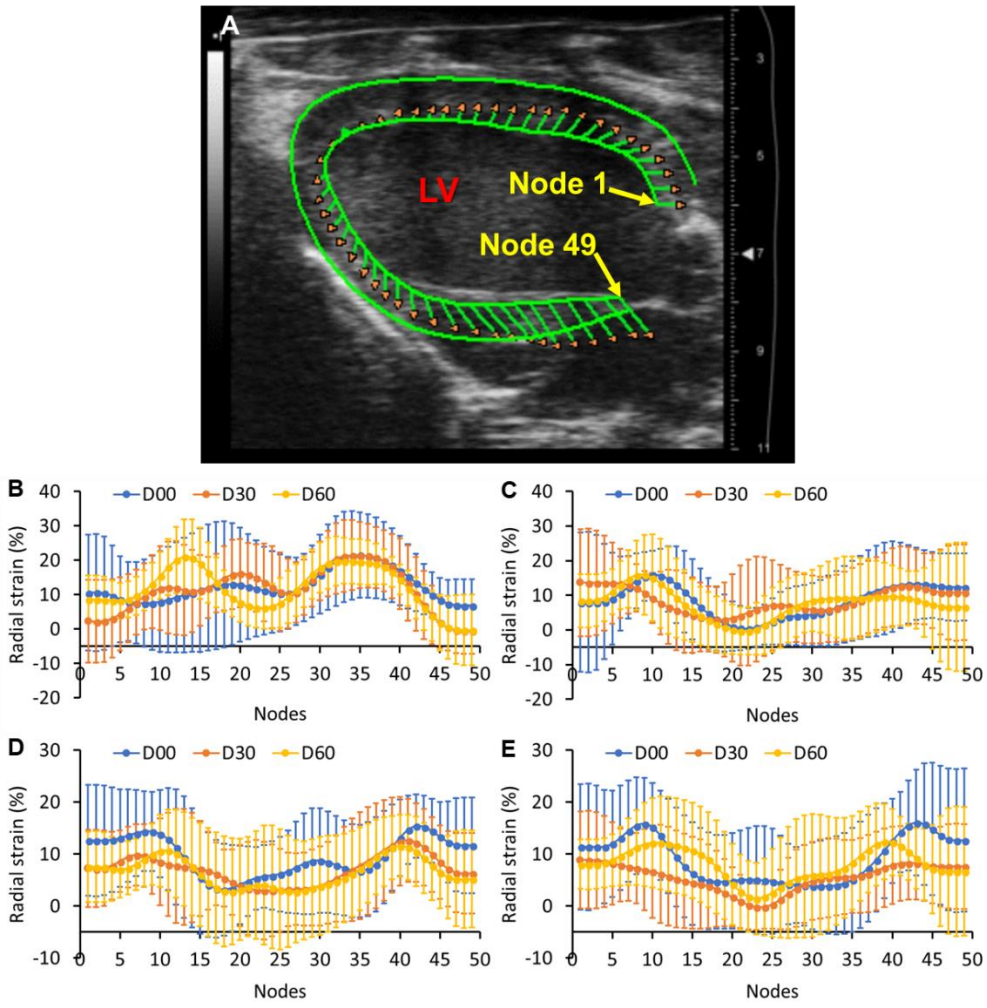

Figure 5.26. Radial strain analysis. (a) Schemes of the 49 nodes on the LV myocardium. Average radial strain of each node for (b) healthy control group, (c) negative control group, (d) hMSC control group, and (e) IGF-loaded SIO-labeled hMSC treatment group. Error bars are standard deviations (n = 12).

To further confirm this improvement, we studied the cardiomegaly by measuring the heart-to-body weight ratio and the pathological changes in the hearts. IGF-loaded SIO-labeled hMSCs transplantation diminished cardiomegaly. The average heart-to-body weight ratio of healthy control, negative control, hMSC control, and IGF-loaded SIO-labeled hMSCs treatment groups were 5.7±0.7, 8.2±2.0, 8.6±0.8, and 7.1±0.8 mg/g, respectively (n=12 for all groups) (**Figure 5.24d&e**). IGF-loaded SIO-labeled hMSCs transplantation decreased the cardiomegaly by 43% ($p = 0.041$) compared to the negative control group.

Heart slices were stained with trichrome staining for fibrosis analysis. **Figure 5.24f** showed a representative heart slice from each group, and fibrosis tissues (blue) were seen from the slices of all diseased groups. We quantified 6 random hearts from each group and each heart was sectioned to 10 μm with every 10th section collected. We analyzed 4 to 13 slices for each group and calculated the percentage of fibrosis with 4 continuous slices that showed a maximum fibrosis and a coefficient of variation less than 15%. The average percentage of fibrosis for negative control, hMSC control, and labeled hMSC treatment groups were 19.2±9.0%, 18.7±12.1%, and 14.6±3.9% (**Figure 5.24g**). Therefore, IGF-loaded SIO increased the efficacy of stem cell therapy in treating ischemia-reperfusion injuries in mice.

Hence, all measurements including echocardiography, heart-to-body weight ratio, and pathological change showed that the IGF-loaded SIO-labeling improved the stem cell treatment efficacy, which indicates the functionality of the SIO. Stem cells may improve the LVEF due to the paracrine factors, recruitment of autologous cells, and decreasing apoptosis of the local cells. Although the IGF-loaded SIO-labeled hMSCs increased the

LVEF, without the hMSCs, the particles alone are unlikely to improve the LVEF because they cannot mediate the local paracrine factors, which has been proved by Roell *et al*.[418]

Hence, another mechanism for this improved stem cell therapy efficacy is likely due to the increased cytokine levels causing by nanoparticles-labeling. We compared the secretome of IGF-loaded SIO-labeled to unlabeled hMSCs. A general increase in levels of cytokines was seen with the addition of IGF-loaded SIO. Many proteins broadly implicated in cardiac regeneration, including vascular endothelial growth factor (VEGF), hepatocyte growth factor (HGF), basic fibroblast growth factor (FGFB), stem cell factor (SCF), and monocyte chemotactic protein-1 (MCP-1) (**Figure 5.27**). IGF-loaded SIO-labeling significantly decreased the secretion of transforming growth factor beta (TGFB) to 22% ($p < 0.05$ when two-tailed homoscedastic t-test were used), which is beneficial because TGFB stops cell cycle and lead to apoptosis.[419] Noticeably, while the SIO alone labeled hMSCs secreted significantly more proinflammtory cytokines than unlabeled hMSCs, the IGF-loading decreased this undesired effect caused by the SIO (**Figure 5.11g** & **Figure 5.27**)

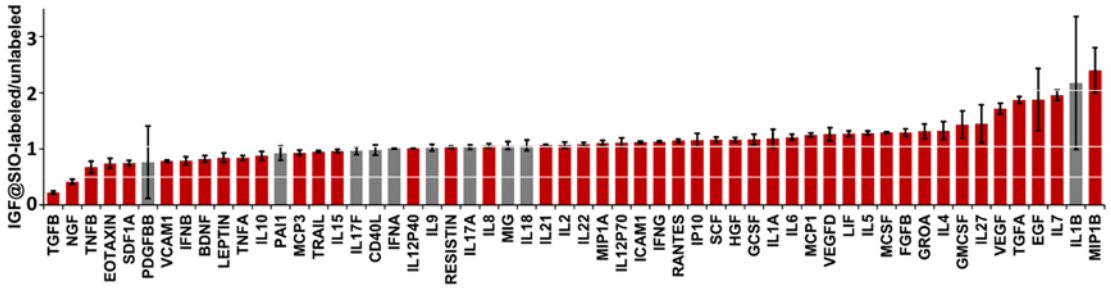

Figure 5.27. Effect of IGF-loaded SIO on secretome of hMSCs. Fold change of cytokines secreted by IGF-loaded SIO-labeled and unlabeled hMSCs. Cytokines secreted by the IGF-loaded SIO-labeled cells were within 1-fold (50% - 200%) of unlabeled cells, except TGFB, NGF, MIP1B, and IL1B. Grey bars indicate a statistically non-significant ($P > 0.05$) change in expression; red bars indicate significance ($P < 0.05$), two-tailed homoscedastic test. Error bars are standard deviation of four replicates.

4. Conclusions

We prepared a superparamagnetic mesocellular foam silica-Fe_3O_4 nanoparticle *via* an *in-situ* growth method. The *in situ* SPIO-conjugation increased the nanoparticles' colloidal stability, zeta-potential, magnetization, and sustained-release profile for IGF. The optimized SIO allowed the enhancement of ultrasound and MRI contrast of cells, sustained release of pro-survival agents to increase cell viability, and magnet-assisted manipulation of cells to improve retention. Moreover, these nanoparticles changed the cytokine levels and improved the efficacy of stem cell therapy. While this structure does not directly report viability, both echocardiography and histology studies showed that SIO-loaded with IGF increased the efficacy of stem cell therapy in treating ischemia-reperfusion injury in mice. This could be improved by studies that correlated an exogenous agent such as the nanoparticles described here *versus* a reporter gene known to report viability.

5. Acknowledgement

The text of Chapter 5, in part, is the reprint of the material as it appears in "Increases Efficacy of Stem Cell Therapy via Triple-functional Inorganic Nanoparticles" by Fang Chen, Eric R. Zhao, Ghanim Hableel, Tao Hu, Taeho Kim, Jingting Li, Natalia I. Gonzalez-Pech, David J. Cheng, Jeanne E. Lemaster, Yijun Xie, Vicki H. Grassian, George L. Sen, Jesse V. Jokerst, to be published, 2019. The dissertation author was the primary researcher of this paper.

APPENDIX

Chapter 1:

SPR, surface plasmon resonance; CT, computerized tomography; MPI, magnetic particle imaging; MRI, magnetic resonance imaging; T1, longitudinal relaxation; T2, transverse relaxation; PAI, photoacoustic imaging; SPECT, single photon emission computed tomography; PET, positron emission tomography; PDT, photodynamic therapy; PTT, photothermal therapy; RES, reticuloendothelial system; US: ultrasound; TEOS, tetraethyl orthosilicate; HU, Hounsfield units; EPR, enhanced permeability and retention; AuGR, Gold nanorod; NPs, nanoparticles; PEG, polyethylene glycol.

Chapter 2:

DSN, discoid silica nanoparticles; ELS, exosome-like silica nanoparticles; SSN, Stöber silica nanospheres; MSN, MCM-41 mesoporous silica nanospheres; MCF, mesocellular foam silica nanoparticles; TSPA, bis(3-trimethoxysilyl-propyl)amine; BTSE, bis(triethoxysilyl) ethane; hMSCs, human mesenchymal stem cells; NTA, nanoparticle tracking analysis.

Chapter 3:

SiC, silicon carbide; 3C-SiC, silicon carbide with cubic symmetric structure; NP, nanoparticles; SiCNWs, silicon carbide nanowires; SiCNPs, silicon carbide nanoparticles; SiCNP80, silicon carbide nanoparticles with an average size of 80 nm; SiCNP600, silicon carbide nanoparticles with an average size of 600 nm; FITC, fluorescein isothiocyanate; MSCs, mesenchymal stem cells; ROS, reactive oxygen species; FDA, food and drug administration; SEM, scanning electron microscope; TEM, transmission electron

microscope; HRTEM, high resolution transmission electron microscope; FFT, fast Fourier transformation; XRD, X-ray diffraction; EDX, energy dispersive X-ray spectra; PA, photoacoustic; RT-PCR, real-time polymerase chain reaction; CDKN, cyclin-dependent kinase inhibitors; CDK, cyclin-dependent kinase; LPL, lipoprotein lipase; PPARG, peroxisome proliferator-activator receptor-gamma2; ALP, alkaline phosphatase; BSP, bone sialoprotein; AGN, aggrecan; COL2A, collagen type II alpha 1; EF1α, elongation factor-1α; C3, complement protein 3; MMP-3, matrix metalloproteinase-3; MCP-1, monocyte chemotactic protein 1; IL-8, interleukin-8.

Chapter 4:

OSNP, organosilica nanoparticles; CTAB, Hexadecyltrimethylammonium bromide; DMHA, dimethylhexadecylamine; DLS, dynamic light scattering; XPS, X-ray photoelectron spectroscopy; ICP-OES, inductively coupled plasma optical emission spectrometer; pKa, acid dissociation constants.

Chapter 5:

SIO, silica-iron oxide; MCF, mesocellular foam silica; SPIO, superparamagnetic iron oxide nanoparticles; P123, Poly(ethylene glycol)-block-poly(propylene glycol)-block-poly(ethylene glycol); MSCs, mesenchymal stem cells; hMSCs, human MSCs; SQUID, superconducting quantum interface device; PBS, phosphate-buffered saline; CD, cluster of differentiation; DMEM, Dulbecco's modification of Eagle medium; MSCBM, mesenchymal stem cells basal medium; IGF, insulin-like growth factor; FOV, field of view; 2D, 2-dimensional; EF, ejection fraction; GLS, global longitudinal strain; VEGF, vascular endothelial growth factor; VCAM-1, vascular cell adhesion molecule-1; MCP-1, monocyte chemotactic protein 1; MMP-3, matrix metalloproteinase-3; TIMP-1, tissue

inhibitor of metalloproteinase-1; A2Macro, alpha-2-macroglobulin; B2M, beta 2 microglobulin; BCA, bicinchoninic acid; LAD, left anterior descending; PE, phycoerythrin; FITC, fluorescein isothiocyanate; APC, allophycocyanin; H&E, Haemotoxylin and Eosin; LVEF, left ventricular ejection fraction; LV, left ventricular.

References

1. Xie, J.; Lee, S.; Chen, X. Nanoparticle-Based Theranostic Agents. *Adv. Drug Del. Rev.* **2010**, 62, 1064-1079.

2. Chen, F.; Hableel, G.; Zhao, E. R.; Jokerst, J. V. Multifunctional Nanomedicine with Silica: Role of Silica in Nanoparticles for Theranostic, Imaging, and Drug Monitoring. *J. Colloid Interface Sci.* **2018**.

3. Chen, F.; Zhao, E.; Kim, T.; Wang, J. X.; Hableel, G.; Reardon, P. J. T.; Ananthakrishna, S. J.; Wang, T. Y.; Arconada-Alvarez, S.; Knowles, J. C.; Jokerst, J. V. Organosilica Nanoparticles with an Intrinsic Secondary Amine: An Efficient and Reusable Adsorbent for Dyes. *Acs Applied Materials & Interfaces* **2017**, 9, 15566-15576.

4. Liu, Z.; Tabakman, S.; Welsher, K.; Dai, H. Carbon Nanotubes in Biology and Medicine: In Vitro and in Vivo Detection, Imaging and Drug Delivery. *Nano Res* **2009**, 2, 85-120.

5. Kostarelos, K.; Lacerda, L.; Pastorin, G.; Wu, W.; WieckowskiSebastien; Luangsivilay, J.; Godefroy, S.; Pantarotto, D.; Briand, J.-P.; Muller, S.; Prato, M.; Bianco, A. Cellular Uptake of Functionalized Carbon Nanotubes Is Independent of Functional Group and Cell Type. *Nat Nano* **2007**, 2, 108-113.

6. Yang, S.-t.; Guo, W.; Lin, Y.; Deng, X.-y.; Wang, H.-f.; Sun, H.-f.; Liu, Y.-f.; Wang, X.; Wang, W.; Chen, M.; Huang, Y.-p.; Sun, Y.-P. Biodistribution of Pristine Single-Walled Carbon Nanotubes in Vivo. *The Journal of Physical Chemistry C* **2007**, 111, 17761-17764.

7. Lu, F.; Gu, L.; Meziani, M. J.; Wang, X.; Luo, P. G.; Veca, L. M.; Cao, L.; Sun, Y.-P. Advances in Bioapplications of Carbon Nanotubes. *Advanced Materials* **2009**, 21, 139-152.

8. Mao, H. Y.; Laurent, S.; Chen, W.; Akhavan, O.; Imani, M.; Ashkarran, A. A.; Mahmoudi, M. Graphene: Promises, Facts, Opportunities, and Challenges in Nanomedicine. *Chem. Rev.* **2013**, 113, 3407-3424.

9. He, Q.; Kiesewetter, D. O.; Qu, Y.; Fu, X.; Fan, J.; Huang, P.; Liu, Y.; Zhu, G.; Liu, Y.; Qian, Z.; Chen, X. Nir-Responsive on-Demand Release of Co from Metal Carbonyl-Caged Graphene Oxide Nanomedicine. *Adv. Mater.* **2015**, 27, 6741-6746.

10. Feng, L.; Liu, Z. Graphene in Biomedicine: Opportunities and Challenges. *Nanomedicine* **2011**, 6, 317-324.

11. Zhang, Y.; Petibone, D.; Xu, Y.; Mahmood, M.; Karmakar, A.; Casciano, D.; Ali, S.; Biris, A. S. Toxicity and Efficacy of Carbon Nanotubes and Graphene: The Utility of Carbon-Based Nanoparticles in Nanomedicine. *Drug Metab. Rev.* **2014**, 46, 232-246.

12. Huang, S. K.; Stauffer, P. R.; Hong, K. L.; Guo, J. W. H.; Phillips, T. L.; Huang, A.;

Papahadjopoulos, D. Liposomes and Hyperthermia in Mice - Increased Tumor Uptake and Therapeutic Efficacy of Doxorubicin in Sterically Stabilized Liposomes. *Cancer Res.* **1994**, 54, 2186-2191.

13. Kong, G.; Anyarambhatla, G.; Petros, W. P.; Braun, R. D.; Colvin, O. M.; Needham, D.; Dewhirst, M. W. Efficacy of Liposomes and Hyperthermia in a Human Tumor Xenograft Model: Importance of Triggered Drug Release. *Cancer Res.* **2000**, 60, 6950-6957.

14. Torchilin, V. P. Recent Advances with Liposomes as Pharmaceutical Carriers. *Nat. Rev. Drug Discov.* **2005**, 4, 145-160.

15. Weng, K. C.; Noble, C. O.; Papahadjopoulos-Sternberg, B.; Chen, F. F.; Drummond, D. C.; Kirpotin, D. B.; Wang, D. H.; Hom, Y. K.; Hann, B.; Park, J. W. Targeted Tumor Cell Internalization and Imaging of Multifunctional Quantum Dot-Conjugated Immunoliposomes in Vitro and in Vivo. *Nano Lett.* **2008**, 8, 2851-2857.

16. Kukowska-Latallo, J. F.; Bielinska, A. U.; Johnson, J.; Spindler, R.; Tomalia, D. A.; Baker, J. R. Efficient Transfer of Genetic Material into Mammalian Cells Using Starburst Polyamidoamine Dendrimers. *Proceedings of the National Academy of Sciences* **1996**, 93, 4897-4902.

17. Gillies, E. R.; Fréchet, J. M. J. Dendrimers and Dendritic Polymers in Drug Delivery. *Drug Discov. Today* **2005**, 10, 35-43.

18. Svenson, S.; Tomalia, D. A. Dendrimers in Biomedical Applications—Reflections on the Field. *Advanced Drug Delivery Reviews* **2012**, 64, Supplement, 102-115.

19. Lee, C. C.; MacKay, J. A.; Frechet, J. M. J.; Szoka, F. C. Designing Dendrimers for Biological Applications. *Nat Biotech* **2005**, 23, 1517-1526.

20. Tomalia, D. A.; Naylor, A. M.; Goddard, W. A. Starburst Dendrimers: Molecular-Level Control of Size, Shape, Surface Chemistry, Topology, and Flexibility from Atoms to Macroscopic Matter. *Angewandte Chemie International Edition in English* **1990**, 29, 138-175.

21. Alexis, F.; Pridgen, E.; Molnar, L. K.; Farokhzad, O. C. Factors Affecting the Clearance and Biodistribution of Polymeric Nanoparticles. *Molecular Pharmaceutics* **2008**, 5, 505-515.

22. Pinto Reis, C.; Neufeld, R. J.; Ribeiro, A. J.; Veiga, F. Nanoencapsulation I. Methods for Preparation of Drug-Loaded Polymeric Nanoparticles. *Nanomedicine: Nanotechnology, Biology and Medicine* **2006**, 2, 8-21.

23. Kumari, A.; Yadav, S. K.; Yadav, S. C. Biodegradable Polymeric Nanoparticles Based Drug Delivery Systems. *Colloids and Surfaces B: Biointerfaces* **2010**, 75, 1-18.

24. Owens Iii, D. E.; Peppas, N. A. Opsonization, Biodistribution, and Pharmacokinetics

of Polymeric Nanoparticles. *International Journal of Pharmaceutics* **2006**, 307, 93-102.

25. Soppimath, K. S.; Aminabhavi, T. M.; Kulkarni, A. R.; Rudzinski, W. E. Biodegradable Polymeric Nanoparticles as Drug Delivery Devices. *Journal of Controlled Release* **2001**, 70, 1-20.

26. Galaev, I. Y.; Mattiasson, B. 'Smart' Polymers and What They Could Do in Biotechnology and Medicine. *Trends in Biotechnology* **1999**, 17, 335-340.

27. Jokerst, J. V.; Van de Sompel, D.; Bohndiek, S. E.; Gambhir, S. S. Cellulose Nanoparticles Are a Biodegradable Photoacoustic Contrast Agent for Use in Living Mice. *Photoacoustics* **2014**, 2, 119-127.

28. Anglin, E. J.; Cheng, L.; Freeman, W. R.; Sailor, M. J. Porous Silicon in Drug Delivery Devices and Materials. *Advanced Drug Delivery Reviews* **2008**, 60, 1266-1277.

29. Tang, F.; Li, L.; Chen, D. Mesoporous Silica Nanoparticles: Synthesis, Biocompatibility and Drug Delivery. *Advanced Materials* **2012**, 24, 1504-1534.

30. Li, Z.; Barnes, J. C.; Bosoy, A.; Stoddart, J. F.; Zink, J. I. Mesoporous Silica Nanoparticles in Biomedical Applications. *Chem. Soc. Rev.* **2012**, 41, 2590-2605.

31. Slowing, I. I.; Vivero-Escoto, J. L.; Wu, C.-W.; Lin, V. S. Y. Mesoporous Silica Nanoparticles as Controlled Release Drug Delivery and Gene Transfection Carriers. *Advanced Drug Delivery Reviews* **2008**, 60, 1278-1288.

32. Chen, F.; Ma, M.; Wang, J.; Wang, F.; Chern, S. X.; Zhao, E. R.; Jhunjhunwala, A.; Darmadi, S.; Chen, H.; Jokerst, J. V. Exosome-Like Silica Nanoparticles: A Novel Ultrasound Contrast Agent for Stem Cell Imaging. *Nanoscale* **2017**, 9, 402-411.

33. Wang, J. X.; Chen, F.; Arconada-Alvarez, S. J.; Hartanto, J.; Yap, L. P.; Park, R.; Wang, F.; Vorobyova, I.; Dagliyan, G.; Conti, P. S.; Jokerst, J. V. A Nano-Scale Tool for Photoacoustic-Based Measurements of Clotting Time and Therapeutic Drug Monitoring of Heparin. *Nano Lett.* **2016**, 16, 6265-6271.

34. Slowing, I.; Trewyn, B. G.; Lin, V. S. Y. Effect of Surface Functionalization of Mcm-41-Type Mesoporous Silica Nanoparticles on the Endocytosis by Human Cancer Cells. *Journal of the American Chemical Society* **2006**, 128, 14792-14793.

35. Lu, J.; Liong, M.; Li, Z.; Zink, J. I.; Tamanoi, F. Biocompatibility, Biodistribution, and Drug-Delivery Efficiency of Mesoporous Silica Nanoparticles for Cancer Therapy in Animals. *Small* **2010**, 6, 1794-1805.

36. Foroutan, F.; Jokerst, J. V.; Gambhir, S. S.; Vermesh, O.; Kim, H.-W.; Knowles, J. C. Sol–Gel Synthesis and Electrospraying of Biodegradable (P2o5)55–(Cao)30–(Na2o)15 Glass Nanospheres as a Transient Contrast Agent for Ultrasound Stem Cell Imaging. *ACS Nano* **2015**, 9, 1868-1877.

37. Bagalkot, V.; Zhang, L.; Levy-Nissenbaum, E.; Jon, S.; Kantoff, P. W.; Langer, R.; Farokhzad, O. C. Quantum Dot - Aptamer Conjugates for Synchronous Cancer Imaging, Therapy, and Sensing of Drug Delivery Based on Bi-Fluorescence Resonance Energy Transfer. *Nano Lett.* **2007**, 7, 3065-3070.

38. Liu, W. H.; Choi, H. S.; Zimmer, J. P.; Tanaka, E.; Frangioni, J. V.; Bawendi, M. Compact Cysteine-Coated Cdse(Zncds) Quantum Dots for in Vivo Applications. *JACS* **2007**, 129, 14530-+.

39. Liu, W.; Howarth, M.; Greytak, A. B.; Zheng, Y.; Nocera, D. G.; Ting, A. Y.; Bawendi, M. G. Compact Biocompatible Quantum Dots Functionalized for Cellular Imaging. *JACS* **2008**, 130, 1274-1284.

40. Smith, A. M.; Duan, H.; Mohs, A. M.; Nie, S. Bioconjugated Quantum Dots for in Vivo Molecular and Cellular Imaging. *Adv. Drug Deliv. Rev.* **2008**, 60, 1226-1240.

41. Wang, L.; Yan, R.; Huo, Z.; Wang, L.; Zeng, J.; Bao, J.; Wang, X.; Peng, Q.; Li, Y. Fluorescence Resonant Energy Transfer Biosensor Based on Upconversion-Luminescent Nanoparticles. *Angew. Chem. Int. Ed.* **2005**, 44, 6054-6057.

42. Chen, G.; Qiu, H.; Prasad, P. N.; Chen, X. Upconversion Nanoparticles: Design, Nanochemistry, and Applications in Theranostics. *Chem. Rev.* **2014**, 114, 5161-5214.

43. Sun, L.-D.; Wang, Y.-F.; Yan, C.-H. Paradigms and Challenges for Bioapplication of Rare Earth Upconversion Luminescent Nanoparticles: Small Size and Tunable Emission/Excitation Spectra. *Acc. Chem. Res.* **2014**, 47, 1001-1009.

44. Lv, R.; Yang, P.; Hu, B.; Xu, J.; Shang, W.; Tian, J. In Situ Growth Strategy to Integrate up-Conversion Nanoparticles with Ultrasmall Cus for Photothermal Theranostics. *ACS Nano* **2017**, 11, 1064-1072.

45. Muhr, V.; Wilhelm, S.; Hirsch, T.; Wolfbeis, O. S. Upconversion Nanoparticles: From Hydrophobic to Hydrophilic Surfaces. *Acc. Chem. Res.* **2014**, 47, 3481-3493.

46. Fang, C.; Zhang, M. Multifunctional Magnetic Nanoparticles for Medical Imaging Applications. *Journal of Materials Chemistry* **2009**, 19, 6258-6266.

47. Gupta, A. K.; Gupta, M. Synthesis and Surface Engineering of Iron Oxide Nanoparticles for Biomedical Applications. *Biomaterials* **2005**, 26, 3995-4021.

48. Laurent, S.; Forge, D.; Port, M.; Roch, A.; Robic, C.; Vander Elst, L.; Muller, R. N. Magnetic Iron Oxide Nanoparticles: Synthesis, Stabilization, Vectorization, Physicochemical Characterizations, and Biological Applications. *Chem. Rev.* **2008**, 108, 2064-2110.

49. Bulte, J. W. M.; Kraitchman, D. L. Iron Oxide Mr Contrast Agents for Molecular and Cellular Imaging. *NMR in Biomedicine* **2004**, 17, 484-499.

50. Tartaj, P.; del Puerto Morales, M.; Veintemillas-Verdaguer, S.; González-Carreño, T.; Serna, C. J. The Preparation of Magnetic Nanoparticles for Applications in Biomedicine. *J. Phys. D: Appl. Phys.* **2003**, 36, R182.

51. Zhen, Z.; Xie, J. Development of Manganese-Based Nanoparticles as Contrast Probes for Magnetic Resonance Imaging. *Theranostics* **2012**, 2, 45-54.

52. Rasmussen, J. W.; Martinez, E.; Louka, P.; Wingett, D. G. Zinc Oxide Nanoparticles for Selective Destruction of Tumor Cells and Potential for Drug Delivery Applications. *Expert Opinion on Drug Delivery* **2010**, 7, 1063-1077.

53. LaVan, D. A.; McGuire, T.; Langer, R. Small-Scale Systems for in Vivo Drug Delivery. *Nat. Biotechnol.* **2003**, 21, 1184.

54. Kim, T.; Lemaster, J. E.; Chen, F.; Li, J.; Jokerst, J. V. Photoacoustic Imaging of Human Mesenchymal Stem Cells Labeled with Prussian Blue-Poly(L-Lysine) Nanocomplexes. *ACS Nano* **2017**, 11, 9022-9032.

55. Jain, P. K.; Huang, X.; El-Sayed, I. H.; El-Sayed, M. A. Noble Metals on the Nanoscale: Optical and Photothermal Properties and Some Applications in Imaging, Sensing, Biology, and Medicine. *Accounts Of Chemical Research* **2008**, 41, 1578-1586.

56. Hu, M.; Chen, J.; Li, Z.-Y.; Au, L.; Hartland, G. V.; Li, X.; Marquez, M.; Xia, Y. Gold Nanostructures: Engineering Their Plasmonic Properties for Biomedical Applications. *Chemical Society Reviews* **2006**, 35, 1084-1094.

57. Ghosh, P.; Han, G.; De, M.; Kim, C. K.; Rotello, V. M. Gold Nanoparticles in Delivery Applications. *Advanced Drug Delivery Reviews* **2008**, 60, 1307-1315.

58. El-Sayed, I. H.; Huang, X.; El-Sayed, M. A. Surface Plasmon Resonance Scattering and Absorption of Anti-Egfr Antibody Conjugated Gold Nanoparticles in Cancer Diagnostics: Applications in Oral Cancer. *Nano Letters* **2005**, 5, 829-834.

59. Daniel, M.-C.; Astruc, D. Gold Nanoparticles: Assembly, Supramolecular Chemistry, Quantum-Size-Related Properties, and Applications toward Biology, Catalysis, and Nanotechnology. *Chem. Rev.* **2004**, 104, 293-346.

60. Chen, Y.; Wang, M.; Mao, C. An Autonomous DNA Nanomotor Powered by a DNA Enzyme. *Angewandte Chemie International Edition* **2004**, 43, 3554-3557.

61. Zheng, J.; Birktoft, J. J.; Chen, Y.; Wang, T.; Sha, R.; Constantinou, P. E.; Ginell, S. L.; Mao, C.; Seeman, N. C. From Molecular to Macroscopic Via the Rational Design of a Self-Assembled 3d DNA Crystal. *Nature* **2009**, 461, 74-77.

62. Roy, K.; Mao, H.-Q.; Huang, S. K.; Leong, K. W. Oral Gene Delivery with Chitosan-DNA Nanoparticles Generates Immunologic Protection in a Murine Model of Peanut Allergy. *Nat Med* **1999**, 5, 387-391.

63. Vijayanathan, V.; Thomas, T.; Thomas, T. J. DNA Nanoparticles and Development of DNA Delivery Vehicles for Gene Therapy. *Biochemistry* **2002**, 41, 14085-14094.

64. Thakor, A. S.; Jokerst, J. V.; Ghanouni, P.; Campbell, J. L.; Mittra, E.; Gambhir, S. S. Clinically Approved Nanoparticle Imaging Agents. *Journal of Nuclear Medicine* **2016**, 57, 1833-1837.

65. McNeil, S. E. Nanotechnology for the Biologist. *J. Leukocyte Biol.* **2005**, 78, 585-594.

66. McNeil, S. E. Nanoparticle Therapeutics: A Personal Perspective. *Wiley Interdisciplinary Reviews: Nanomedicine and Nanobiotechnology* **2009**, 1, 264-271.

67. Sun, T.; Zhang, Y. S.; Pang, B.; Hyun, D. C.; Yang, M.; Xia, Y. Engineered Nanoparticles for Drug Delivery in Cancer Therapy. *Angew. Chem. Int. Ed.* **2014**, 53, 12320-12364.

68. Foroutan, F.; Jokerst, J. V.; Gambhir, S. S.; Vermesh, O.; Kim, H. W.; Knowles, J. C. Sol-Gel Synthesis and Electrospraying of Biodegradable (P2o5)55-(Cao)30-(Na2o)15 Glass Nanospheres as a Transient Contrast Agent for Ultrasound Stem Cell Imaging. *ACS Nano* **2015**, 9, 1868-1877.

69. Wang, J.; Jokerst, J. V. Stem Cell Imaging: Tools to Improve Cell Delivery and Viability. *Stem Cells Int* **2016**, 2016, 9240652.

70. Lemaster, J. E.; Jokerst, J. V. What Is New in Nanoparticle-Based Photoacoustic Imaging? *Wiley Interdisciplinary Reviews: Nanomedicine and Nanobiotechnology* **2017**, 9, e1404-n/a.

71. Ruan, Q.; Zhu, Y.; Li, F.; Xiao, J.; Zeng, Y.; Xu, F. *Investigation of Layer-by-Layer Assembled Heparin and Chitosan Multilayer Films Via Electrochemical Spectroscopy*. 2009; Vol. 333, p 725-733.

72. Huang, X.; Jain, P. K.; El-Sayed, I. H.; El-Sayed, M. A. Gold Nanoparticles: Interesting Optical Properties and Recent Applications in Cancer Diagnostics and Therapy. *Nanomedicine* **2007**, 2, 681-693.

73. Nirmal, M.; Brus, L. Luminescence Photophysics in Semiconductor Nanocrystals. *Accounts Of Chemical Research* **1999**, 32, 407-414.

74. He, S.; Johnson, N. J. J.; Nguyen Huu, V. A.; Cory, E.; Huang, Y.; Sah, R. L.; Jokerst, J. V.; Almutairi, A. Simultaneous Enhancement of Photoluminescence, Mri Relaxivity, and Ct Contrast by Tuning the Interfacial Layer of Lanthanide Heteroepitaxial Nanoparticles. *Nano Lett.* **2017**, 17, 4873-4880.

75. Zeng, S.; Baillargeat, D.; Ho, H.-P.; Yong, K.-T. Nanomaterials Enhanced Surface Plasmon Resonance for Biological and Chemical Sensing Applications. *Chemical Society Reviews* **2014**, 43, 3426-3452.

76. Jokerst, J. V.; Cole, A. J.; Van de Sompel, D.; Gambhir, S. S. Gold Nanorods for Ovarian Cancer Detection with Photoacoustic Imaging and Resection Guidance Via Raman Imaging in Living Mice. *ACS Nano* **2012**, 6, 10366-10377.

77. Chen, Z.; Ma, L.; Liu, Y.; Chen, C. Applications of Functionalized Fullerenes in Tumor Theranostics. *Theranostics* **2012**, 2, 238.

78. Zhang, Y.; Long, M.; Huang, P.; Yang, H.; Chang, S.; Hu, Y.; Tang, A.; Mao, L. Emerging Integrated Nanoclay-Facilitated Drug Delivery System for Papillary Thyroid Cancer Therapy. *Scientific reports* **2016**, 6, 33335.

79. Yang, H.; Mao, H.; Wan, Z.; Zhu, A.; Guo, M.; Li, Y.; Li, X.; Wan, J.; Yang, X.; Shuai, X. Micelles Assembled with Carbocyanine Dyes for Theranostic near-Infrared Fluorescent Cancer Imaging and Photothermal Therapy. *Biomaterials* **2013**, 34, 9124-9133.

80. Barua, S.; Mitragotri, S. Challenges Associated with Penetration of Nanoparticles across Cell and Tissue Barriers: A Review of Current Status and Future Prospects. *Nano Today* **2014**, 9, 223-243.

81. McNeil, S. E. Nanoparticle Therapeutics: A Personal Perspective. *Wiley interdisciplinary reviews. Nanomedicine and nanobiotechnology* **2009**, 1, 264-271.

82. Kempen, P. J.; Kircher, M. F.; de la Zerda, A.; Zavaleta, C. L.; Jokerst, J. V.; Mellinghoff, I. K.; Gambhir, S. S.; Sinclair, R. A Correlative Optical Microscopy and Scanning Electron Microscopy Approach to Locating Nanoparticles in Brain Tumors. *Micron (Oxford, England : 1993)* **2015**, 68, 70-76.

83. Jokerst, J. V.; Chen, Z.; Xu, L.; Nolley, R.; Chang, E.; Mitchell, B.; Brooks, J. D.; Gambhir, S. S. A Magnetic Bead-Based Sensor for the Quantification of Multiple Prostate Cancer Biomarkers. *PLOS ONE* **2015**, 10, e0139484.

84. Alivisatos, A. P.; Andrews, A. M.; Boyden, E. S.; Chun, M.; Church, G. M.; Deisseroth, K.; Donoghue, J. P.; Fraser, S. E.; Lippincott-Schwartz, J.; Looger, L. L.; Masmanidis, S.; McEuen, P. L.; Nurmikko, A. V.; Park, H.; Peterka, D. S.; Reid, C.; Roukes, M. L.; Scherer, A.; Schnitzer, M.; Sejnowski, T. J.; Shepard, K. L.; Tsao, D.; Turrigiano, G.; Weiss, P. S.; Xu, C.; Yuste, R.; Zhuang, X. Nanotools for Neuroscience and Brain Activity Mapping. *ACS Nano* **2013**, 7, 1850-1866.

85. Li, M.; Yang, X. J.; Ren, J. S.; Qu, K. G.; Qu, X. G. Using Graphene Oxide High near-Infrared Absorbance for Photothermal Treatment of Alzheimer's Disease. *Advanced Materials* **2012**, 24, 1722-1728.

86. Suarez, S.; Almutairi, A.; Christman, K. L. Micro- and Nanoparticles for Treating Cardiovascular Disease. *Biomaterials Science* **2015**, 3, 564-580.

87. Mulder, W. J. M.; Fayad, Z. A. Nanomedicine Captures Cardiovascular Disease. *Arteriosclerosis, Thrombosis, and Vascular Biology* **2008**, 28, 801-802.

88. Tai, J. H.; Foster, P.; Rosales, A.; Feng, B.; Hasilo, C.; Martinez, V.; Ramadan, S.; Snir, J.; Melling, C. W. J.; Dhanvantari, S.; Rutt, B.; White, D. J. G. Imaging Islets Labeled with Magnetic Nanoparticles at 1.5 Tesla. *Diabetes* **2006**, 55, 2931-2938.

89. Ma, Z.; Lim, T. M.; Lim, L.-Y. Pharmacological Activity of Peroral Chitosan–Insulin Nanoparticles in Diabetic Rats. *International Journal of Pharmaceutics* **2005**, 293, 271-280.

90. Ho, I. T.; Sessler, J. L.; Gambhir, S. S.; Jokerst, J. V. Parts Per Billion Detection of Uranium with a Porphyrinoid-Containing Nanoparticle and in Vivo Photoacoustic Imaging. *Analyst* **2015**, 140, 3731-3737.

91. Gibney, M. Cornell Nanosized 'Dots' for Diagnostics May Now Deliver Drugs **2013**.

92. Lin, W.; Huang, Y.-w.; Zhou, X.-D.; Ma, Y. In Vitro Toxicity of Silica Nanoparticles in Human Lung Cancer Cells. *Toxicol Appl Pharmacol* **2006**, 217, 252-259.

93. Almeida, J. P.; Chen, A. L.; Foster, A.; Drezek, R. In Vivo Biodistribution of Nanoparticles. *Nanomedicine (London, England)* **2011**, 6, 815-835.

94. Kolbe, G. Das Komplexchemische Verhalten Der Kieselsäure. 1956.

95. Stöber, W.; Fink, A.; Bohn, E. Controlled Growth of Monodisperse Silica Spheres in the Micron Size Range. *J. Colloid Interface Sci.* **1968**, 26, 62-69.

96. Yanagisawa, T.; Shimizu, T.; Kuroda, K.; Kato, C. The Preparation of Alkyltriinethylaininonium–Kaneinite Complexes and Their Conversion to Microporous Materials. *Bulletin of the Chemical Society of Japan* **1990**, 63, 988-992.

97. Beck, J.; Vartuli, J.; Roth, W. J.; Leonowicz, M.; Kresge, C.; Schmitt, K.; Chu, C.; Olson, D. H.; Sheppard, E. A New Family of Mesoporous Molecular Sieves Prepared with Liquid Crystal Templates. *Journal of the American Chemical Society* **1992**, 114, 10834-10843.

98. Kresge, C. T.; Leonowicz, M. E.; Roth, W. J.; Vartuli, J. C.; Beck, J. S. Ordered Mesoporous Molecular-Sieves Synthesized by a Liquid-Crystal Template Mechanism. *Nature* **1992**, 359, 710-712.

99. Wan, Y.; Zhao, D. Y. On the Controllable Soft-Templating Approach to Mesoporous Silicates. *Chem. Rev.* **2007**, 107, 2821-2860.

100. Zhang, T.; Ge, J.; Hu, Y.; Zhang, Q.; Aloni, S.; Yin, Y. Formation of Hollow Silica Colloids through a Spontaneous Dissolution–Regrowth Process. *Angew. Chem. Int. Ed.* **2008**, 47, 5806-5811.

101. Chen, F.; Hong, H.; Shi, S.; Goel, S.; Valdovinos, H. F.; Hernandez, R.; Theuer, C. P.; Barnhart, T. E.; Cai, W. Engineering of Hollow Mesoporous Silica Nanoparticles for Remarkably Enhanced Tumor Active Targeting Efficacy. *Sci. Rep.* **2014**, 4.

102. Zhang, K.; Chen, H.; Guo, X.; Zhang, D.; Zheng, Y.; Zheng, H.; Shi, J. Double-Scattering/Reflection in a Single Nanoparticle for Intensified Ultrasound Imaging. *Sci Rep* **2015**, 5, 8766-8776.

103. Schmidt-Winkel, P.; Lukens, W. W.; Zhao, D.; Yang, P.; Chmelka, B. F.; Stucky, G. D. Mesocellular Siliceous Foams with Uniformly Sized Cells and Windows. *JACS* **1999**, 121, 254-255.

104. Fan, R.; Wu, Y.; Li, D.; Yue, M.; Majumdar, A.; Yang, P. Fabrication of Silica Nanotube Arrays from Vertical Silicon Nanowire Templates. *Journal of the American Chemical Society* **2003**, 125, 5254-5255.

105. Kumar, R.; Roy, I.; Ohulchanskyy, T. Y.; Goswami, L. N.; Bonoiu, A. C.; Bergey, E. J.; Tramposch, K. M.; Maitra, A.; Prasad, P. N. Covalently Dye-Linked, Surface-Controlled, and Bioconjugated Organically Modified Silica Nanoparticles as Targeted Probes for Optical Imaging. *ACS Nano* **2008**, 2, 449-456.

106. Bagwe, R. P.; Hilliard, L. R.; Tan, W. Surface Modification of Silica Nanoparticles to Reduce Aggregation and Nonspecific Binding. *Langmuir* **2006**, 22, 4357-4362.

107. Tsai, C.-P.; Chen, C.-Y.; Hung, Y.; Chang, F.-H.; Mou, C.-Y. Monoclonal Antibody-Functionalized Mesoporous Silica Nanoparticles (Msn) for Selective Targeting Breast Cancer Cells. *J. Mater. Chem.* **2009**, 19, 5737-5743.

108. Yang, H.; Zhuang, Y.; Hu, H.; Du, X.; Zhang, C.; Shi, X.; Wu, H.; Yang, S. Silica-Coated Manganese Oxide Nanoparticles as a Platform for Targeted Magnetic Resonance and Fluorescence Imaging of Cancer Cells. *Adv. Funct. Mater.* **2010**, 20, 1733-1741.

109. Lee, J. E.; Lee, N.; Kim, H.; Kim, J.; Choi, S. H.; Kim, J. H.; Kim, T.; Song, I. C.; Park, S. P.; Moon, W. K.; Hyeon, T. Uniform Mesoporous Dye-Doped Silica Nanoparticles Decorated with Multiple Magnetite Nanocrystals for Simultaneous Enhanced Magnetic Resonance Imaging, Fluorescence Imaging, and Drug Delivery. *JACS* **2010**, 132, 552-557.

110. Zhu, Y.; Fujiwara, M. Installing Dynamic Molecular Photomechanics in Mesopores: A Multifunctional Controlled-Release Nanosystem. *Angew. Chem. Int. Ed.* **2007**, 46, 2241-2244.

111. Lai, J. P.; Shah, B. P.; Garfunkel, E.; Lee, K. B. Versatile Fluorescence Resonance Energy Transfer-Based Mesoporous Silica Nanoparticles for Real-Time Monitoring of Drug Release. *Acs Nano* **2013**, 7, 2741-2750.

112. Shen, D.; Yang, J.; Li, X.; Zhou, L.; Zhang, R.; Li, W.; Chen, L.; Wang, R.; Zhang, F.; Zhao, D. Biphase Stratification Approach to Three-Dimensional Dendritic Biodegradable Mesoporous Silica Nanospheres. *Nano Lett.* **2014**, 14, 923-932.

113. Park, J.-H.; Gu, L.; Maltzahn, G. v.; Ruoslahti, E.; Bhatia, S. N.; Sailor, M. J. Biodegradable Luminescent Porous Silicon Nanoparticles for in Vivo Applications. *Nature Mater.* **2009**, 8, 331-336.

114. Kempen, P. J.; Greasley, S.; Parker, K. A.; Campbell, J. L.; Chang, H.-Y.; Jones, J. R.; Sinclair, R.; Gambhir, S. S.; Jokerst, J. V. Theranostic Mesoporous Silica Nanoparticles Biodegrade after Pro-Survival Drug Delivery and Ultrasound/Magnetic Resonance Imaging of Stem Cells. *Theranostics* **2015**, 5, 631-642.

115. Liu, T.; Li, L.; Teng, X.; Huang, X.; Liu, H.; Chen, D.; Ren, J.; He, J.; Tang, F. Single and Repeated Dose Toxicity of Mesoporous Hollow Silica Nanoparticles in Intravenously Exposed Mice. *Biomaterials* **2011**, 32, 1657-1668.

116. Rimal, B.; Greenberg, A. K.; Rom, W. N. Basic Pathogenetic Mechanisms in Silicosis: Current Understanding. *Curr Opin Pulm Med* **2005**, 11, 169-173.

117. Napierska, D.; Thomassen, L. C. J.; Rabolli, V.; Liston, D.; Gonzalez, L.; Kirsch-Volders, M.; Martens, J. A.; Hoet, P. H. Size-Dependent Cytotoxicity of Monodisperse Silica Nanoparticles in Human Endothelial Cells. *Small* **2009**, 5, 846-853.

118. Nishimori, H.; Kondoh, M.; Isoda, K.; Tsunoda, S.-i.; Tsutsumi, Y.; Yagi, K. Silica Nanoparticles as Hepatotoxicants. *European Journal of Pharmaceutics and Biopharmaceutics* **2009**, 72, 496-501.

119. Zhang, H. Y.; Dunphy, D. R.; Jiang, X. M.; Meng, H.; Sun, B. B.; Tarn, D.; Xue, M.; Wang, X.; Lin, S. J.; Ji, Z. X.; Li, R. B.; Garcia, F. L.; Yang, J.; Kirk, M. L.; Xia, T.; Zink, J. I.; Nel, A.; Brinker, C. J. Processing Pathway Dependence of Amorphous Silica Nanoparticle Toxicity: Colloidal Vs Pyrolytic. *JACS* **2012**, 134, 15790-15804.

120. Fu, C.; Liu, T.; Li, L.; Liu, H.; Chen, D.; Tang, F. The Absorption, Distribution, Excretion and Toxicity of Mesoporous Silica Nanoparticles in Mice Following Different Exposure Routes. *Biomaterials* **2013**, 34, 2565-2575.

121. Mamaeva, V.; Sahlgren, C.; Lindén, M. Mesoporous Silica Nanoparticles in Medicine—Recent Advances. *Adv. Drug Del. Rev.* **2013**, 65, 689-702.

122. Elsabahy, M.; Wooley, K. L. Cytokines as Biomarkers of Nanoparticle Immunotoxicity. *Chem. Soc. Rev.* **2013**, 42, 5552-5576.

123. Cauda, V.; Schlossbauer, A.; Bein, T. Bio-Degradation Study of Colloidal Mesoporous Silica Nanoparticles: Effect of Surface Functionalization with Organo-Silanes and Poly(Ethylene Glycol). *Microporous and Mesoporous Materials* **2010**, 132, 60-71.

124. Hao, N.; Liu, H.; Li, L.; Chen, D.; Li, L.; Tang, F. In Vitro Degradation Behavior of Silica Nanoparticles under Physiological Conditions. *J Nanosci Nanotechnol* **2012**, 12, 6346-6354.

125. Zhai, W.; He, C.; Wu, L.; Zhou, Y.; Chen, H.; Chang, J.; Zhang, H. Degradation of Hollow Mesoporous Silica Nanoparticles in Human Umbilical Vein Endothelial Cells. *Journal of Biomedical Materials Research Part B: Applied Biomaterials* **2012**, 100B, 1397-1403.

126. Labbaf, S.; Tsigkou, O.; Müller, K. H.; Stevens, M. M.; Porter, A. E.; Jones, J. R. Spherical Bioactive Glass Particles and Their Interaction with Human Mesenchymal Stem Cells in Vitro. *Biomaterials* **2011**, 32, 1010-1018.

127. Zhao, Y.; Vivero-Escoto, J. L.; Slowing, II; Trewyn, B. G.; Lin, V. S. Capped Mesoporous Silica Nanoparticles as Stimuli-Responsive Controlled Release Systems for Intracellular Drug/Gene Delivery. *Expert Opin Drug Deliv* **2010**, 7, 1013-1029.

128. Jokerst, J. V.; Lobovkina, T.; Zare, R. N.; Gambhir, S. S. Nanoparticle Pegylation for Imaging and Therapy. *Nanomedicine* **2011**, 6, 715-728.

129. Hartanto, J.; Jokerst, J. V. Nanoparticles for Ultrasound-Guided Imaging of Cell Implantation. In *Design and Applications of Nanoparticles in Biomedical Imaging*, Bulte, J. W. M.; Modo, M. M. J., Eds. Springer International Publishing: Cham, 2017; pp 299-314.

130. Zhou, Y.; Han, X.; Jing, X.; Chen, Y. Construction of Silica-Based Micro/Nanoplatforms for Ultrasound Theranostic Biomedicine. *Adv Healthc Mater* **2017**, 6.

131. Ahn, B.; Park, J.; Singha, K.; Park, H.; Kim, W. J. Mesoporous Silica Nanoparticle-Based Cisplatin Prodrug Delivery and Anticancer Effect under Reductive Cellular Environment. *Journal of Materials Chemistry B* **2013**, 1, 2829-2836.

132. Zhang, W.; Shen, J.; Su, H.; Mu, G.; Sun, J.-H.; Tan, C.-P.; Liang, X.-J.; Ji, L.-N.; Mao, Z.-W. Co-Delivery of Cisplatin Prodrug and Chlorin E6 by Mesoporous Silica Nanoparticles for Chemo-Photodynamic Combination Therapy to Combat Drug Resistance. *ACS Applied Materials & Interfaces* **2016**, 8, 13332-13340.

133. Min, Y.; Li, J.; Liu, F.; Yeow, E. K. L.; Xing, B. Near-Infrared Light-Mediated Photoactivation of a Platinum Antitumor Prodrug and Simultaneous Cellular Apoptosis Imaging by Upconversion-Luminescent Nanoparticles. *Angew. Chem.* **2014**, 126, 1030-1034.

134. Yilmaz, M. D.; Xue, M.; Ambrogio, M. W.; Buyukcakir, O.; Wu, Y.; Frasconi, M.; Chen, X.; Nassar, M. S.; Stoddart, J. F.; Zink, J. I. Sugar and Ph Dual-Responsive Mesoporous Silica Nanocontainers Based on Competitive Binding Mechanisms. *Nanoscale* **2014**, 7, 1067-1072.

135. Li, X.; Zhou, L.; Wei, Y.; El-Toni, A. M.; Zhang, F.; Zhao, D. Anisotropic Growth-Induced Synthesis of Dual-Compartment Janus Mesoporous Silica Nanoparticles for Bimodal Triggered Drugs Delivery. *JACS* **2014**, 136, 15086-15092.

136. Khashab, N. M.; Trabolsi, A.; Lau, Y. A.; Ambrogio, M. W.; Friedman, D. C.; Khatib, H. A.; Zink, J. I.; Stoddart, J. F. Redox- and Ph-Controlled Mechanized Nanoparticles. *Eur. J. Org. Chem.* **2009**, 2009, 1669-1673.

137. Qin, Z.; Joo, J.; Gu, L.; Sailor, M. J. Size Control of Porous Silicon Nanoparticles by

Electrochemical Perforation Etching. *Particle & Particle Systems Characterization* **2014**, 31, 252-256.

138. Zhao, D.; Feng, J.; Huo, Q.; Melosh, N.; Fredrickson, G. H.; Chmelka, B. F.; Stucky, G. D. Triblock Copolymer Syntheses of Mesoporous Silica with Periodic 50 to 300 Angstrom Pores. *Science* **1998**, 279, 548-552.

139. Kaehr, B.; Townson, J. L.; Kalinich, R. M.; Awad, Y. H.; Swartzentruber, B. S.; Dunphy, D. R.; Brinker, C. J. Cellular Complexity Captured in Durable Silica Biocomposites. *Proceedings of the National Academy of Sciences* **2012**, 109, 17336-17341.

140. Lou, Y.-R.; Kanninen, L.; Kaehr, B.; Townson, J. L.; Niklander, J.; Harjumäki, R.; Brinker, C. J.; Yliperttula, M. Silica Bioreplication Preserves Three-Dimensional Spheroid Structures of Human Pluripotent Stem Cells and Hepg2 Cells. *Scientific reports* **2015**, 5.

141. Garrett, P. *Defoaming: Theory and Industrial Applications*. CRC Press: 1992; Vol. 45.

142. Anglin, E. J.; Cheng, L.; Freeman, W. R.; Sailor, M. J. Porous Silicon in Drug Delivery Devices and Materials. *Adv Drug Deliv Rev* **2008**, 60, 1266-1277.

143. Zhao, B.; Brittain, W. J. Polymer Brushes: Surface-Immobilized Macromolecules. *Prog. Polym. Sci.* **2000**, 25, 677-710.

144. Belder, G. F.; ten Brinke, G.; Hadziioannou, G. Influence of Anchor Block Size on the Thickness of Adsorbed Block Copolymer Layers. *Langmuir* **1997**, 13, 4102-4105.

145. Peng, J. F.; He, X. X.; Wang, K. M.; Tan, W. H.; Wang, Y.; Liu, Y. Noninvasive Monitoring of Intracellular Ph Change Induced by Drug Stimulation Using Silica Nanoparticle Sensors. *Anal. Bioanal. Chem.* **2007**, 388, 645-654.

146. Wang, Y.; Sun, Y.; Wang, J.; Yang, Y.; Li, Y.; Yuan, Y.; Liu, C. Charge-Reversal Aptes-Modified Mesoporous Silica Nanoparticles with High Drug Loading and Release Controllability. *ACS applied materials & interfaces* **2016**, 8, 17166-17175.

147. Jin, Q.; Lin, C. Y.; Kang, S. T.; Chang, Y. C.; Zheng, H.; Yang, C. M.; Yeh, C. K. Superhydrophobic Silica Nanoparticles as Ultrasound Contrast Agents. *Ultrason. Sonochem.* **2017**, 36, 262-269.

148. He, Q.; Zhang, Z.; Gao, F.; Li, Y.; Shi, J. In Vivo Biodistribution and Urinary Excretion of Mesoporous Silica Nanoparticles: Effects of Particle Size and Pegylation. *Small* **2011**, 7, 271-280.

149. Cauda, V.; Argyo, C.; Bein, T. Impact of Different Pegylation Patterns on the Long-Term Bio-Stability of Colloidal Mesoporous Silica Nanoparticles. *J. Mater. Chem.* **2010**, 20, 8693-8699.

150. He, X. X.; Wang, K. M.; Tan, W. H.; Liu, B.; Lin, X.; He, C. M.; Li, D.; Huang, S. S.; Li, J. Bioconjugated Nanoparticles for DNA Protection from Cleavage. *JACS* **2003**, 125, 7168-7169.

151. Tan, W. H.; Wang, K. M.; He, X. X.; Zhao, X. J.; Drake, T.; Wang, L.; Bagwe, R. P. Bionanotechnology Based on Silica Nanoparticles. *Medicinal Research Reviews* **2004**, 24, 621-638.

152. Shaffer, T. M.; Harmsen, S.; Khwaja, E.; Kircher, M. F.; Drain, C. M.; Grimm, J. Stable Radiolabeling of Sulfur-Functionalized Silica Nanoparticles with Copper-64. *Nano Lett.* **2016**, 16, 5601-5604.

153. van Vlerken, L. E.; Vyas, T. K.; Amiji, M. M. Poly(Ethylene Glycol)-Modified Nanocarriers for Tumor-Targeted and Intracellular Delivery. *Pharm. Res.* **2007**, 24, 1405-1414.

154. Zhang, X.; Shi, F.; Niu, J.; Jiang, Y. G.; Wang, Z. Q. Superhydrophobic Surfaces: From Structural Control to Functional Application. *J. Mater. Chem.* **2008**, 18, 621-633.

155. Jin, Q. F.; Lin, C. Y.; Kang, S. T.; Chang, Y. C.; Zheng, H. R.; Yang, C. M.; Yeh, C. K. Superhydrophobic Silica Nanoparticles as Ultrasound Contrast Agents. *Ultrason. Sonochem.* **2017**, 36, 262-269.

156. Zhang, P.; Kong, J. Doxorubicin-Tethered Fluorescent Silica Nanoparticles for Ph-Responsive Anticancer Drug Delivery. *Talanta* **2015**, 134, 501-507.

157. Popat, A.; Liu, J.; Lu, G. Q. M.; Qiao, S. Z. A Ph-Responsive Drug Delivery System Based on Chitosan Coated Mesoporous Silica Nanoparticles. *J. Mater. Chem.* **2012**, 22, 11173-11178.

158. Agostini, A.; Mondragón, L.; Coll, C.; Aznar, E.; Marcos, M. D.; Martínez-Máñez, R.; Sancenón, F.; Soto, J.; Pérez-Payá, E.; Amorós, P. Dual Enzyme-Triggered Controlled Release on Capped Nanometric Silica Mesoporous Supports. *ChemistryOpen* **2012**, 1, 17-20.

159. Chen, F.; Zhu, Y. Chitosan Enclosed Mesoporous Silica Nanoparticles as Drug Nano-Carriers: Sensitive Response to the Narrow Ph Range. *Microporous Mesoporous Mater.* **2012**, 150, 83-89.

160. Fu, J.; Zhao, Y.; Zhu, Y.; Chen, F. Organics Modified Mesoporous Silica for Controlled Drug Delivery Systems. *Nanomaterials in Drug Delivery, Imaging, and Tissue Engineering*, 237-268.

161. Monaco, I.; Arena, F.; Biffi, S.; Locatelli, E.; Bortot, B.; La Cava, F.; Marini, G. M.; Severini, G. M.; Terreno, E.; Comes Franchini, M. Synthesis of Lipophilic Core-Shell Fe3o4@Sio2@Au Nanoparticles and Polymeric Entrapment into Nanomicelles: A Novel Nanosystem for in Vivo Active Targeting and Magnetic Resonance-Photoacoustic Dual Imaging. *Bioconjug Chem* **2017**, 28, 1382-1390.

162. Popat, A.; Hartono, S. B.; Stahr, F.; Liu, J.; Qiao, S. Z.; Qing Lu, G. Mesoporous Silica Nanoparticles for Bioadsorption, Enzyme Immobilisation, and Delivery Carriers. *Nanoscale* **2011**, 3, 2801-2818.

163. Chen, F.; Hong, H.; Zhang, Y.; Valdovinos, H. F.; Shi, S.; Kwon, G. S.; Theuer, C. P.; Barnhart, T. E.; Cai, W. In Vivo Tumor Targeting and Image-Guided Drug Delivery with Antibody-Conjugated, Radiolabeled Mesoporous Silica Nanoparticles. *ACS Nano* **2013**, 7, 9027-9039.

164. Santra, S.; Bagwe, R. P.; Dutta, D.; Stanley, J. T.; Walter, G. A.; Tan, W.; Moudgil, B. M.; Mericle, R. A. Synthesis and Characterization of Fluorescent, Radio-Opaque, and Paramagnetic Silica Nanoparticles for Multimodal Bioimaging Applications. *Adv. Mater.* **2005**, 17, 2165-2169.

165. Chen, Y. S.; Frey, W.; Kim, S.; Kruizinga, P.; Homan, K.; Emelianov, S. Silica-Coated Gold Nanorods as Photoacoustic Signal Nanoamplifiers. *Nano Lett.* **2011**, 11, 348-354.

166. Zhao, W.; Gu, J.; Zhang, L.; Chen, H.; Shi, J. Fabrication of Uniform Magnetic Nanocomposite Spheres with a Magnetic Core/Mesoporous Silica Shell Structure. *JACS* **2005**, 127, 8916-8917.

167. Wang, H.; Brandl, D. W.; Nordlander, P.; Halas, N. J. Plasmonic Nanostructures: Artificial Molecules. *Acc. Chem. Res.* **2007**, 40, 53-62.

168. Zhang, F.; Braun, G. B.; Shi, Y.; Zhang, Y.; Sun, X.; Reich, N. O.; Zhao, D.; Stucky, G. Fabrication of Ag@Sio2@Y2o3:Er Nanostructures for Bioimaging: Tuning of the Upconversion Fluorescence with Silver Nanoparticles. *JACS* **2010**, 132, 2850-2851.

169. Anderson, B. D.; Wu, W.-C.; Tracy, J. B. Silica Overcoating of Cdse/Cds Core/Shell Quantum Dot Nanorods with Controlled Morphologies. *Chem. Mater.* **2016**, 28, 4945-4952.

170. Rieter, W. J.; Kim, J. S.; Taylor, K. M. L.; An, H.; Lin, W.; Tarrant, T.; Lin, W. Hybrid Silica Nanoparticles for Multimodal Imaging. *Angew. Chem.* **2007**, 119, 3754-3756.

171. Jokerst, J. V.; Khademi, C.; Gambhir, S. S. Intracellular Aggregation of Multimodal Silica Nanoparticles for Ultrasound-Guided Stem Cell Implantation. *Science Translational Medicine* **2013**, 5, 177ra135.

172. Liz-Marzán, L. M.; Giersig, M.; Mulvaney, P. Synthesis of Nanosized Gold−Silica Core−Shell Particles. *Langmuir* **1996**, 12, 4329-4335.

173. Liu, N.; Prall, B. S.; Klimov, V. I. Hybrid Gold/Silica/Nanocrystal-Quantum-Dot Superstructures: Synthesis and Analysis of Semiconductor−Metal Interactions. *JACS* **2006**, 128, 15362-15363.

174. Pohaku Mitchell, K. K.; Liberman, A.; Kummel, A. C.; Trogler, W. C. Iron(Iii)-

Doped, Silica Nanoshells: A Biodegradable Form of Silica. *JACS* **2012**, 134, 13997-14003.

175. Bae, S. W.; Tan, W.; Hong, J.-I. Fluorescent Dye-Doped Silica Nanoparticles: New Tools for Bioapplications. *Chem. Commun.* **2012**, 48, 2270-2282.

176. Zhao, X.; Bagwe, R. P.; Tan, W. Development of Organic-Dye-Doped Silica Nanoparticles in a Reverse Microemulsion. *Adv. Mater.* **2004**, 16, 173-176.

177. Wang, L.; Yang, C.; Tan, W. Dual-Luminophore-Doped Silica Nanoparticles for Multiplexed Signaling. *Nano Lett.* **2005**, 5, 37-43.

178. Santra, S.; Wang, K. M.; Tapec, R.; Tan, W. H. Development of Novel Dye-Doped Silica Nanoparticles for Biomarker Application. *Journal of Biomedical Optics* **2001**, 6, 160-166.

179. Zoetelief, J. Physics in Nuclear Medicine, 4th Edition. *Radiat. Prot. Dosimet.* **2014**, 158, 501-503.

180. James, M. L.; Gambhir, S. S. A Molecular Imaging Primer: Modalities, Imaging Agents, and Applications. *Physiological Reviews* **2012**, 92, 897-965.

181. Weishaupt, D.; Köchli, V.; Marincek, B.; Kim, E. E. How Does Mri Work? An Introduction to the Physics and Function of Magnetic Resonance Imaging. *Journal of Nuclear Medicine* **2007**, 48, 1910-1910.

182. Gambhir, J. V. J. a. S. S. Development of Appropriate Imaging Methods to Trace Cell Fate, Engraftment, and Cell Survival In *Translational Regenerative Medicine*, A. Atala and J. G. Allickson, E., Ed. Academic Press: Boston, Mass, USA, 2015; pp 529–537.

183. James, M. L.; Gambhir, S. S. A Molecular Imaging Primer: Modalities, Imaging Agents, and Applications. *Physiol. Rev.* **2012**, 92, 897-965.

184. Lisle, D. A. *Imaging for Students Fourth Edition*. CRC Press: 2012.

185. Medintz, I. L.; Uyeda, H. T.; Goldman, E. R.; Mattoussi, H. Quantum Dot Bioconjugates for Imaging, Labelling and Sensing. *Nat Mater* **2005**, 4, 435-446.

186. Pu, K.; Shuhendler, A. J.; Jokerst, J. V.; Mei, J.; Gambhir, S. S.; Bao, Z.; Rao, J. Semiconducting Polymer Nanoparticles as Photoacoustic Molecular Imaging Probes in Living Mice. *Nature nanotechnology* **2014**, 9, 233-239.

187. Gleich, B.; Weizenecker, J. Tomographic Imaging Using the Nonlinear Response of Magnetic Particles. *Nature* **2005**, 435, 1214-1217.

188. Ganta, S.; Devalapally, H.; Shahiwala, A.; Amiji, M. A Review of Stimuli-Responsive Nanocarriers for Drug and Gene Delivery. *J. Controlled Release* **2008**, 126, 187-204.

189. Greish, K. Enhanced Permeability and Retention (Epr) Effect for Anticancer

Nanomedicine Drug Targeting. *Cancer Nanotechnology: Methods and Protocols* **2010**, 25-37.

190. Siegel, R. A.; Rathbone, M. J. Overview of Controlled Release Mechanisms. In *Fundamentals and Applications of Controlled Release Drug Delivery*, Springer: 2012; pp 19-43.

191. Singh, N.; Karambelkar, A.; Gu, L.; Lin, K.; Miller, J. S.; Chen, C. S.; Sailor, M. J.; Bhatia, S. N. Bioresponsive Mesoporous Silica Nanoparticles for Triggered Drug Release. *Journal of the American Chemical Society* **2011**, 133, 19582-19585.

192. Bromberg, L. E.; Ron, E. S. Temperature-Responsive Gels and Thermogelling Polymer Matrices for Protein and Peptide Delivery. *Adv. Drug Del. Rev.* **1998**, 31, 197-221.

193. Sershen, S.; Westcott, S.; Halas, N.; West, J. Temperature-Sensitive Polymer–Nanoshell Composites for Photothermally Modulated Drug Delivery. *Journal of biomedical materials research* **2000**, 51, 293-298.

194. Chung, J.; Yokoyama, M.; Yamato, M.; Aoyagi, T.; Sakurai, Y.; Okano, T. Thermo-Responsive Drug Delivery from Polymeric Micelles Constructed Using Block Copolymers of Poly (N-Isopropylacrylamide) and Poly (Butylmethacrylate). *J. Controlled Release* **1999**, 62, 115-127.

195. Chattopadhyay, P.; Gupta, R. B. Supercritical Co2 Based Production of Magnetically Responsive Micro-and Nanoparticles for Drug Targeting. *Industrial & engineering chemistry research* **2002**, 41, 6049-6058.

196. Giri, S.; Trewyn, B. G.; Stellmaker, M. P.; Lin, V. S. Y. Stimuli-Responsive Controlled-Release Delivery System Based on Mesoporous Silica Nanorods Capped with Magnetic Nanoparticles. *Angew. Chem. Int. Ed.* **2005**, 44, 5038-5044.

197. Zhu, Y.; Liu, H.; Li, F.; Ruan, Q.; Wang, H.; Fujiwara, M.; Wang, L.; Lu, G. Dipolar Molecules as Impellers Achieving Electric-Field-Stimulated Release. *JACS* **2010**, 132, 1450-1451.

198. Mal, N. K.; Fujiwara, M.; Tanaka, Y. Photocontrolled Reversible Release of Guest Molecules from Coumarin-Modified Mesoporous Silica. *Nature* **2003**, 421, 350-353.

199. Mal, N. K.; Fujiwara, M.; Tanaka, Y.; Taguchi, T.; Matsukata, M. Photo-Switched Storage and Release of Guest Molecules in the Pore Void of Coumarin-Modified Mcm-41. *Chemistry of Materials* **2003**, 15, 3385-3394.

200. Hrubý, M.; Koňák, Č.; Ulbrich, K. Polymeric Micellar Ph-Sensitive Drug Delivery System for Doxorubicin. *J. Controlled Release* **2005**, 103, 137-148.

201. He, Q.; Gao, Y.; Zhang, L.; Zhang, Z.; Gao, F.; Ji, X.; Li, Y.; Shi, J. A Ph-Responsive Mesoporous Silica Nanoparticles-Based Multi-Drug Delivery System for Overcoming

Multi-Drug Resistance. *Biomaterials* **2011**, 32, 7711-7720.

202. Trewyn, B. G.; Giri, S.; Slowing, I. I.; Lin, V. S.-Y. Mesoporous Silica Nanoparticle Based Controlled Release, Drug Delivery, and Biosensor Systems. *Chem. Commun.* **2007**, 3236-3245.

203. Bernardos, A.; Mondragon, L.; Aznar, E.; Marcos, M. D.; Martínez-Máñez, R. n.; Sancenón, F. l.; Soto, J.; Barat, J. M.; Pérez-Payá, E.; Guillem, C. Enzyme-Responsive Intracellular Controlled Release Using Nanometric Silica Mesoporous Supports Capped with "Saccharides". *Acs Nano* **2010**, 4, 6353-6368.

204. Climent, E.; Bernardos, A.; Martinez-Manez, R.; Maquieira, A.; Marcos, M. D.; Pastor-Navarro, N.; Puchades, R.; Sancenón, F.; Soto, J.; Amorós, P. Controlled Delivery Systems Using Antibody-Capped Mesoporous Nanocontainers. *JACS* **2009**, 131, 14075-14080.

205. Ahmad, S. S.; Duke, S.; Jena, R.; Williams, M. V.; Burnet, N. G. Advances in Radiotherapy. *Bmj* **2012**, 345, e7765.

206. Meek, A. G. Breast Radiotherapy and Lymphedema. *Cancer* **1998**, 83, 2788-2797.

207. Taylor, C. W.; Nisbet, A.; McGale, P.; Darby, S. C. Cardiac Exposures in Breast Cancer Radiotherapy: 1950s–1990s. *International Journal of Radiation Oncology • Biology • Physics* 69, 1484-1495.

208. Falk, M. H.; Issels, R. D. Hyperthermia in Oncology. *Int J Hyperthermia* **2001**, 17, 1-18.

209. Wust, P.; Hildebrandt, B.; Sreenivasa, G.; Rau, B.; Gellermann, J.; Riess, H.; Felix, R.; Schlag, P. M. Hyperthermia in Combined Treatment of Cancer. *Lancet Oncol* **2002**, 3, 487-497.

210. van der Zee, J. Heating the Patient: A Promising Approach? *Ann. Oncol.* **2002**, 13, 1173-1184.

211. Mallory, M.; Gogineni, E.; Jones, G. C.; Greer, L.; Simone, C. B., II Therapeutic Hyperthermia: The Old, the New, and the Upcoming. *Critical Reviews in Oncology / Hematology* 97, 56-64.

212. Hauck, T. S.; Jennings, T. L.; Yatsenko, T.; Kumaradas, J. C.; Chan, W. C. W. Enhancing the Toxicity of Cancer Chemotherapeutics with Gold Nanorod Hyperthermia. *Advanced Materials* **2008**, 20, 3832-3838.

213. Huang, X.; Jain, P. K.; El-Sayed, I. H.; El-Sayed, M. A. Plasmonic Photothermal Therapy (Pptt) Using Gold Nanoparticles. *Lasers in Medical Science* **2007**, 23, 217.

214. Yang, K.; Zhang, S.; Zhang, G.; Sun, X.; Lee, S.-T.; Liu, Z. Graphene in Mice: Ultrahigh in Vivo Tumor Uptake and Efficient Photothermal Therapy. *Nano Lett.* **2010**,

10, 3318-3323.

215. Ohulchanskyy, T. Y.; Roy, I.; Goswami, L. N.; Chen, Y.; Bergey, E. J.; Pandey, R. K.; Oseroff, A. R.; Prasad, P. N. Organically Modified Silica Nanoparticles with Covalently Incorporated Photosensitizer for Photodynamic Therapy of Cancer. *Nano Lett.* **2007**, 7, 2835-2842.

216. Guo, Y.; Kumar, M.; Zhang, P. Nanoparticle-Based Photosensitizers under Cw Infrared Excitation. *Chem. Mater.* **2007**, 19, 6071-6072.

217. Zhang, P.; Steelant, W.; Kumar, M.; Scholfield, M. Versatile Photosensitizers for Photodynamic Therapy at Infrared Excitation. *J. Am. Chem. Soc.* **2007**, 129, 4526-4527.

218. Cheng, S.-H.; Lee, C.-H.; Yang, C.-S.; Tseng, F.-G.; Mou, C.-Y.; Lo, L.-W. Mesoporous Silica Nanoparticles Functionalized with an Oxygen-Sensing Probe for Cell Photodynamic Therapy: Potential Cancer Theranostics. *J. Mater. Chem.* **2009**, 19, 1252-1257.

219. Blattman, J. N.; Greenberg, P. D. Cancer Immunotherapy: A Treatment for the Masses. *Science* **2004**, 305, 200-205.

220. Wang, X.; Li, X.; Ito, A.; Sogo, Y.; Ohno, T. Particle-Size-Dependent Toxicity and Immunogenic Activity of Mesoporous Silica-Based Adjuvants for Tumor Immunotherapy. *Acta Biomater.* **2013**, 9, 7480-7489.

221. Kiessling, F.; Mertens, M. E.; Grimm, J.; Lammers, T. Nanoparticles for Imaging: Top or Flop? *Radiology* **2014**, 273, 10-28.

222. Rogosnitzky, M.; Branch, S. Gadolinium-Based Contrast Agent Toxicity: A Review of Known and Proposed Mechanisms. *BioMetals* **2016**, 29, 365-376.

223. Sweeney, S. K.; Luo, Y.; O'Donnell, M. A.; Assouline, J. Nanotechnology and Cancer: Improving Real-Time Monitoring and Staging of Bladder Cancer with Multimodal Mesoporous Silica Nanoparticles. *Cancer Nanotechnology* **2016**, 7, 3.

224. Chan, M.-H.; Lin, H.-M. Preparation and Identification of Multifunctional Mesoporous Silica Nanoparticles for In vitro and In vivo Dual-Mode Imaging, Theranostics, and Targeted Tracking. *Biomaterials* **2015**, 46, 149-158.

225. Choi, J.; Kim, K.; Kim, T.; Liu, G.; Bar-Shir, A.; Hyeon, T.; McMahon, M. T.; Bulte, J. W.; Fisher, J. P.; Gilad, A. A. Multimodal Imaging of Sustained Drug Release from 3-D Poly (Propylene Fumarate)(Ppf) Scaffolds. *J. Controlled Release* **2011**, 156, 239-245.

226. Monaco, I.; Arena, F.; Biffi, S.; Locatelli, E.; Bortot, B.; La Cava, F.; Marini, G. M.; Severini, G. M.; Terreno, E.; Comes Franchini, M. Synthesis of Lipophilic Core–Shell Fe3o4@Sio2@Au Nanoparticles and Polymeric Entrapment into Nanomicelles: A Novel Nanosystem for in Vivo Active Targeting and Magnetic Resonance–Photoacoustic Dual Imaging. *Bioconj. Chem.* **2017**, 28, 1382-1390.

227. Zhang, Z.; Wang, L.; Wang, J.; Jiang, X.; Li, X.; Hu, Z.; Ji, Y.; Wu, X.; Chen, C. Mesoporous Silica-Coated Gold Nanorods as a Light-Mediated Multifunctional Theranostic Platform for Cancer Treatment. *Adv. Mater.* **2012**, 24, 1418-1423.

228. Kircher, M. F.; de la Zerda, A.; Jokerst, J. V.; Zavaleta, C. L.; Kempen, P. J.; Mittra, E.; Pitter, K.; Huang, R.; Campos, C.; Habte, F.; Sinclair, R.; Brennan, C. W.; Mellinghoff, I. K.; Holland, E. C.; Gambhir, S. S. A Brain Tumor Molecular Imaging Strategy Using a New Triple-Modality Mri-Photoacoustic-Raman Nanoparticle. *Nat. Med.* **2012**, 18, 829-834.

229. Gruenhagen, J. A.; Lai, C.-Y.; Radu, D. R.; Lin, V. S. Y.; Yeung, E. S. Real-Time Imaging of Tunable Adenosine 5-Triphosphate Release from an Mcm-41-Type Mesoporous Silica Nanosphere-Based Delivery System. *Appl. Spectrosc.* **2005**, 59, 424-431.

230. Lai, J. P.; Shah, B. R.; Zhang, Y. X.; Yang, L. T.; Lee, K. B. Real-Time Monitoring of Atp-Responsive Drug Release Using Mesoporous-Silica-Coated Multicolor Upconversion Nanoparticles. *Acs Nano* **2015**, 9, 5234-5245.

231. Liu, J. N.; Bu, J. W.; Bu, W. B.; Zhang, S. J.; Pan, L. M.; Fan, W. P.; Chen, F.; Zhou, L. P.; Peng, W. J.; Zhao, K. L.; Du, J. L.; Shi, J. L. Real-Time in Vivo Quantitative Monitoring of Drug Release by Dual-Mode Magnetic Resonance and Upconverted Luminescence Imaging. *Angewandte Chemie-International Edition* **2014**, 53, 4551-4555.

232. Anselmo, A. C.; Mitragotri, S. A Review of Clinical Translation of Inorganic Nanoparticles. *The AAPS Journal* **2015**, 17, 1041-1054.

233. Wilhelm, S.; Tavares, A. J.; Dai, Q.; Ohta, S.; Audet, J.; Dvorak, H. F.; Chan, W. C. W. Analysis of Nanoparticle Delivery to Tumours. *Nature Reviews Materials* **2016**, 1, 16014.

234. Bohndiek, S. E.; Sasportas, L. S.; Machtaler, S.; Jokerst, J. V.; Hori, S.; Gambhir, S. S. Photoacoustic Tomography Detects Early Vessel Regression and Normalization During Ovarian Tumor Response to the Antiangiogenic Therapy Trebananib. *J Nucl Med* **2015**, 56, 1942-1947.

235. Morris, R. J.; Liu, Y.; Marles, L.; Yang, Z.; Trempus, C.; Li, S.; Lin, J. S.; Sawicki, J. A.; Cotsarelis, G. Capturing and Profiling Adult Hair Follicle Stem Cells. *Nat Biotech* **2004**, 22, 411-417.

236. Shen, W.-B.; Plachez, C.; Tsymbalyuk, O.; Tsymbalyuk, N.; Xu, S.; Smith, A.; Michel, S.; Yarnell, D.; Mullins, R.; Gulapalli, R.; Puche, A.; Simard, J. M.; Fishman, P. S.; Yarowsky, P. Cell-Based Therapy in Tbi: Magnetic Retention of Neural Stem Cells in Vivo. *Cell transplantation* **2016**, 25, 1085-1099.

237. Sanganalmath, S. K.; Bolli, R. Cell Therapy for Heart Failure: A Comprehensive Overview of Experimental and Clinical Studies, Current Challenges, and Future Directions. *Circ Res* **2013**, 113, 810-834.

238. Rodriguez-Porcel, M.; Gheysens, O.; Chen, I. Y.; Wu, J. C.; Gambhir, S. S. Image-Guided Cardiac Cell Delivery Using High-Resolution Small-Animal Ultrasound. *Mol Ther* **2005**, 12, 1142-1147.

239. Vunjak-Novakovic, G.; Lui, K. O.; Tandon, N.; Chien, K. R. Bioengineering Heart Muscle: A Paradigm for Regenerative Medicine. *Annu Rev Biomed Eng* **2011**, 13, 245-267.

240. Kraitchman, D. L.; Heldman, A. W.; Atalar, E.; Amado, L. C.; Martin, B. J.; Pittenger, M. F.; Hare, J. M.; Bulte, J. W. M. In Vivo Magnetic Resonance Imaging of Mesenchymal Stem Cells in Myocardial Infarction. *Circulation* **2003**, 107, 2290-2293.

241. Rodriguez-Porcel, M.; Gheysens, O.; Chen, I. Y.; Wu, J. C.; Gambhir, S. S. Image-Guided Cardiac Cell Delivery Using High-Resolution Small-Animal Ultrasound. *Mol Ther* **2005**, 12, 1142-1147.

242. Jokerst, J. V.; Khademi, C.; Gambhir, S. S. *Intracellular Aggregation of Multimodal Silica Nanoparticles for Ultrasound-Guided Stem Cell Implantation*. Science Translational Medicine: 2013; Vol. 5, p 177ra135-177ra135.

243. Bara, C.; Ghodsizad, A.; Niehaus, M.; Makoui, M.; Piechaczek, C.; Martin, U.; Warnecke, G.; Karck, M.; Gams, E.; Klein, H. M.; Haverich, A.; Ruhparwar, A. In Vivo Echocardiographic Imaging of Transplanted Human Adult Stem Cells in the Myocardium Labeled with Clinically Applicable Clinimacs Nanoparticles. *Journal of the American Society of Echocardiography* **2006**, 19, 563-568.

244. Naumova, A. V.; Modo, M.; Moore, A.; Murry, C. E.; Frank, J. A. Clinical Imaging in Regenerative Medicine. *Nat Biotech* **2014**, 32, 804-818.

245. Cui, W.; Tavri, S.; Benchimol, M. J.; Itani, M.; Olson, E. S.; Zhang, H.; Decyk, M.; Ramirez, R. G.; Barback, C. V.; Kono, Y.; Mattrey, R. F. Neural Progenitor Cells Labeling with Microbubble Contrast Agent for Ultrasound Imaging in Vivo. *Biomaterials* **2013**, 34, 4926-4935.

246. Castaneda, R. T.; Khurana, A.; Khan, R.; Daldrup-Link, H. E. Labeling Stem Cells with Ferumoxytol, an Fda-Approved Iron Oxide Nanoparticle. *JoVE (Journal of Visualized Experiments)* **2011**, 57, e3482-e3482.

247. Park, J. I.; Jagadeesan, D.; Williams, R.; Oakden, W.; Chung, S.; Stanisz, G. J.; Kumacheva, E. Microbubbles Loaded with Nanoparticles: A Route to Multiple Imaging Modalities. *ACS Nano* **2010**, 4, 6579-6586.

248. Ommen, S.; Nishimura, R.; Appleton, C.; Miller, F.; Oh, J.; Redfield, M.; Tajik, A. Clinical Utility of Doppler Echocardiography and Tissue Doppler Imaging in the Estimation of Left Ventricular Filling Pressures a Comparative Simultaneous Doppler-Catheterization Study. *Circulation* **2000**, 102, 1788-1794.

249. Sandrin, L.; Fourquet, B.; Hasquenoph, J.-M.; Yon, S.; Fournier, C.; Mal, F.;

Christidis, C.; Ziol, M.; Poulet, B.; Kazemi, F. Transient Elastography: A New Noninvasive Method for Assessment of Hepatic Fibrosis. *Ultrasound Med. Biol.* **2003**, 29, 1705-1713.

250. Ku, G.; Fornage, B. D.; Jin, X.; Xu, M.; Hunt, K. K.; Wang, L. V. Thermoacoustic and Photoacoustic Tomography of Thick Biological Tissues toward Breast Imaging. *Technology in cancer research & treatment* **2005**, 4, 559-565.

251. Klibanov, A. L. Microbubble Contrast Agents: Targeted Ultrasound Imaging and Ultrasound-Assisted Drug-Delivery Applications. *Investigative Radiology* **2006**, 41, 354-362.

252. Mattrey, R. F.; Strich, G.; Shelton, R. E.; Gosink, B. B.; Leopold, G. R.; Lee, T.; Forsythe, J. Perfluorochemicals as Us Contrast Agents for Tumor Imaging and Hepatosplenography: Preliminary Clinical Results. *Radiology* **1987**, 163, 339-343.

253. Wilson, K. E.; Wang, T. Y.; Willmann, J. K. Acoustic and Photoacoustic Molecular Imaging of Cancer. *Journal of Nuclear Medicine* **2013**, 54, 1851-1854.

254. Hu, H.; Zhou, H.; Du, J.; Wang, Z.; An, L.; Yang, H.; Li, F.; Wu, H.; Yang, S. Biocompatiable Hollow Silica Microspheres as Novel Ultrasound Contrast Agents for in Vivo Imaging. *Journal of Materials Chemistry* **2011**, 21, 6576-6583.

255. Milgroom, A.; Intrator, M.; Madhavan, K.; Mazzaro, L.; Shandas, R.; Liu, B.; Park, D. Mesoporous Silica Nanoparticles as a Breast-Cancer Targeting Ultrasound Contrast Agent. *Colloids Surf. B. Biointerfaces* **2014**, 116, 652-657.

256. Ma, M.; Chen, H.; Shi, J. Construction of Smart Inorganic Nanoparticle-Based Ultrasound Contrast Agents and Their Biomedical Applications. *Science Bulletin* **2015**, 60, 1170-1183.

257. Benezra, M.; Penate-Medina, O.; Zanzonico, P. B.; Schaer, D.; Ow, H.; Burns, A.; DeStanchina, E.; Longo, V.; Herz, E.; Iyer, S.; Wolchok, J.; Larson, S. M.; Wiesner, U.; Bradbury, M. S. Multimodal Silica Nanoparticles Are Effective Cancer-Targeted Probes in a Model of Human Melanoma. *The Journal of Clinical Investigation* **2011**, 121, 2768-2780.

258. Liberman, A.; Mendez, N.; Trogler, W. C.; Kummel, A. C. Synthesis and Surface Functionalization of Silica Nanoparticles for Nanomedicine. *Surf. Sci. Rep.* **2014**, 69, 132-158.

259. Colilla, M.; Gonzalez, B.; Vallet-Regi, M. Mesoporous Silica Nanoparticles for the Design of Smart Delivery Nanodevices. *Biomaterials Science* **2013**, 1, 114-134.

260. Croissant, J. G.; Cattoen, X.; Wong Chi Man, M.; Durand, J.-O.; Khashab, N. M. Syntheses and Applications of Periodic Mesoporous Organosilica Nanoparticles. *Nanoscale* **2015**, 7, 20318-20334.

261. Zhang, K.; Xu, L.-L.; Jiang, J.-G.; Calin, N.; Lam, K.-F.; Zhang, S.-J.; Wu, H.-H.; Wu, G.-D.; Albela, B.; Bonneviot, L.; Wu, P. Facile Large-Scale Synthesis of Monodisperse Mesoporous Silica Nanospheres with Tunable Pore Structure. *JACS* **2013**, 135, 2427-2430.

262. Kruk, M. Access to Ultralarge-Pore Ordered Mesoporous Materials through Selection of Surfactant/Swelling-Agent Micellar Templates. *Acc. Chem. Res.* **2012**, 45, 1678-1687.

263. Liberman, A.; Martinez, H. P.; Ta, C. N.; Barback, C. V.; Mattrey, R. F.; Kono, Y.; Blair, S. L.; Trogler, W. C.; Kummel, A. C.; Wu, Z. Hollow Silica and Silica-Boron Nano/Microparticles for Contrast-Enhanced Ultrasound to Detect Small Tumors. *Biomaterials* **2012**.

264. Chen, F.; Zhu, Y. Chitosan Enclosed Mesoporous Silica Nanoparticles as Drug Nano-Carriers: Sensitive Response to the Narrow Ph Range. *Microporous and Mesoporous Materials* **2012**, 150, 83-89.

265. Zhang, Y.; Jiang, T.; Zhang, Q.; Wang, S. Inclusion of Telmisartan in Mesocellular Foam Nanoparticles: Drug Loading and Release Property. *European Journal of Pharmaceutics and Biopharmaceutics* **2010**, 76, 17-23.

266. Abràmoff, M. D.; Magalhães, P. J.; Ram, S. J. Image Processing with Imagej. *Biophotonics international* **2004**, 11, 36-42.

267. Lin, P. L.; Eckersley, R. J.; Hall, E. A. Ultrabubble: A Laminated Ultrasound Contrast Agent with Narrow Size Range. *Adv. Mater.* **2009**, 21, 3949-3952.

268. Chung, T.-H.; Wu, S.-H.; Yao, M.; Lu, C.-W.; Lin, Y.-S.; Hung, Y.; Mou, C.-Y.; Chen, Y.-C.; Huang, D.-M. The Effect of Surface Charge on the Uptake and Biological Function of Mesoporous Silica Nanoparticles in 3t3-L1 Cells and Human Mesenchymal Stem Cells. *Biomaterials* **2007**, 28, 2959-2966.

269. Lin, Y.-S.; Abadeer, N.; Hurley, K. R.; Haynes, C. L. Ultrastable, Redispersible, Small, and Highly Organomodified Mesoporous Silica Nanotherapeutics. *JACS* **2011**, 133, 20444-20457.

270. Durfee, P. N.; Lin, Y.-S.; Dunphy, D. R.; Muñiz, A. J.; Butler, K. S.; Humphrey, K. R.; Lokke, A. J.; Agola, J. O.; Chou, S. S.; Chen, I. M.; Wharton, W.; Townson, J. L.; Willman, C. L.; Brinker, C. J. Mesoporous Silica Nanoparticle-Supported Lipid Bilayers (Protocells) for Active Targeting and Delivery to Individual Leukemia Cells. *ACS Nano* **2016**, 10, 8325-8345.

271. Théry, C.; Amigorena, S.; Raposo, G.; Clayton, A. Isolation and Characterization of Exosomes from Cell Culture Supernatants and Biological Fluids. In *Current Protocols in Cell Biology*, John Wiley & Sons, Inc.: 2001.

272. Casciaro, S.; Conversano, F.; Ragusa, A.; Malvindi, M. A.; Franchini, R.; Greco, A.; Pellegrino, T.; Gigli, G. Optimal Enhancement Configuration of Silica Nanoparticles for

Ultrasound Imaging and Automatic Detection at Conventional Diagnostic Frequencies. *Invest Radiol* **2010**, 45, 715-724.

273. Chiriacò, F.; Conversano, F.; Soloperto, G.; Casciaro, E.; Ragusa, A.; Sbenaglia, E.; Dipaola, L.; Casciaro, S. Epithelial Cell Biocompatibility of Silica Nanospheres for Contrast-Enhanced Ultrasound Molecular Imaging. *J. Nanopart. Res.* **2013**, 15, 1-13.

274. Rahman, I. A.; Vejayakumaran, P.; Sipaut, C. S.; Ismail, J.; Chee, C. K. Size-Dependent Physicochemical and Optical Properties of Silica Nanoparticles. *Mater. Chem. Phys.* **2009**, 114, 328-332.

275. Szekeres, M.; Toth, J.; Dekany, I. Specific Surface Area of Stoeber Silica Determined by Various Experimental Methods. *Langmuir* **2002**, 18, 2678-2685.

276. Don, C. W.; Murry, C. E. Improving Survival and Efficacy of Pluripotent Stem Cell-Derived Cardiac Grafts. *J. Cell. Mol. Med.* **2013**, 17, 1355-1362.

277. Kutschka, I.; Kofidis, T.; Chen, I. Y.; von Degenfeld, G.; Zwierzchoniewska, M.; Hoyt, G.; Arai, T.; Lebl, D. R.; Hendry, S. L.; Sheikh, A. Y.; Cooke, D. T.; Connolly, A.; Blau, H. M.; Gambhir, S. S.; Robbins, R. C. Adenoviral Human Bcl-2 Transgene Expression Attenuates Early Donor Cell Death after Cardiomyoblast Transplantation into Ischemic Rat Hearts. *Circulation* **2006**, 114, I-174-I-180.

278. Niedermayer, S.; Weiss, V.; Herrmann, A.; Schmidt, A.; Datz, S.; Müller, K.; Wagner, E.; Bein, T.; Bräuchle, C. Multifunctional Polymer-Capped Mesoporous Silica Nanoparticles for Ph-Responsive Targeted Drug Delivery. *Nanoscale* **2015**, 7, 7953-7964.

279. Palanikumar, L.; Choi, E. S.; Cheon, J. Y.; Joo, S. H.; Ryu, J. H. Noncovalent Polymer-Gatekeeper in Mesoporous Silica Nanoparticles as a Targeted Drug Delivery Platform. *Adv. Funct. Mater.* **2015**, 25, 957-965.

280. Laflamme, M. A.; Chen, K. Y.; Naumova, A. V.; Muskheli, V.; Fugate, J. A.; Dupras, S. K.; Reinecke, H.; Xu, C.; Hassanipour, M.; Police, S. Cardiomyocytes Derived from Human Embryonic Stem Cells in Pro-Survival Factors Enhance Function of Infarcted Rat Hearts. *Nat. Biotechnol.* **2007**, 25, 1015-1024.

281. Davis, M. E.; Hsieh, P. C.; Takahashi, T.; Song, Q.; Zhang, S.; Kamm, R. D.; Grodzinsky, A. J.; Anversa, P.; Lee, R. T. Local Myocardial Insulin-Like Growth Factor 1 (Igf-1) Delivery with Biotinylated Peptide Nanofibers Improves Cell Therapy for Myocardial Infarction. *Proceedings of the National Academy of Sciences* **2006**, 103, 8155-8160.

282. Haider, H. K.; Jiang, S.; Idris, N. M.; Ashraf, M. Igf-1–Overexpressing Mesenchymal Stem Cells Accelerate Bone Marrow Stem Cell Mobilization Via Paracrine Activation of Sdf-1α/Cxcr4 Signaling to Promote Myocardial Repair. *Circul. Res.* **2008**, 103, 1300-1308.

283. Yakimova, R.; Petoral, R. M.; Yazdi, G. R.; Vahlberg, C.; Spetz, A. L.; Uvdal, K. Surface Functionalization and Biomedical Applications Based on Sic. *Journal of Physics*

D-Applied Physics **2007**, 40, 6435-6442.

284. Cacchioli, A.; Ravanetti, F.; Alinovi, R.; Pinelli, S.; Rossi, F.; Negri, M.; Bedogni, E.; Campanini, M.; Galetti, M.; Goldoni, M.; Lagonegro, P.; Alfieri, R.; Bigi, F.; Salviati, G. Cytocompatibility and Cellular Internalization Mechanisms of Sic/Sio2 Nanowires. *Nano Lett.* **2014**, 14, 4368-4375.

285. Saddow, S. E.; Agarwal, A. *Advances in Silicon Carbide Processing and Applications*. Artech House: 2004.

286. Botsoa, J.; Lysenko, V.; Géloën, A.; Marty, O.; Bluet, J. M.; Guillot, G. Application of 3c-Sic Quantum Dots for Living Cell Imaging. *Appl. Phys. Lett.* **2008**, 92, 173902.

287. Seong, H. K.; Choi, H. J.; Lee, S. K.; Lee, J. I.; Choi, D. J. Optical and Electrical Transport Properties in Silicon Carbide Nanowires. *Appl. Phys. Lett.* **2004**, 85, 1256-1258.

288. Tatti, R.; Timpel, M.; Nardi, M. V.; Fabbri, F.; Rossi, R.; Pasquardini, L.; Chiasera, A.; Aversa, L.; Koshmak, K.; Giglia, A.; Pasquali, L.; Rimoldi, T.; Cristofolini, L.; Attolini, G.; Varas, S.; Iannotta, S.; Verucchi, R.; Salviati, G. Functionalization of Sic/Siox Nanowires with a Porphyrin Derivative: A Hybrid Nanosystem for X-Ray Induced Singlet Oxygen Generation. *Molecular Systems Design & Engineering* **2017**, 2, 165-172.

289. Rossi, F.; Lagonegro, P.; Negri, M.; Fabbri, F.; Salviati, G.; Alinovi, R.; Pinelli, S.; Ravanetti, F.; Cacchioli, A.; Bedogni, E.; Bigi, F.; Rimoldi, T.; Cristofolini, L.; Galli, C.; Smerieri, A.; Macaluso, G. M. Silicon Carbide-Based Nanowires for Biomedical Applications. **2016**, 311-342.

290. Bano, E.; Fradetal, L.; Ollivier, M.; Choi, J.-H.; Stambouli, V. Sic Nanowire-Based Transistors for Electrical DNA Detection. **2016**, 261-310.

291. Knaack, G. L.; Charkhkar, H.; Cogan, S. F.; Pancrazio, J. J. Amorphous Silicon Carbide for Neural Interface Applications. **2016**, 249-260.

292. Iannotta, S.; Romeo, A.; D'Angelo, P.; Tarabella, G. Sic Biosensing and Electrochemical Sensing: State of the Art and Perspectives. **2016**, 143-177.

293. Zhang, L. G.; Yang, W. Y.; Jin, H.; Zheng, Z. H.; Xie, Z. P.; Miao, H. Z.; An, L. N. Ultraviolet Photoluminescence from 3c-Sic Nanorods. *Appl. Phys. Lett.* **2006**, 89.

294. Fan, J. Y.; Wu, X. L.; Chu, P. K. Low-Dimensional Sic Nanostructures: Fabrication, Luminescence, and Electrical Properties. *Progress in Materials Science* **2006**, 51, 983-1031.

295. Wu, X. L.; Fan, J. Y.; Qiu, T.; Yang, X.; Siu, G. G.; Chu, P. K. Experimental Evidence for the Quantum Confinement Effect in 3c-Sic Nanocrystallites. *Phys. Rev. Lett.* **2005**, 94, 026102.

296. Fan, J.; Wu, X.; Chu, P. K. Low-Dimensional Sic Nanostructures: Fabrication,

Luminescence, and Electrical Properties. *Progress in Materials Science* **2006**, 51, 983-1031.

297. Seleverstov, O.; Zabirnyk, O.; Zscharnack, M.; Bulavina, L.; Nowicki, M.; Heinrich, J.-M.; Yezhelyev, M.; Emmrich, F.; O'Regan, R.; Bader, A. Quantum Dots for Human Mesenchymal Stem Cells Labeling. A Size-Dependent Autophagy Activation. *Nano Lett.* **2006**, 6, 2826-2832.

298. Jokerst, J. V.; Gambhir, S. S. Molecular Imaging with Theranostic Nanoparticles. *Acc. Chem. Res.* **2011**, 44, 1050-1060.

299. Li, G. Y.; Li, X. D.; Chen, Z. D.; Wang, J.; Wang, H.; Cho, R. C. Large Areas of Centimeters-Long Sic Nanowires Synthesized by Pyrolysis of a Polymer Precursor by a Cvd Route. *Journal of Physical Chemistry C* **2009**, 113, 17655-17660.

300. Li, G. Y.; Ma, J.; Peng, G.; Chen, W.; Chu, Z. Y.; Li, Y. H.; Hu, T. J.; Li, X. D. Room-Temperature Humidity-Sensing Performance of Sic Nanopaper. *Acs Applied Materials & Interfaces* **2014**, 6, 22673-22679.

301. Allen, M.; Butter, R.; Chandra, L.; Lettington, A.; Rushton, N. Toxicity of Particulate Silicon Carbide for Macrophages, Fibroblasts and Osteoblast-Like Cells in Vitro. *Biomed Mater Eng* **1995**, 5, 151-159.

302. Mzyk, A.; Major, R.; Lackner, J. M.; Bruckert, F.; Major, B. Cytotoxicity Control of Sic Nanoparticles Introduced into Polyelectrolyte Multilayer Films. *RSC Advances* **2014**, 4, 31948-31954.

303. Derfus, A. M.; Chan, W. C. W.; Bhatia, S. N. Probing the Cytotoxicity of Semiconductor Quantum Dots. *Nano Lett.* **2004**, 4, 11-18.

304. Bilberg, K.; Hovgaard, M. B.; Besenbacher, F.; Baatrup, E. In Vivo Toxicity of Silver Nanoparticles and Silver Ions in Zebrafish (Danio Rerio). *J Toxicol* **2012**, 2012, 293784.

305. Ekkapongpisit, M.; Giovia, A.; Follo, C.; Caputo, G.; Isidoro, C. Biocompatibility, Endocytosis, and Intracellular Trafficking of Mesoporous Silica and Polystyrene Nanoparticles in Ovarian Cancer Cells: Effects of Size and Surface Charge Groups. *International journal of nanomedicine* **2012**, 7, 4147.

306. Bhirde, A.; Xie, J.; Swierczewska, M.; Chen, X. Nanoparticles for Cell Labeling. *Nanoscale* **2011**, 3, 142-153.

307. El-Gamel, N. E. A. Silver(I) Complexes as Precursors to Produce Silver Nanowires: Structure Characterization, Antimicrobial Activity and Cell Viability. *Dalton Transactions* **2013**, 42, 9884-9892.

308. Peng, P.; Lu, Y.; Liu, X. Y.; Feng, C. X. Study of Preceramic Polymers. *Microchem. J.* **1996**, 53, 273-281.

309. Chen, F.; Li, G.; Zhao, E. R.; Li, J.; Hableel, G.; Lemaster, J. E.; Bai, Y.; Sen, G. L.; Jokerst, J. V. Cellular Toxicity of Silicon Carbide Nanomaterials as a Function of Morphology. *Biomaterials* **2018**, 179, 60-70.

310. Jokerst, J. V.; Thangaraj, M.; Kempen, P. J.; Sinclair, R.; Gambhir, S. S. Photoacoustic Imaging of Mesenchymal Stem Cells in Living Mice Via Silica-Coated Gold Nanorods. *ACS Nano* **2012**, 6, 5920-5930.

311. Katsen-Globa, A.; Meiser, I.; Petrenko, Y. A.; Ivanov, R. V.; Lozinsky, V. I.; Zimmermann, H.; Petrenko, A. Y. Towards Ready-to-Use 3-D Scaffolds for Regenerative Medicine: Adhesion-Based Cryopreservation of Human Mesenchymal Stem Cells Attached and Spread within Alginate-Gelatin Cryogel Scaffolds. *J. Mater. Sci. Mater. Med.* **2014**, 25, 857-871.

312. Tylek, T.; Schlegelmilch, K.; Ewald, A.; Rudert, M.; Jakob, F.; Groll, J. Cell Communication Modes and Bidirectional Mitochondrial Exchange in Direct and Indirect Macrophage/Hmsc Co-Culture Models. In *BioNanoMaterials*, 2017; Vol. 18.

313. Gong, Z.; Niklason, L. E. Small-Diameter Human Vessel Wall Engineered from Bone Marrow-Derived Mesenchymal Stem Cells (Hmscs). *The FASEB journal : official publication of the Federation of American Societies for Experimental Biology* **2008**, 22, 1635-1648.

314. L. Ramos, T.; Sánchez-Abarca, L. I.; Muntión, S.; Preciado, S.; Puig, N.; López-Ruano, G.; Hernández-Hernández, Á.; Redondo, A.; Ortega, R.; Rodríguez, C.; Sánchez-Guijo, F.; del Cañizo, C. Msc Surface Markers (Cd44, Cd73, and Cd90) Can Identify Human Msc-Derived Extracellular Vesicles by Conventional Flow Cytometry. *Cell Communication and Signaling : CCS* **2016**, 14, 2.

315. Dominici, M.; Le Blanc, K.; Mueller, I.; Slaper-Cortenbach, I.; Marini, F.; Krause, D.; Deans, R.; Keating, A.; Prockop, D.; Horwitz, E. Minimal Criteria for Defining Multipotent Mesenchymal Stromal Cells. The International Society for Cellular Therapy Position Statement. *Cytotherapy* **2006**, 8, 315-317.

316. Pierelli, L.; Bonanno, G.; Rutella, S.; Marone, M.; Scambia, G.; Leone, G. Cd105 (Endoglin) Expression on Hematopoietic Stem/Progenitor Cells. *Leuk. Lymphoma* **2001**, 42, 1195-1206.

317. Regateiro, F. S.; Cobbold, S. P.; Waldmann, H. Cd73 and Adenosine Generation in the Creation of Regulatory Microenvironments. *Clin. Exp. Immunol.* **2013**, 171, 1-7.

318. Wetzel, A.; Chavakis, T.; Preissner, K. T.; Sticherling, M.; Haustein, U.-F.; Anderegg, U.; Saalbach, A. Human Thy-1 (Cd90) on Activated Endothelial Cells Is a Counterreceptor for the Leukocyte Integrin Mac-1 (Cd11b/Cd18). *The Journal of Immunology* **2004**, 172, 3850-3859.

319. Li, J.; Pei, M. Cell Senescence: A Challenge in Cartilage Engineering and Regeneration. *Tissue Engineering Part B: Reviews* **2012**, 18, 270-287.

320. Heymer, A.; Haddad, D.; Weber, M.; Gbureck, U.; Jakob, P. M.; Eulert, J.; Nöth, U. Iron Oxide Labelling of Human Mesenchymal Stem Cells in Collagen Hydrogels for Articular Cartilage Repair. *Biomaterials* **2008**, 29, 1473-1483.

321. Batsali, A. K.; Pontikoglou, C.; Koutroulakis, D.; Pavlaki, K. I.; Damianaki, A.; Mavroudi, I.; Alpantaki, K.; Kouvidi, E.; Kontakis, G.; Papadaki, H. A. Differential Expression of Cell Cycle and Wnt Pathway-Related Genes Accounts for Differences in the Growth and Differentiation Potential of Wharton's Jelly and Bone Marrow-Derived Mesenchymal Stem Cells. *Stem Cell Research & Therapy* **2017**, 8, 102.

322. Deshmane, S. L.; Kremlev, S.; Amini, S.; Sawaya, B. E. Monocyte Chemoattractant Protein-1 (Mcp-1): An Overview. *J. Interferon Cytokine Res.* **2009**, 29, 313-326.

323. Gerszten, R. E.; Garcia-Zepeda, E. A.; Lim, Y.-C.; Yoshida, M.; Ding, H. A.; Gimbrone Jr, M. A.; Luster, A. D.; Luscinskas, F. W.; Rosenzweig, A. Mcp-1 and Il-8 Trigger Firm Adhesion of Monocytes to Vascular Endothelium under Flow Conditions. *Nature* **1999**, 398, 718.

324. Gerhardt, C. C.; Romero, I. A.; Cancello, R.; Camoin, L.; Strosberg, A. D. Chemokines Control Fat Accumulation and Leptin Secretion by Cultured Human Adipocytes. *Mol. Cell. Endocrinol.* **2001**, 175, 81-92.

325. Sahu, A.; Lambris, J. D. Structure and Biology of Complement Protein C3, a Connecting Link between Innate and Acquired Immunity. *Immunol. Rev.* **2001**, 180, 35-48.

326. Matsuyama, W.; Nakagawa, M.; Takashima, H.; Muranaga, F.; Sano, Y.; Osame, M. Molecular Analysis of Hereditary Deficiency of the Third Component of Complement (C3) in Two Sisters. *Internal Medicine* **2001**, 40, 1254-1258.

327. Almalki, S. G.; Agrawal, D. K. Effects of Matrix Metalloproteinases on the Fate of Mesenchymal Stem Cells. *Stem Cell Research & Therapy* **2016**, 7, 129.

328. Cathcart, J.; Pulkoski-Gross, A.; Cao, J. Targeting Matrix Metalloproteinases in Cancer: Bringing New Life to Old Ideas. *Genes & Diseases* **2015**, 2, 26-34.

329. Laflamme, M. A.; Chen, K. Y.; Naumova, A. V.; Muskheli, V.; Fugate, J. A.; Dupras, S. K.; Reinecke, H.; Xu, C.; Hassanipour, M.; Police, S.; O'Sullivan, C.; Collins, L.; Chen, Y.; Minami, E.; Gill, E. A.; Ueno, S.; Yuan, C.; Gold, J.; Murry, C. E. Cardiomyocytes Derived from Human Embryonic Stem Cells in Pro-Survival Factors Enhance Function of Infarcted Rat Hearts. *Nat Biotech* **2007**, 25, 1015-1024.

330. Bolli, R.; Chugh, A. R.; D'Amario, D.; Loughran, J. H.; Stoddard, M. F.; Ikram, S.; Beache, G. M.; Wagner, S. G.; Leri, A.; Hosoda, T.; Sanada, F.; Elmore, J. B.; Goichberg, P.; Cappetta, D.; Solankhi, N. K.; Fahsah, I.; Rokosh, D. G.; Slaughter, M. S.; Kajstura, J.; Anversa, P. Cardiac Stem Cells in Patients with Ischaemic Cardiomyopathy (Scipio): Initial Results of a Randomised Phase 1 Trial. *Lancet* **2011**, 378, 1847-1857.

331. Saddow, S. E. Silicon Carbide Materials For biomedical Applications. **2016**, 1-25.

332. Xu, S. J.; Yu, M. B.; Rusli; Yoon, S. F.; Che, C. M. Time-Resolved Photoluminescence Spectra of Strong Visible Light-Emitting Sic Nanocrystalline Films on Si Deposited by Electron-Cyclotron-Resonance Chemical-Vapor Deposition. *Applied Physics Letters* **2000**, 76, 2550-2552.

333. Fan, J. Y.; Li, H. X.; Iiang, J.; So, L. K. Y.; Lam, Y. W.; Chu, P. K. 3c-Sic Nanocrystals as Fluorescent Biological Labels. *Small* **2008**, 4, 1058-1062.

334. Zakharko, Y.; Serdiuk, T.; Nychyporuk, T.; Geloen, A.; Lemiti, M.; Lysenko, V. Plasmon-Enhanced Photoluminescence of Sic Quantum Dots for Cell Imaging Applications. *Plasmonics* **2012**, 7, 725-732.

335. Beke, D.; Szekrenyes, Z.; Palfi, D.; Rona, G.; Balogh, I.; Maak, P. A.; Katona, G.; Czigany, Z.; Kamaras, K.; Rozsa, B.; Buday, L.; Vertessy, B.; Gali, A. Silicon Carbide Quantum Dots for Bioimaging. *J. Mater. Res.* **2013**, 28, 205-209.

336. Rogov, A.; Rogov, A.; Mugnier, Y.; Le Dantec, R.; Lysenko, V.; Geloen, A.; Timoshenko, V.; Joulaud, C.; Kyrychenko, A.; Tishchenko, I. In *Nonlinear Optical Properties of Silicon Carbide (Sic) Nanoparticles by Carbothermal Reduction*, Colloidal Nanoparticles for Biomedical Applications XI, International Society for Optics and Photonics: 2016; p 972213.

337. Boksebeld, M.; Kilin, V.; Geloen, A.; Ceccone, G.; Jaffal, A.; Schmidt, C.; Alekseev, S.; Lysenko, V.; Wolf, J.-P.; Bonacina, L. Folate-Modified Silicon Carbide Nanoparticles as Multiphoton Imaging Nanoprobes for Cancer-Cell-Specific Labeling. *RSC Advances* **2017**, 7, 27361-27369.

338. Xu, M. H.; Wang, L. H. V. Photoacoustic Imaging in Biomedicine. *Rev. Sci. Instrum.* **2006**, 77.

339. Mercado, C.; Welling, J.; Oliva, M.; Li, J.; Gurung, R.; Ruit, S.; Tabin, G.; Chang, D.; Myung, D. Clinical Application of a Smartphone-Based Ophthalmic Camera Adapter in under-Resourced Settings in Nepal. *Journal of Mobile Technology in Medicine* **2017**, 6, 34-42.

340. Singh, B. P.; Jena, J.; Besra, L.; Bhattacharjee, S. Dispersion of Nano-Silicon Carbide (Sic) Powder in Aqueous Suspensions. *J. Nanopart. Res.* **2007**, 9, 797-806.

341. La Via, F.; Severino, A.; Anzalone, R.; Bongiorno, C.; Litrico, G.; Mauceri, M.; Schoeler, M.; Schuh, P.; Wellmann, P. From Thin Film to Bulk 3c-Sic Growth: Understanding the Mechanism of Defects Reduction. *Mater. Sci. Semicond. Process.* **2018**, 78, 57-68.

342. Fan, J.; Chu, P. K. Group Iv Nanoparticles: Synthesis, Properties, and Biological Applications. *Small* **2010**, 6, 2080-2098.

343. Heinrich, J. L.; Curtis, C. L.; Credo, G. M.; Kavanagh, K. L.; Sailor, M. J. Luminescent Colloidal Si Suspensions from Porous Si. *Science* **1992**, 255, 66-68.

344. Yao, J.; Wang, L. V. Sensitivity of Photoacoustic Microscopy. *Photoacoustics* **2014**, 2, 87-101.

345. Yoon, H.; Luke, G. P.; Emelianov, S. Y. Impact of Depth-Dependent Optical Attenuation on Wavelength Selection for Spectroscopic Photoacoustic Imaging. *Photoacoustics* **2018**, 12, 46-54.

346. Zhang, B.; Fang, C.-Y.; Chang, C.-C.; Peterson, R.; Maswadi, S.; Glickman, R. D.; Chang, H.-C.; Ye, J. Y. Photoacoustic Emission from Fluorescent Nanodiamonds Enhanced with Gold Nanoparticles. *Biomedical optics express* **2012**, 3, 1662-1629.

347. Su, X.; Kuang, L.; Battle, C.; Shaner, T.; Mitchell, B. S.; Fink, M. J.; Jayawickramarajah, J. Mild Two-Step Method to Construct DNA-Conjugated Silicon Nanoparticles: Scaffolds for the Detection of Microrna-21. *Bioconj. Chem.* **2014**, 25, 1739-1743.

348. Slowing, II; Vivero-Escoto, J. L.; Wu, C. W.; Lin, V. S. Mesoporous Silica Nanoparticles as Controlled Release Drug Delivery and Gene Transfection Carriers. *Adv Drug Deliv Rev* **2008**, 60, 1278-1288.

349. Wang, Y.; Pu, K.-Y.; Liu, B. Anionic Conjugated Polymer with Aptamer-Functionalized Silica Nanoparticle for Label-Free Naked-Eye Detection of Lysozyme in Protein Mixtures. *Langmuir* **2010**, 26, 10025-10030.

350. Mahmoodi, N. M.; Maghsoudi, A.; Najafi, F.; Jalili, M.; Kharrati, H. Primary-Secondary Amino Silica Nanoparticle: Synthesis and Dye Removal from Binary System. *Desalination and Water Treatment* **2014**, 52, 7784-7796.

351. Mahmoodi, N. M.; Khorramfar, S.; Najafi, F. Amine-Functionalized Silica Nanoparticle: Preparation, Characterization and Anionic Dye Removal Ability. *Desalination* **2011**, 279, 61-68.

352. Karim, A. H.; Jalil, A. A.; Triwahyono, S.; Sidik, S. M.; Kamarudin, N. H. N.; Jusoh, R.; Jusoh, N. W. C.; Hameed, B. H. Amino Modified Mesostructured Silica Nanoparticles for Efficient Adsorption of Methylene Blue. *J. Colloid Interface Sci.* **2012**, 386, 307-314.

353. Nayab, S.; Farrukh, A.; Oluz, Z.; Tuncel, E. l.; Tariq, S. R.; Rahman, H. u.; Kirchhoff, K.; Duran, H.; Yameen, B. Design and Fabrication of Branched Polyamine Functionalized Mesoporous Silica: An Efficient Absorbent for Water Remediation. *ACS applied materials & interfaces* **2014**, 6, 4408-4417.

354. Yan, Z.; Tao, S. Y.; Yin, J. X.; Li, G. T. Mesoporous Silicas Functionalized with a High Density of Carboxylate Groups as Efficient Absorbents for the Removal of Basic Dyestuffs. *J. Mater. Chem.* **2006**, 16, 2347-2353.

355. Ho, K. Y.; McKay, G.; Yeung, K. L. Selective Adsorbents from Ordered Mesoporous Silica. *Langmuir* **2003**, 19, 3019-3024.

356. Krysztafkiewicz, A.; Binkowski, S.; Jesionowski, T. Adsorption of Dyes on a Silica Surface. *Appl. Surf. Sci.* **2002**, 199, 31-39.

357. Etienne, M.; Walcarius, A. Analytical Investigation of the Chemical Reactivity and Stability of Aminopropyl-Grafted Silica in Aqueous Medium. *Talanta* **2003**, 59, 1173-1188.

358. Asenath Smith, E.; Chen, W. How to Prevent the Loss of Surface Functionality Derived from Aminosilanes. *Langmuir* **2008**, 24, 12405-12409.

359. Wang, Y.; Gao, Q.; You, Q.; Liao, G.; Xia, H.; Wang, D. Porous Polyimide Framework: A Novel Versatile Adsorbent for Highly Efficient Removals of Azo Dye and Antibiotic. *React. Funct. Polym.* **2016**, 103, 9-16.

360. Kallury, K. M. R.; Debono, R. F.; Krull, U. J.; Thompson, M. Covalent Binding of Amino, Carboxy, and Nitro-Substituted Aminopropyltriethoxysilanes to Oxidized Silicon Surfaces and Their Interaction with Octadecanamine and Octadecanoic Acid Studied by X-Ray Photoelectron Spectroscopy and Ellipsometry. *J. Adhes. Sci. Technol.* **1991**, 5, 801-814.

361. Asenath-Smith, E.; Chen, W. How to Prevent the Loss of Surface Functionality Derived from Aminosilanes. *Langmuir* **2008**, 24, 12405-12409.

362. Asefa, T.; MacLachlan, M. J.; Coombs, N.; Ozin, G. A. Periodic Mesoporous Organosilicas with Organic Groups inside the Channel Walls. *Nature* **1999**, 402, 867-871.

363. Hao, N.; Yang, H.; Li, L.; Li, L.; Tang, F. The Shape Effect of Mesoporous Silica Nanoparticles on Intracellular Reactive Oxygen Species in A375 Cells. *New J. Chem.* **2014**, 38, 4258-4266.

364. Raghava Rao, J.; Chandrababu, N. K.; Muralidharan, C.; Nair, B. U.; Rao, P. G.; Ramasami, T. Recouping the Wastewater: A Way Forward for Cleaner Leather Processing. *Journal of Cleaner Production* **2003**, 11, 591-599.

365. Tamura, Z.; Maeda, M. [Differences between Phthaleins and Sulfonphthaleins]. *Yakugaku Zasshi* **1997**, 117, 764-770.

366. Ghaly, A.; Ananthashankar, R.; Alhattab, M.; Ramakrishnan, V. Production, Characterization and Treatment of Textile Effluents: A Critical Review. *Journal of Chemical Engineering & Process Technology* **2014**, 5, 1-18.

367. Larson, J. W.; McMahon, T. B. Gas-Phase Bihalide and Pseudobihalide Ions. An Ion Cyclotron Resonance Determination of Hydrogen Bond Energies in Xhy- Species (X, Y = F, Cl, Br, Cn). *Inorg. Chem.* **1984**, 23, 2029-2033.

368. He, X.; Male, K. B.; Nesterenko, P. N.; Brabazon, D.; Paull, B.; Luong, J. H. Adsorption and Desorption of Methylene Blue on Porous Carbon Monoliths and Nanocrystalline Cellulose. *ACS applied materials & interfaces* **2013**, 5, 8796-8804.

369. Merouani, S.; Hamdaoui, O.; Saoudi, F.; Chiha, M. Sonochemical Degradation of Rhodamine B in Aqueous Phase: Effects of Additives. *Chem. Eng. J.* **2010**, 158, 550-557.

370. Sabnis, R. *Handbook of Biological Dyes and Stains: Synthesis and Industrial Applications*. 1st ed.; John Wiley & Sons: Hoboken, 2010.

371. Lagergren, S. About the Theory of So-Called Adsorption of Soluble Substances. *Kungliga Svenska Vetenskapsakademiens Handlingar* **1898**, 24, 1-39.

372. Ho, Y.-S.; McKay, G. Sorption of Dye from Aqueous Solution by Peat. *Chem. Eng. J.* **1998**, 70, 115-124.

373. Foo, K. Y.; Hameed, B. H. Insights into the Modeling of Adsorption Isotherm Systems. *Chem. Eng. J.* **2010**, 156, 2-10.

374. Farrukh, A.; Akram, A.; Ghaffar, A.; Hanif, S.; Hamid, A.; Duran, H.; Yameen, B. Design of Polymer-Brush-Grafted Magnetic Nanoparticles for Highly Efficient Water Remediation. *ACS applied materials & interfaces* **2013**, 5, 3784-3793.

375. Abdullah, N.; Othaman, R.; Abdullah, I.; Jon, N.; Baharum, A. Studies on the Adsorption of Phenol Red Dye Using Silica-Filled Enr/Pvc Beads. *Journal of Emerging Trends in Engineering and Applied Sciences* **2012**, 3, 845-850.

376. Mittal, A.; Kaur, D.; Malviya, A.; Mittal, J.; Gupta, V. Adsorption Studies on the Removal of Coloring Agent Phenol Red from Wastewater Using Waste Materials as Adsorbents. *J. Colloid Interface Sci.* **2009**, 337, 345-354.

377. Zhou, L.; Gao, C.; Xu, W. Magnetic Dendritic Materials for Highly Efficient Adsorption of Dyes and Drugs. *ACS applied materials & interfaces* **2010**, 2, 1483-1491.

378. Lin, S.-H.; Juang, R.-S. Adsorption of Phenol and Its Derivatives from Water Using Synthetic Resins and Low-Cost Natural Adsorbents: A Review. *J. Environ. Manage.* **2009**, 90, 1336-1349.

379. Ahmaruzzaman, M. Adsorption of Phenolic Compounds on Low-Cost Adsorbents: A Review. *Adv. Colloid Interface Sci.* **2008**, 143, 48-67.

380. Forouzanfar, M. H.; Moran, A. E.; Flaxman, A. D.; Roth, G.; Mensah, G. A.; Ezzati, M.; Naghavi, M.; Murray, C. J. Assessing the Global Burden of Ischemic Heart Disease, Part 2: Analytic Methods and Estimates of the Global Epidemiology of Ischemic Heart Disease in 2010. *Global Heart* **2012**, 7, 331-342.

381. Laflamme, M. A.; Murry, C. E. Heart Regeneration. *Nature* **2011**, 473, 326-335.

382. Burridge, P. W.; Sharma, A.; Wu, J. C. Genetic and Epigenetic Regulation of Human Cardiac Reprogramming and Differentiation in Regenerative Medicine. *Annu. Rev. Genet.* **2015**, 49, 461-484.

383. Lee, R. T.; Walsh, K. The Future of Cardiovascular Regenerative Medicine. *Circulation* **2016**, 133, 2618-2625.

384. Meyer, G. P.; Wollert, K. C.; Lotz, J.; Steffens, J.; Lippolt, P.; Fichtner, S.; Hecker, H.; Schaefer, A.; Arseniev, L.; Hertenstein, B. Intracoronary Bone Marrow Cell Transfer after Myocardial Infarction: Eighteen Months' Follow-up Data from the Randomized, Controlled Boost (Bone Marrow Transfer to Enhance St-Elevation Infarct Regeneration) Trial. *Circulation* **2006**, 113, 1287-1294.

385. Lee, R. H.; Pulin, A. A.; Seo, M. J.; Kota, D. J.; Ylostalo, J.; Larson, B. L.; Semprun-Prieto, L.; Delafontaine, P.; Prockop, D. J. Intravenous Hmscs Improve Myocardial Infarction in Mice Because Cells Embolized in Lung Are Activated to Secrete the Anti-Inflammatory Protein Tsg-6. *Cell stem cell* **2009**, 5, 54-63.

386. Hoover-Plow, J.; Gong, Y. Challenges for Heart Disease Stem Cell Therapy. *Vascular Health and Risk Management* **2012**, 8, 99-113.

387. Mohr, A.; Zwacka, R. The Future of Mesenchymal Stem Cell-Based Therapeutic Approaches for Cancer - from Cells to Ghosts. *Cancer Lett.* **2018**, 414, 239-249.

388. Nguyen, P. K.; Lan, F.; Wang, Y. M.; Wu, J. C. Imaging Guiding the Clinical Translation of Cardiac Stem Cell Therapy. *Circul. Res.* **2011**, 109, 962-979.

389. Shen, H.; Cui, G.; Li, Y.; Ye, W.; Sun, Y.; Zhang, Z.; Li, J.; Xu, G.; Zeng, X.; Zhang, Y.; Zhang, W.; Huang, Z.; Chen, W.; Shen, Z. Follistatin-Like 1 Protects Mesenchymal Stem Cells from Hypoxic Damage and Enhances Their Therapeutic Efficacy in a Mouse Myocardial Infarction Model. *Stem Cell Research & Therapy* **2019**, 10, 17-30.

390. Christman, K. L.; Vardanian, A. J.; Fang, Q.; Sievers, R. E.; Fok, H. H.; Lee, R. J. Injectable Fibrin Scaffold Improves Cell Transplant Survival, Reduces Infarct Expansion, and Induces Neovasculature Formation in Ischemic Myocardium. *J. Am. Coll. Cardiol.* **2004**, 44, 654-660.

391. Cheng, K.; Li, T.-S.; Malliaras, K.; Davis, D. R.; Zhang, Y.; Marbán, E. Magnetic Targeting Enhances Engraftment and Functional Benefit of Iron-Labeled Cardiosphere-Derived Cells in Myocardial Infarction. *Circul. Res.* **2010**, 106, 1570-1581.

392. Ottersbach, A.; Mykhaylyk, O.; Heidsieck, A.; Eberbeck, D.; Rieck, S.; Zimmermann, K.; Breitbach, M.; Engelbrecht, B.; Brügmann, T.; Hesse, M.; Welz, A.; Sasse, P.; Wenzel, D.; Plank, C.; Gleich, B.; Hölzel, M.; Bloch, W.; Pfeifer, A.; Fleischmann, B. K.; Roell, W. Improved Heart Repair Upon Myocardial Infarction: Combination of Magnetic Nanoparticles and Tailored Magnets Strongly Increases Engraftment of Myocytes. *Biomaterials* **2018**, 155, 176-190.

393. Moysidis, S. N.; Alvarez-Delfin, K.; Peschansky, V. J.; Salero, E.; Weisman, A. D.; Bartakova, A.; Raffa, G. A.; Merkhofer, R. M.; Kador, K. E.; Kunzevitzky, N. J.; Goldberg, J. L. Magnetic Field-Guided Cell Delivery with Nanoparticle-Loaded Human Corneal Endothelial Cells. *Nanomed. Nanotechnol. Biol. Med.* **2015**, 11, 499-509.

394. Ruan, J.; Ji, J.; Song, H.; Qian, Q.; Wang, K.; Wang, C.; Cui, D. Fluorescent Magnetic Nanoparticle-Labeled Mesenchymal Stem Cells for Targeted Imaging and Hyperthermia Therapy of in Vivo Gastric Cancer. *Nanoscale Reseach Letters* **2012**, 7, 309-320.

395. Zhu, K.; Li, J.; Wang, Y.; Lai, H.; Wang, C. Nanoparticles-Assisted Stem Cell Therapy for Ischemic Heart Disease. *Stem Cells International* **2016**, 2016, 1384658-1384664.

396. Tong, C. L.; Eroglu, E.; Raston, C. L. In Situ Synthesis of Phosphate Binding Mesocellular Siliceous Foams Impregnated with Iron Oxide Nanoparticles. *RSC Advances* **2014**, 4, 46718-46722.

397. Lee, S. S.; Riduan, S. N.; Erathodiyil, N.; Lim, J.; Cheong, J. L.; Cha, J.; Han, Y.; Ying, J. Y. Magnetic Nanoparticles Entrapped in Siliceous Mesocellular Foam: A New Catalyst Support. *Chemistry* **2012**, 18, 7394-7403.

398. Mascolo, M.; Pei, Y.; Ring, T. Room Temperature Co-Precipitation Synthesis of Magnetite Nanoparticles in a Large Ph Window with Different Bases. *Materials* **2013**, 6, 5549-5567.

399. Gu, L.; Park, J.-H.; Duong, K. H.; Ruoslahti, E.; Sailor, M. J. Magnetic Luminescent Porous Silicon Microparticles for Localized Delivery of Molecular Drug Payloads. *Small* **2010**, 6, 2546-2552.

400. Zhu, Y. *Modern Techniques for Characterizing Magnetic Materials*. Springer Science & Business Media: 2005.

401. Sunday, K. J. *Development of Ferrite-Coated Soft Magnetic Composites: Correlation of Microstructure to Magnetic Properties*. 2017.

402. Kolhatkar, A. G.; Jamison, A. C.; Litvinov, D.; Willson, R. C.; Lee, T. R. Tuning the Magnetic Properties of Nanoparticles. *International journal of molecular sciences* **2013**, 14, 15977-16009.

403. Nidhin, M.; Indumathy, R.; Sreeram, K.; Nair, B. U. Synthesis of Iron Oxide Nanoparticles of Narrow Size Distribution on Polysaccharide Templates. *Bull. Mater. Sci.* **2008**, 31, 93-96.

404. Doherty, G. J.; McMahon, H. T. Mechanisms of Endocytosis. *Annu. Rev. Biochem.* **2009**, 78, 857-902.

405. Rodriguez-Porcel, M.; Gheysens, O.; Chen, I. Y.; Wu, J. C.; Gambhir, S. S. Image-Guided Cardiac Cell Delivery Using High-Resolution Small-Animal Ultrasound. *Mol.*

Ther. **2005**, 12, 1142-1147.

406. Tong, S.; Hou, S.; Zheng, Z.; Zhou, J.; Bao, G. Coating Optimization of Superparamagnetic Iron Oxide Nanoparticles for High T2 Relaxivity. *Nano Lett.* **2010**, 10, 4607-4613.

407. Lee, N.; Kim, H.; Choi, S. H.; Park, M.; Kim, D.; Kim, H.-C.; Choi, Y.; Lin, S.; Kim, B. H.; Jung, H. S.; Kim, H.; Park, K. S.; Moon, W. K.; Hyeon, T. Magnetosome-Like Ferrimagnetic Iron Oxide Nanocubes for Highly Sensitive Mri of Single Cells and Transplanted Pancreatic Islets. *Proceedings of the National Academy of Sciences* **2011**, 108, 2662-2667.

408. Xie, X.; Shen, Y.; Chen, J.; Huang, Z.; Ge, J. Mineralocorticoid Receptor Deficiency Improves the Therapeutic Effects of Mesenchymal Stem Cells for Myocardial Infarction Via Enhanced Cell Survival. *J. Cell. Mol. Med.* **2019**, 23, 1246-1256.

409. Schmidt, M. B.; Chen, E. H.; Lynch, S. E. A Review of the Effects of Insulin-Like Growth Factor and Platelet Derived Growth Factor on in Vivo Cartilage Healing and Repair. *Osteoarthritis Cartilage* **2006**, 14, 403-412.

410. Pervin, F.; Chen, W. W. Mechanically Similar Gel Simulants for Brain Tissues. *Dynamic Behavior of Materials* **2011**, 1, 9-13.

411. Chiu, J.-J.; Chien, S. Effects of Disturbed Flow on Vascular Endothelium: Pathophysiological Basis and Clinical Perspectives. *Physiol. Rev.* **2011**, 91, 327-387.

412. Jiang, Y.; Kohara, K.; Hiwada, K. Low Wall Shear Stress in Carotid Arteries in Subjects with Left Ventricular Hypertrophy. *American Journal of Hypertension* **2000**, 13, 892-898.

413. Yamada, S.; Arrell, D. K.; Martinez-Fernandez, A.; Behfar, A.; Kane, G. C.; Perez-Terzic, C. M.; Crespo-Diaz, R. J.; McDonald, R. J.; Wyles, S. P.; Zlatkovic-Lindor, J.; Nelson, T. J.; Terzic, A. Regenerative Therapy Prevents Heart Failure Progression in Dyssynchronous Nonischemic Narrow Qrs Cardiomyopathy. *Journal of the American Heart Association* **2015**, 4, e001614.

414. Xiao, Y.-F.; Min, J.-Y.; Morgan, J. P. Immunosuppression and Xenotransplantation of Cells for Cardiac Repair. *The Annals of Thoracic Surgery* **2004**, 77, 737-744.

415. Golpanian, S.; Schulman, I. H.; Ebert, R. F.; Heldman, A. W.; DiFede, D. L.; Yang, P. C.; Wu, J. C.; Bolli, R.; Perin, E. C.; Moye, L.; Simari, R. D.; Wolf, A.; Hare, J. M.; Cardiovasc Cell, T. Concise Review: Review and Perspective of Cell Dosage and Routes of Administration from Preclinical and Clinical Studies of Stem Cell Therapy for Heart Disease. *Stem Cells Translational Medicine* **2016**, 5, 186-191.

416. Nguyen, P. K.; Rhee, J. W.; Wu, J. C. Adult Stem Cell Therapy and Heart Failure, 2000 to 2016 a Systematic Review. *Jama Cardiology* **2016**, 1, 831-841.

417. Reisner, S. A.; Lvsvanskv, P.; Agmon, Y.; Mutlak, D.; Lcssick, J.; Friccinian, Z. Global Longitudinal Strain: A Novel Index of Left Ventricular Systolic Function. *Journal of the American Society of Echocardiography* **2004**, 17, 630-633.

418. Ottersbach, A.; Mykhaylyk, O.; Heidsieck, A.; Eberbeck, D.; Rieck, S.; Zimmermann, K.; Breitbach, M.; Engelbrecht, B.; Brugmann, T.; Hesse, M.; Welz, A.; Sasse, P.; Wenzel, D.; Plank, C.; Gleich, B.; Holzel, M.; Bloch, W.; Pfeifer, A.; Fleischmann, B. K.; Roell, W. Improved Heart Repair Upon Myocardial Infarction: Combination of Magnetic Nanoparticles and Tailored Magnets Strongly Increases Engraftment of Myocytes. *Biomaterials* **2018**, 155, 176-190.

419. Hanahan, D.; Weinberg, R. A. The Hallmarks of Cancer. *Cell* **2000**, 100, 57-70.